This is to certify that the

dissertation entitled

Perpendicular Giant Magnetoresistance: Study and Application of Spin Dependent Scattering in Magnetic Multilayers of Co/Cu and $Ni_{84}Fe_{16}$/Cu.

presented by

Paul Robert Joseph Holody

has been accepted towards fulfillment
of the requirements for

Ph.D. degree in Physics

Major professor

Date 3/27/96

Perpendicular Giant Magnetoresistance: Study and Application of Spin Dependent Scattering in Magnetic Multilayers of Co/Cu and $Ni_{84}Fe_{16}$/Cu.

By

Paul Robert Joseph Holody

A DISSERTATION

Submitted to
Michigan State University
in partial fulfillment of the requirements
for the degree of

DOCTOR OF PHILOSOPHY

Department of Physics and Astronomy

1996

ABSTRACT

Perpendicular Giant Magnetoresistance: Study and Application of Spin Dependent Scattering in Magnetic Multilayers of Co/Cu and $Ni_{84}Fe_{16}$/Cu.

By

Paul Robert Joseph Holody

Perpendicular transport through magnetic multilayers has been successfully described by the two spin channel model. In the limit where spin flip scattering can be neglected, the transport current is carried by parallel channels of spin up and spin down electrons. Large negative magnetoresistances arise from spin dependent scattering occurring in these channels. Electrons with spins parallel to the local magnetization undergo a different amount of scattering from those with spins antiparallel to the local magnetization. Consequently the multilayer's resistance can be controlled by the relative orientation of the ferromagnetic layers' magnetizations. Usually with the relative orientation antiparallel (parallel) the multilayer has a high (low) resistance.

In this dissertation, an analysis of perpendicular transport measurements in the context of the two spin channel model provides quantitative information about the amounts of spin dependent scattering at the Ferromagnetic/Normal metal interfaces and in the bulk Ferromagnet metal for the Co/Cu and $Ni_{84}Fe_{16}$/Cu systems ($Ni_{84}Fe_{16}$=Py). This is essen-

tial t

Magnet

scatter

scatter

determi

previous

Mea

study th

is preser

the two

magneto

results ju

The

commerc

multilaye

which ha

high as

extend su

tial to the understanding of the scattering mechanisms involved in Giant Magnetoresistance. Our results show a significant bulk contribution to the spin dependent scattering; but, it is the interfaces which make the larger contribution to spin dependent scattering in these systems. A larger bulk spin dependent scattering asymmetry was determined for the Py/Cu multilayers, but not as large as expected from data derived previously from ternary alloys.

Measurements were made on several Co/CuX series (where X=Pt, Mn, Ge and Ni) to study the transport properties of magnetic multilayers when significant spin flip scattering is present in the system. Analysis was done using the Valet-Fert theory which generalizes the two spin channel model to include finite spin diffusion lengths. A sharp drop in the magnetoresistance is observed when the spin diffusion length $\approx$ layer thickness. These results justify the infinite spin diffusion length assumed in the previous Co/Cu study.

The transport properties of magnetic multilayers have an enormous potential for commercial applications. As a way of demonstrating the utility of multilayers, several multilayer systems were designed to meet specific requirements. These included systems which had positive magnetoresistances as well as systems which exhibited $(\Delta R/R)/\Delta H$ as high as 10%/Oe in very low magnetic fields at 4.2K. Several attempts were made to extend such high sensitivities to room temperature.

To my parents

ACKNOWLEDGMENTS

Many thanks go to my thesis advisor, Professor Peter A. Schroeder for his guidance and support for the duration of this project. I am especially grateful for his patience and encouragement during the writing of this dissertation. I would also like to thank Professors Jack Bass and William P. Pratt, Jr. for their helpful insights and enthusiastic discussions. It has been a very rewarding experience to be part of such a dynamic research group.

A special thanks goes to Reza Loloee for his help and instruction. Thanks are due to Tom Palazzolo, Jim Muns and Tom Hudson for their input on design and to Vivion Shull and Carol Flegler for their help with the EDX studies. Discussions with my co-workers: S.F. Lee, Q. Yang, L.L. Henry, W.C. Chiang, S.H. Hsu and S. Steenwyk have contributed greatly to my understanding. Also, our collaborators in Orsay: A. Fert, A. Barthélémy, J.L. Duvail, L.B. Steren and R. Morel have made many insightful comments and suggestions on this project.

I am the most thankful to my parents and brothers for their generous love and support over the past 29 years. A big GWI goes to Pat, Rob, Duane, Tim and Mike for their invaluable friendship the past 13 years. I would also like to thank Mike Franklin for getting me out of the PA building for some "hoops" on a semi-regular basis.

I would like to acknowledge the Ford Scientific Laboratory for their generosity in funding my assistantship. Additional financial support for this project was generously provided by the National Science Foundation through MR-SEC and the US-France Cooperative Program and by Michigan State University's Center for Fundamental Materials Research.

TABLE OF CONTENTS

LIST OF TABLES

5.10

5.11

5.12

6.1

6.2

6.3

6.4

6.5

6.6

6.7a

6.7b

6.8a

LIST OF FIGURES

2.3 D
la

2.4 D
H
w
in
vie
ab
co

2.5 Sch

3.1 Sch
mul

3.2 θ-2θ
Cu

3.3 θ-2θ
Cu

3.4 θ-2θ
Cu

3.5 Nb s
and

3.6 Sche
long

3.7 Sche

4.1 S
ar
ba
fe

4.2 Sc
the
sa

4.3 Eq

4.4 Th
bil
va
mu

4.5 Th
bil
va
10
72

4.6 Eff
me
sp

4.7 Sch
mu
cur

4.8 Spi
Sca
cla

5.1 T
m

5.2 M
th
g

5.3 P
[C
AR
√A
to a

5.4 Plo
[Co
AR
√A
to al

5.5 Plots
[Co
AR
√AR
to all

5.6 AR_T
The l
to all
state

5.7 The f
[Py6
much

5.8 The
Py(5.0
for the

6.4

6.5

6.6

6.7

6.8

6.9

6.10

6.11

6.12

6.13

6.14

6.15

6.16

6.17

6.18

6.19

Chapter 1:

Introduction to Giant Magnetoresistance

Magnetoresistance is the change in electrical resistance of a material in response to a magnetic field. All metals, pure or alloyed, have a magnetoresistance (MR) due to the Lorentz force which arises from the motion of electrons in a magnetic field. This effect increases a material's electrical resistivity with an applied magnetic field. The effect is very small at room temperatures[1] and will not be of concern in this work. In very pure metals, the MR changes monotonically with increasing applied field, and the MR is defined relative to the initial H=0 resistance.

Some ferromagnetic alloys such as permalloy ($Ni_{80}Fe_{20}$) exhibit an enhanced MR due to the spontaneous resistivity anisotropy of the material. (Permalloy will be represented by the symbol Py unless otherwise stated.) With this type of magnetoresistance (AMR) the resistance of a material depends on the relative orientation of the current through the material and the magnetization of the material[2]. Typically this effect gives MR's of a few

percent. The AMR of permalloy films has been utilized since 1991 by IBM for read heads in hard disk drives[3].

Technological advances during the past decade have allowed almost atomic control of the deposition process in making thin metallic films. This has allowed the study of artificially grown layered metallic structures. Of great interest both academically and technologically, is the recently emerging field of magnetic multilayers. A magnetic multilayer is composed of a single, repeated unit cell, typically a ferromagnetic (F) layer such as Co and a "normal", non-magnetic (N) layer like Cu, written as F/N or Co/Cu. The unit cell may indeed be more complex[4], as will be demonstrated later, and recently the properties of magnetic multilayers composed of only F metals[5] have been explored. These structures exhibit large changes in resistivity in response to a magnetic field. This type of magnetoresistance is called Giant Magnetoresistance (GMR).

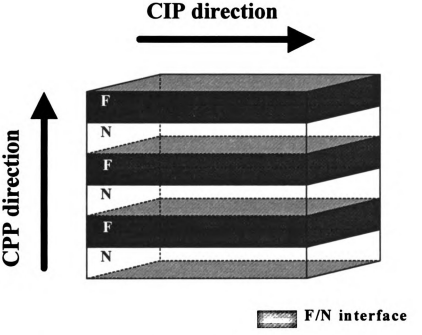

Figure 1.1: Flow of the measuring current for the CIP and CPP geometries.

Fo

is mea

to the

resista

1.1.

Gra

shown i

magnetic

saturation

state of t

the H_s sta

useful to

Where R_s

This s

defined in

H_s, usuall

resistance

highest sa

discussed.

For layered GMR structures there are two types of MR measurements. The resistance is measured with either the current flowing along the plane of the layers or perpendicular to the plane of the layers. These are, respectively, the so called current-in-plane or CIP resistance and the current-perpendicular-to-plane or CPP resistance, illustrated in Figure 1.1.

Graphs of CIP and CPP resistance as a function of field for a Co/Cu sample are shown in Figure 1.2. One of the differences between the MR of metals and that of magnetic multilayers is that the MR of magnetic multilayers usually saturates at a saturation field of H_S as in Figure 1.2. The saturated resistance represents a better defined state of the system than the H=0 state since the magnetic configuration of the sample in the H_S state is known. (Further discussion of this is given later.) Consequently it is more useful to define the MR by equation 1.1.

$$MR = \frac{R(H) - R(H_S)}{R(H_S)} \qquad 1.1$$

Where R(H) is the resistance in field H.

This study will focus on three specific states of a multilayer's CPP resistance. As defined in Figure 1.2, these states are: (1) The initial, as prepared, state of the resistance, H_0, usually the sample's highest resistance state. (2) The saturated state, H_S, the sample's resistance after all the F layer moments have been aligned. (3) The peak state, H_P, the highest sample resistance after saturation. A demagnetized state, H_D, will also be briefly discussed.

R_{CPP} (mΩ)

Figure 1.2: Th
a) CPP and b)
a Nb Co/9 Cu
thin film of Co

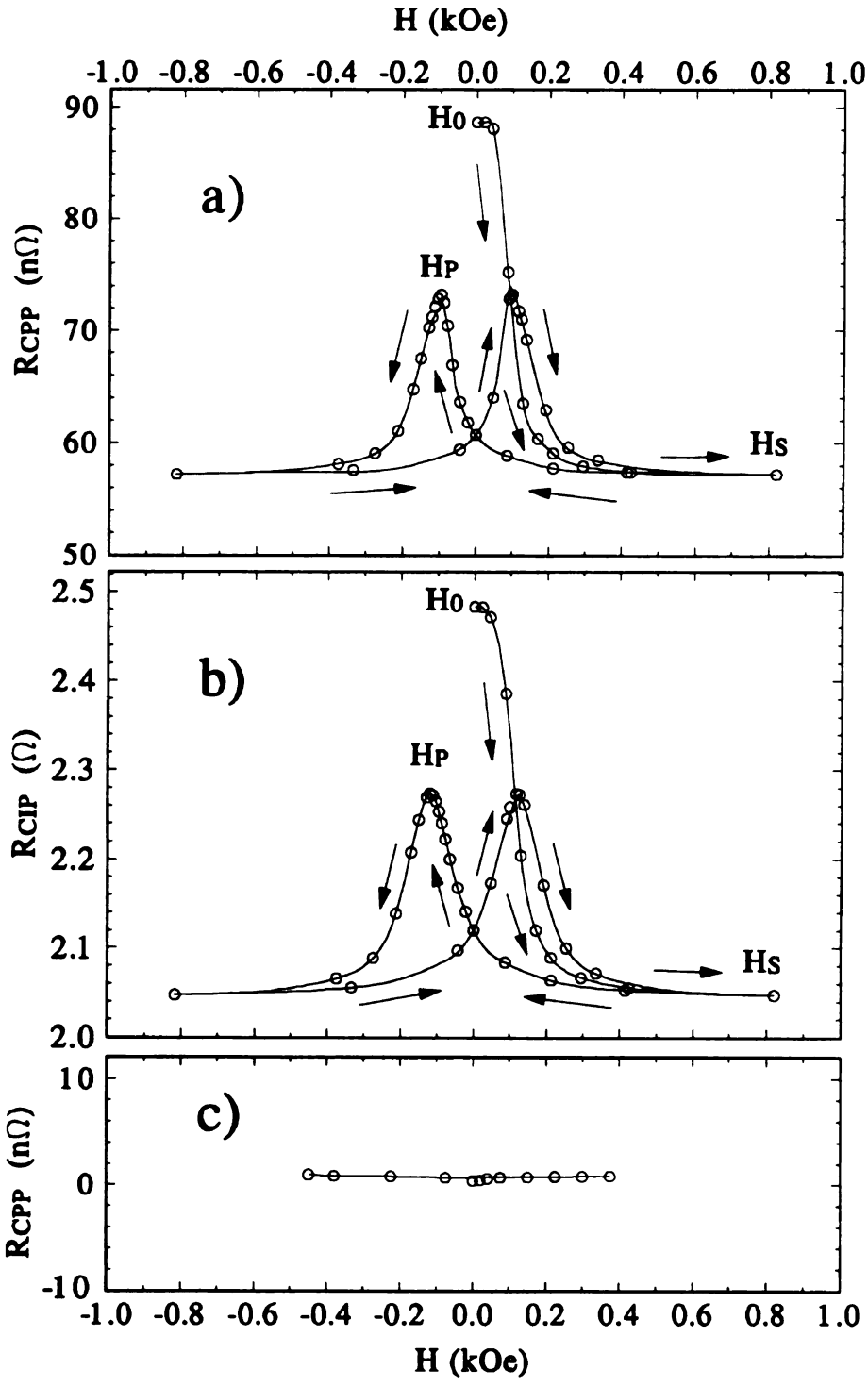

Figure 1.2: The field dependent resistance of a *[Co(6.0nm)/Cu(6.0)]×60* multilayer in the a) CPP and b) CIP geometries. For comparison, c) the field dependent CPP resistance of a *Nb/Co(9.0nm)/Nb* trilayer is shown. Note that the change in resistance for the single thin film of Co is orders of magnitude smaller than it is for the multilayer.

Alth

discover

Universit

of artific

applied fi

given the

much larg

have repo

IBM Alma

position in

The Fe

Grünberg's

layers in tr

Parkin four

ferromagnet

Oscillations

52 for an ex

with increasi

showed that

multilayered s

The mech

conduction ele

Although unusual MR effects in magnetic multilayers were reported earlier[6], the discovery of MR in magnetic mulilayers is attributed to Albert Fert's group at the Université of Paris-Sud in Orsay, France[7], who observed large changes in the resistivity of artificially layered Fe/Cr films. Upon saturating these Fe/Cr multilayers in a 20kOe applied field, they observed a reduction of up to 50% in the resistivity. This effect was given the name Giant Magnetoresistance (GMR) because the magnitude of the MR is much larger than the MR observed in the isolated F metal. Since then numerous groups have reported GMR effects in many different F/N systems. Most notably Stuart Parkin of IBM Almaden has provided a systematic study of the elements as a function of their position in the periodic table[8].

The Fe/Cr multilayer experiments done in Fert's groups were prompted by Grünberg's[9] 1986 discovery of antiferromagnetic exchange coupling between the Fe layers in trilayer sandwiches of Fe/Cr/Fe for a Cr thickness of 1.0nm. Later in 1990, Parkin found that this exchange coupling oscillated between antiferromagnetic and ferromagnetic depending on the thickness of the non-magnetic spacer layer[10]. Oscillations in the MR accompanied the oscillations in the exchange coupling (see Figure 5.2 for an example of such oscillations). The strength of the coupling also diminished with increasing spacer thickness. Subsequent investigations by Parkin[8,10,11] and others[12] showed that this oscillating exchange coupling existed for several different F/N multilayered systems.

The mechanism responsible for GMR is the spin-dependent scattering of the conduction electrons at the F/N interfaces and in the bulk F layers. In a ferromagnetic *3d*

transition

spin-dow

which dep

to the loc

carry the c

In a m

electron sp

coupling w

shown sch

magnetizat

magnetizati

electrons tha

keeping trac

direction of

upon whether

magnetizatio

both the spin u

length of the m

can be overco

configuration o

electrons in one

the other spin c

transition metal, the *d* band is shifted in energy becoming asymmetric for spin-up and spin-down electrons. Later we will show that this leads to conduction electron scattering which depends on whether the electrons have their spins oriented parallel or antiparallel to the local magnetization. Neglecting spin-flips, these two spin channels independently carry the current in parallel.

In a multilayer, the magnetization of each F layer defines up and down for the electron spins. For an appropriate choice of the thickness of the N metal, exchange coupling will magnetically order the multilayer antiferromagnetically (AF)[8,10,11,12], as shown schematically in Figure 1.3. Strong AF coupling forces adjacent F layer magnetizations to be antiparallel. (This antiparallel configuration of F layer magnetizations will be designated as the *AP state* of the sample.) Therefore conduction electrons that were spin up in one layer are now spin down in the next. As a way of keeping track of each spin channel, an absolute spin direction may be defined as the direction of the applied field. In this absolute frame, the scattering rates now depend upon whether electrons have their spins oriented either parallel or antiparallel to the local magnetization, i.e. the magnetization of a particular F layer. In the AP state, electrons in both the spin up and spin down channels undergo the same amount of scattering over the length of the multilayer. With a sufficiently large applied field the exchange coupling can be overcome, forcing every F layer to be parallel to one another. (The parallel configuration of F layer magnetizations will be designated as the *P state*.) In the P state, electrons in one spin channel (down for example) will be scattered less than electrons in the other spin channel throughout the entire multilayer. This in effect short circuits the

current through one of the spin channels (down in this example) resulting in a lowering of the sample's overall resistance. The resulting change in resistivity is generally negative (the resistance drops), but later in this study a positive GMR will be discussed in detail, with the main point that multilayers may easily be designed to meet specific needs.

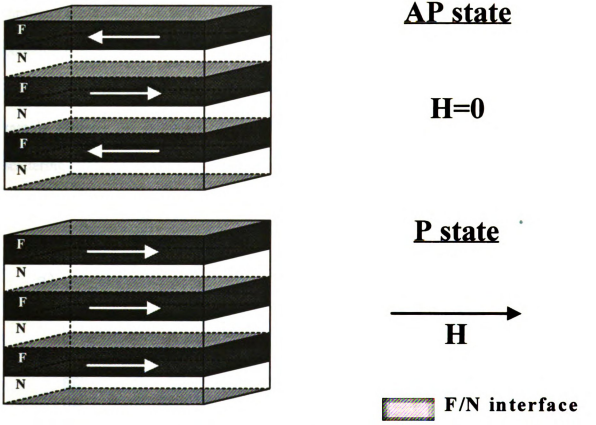

Figure 1.3: A representation of the antiparallel (AP) and parallel (P) configurations of the F layer moments.

There are at least two possible causes for spin dependent scattering. The first cause will be treated in detail in section 4.1 and reflects that electron scattering from impurities depends on the density of states of the spin up and spin down electrons. In Figure 1.4 a schematic representation of the density of states is shown for a) a normal metal and b) a

ferromag

is paralle

of states

different s

through th

potential is

potential d

sample cha

scattering ra

a)

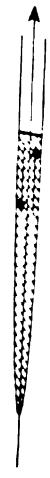

4s

Figure 1.4: Sch

non-magnetic ma

ferromagnetic metal like Co. The scattering of an electron depends upon whether its spin is parallel or antiparallel to the local magnetic moment, a result of the spin-split density of states in F metals like Fe, Co and Ni. This spin dependence in the *d* band causes different scattering rates for spin up electrons and spin down electrons as they propagate through the sample. The second cause of spin dependent scattering is that the multilayer potential is itself spin dependent so that electrons in the spin down channel experience a potential different from those electrons in the spin up channel. Applying a field to the sample changes the potentials in each channel which correspond to changes in the scattering rates of both spin up and spin down electrons.

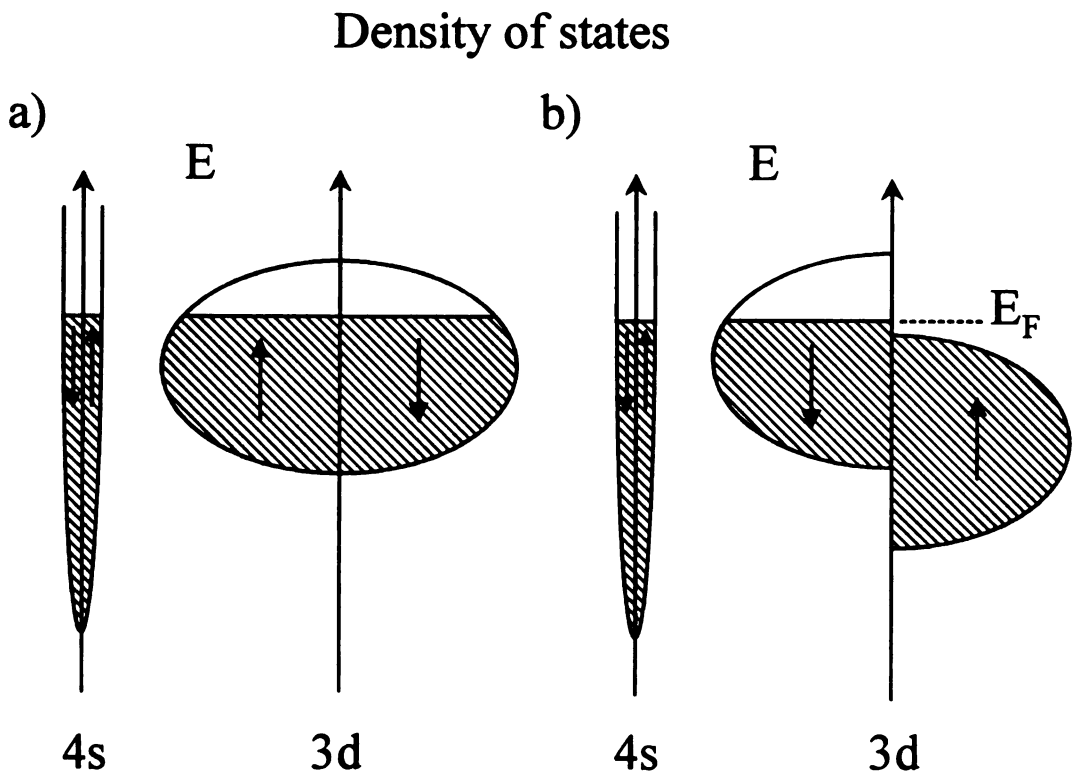

Figure 1.4: Schematic representation of the density of states in the *s* and *d* bands of a) a non-magnetic metal and b) a ferromagnetic metal, like Co.

Exp

for the C

a multilay

gives a sca

10-100mΩ

the Nb str

multilayer

will be un

measuremen

top Nb lead.

Nb strips an

potential dro

multilayer re

SQUID circui

Recently,

sample's area

Naval Researc

create pillars w

spin valves[5].

deposited multi

Experimentally the CIP resistances typically range from 0.01Ω to 1.0Ω while those for the CPP depend critically on the cross sectional area of the sample since the length of a multilayer is typically between 100-1000nm. In these studies an *in-situ* masking system gives a sample area of ≈ 1.2 mm^2, illustrated in Figure 1.5, resulting in CPP resistances of 10-100nΩ[13]. The current is injected into the Nb pads labeled by I in Figure 1.5. At 4.2K the Nb strips are superconducting, forming an equipotential surface above and below the multilayer. Since the superconducting Nb leads are equipotentials the current distribution will be uniform over the cross sectional area of the sample, which is important for a direct measurement of the intrinsic MR. The current takes the path of least resistance from the top Nb lead, perpendicularly through that section of multilayer sandwiched between the Nb strips and into the bottom Nb lead. The multilayer is not superconducting and a potential drop occurs across the multilayer. The large cross sectional area of the multilayer relative to its total thickness requires attaching a sensitive detector, namely a SQUID circuit, across the Nb pads labeled V in Figure 1.5 to measure the potential drop.

Recently, M.A.M. Gijs, *et al.*[14] used complex lithographic techniques to reduce the sample's area to a few μm^2, giving a CPP resistance of 0.01Ω. Another group at the Naval Research Laboratory headed by G. Prinz has also used lithographic techniques to create pillars with small cross sections (less than 5μm^2) for CPP-MR measurements of spin valves[15]. CPP-MR measurements have also been made on electro-chemically deposited multilayers of Co/Cu in nanopores 100nm in width[16,17,18].

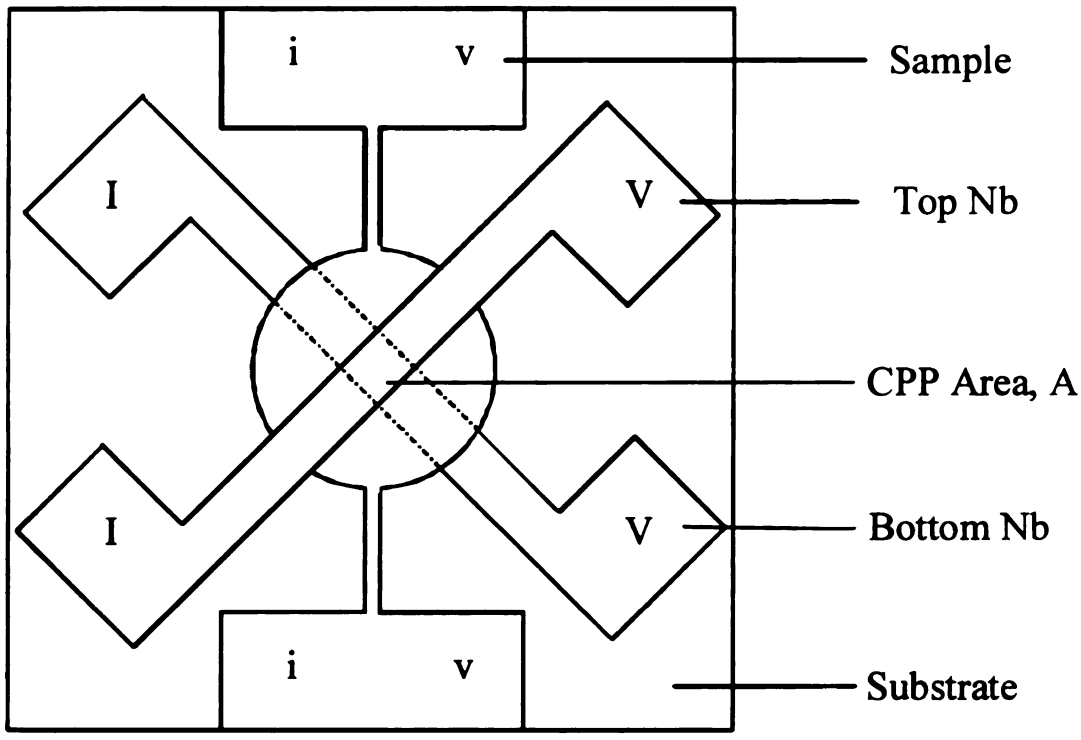

Figure 1.5: The sample shape used for measuring both the CPP resistance ($R=V/I$) and the CIP resistance ($R=v/i$). The CIP resistance is dominated by the narrow strips above and below the circular region of the sample.

In the CIP geometry, the separation of the bulk asymmetry parameters (defined in chapter 4) from the interface asymmetry parameters is quite difficult. This is due to the non-uniform current distribution throughout the multilayer, both layer to layer and within each layer. The current carried by both the F layers and the N layers is connected through the transmission of electrons at the F/N interfaces. Spin-polarized electrons emerging from one F layer undergo spin-dependent scattering at the F/N interface or in the bulk F material of the adjacent F layers. This requires that an electron be able to sample at least two F layers before being scattered, meaning that it is heavily dependent upon the elastic

mean fre

less than

greater th

are no lo

scale in th

The C

through th

(or the *eff*

causing a

accumulatio

equilibrate t

relaxation ma

locally, or do

to the drivin

relaxation pro

observed. Th

which an elec

longer than t

fundamental le

sample in the

scattering para

mean free path (mfp) of the electron. For sputtered samples the elastic mfp is generally less than 10nm. For samples with t_F (the F layer thickness) or t_N (the N layer thickness) greater than the elastic mfp, the CIP-MR decreases because the spin polarized electrons are no longer able to propagate to the next F layer and therefore the fundamental length scale in the CIP geometry is defined by the elastic mfp.

The CPP geometry is not plagued by this problem, all the electrons must propagate through the entire multilayer and thereby sample each F layer. It is the chemical potential (or the *effective* electric field) within a multilayer which varies from layer to layer causing a build-up of spin at the F/N interfaces. The new phenomenon of spin accumulation at the F/N interfaces only exists for the CPP geometry[19]. Working to equilibrate the spin asymmetry at the interfaces are spin relaxation processes. Spin relaxation may occur by either spin flip scattering[20], which mixes the two spin currents locally, or domain structure in the F layers[21], which tends to drive spin currents transverse to the driving current. It is the interplay between the spin accumulation and spin relaxation processes that determines the length scale over which large MR's may be observed. This length is called the spin diffusion length, ℓ_{sf}, a measure of the length over which an electron's spin remains polarized. The spin diffusion length is typically much longer than the elastic mfp in the CPP geometry and therefore ℓ_{sf} becomes the fundamental length scale of the system[20,22]. Since the current is the same throughout the sample in the CPP case, it is now possible to experimentally access the spin dependent scattering parameters which we will refer to as the asymmetry parameters both at the F/N

interface

applicati

Many

applicatio

with Dr.

demonstra

up to freq

sensing cir

GMR sens

A biasing fi

state. As a t

detected by

voltage fluct

voltage corre

output clearly

magnitude is

sensors whose

sensors surpas

sensitivity and

interfaces and in the bulk F layers. The CPP geometry is also advantageous from an applications point of view because the CPP-MR is typically double that of the CIP-MR.

Many in industry have recognized that GMR has a great potential for sensor applications including read heads in hard disk drives. Experiments done in conjunction with Dr. H. Holloway of the Ford Scientific Laboratory in Dearborn, Michigan have demonstrated the ability of GMR multilayers to detect magnetic field pulses of ≈300Oe up to frequencies of 1.0kHz. Figure 1.6 shows schematically, the layout of the simple sensing circuit and the timing gear used. A constant current of 1.0mA is put through a GMR sensing resistor specifically made by lithography to give a high 1.0kΩ resistance. A biasing field supplied by a small magnet puts the sensor in an intermediate resistance state. As a tooth on the gear rotates past the GMR film, the biasing field is modified and detected by an oscillation in the film's resistance. The changing resistance causes a voltage fluctuation easily measured with an oscilloscope. Each valley in the output voltage corresponds to the closest approach of a tooth on the gear to the GMR film. The output clearly shows when the missing tooth has rotated past the sensor. The signal magnitude is independent of frequency, an advantage compared with induction coil sensors whose response varies with the frequency of the fluctuations in the flux. GMR sensors surpass currently used Si Hall effect sensors by at least one order of magnitude in sensitivity and should be comparable in production cost in the near future.

a)

b)

Figure 1.6:
lithographically
The narrower p
clearly visible a
sensor's resistan

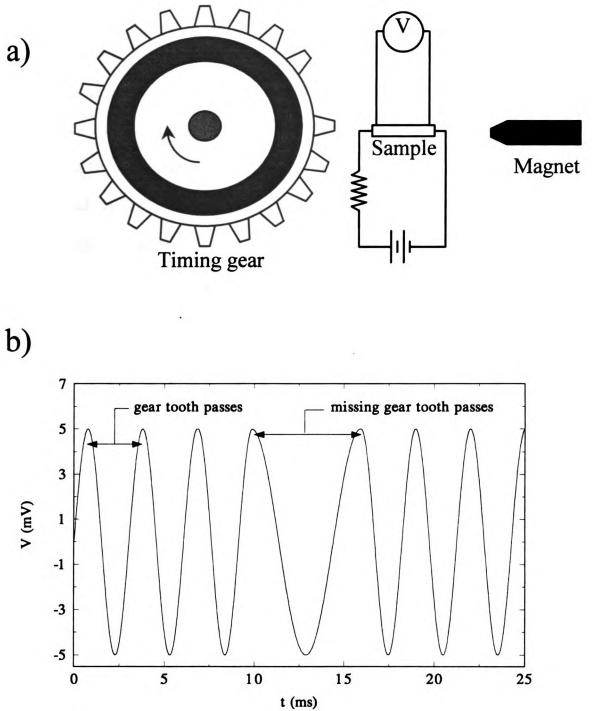

Figure 1.6: Pictured in a) is a schematic of prototype GMR sensor, using a lithographically patterned Co/Cu multilayer. Plotted in b) is the output of such a sensor. The narrower peaks are the teeth of the gear passing the sensor. The missing tooth is clearly visible as it passes. The peak to peak voltage corresponds to a 25% drop in the sensor's resistance.

The spin-dependent scattering processes can in principle take place both at the F/N interface and in the bulk F metal. The main goal of this study will be to both separate and quantify the amount of spin-dependent scattering at the F/N interfaces and in the bulk F layers for Co/Cu and $Ni_{84}Fe_{16}$/Cu multilayers ($Ni_{84}Fe_{16}$ will from here on be referred to as Py or permalloy unless otherwise noted).

This study utilizes techniques pioneered at MSU to measure the CPP-MR of several magnetic multilayer systems[13]. Chapter 2 deals with the fabrication of both CIP and CPP sputtered magnetic multilayered films. Chapter 3 describes the characterization of these sputtered films by several methods including: X-Ray Diffraction (XRD), X-Ray fluorescence (EDS), Cross-sectional Transmission Electron Microscopy (XTEM) and Nuclear Magnetic Resonance (NMR). Chapter 4 describes the theory of CPP GMR used in deriving the spin asymmetry parameters. Chapter 5 contains the measurements and analyses of the CPP-MR data for the relatively simple Co/Cu and Py/Cu systems to determine the spin asymmetry parameters of these two systems. Chapter 6 contains measurements made on more complex multilayer systems including: (1) The variation of the spin diffusion length of Cu via impurity scattering in Co/CuX multilayers where X=Pt, Mn, Ge and Ni. (2) The creation of large MR's (both CPP and CIP) at low temperatures for the Co/Ag/Py/Ag system by utilizing the different coercive forces of Co and Py, instead of exchange forces, to form an AP state. (3) The first measurements of a positive GMR in both CIP and CPP geometries using layers of Fe, Cr and Cu (CIP) and Co, Cu and FeV (CPP). All of these are aimed to show the predictability of more complex systems based on measurements of previously simpler magnetic multilayer

structure

specific

P.M. Le
397 (1995

[1] I.A. Car
North Ho

[2] K. Derby

[3] T. Valet,
A. Fert, Ap
Loloee and
Loloee, L.L
(1995).

[4] B. Dieny,
Metin, D.T.
Gallego, S.K
(1995); L.L
Bass, submit

[5] H. Sato, P
Superlattices
Selden, Phys.

[6] M.N. Baibic
Creuzet, A. Fr

[7] S.S.P. Parkin,

[8] P. Grunberg, P
2442 (1986).

[9] S.S.P. Parkin,

[10] S.S.P Parkin, P

[11] D.H. Mosca, F
Mag. Mat. **94**, L

structures as well as demonstrate that new materials may be engineered to meet very specific requirements.

---

[1] P.M. Levy, Solid State Physics, edited by D. Turnbull and H. Ehrenreich, Vol. 40, p. 397 (1995).

[2] I.A. Campbell and A. Fert, Ferromagnetic Materials, Vol. 3, edited by E.P. Wohlfarth, North Holland, p. 752 (1982).

[3] K. Derbyshire and E. Korczynski, Solid State Technology, Sept., 57 (1995).

[4] T. Valet, J.C. Jacquet, P. Galtier, J.M. Coutellier, L.G. Pereira, R. Morel, D. Lottis and A. Fert, Appl. Phys. Lett. **61**, 3187 (1992); P. Holody, L.B. Steren, R. Morel, A. Fert, R. Loloee and P.A. Schroeder, Phys. Rev. **B50**, 12999 (1994); Q. Yang, P. Holody, R. Loloee, L.L. Henry, W.P. Pratt Jr., P.A. Schroeder and J. Bass, Phys. Rev. **B51**, 3226 (1995).

[5] B. Dieny, V.S. Speriosu, B.A. Gurney, S.S.P. Parkin, D.R. Wilhoit, K.P. Roche, S. Metin, D.T. Peterson and S. Nadimi, J. Magn. Magn. Mater. **93**, 101 (1991); J.M. Gallego, S.K. Kim, T.J. Moran, D.L. Lederman and I.K. Schuller, Phys Rev. **B51**, 2550 (1995); L.L. Henry, M. Oonk, R. Loloee, Q. Yang, W.C. Chiang, W.P. Pratt Jr. and J. Bass, submitted to J. Magn. Magn. Mater. (1995).

[6] H. Sato, P.A. Schroeder, J.M. Slaughter, W.P. Pratt Jr. and W. Abdul-Razzaq, Superlattices Microstruct. **4**, 45 (1987); E. Velu, C. Dupas, D. Renard, J.P. Renard and J. Seiden, Phys. Rev. **B37**, 668 (1988).

[7] M.N. Baibich, J.M. Broto, A. Fert, F. Nguygen Van Dau, F. Petroff, P. Etienne, G. Creuzet, A. Friederich and J. Chazelas, Phys. Rev. Lett. **61**, 2472 (1988).

[8] S.S.P. Parkin, Phys. Rev. Lett. **67**, 3598 (1991).

[9] P. Grunberg, R. Schreiber, Y. Pang, M.B. Brodsky and H. Sowers, Phys. Rev. Lett. **57**, 2442 (1986).

[10] S.S.P. Parkin, N. More and K.P. Roche, Phys. Rev. Lett. **64**, 2304 (1990).

[11] S.S.P Parkin, R. Bhadra and K.P. Roche, Phys Rev. Lett. **66**, 2252 (1991).

[12] D.H. Mosca, F. Petroff, A. Fert, P.A. Schroeder, W.P. Pratt Jr. and R. Loloee, J. Mag. Mag. Mat. **94**, L1 (1991).

[1] W.P. P
Rev. Lett

[2] M.A.M

[3] W. Vav
(1995).

[4] T.M. W

[5] A. Bond

[6] L. Pirau
A. Fert, A

[7] Referen
magnetic l

[8] T. Vale
(1993).

[9] S. Zhang

[10] H. Camb
B47, 6776

[13] W.P. Pratt Jr., S.F. Lee, J.M. Slaughter, R. Loloee, P.A. Schroeder and J. Bass, Phys. Rev. Lett. **66**, 3060 (1991).

[14] M.A.M. Gijs, S.K.J. Lenczowski and J.B. Giesbers, Phys. Rev. Lett. **70**, 3343 (1993).

[15] W. Vavra, S.F. Cheng, A. Fink, J.J. Krebs and G.A. Prinz, Appl. Phys. Lett. **66**, 2579 (1995).

[16] T.M. Whitney, J.S. Jiang, P.C. Searson and C.L. Chien, Science **261**, 1316 (1993).

[17] A. Bondel, J.P. Meier, B. Doudin and J.P. Ansermet, Appl. Phys. Lett. **65**, 3019 (1994).

[18] L. Piraux, J.M. George, J.F. Despres, C. Leroy, E. Ferain, R. Legras, K. Ounadjela and A. Fert, Appl. Phys. Lett. **65**, 2484 (1994).

[19] Reference 21 has shown that spin accumulation may occur in the CIP geometry if the magnetic layers are not single domain.

[20] T. Valet and A. Fert, Phys. Rev. **B48**, 7099 (1993); J. Magn. Magn. Mater. **121**, 378 (1993).

[21] S. Zhang and P.M. Levy, Phys. Rev. **B50**, 6089 (1994).

[22] H. Camblong, et al., Phys. Rev. **B47**, 4735 (1993); S. Zhang and P. Levy, Phys. Rev. **B47**, 6776 (1993).

2.1 In

The

State U

sputterin

system a

sources i

Durin

atoms of

Illustrate

A positive

from the f

target at a

forms a pla

confinemer

negative 20

target, knoc

Chapter 2:

Sample Preparation and Fabrication

2.1 Introduction

The multilayered films fabricated for this study were deposited here, at Michigan State University, using the computer controlled ultra high vacuum DC magnetron sputtering system located in the basement of the Physics & Astronomy Building. This system allows deposition from up to four different L.M. Simard "Tri-Mag" sputtering sources in a single run.

During sputtering, Ar ions from an Ar plasma bombard the target material causing atoms of this material to be ejected. A basic description of the sputtering mechanism is illustrated in Figure 2.1. Electrons are thermionically emitted from the tantalum filament. A positive 50-60V potential between the filament and anode pulls these electrons away from the filament and to the anode. Ar gas is injected inside the gun housing near the target at a rate of 45cm^3/min. The Ar becomes ionized through electron collision and forms a plasma limited to the region just above the target by two powerful magnets and a confinement shield. This results in the creation of a stable plasma current of 5-7A. A negative 200-600kV potential applied to the target accelerates the ionized Ar to strike the target, knocking atoms off the surface. This produces a beam of target atoms, typically

0.5-1.0A. A substrate placed ~12cm above the target collects the material from this beam at a rate determined by the target voltage and the plasma current.

Although the plasma easily ejects material from the target surface, most of the kinetic energy from the Ar ions is deposited as heat in the target. To avoid melting, the target was water cooled. After the Ar ions hit the target, they capture an electron from the surface of the metal and are reemitted as neutral Ar atoms. Electrically conducting targets must be used to provide these electrons.

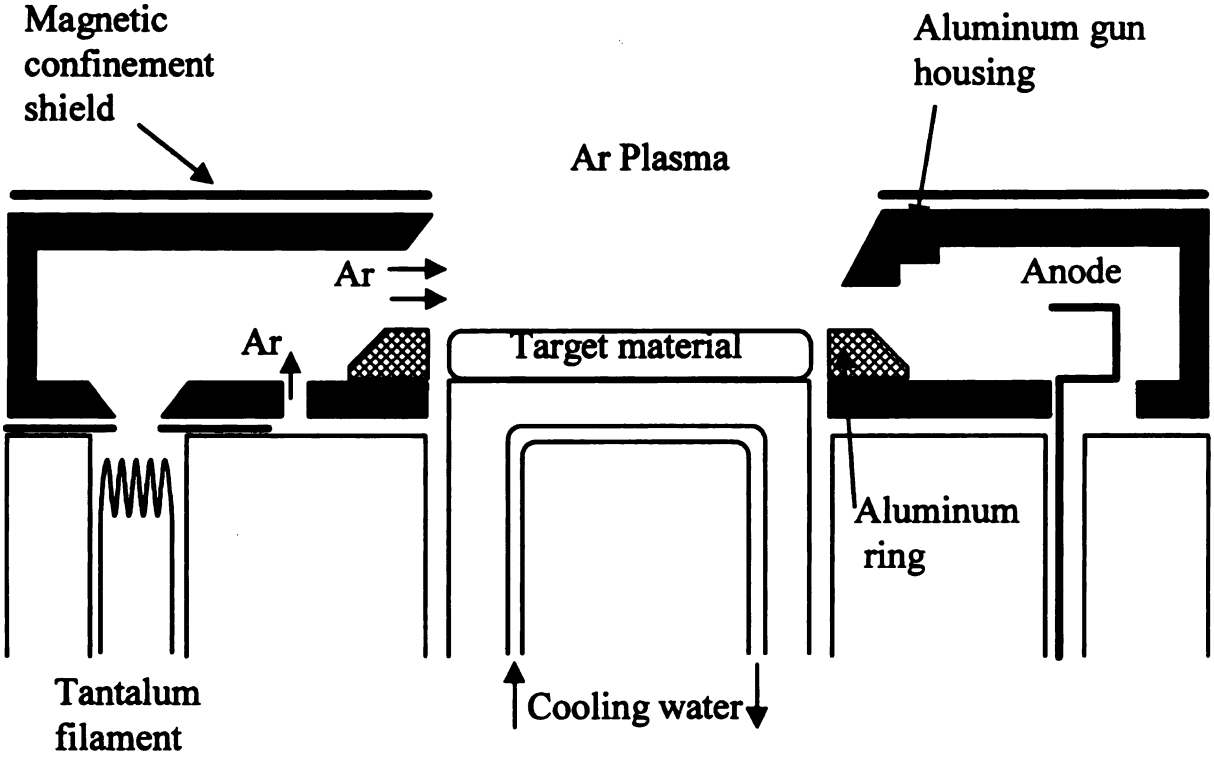

Figure 2.1: A cross section of the triode magnetron sputtering gun used in fabricating the samples for this study.

SPAM

Chin
with

Figure 2.
over the
deposition
substrate i

The fo
as illustrate
to block th
top to allov
over the gu
be protecte
selected gu

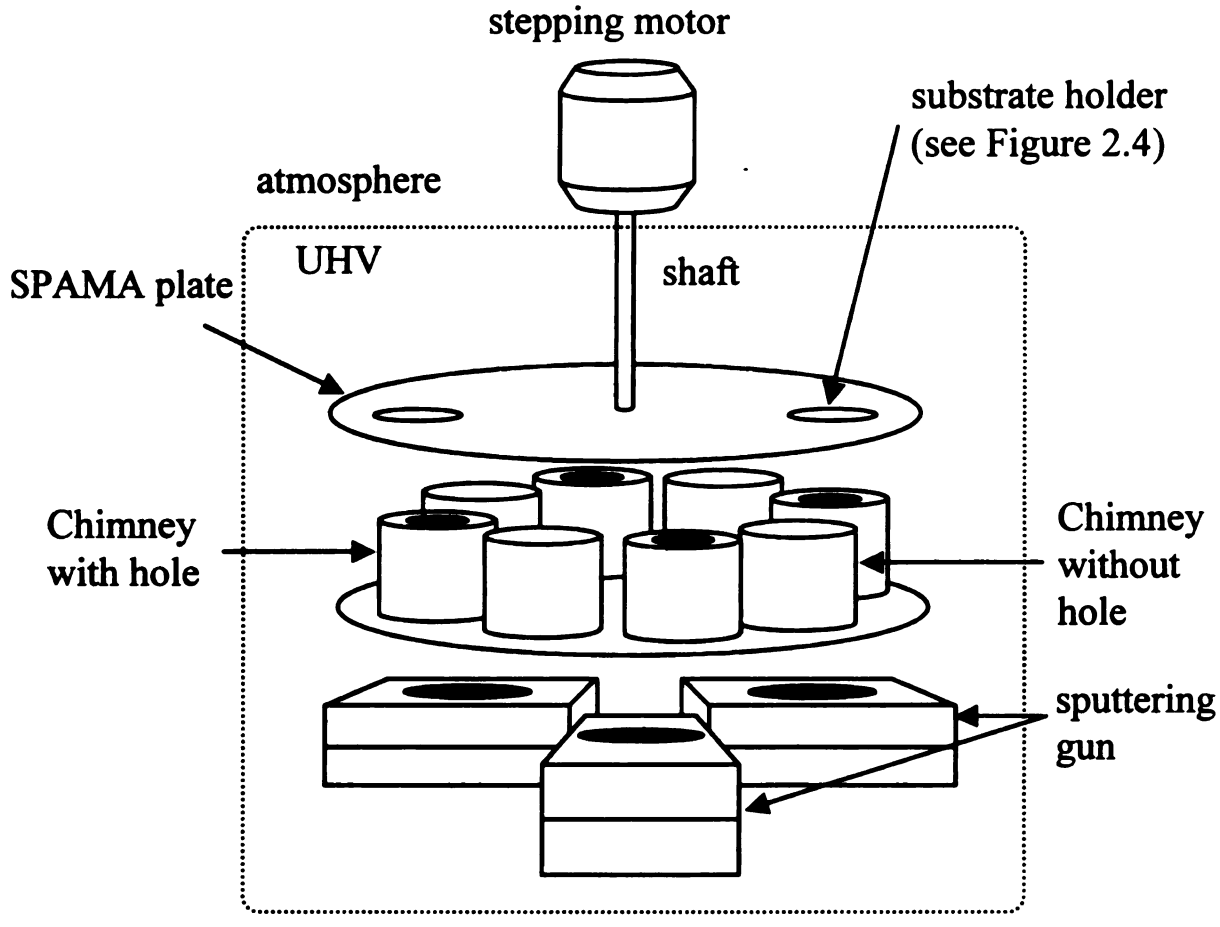

Figure 2.2: A schematic of the sputtering systems is shown. Chimneys are able to rotate over the sputtering guns to block deposition (chimney without hole) or collimate a deposition beam (chimney with hole). A computer controlled stepping motor rotates a substrate into position. Only three of the four guns are shown for clarity.

The four sputtering guns are situated on the bottom of a cylindrical vacuum chamber, as illustrated in Figure 2.2. Above each gun is a set of two chimneys, one without a hole to block the deposition beam from reaching the substrate and the other with hole in the top to allow deposition. After deposition, the chimney without the hole is rotated back over the gun to prevent deposition of unwanted material before an exposed substrate can be protected. A computer controlled stepper motor rotates the substrate above the selected gun until the preset thickness, determined by the deposition rate, has been

deposited

more sou

2.2 Pr

The sy

from run t

roughly 1 p

with a stair

the previou

impurities i

exclusively

cleaning wa

masks as w

subject to tha

The limit

materials wer

the chimneys

magnetic shie

which was onl

2.3 Subst

All samples

substrates were

wafers of resis

taken to see that

SPAM plate

deposited. Multilayers are grown by sequentially rotating the substrate between two or more sources.

2.2 Preparation of the System

The system was prepared in the same manner for each run to limit sample variations from run to run. The gun parts for each source were cleaned in an acid bath containing roughly 1 part HF, 9 parts HNO_3 and 3 parts distilled H_2O. Each gun part was scrubbed with a stainless steel wire brush and then rinsed in distilled H_2O to remove material from the previous run. Each target material had its own gun to help minimize chemical impurities in the samples. For example, parts used to sputter Co were used to sputter Co exclusively. To remove any small particles loosen by scrubbing a 6 minute ultrasonic cleaning was done, first in acetone and then in ethyl alcohol. All substrate holders and masks as well as the sample positioning and masking apparatus (SPAMA) plate were subject to the same cleaning procedure.

The limited number of chimneys forced their reuse in every run even though different materials were being sputtered. To help prevent cross contamination from previous runs, the chimneys were wrapped in Al foil each time a new material was to be sputtered. The magnetic shields were not cleaned. However, each gun had its own magnetic shield which was only used for a specific target material.

2.3 Substrates and Holders

All samples made for this study were grown on (001) oriented Si substrates. The substrates were cut into half inch squares from 3 inch, 0.5mm thick, boron-doped, silicon wafers of resistivity 10Ω-cm purchased from Silicon Quest International. Care was taken to see that the substrates fit snugly into the sample holders to prevent sliding as the SPAMA plate rotated. They were then sequentially washed ultrasonically in the

following

prepared

concentra

substrates

on the SP

Loadin

buildup o

could be va

for eight su

Two types

designed to

permitted e

covered an

holder was

allowed the

third holder

presence of

between two

substrate. as

expose an are

following: alconox and deionized water, deionized water, acetone, and alcohol. Samples prepared for CIP measurements were then hydrogen terminated by etching in concentrated HF for one minute followed by dips in deionized water and alcohol. All substrates were stored in alcohol until loading occurred. Prior to loading into the holders on the SPAMA plate, the substrates were blown dry using N_2 gas.

Loading was performed quickly just before the system was closed to minimize the buildup of atmospheric hydrocarbons. The number of samples made during each run could be varied according the configuration of the SPAMA plate. The plate has positions for eight substrate holders and two for film thickness monitors, as shown in Figure 2.3. Two types of substrate holders were used for the bulk of this study. The first was designed to hold two substrates, as illustrated in Figure 2.4a. A single holed shutter permitted each substrate to be exposed separately. Films made with these holders covered an area slightly less than the half inch square of the substrate itself. The second holder was designed to hold a single substrate. A manually rotatable masking system allowed the film to be patterned *in situ* as the run progressed, as shown in Figure 2.4b. A third holder used near the end of this study was designed for sputtering samples in the presence of a magnetic field. These hold a single half inch square substrate centered between two NdFeB magnets so that the direction of the field lies in the plane of the substrate, as indicated in Figure 2.4c. A shutter was manually slid back and forth to expose an area slightly less than the substrate.

Sam
posit

Film th
position

Figure 2.3
layout.

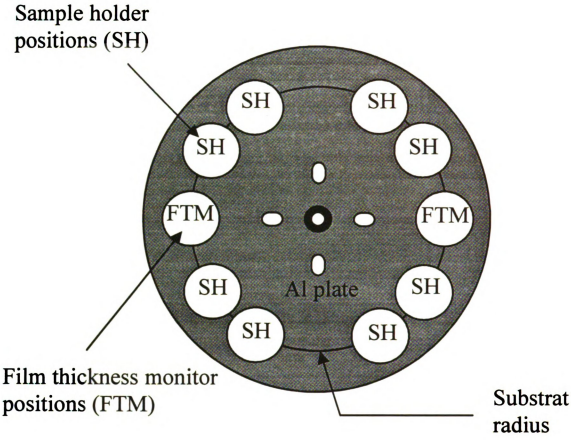

Figure 2.3: Diagram of the Sample Positioning and Masking Apparatus (SPAMA) plate layout.

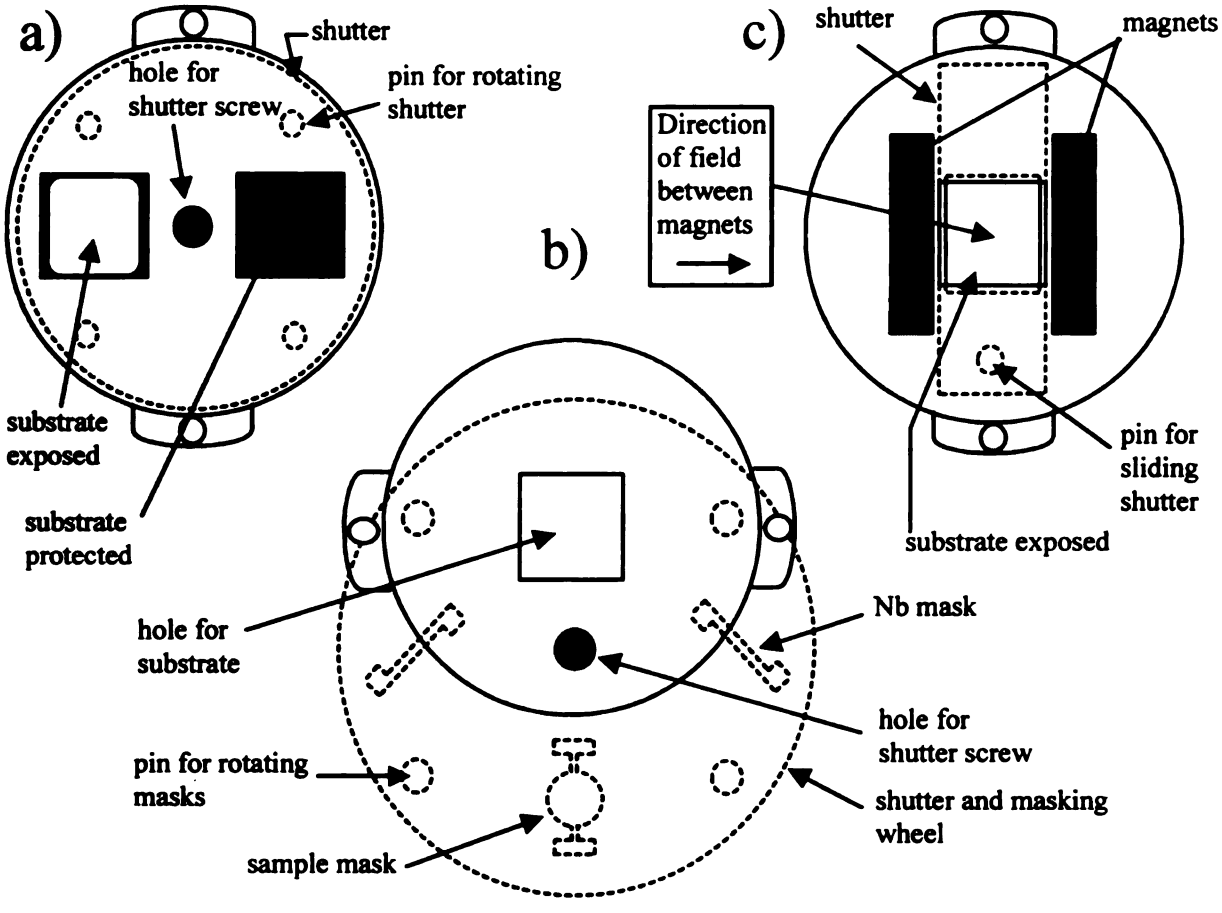

Figure 2.4: Diagrams for the various substrate holders used during the course of this study. Holder a) was used to make CIP multilayers and single layer thin films. Holder b) was used to make the CPP samples. Holder c) was used to sputter CIP multilayers in a strong magnetic field. Dashed lines indicate the shutters which are hidden from view when looking down through the substrate hole. The shutters could be rotated about their center by pulling on one of the pins for rotating with an externally controlled wobble stick.

2.4 Vacuum

The sputtering chamber is UHV compatible reaching an ultimate background pressure of between 1 and 2 $x10^{-8}$ torr. A high speed CTI Cryo Torr 8 cryopump is used to pump down the system. A pressure of 5 $x10^{-6}$ torr is achieved just 15 minutes after closing but to go lower the system is baked overnight (~12 hours) at 60 °C. Upon cooling to room temperature, the gate valve is opened completely and a pressure of roughly 8 $x10^{-8}$ torr is

measure

Cooling

pressure

torr. Th

the flang

with a m

The p

the M19

He. H_2O.

H_2O vap

lower.

2.5 Co

The co

W.P. Pratt

0000 psi

of 1 4 inch

pressure ga

the SPAM

located at th

four copper

the high pre

evaporates a

vented to th

exchanger co

chamber be

measured. The system is then left to pump for 24 hours finally reaching 2 x10^{-8} torr. Cooling the substrates with liquid N_2 for one hour prior to sputtering tends to lower this pressure somewhat but generally the final background pressure never dips below 1 x10^{-8} torr. The system is capable of lower background pressures but the viton gasket sealing the flange between the top and the main parts of the chamber would have to be replaced with a metal gasket such as copper or indium and then be bolted tight.

The partial pressures of the background gases inside the chamber are measured using the M100 Quadrapole Gas Analyzer purchased from Dycor Electronics. These gases are He, H_2O, N_2, O_2 and Ar. Partial pressures of between 10^{-8} and 10^{-9} torr are measured for H_2O vapor and N_2 gas. The other gases have pressures at least an order of magnitude lower.

2.5 Cooling System

The cooling system for the SPAMA plate was designed and built by C. Fierz and W.P. Pratt, Jr. is illustrated in Figure 2.5. An external heat exchanger has high pressure (1000 psi) N_2 gas flowing through a 1/16 inch stainless steel tube welded inside a length of 1/4 inch copper tubing, through which liquid N_2 is constantly flowing. The high pressure gas is then forced into a capillary that runs inside the length of the shaft holding the SPAMA plate, into a second heat exchanger consisting of a tiny copper reservoir located at the bottom of the shaft. The second heat exchanger is thermally connected via four copper rods to the SPAMA plate. The constriction caused by the capillary forces the high pressure N_2 gas to condense into liquid N_2 as it travels to the reservoir where it evaporates and returns via the capillary up the shaft to a second stainless steel tube and is vented to the outside. The larger copper tube carrying the liquid N_2 in the first heat exchanger continues on to a large internal ring (Meissner trap) around the top of the chamber before being vented to the outside. This helps to freeze out impurities inside the

chambe

impor

assemb

Figure 2.5:

chamber. A thermocouple is placed on this loop to confirm that liquid N_2 is flowing. An important part of this design is the use of small capillaries which permit the whole assembly of the 2nd heat exchanger and SPAMA plate to rotate.

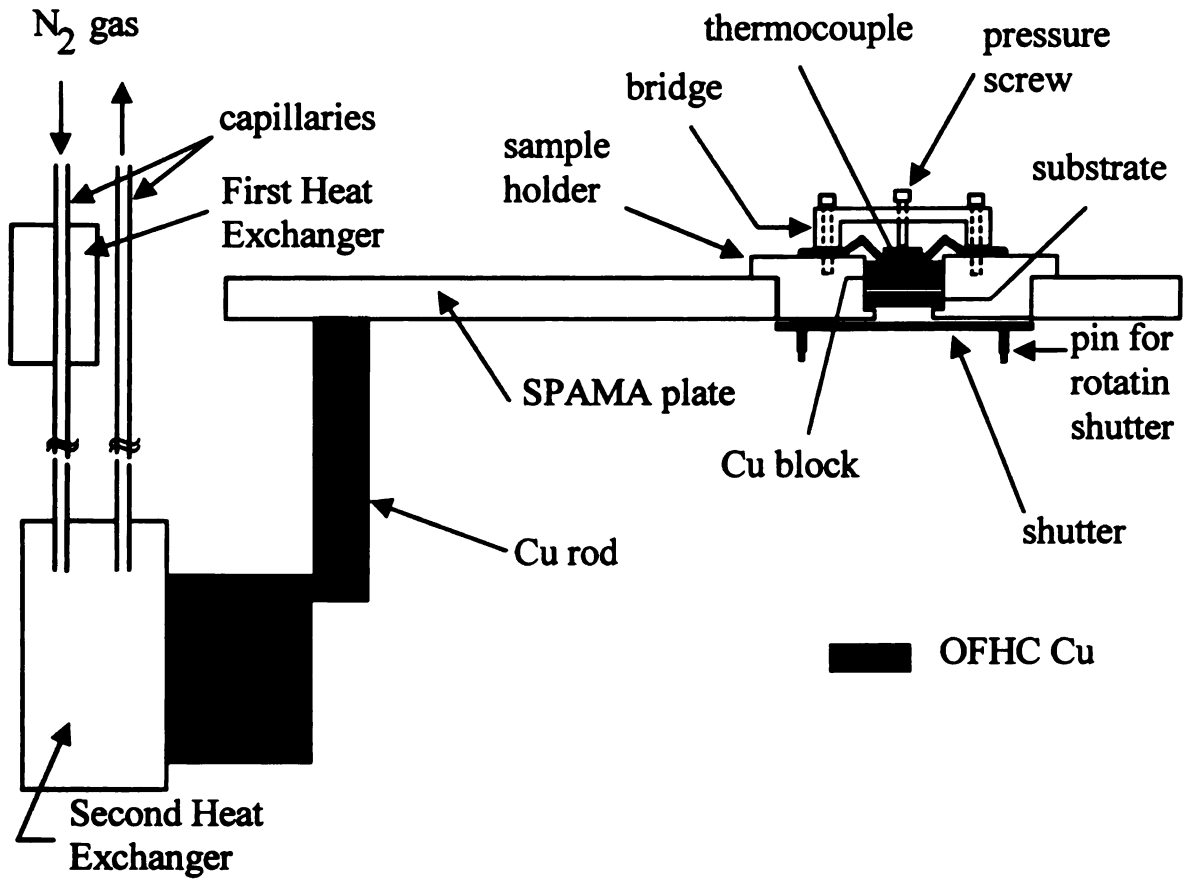

Figure 2.5: Schematic cross section of the cooling system with CIP holder (Figure 2.4a).

A s

SPAM

SPAM

SPAM

shown i

mechan

the temp

minimiz

range. th

The

two 30 l

dewar.

the 30 li

release o

2.6 Fa

Just b

pressure d

As a furth

and then

throughou

the gate va

The ru

which take

ran to run

different ru

A small copper block is placed behind each substrate and bolted firmly to the SPAMA plate. This serves two purposes: (a) It keeps the substrate from moving as the SPAMA plate rotates from source to source. (b) It thermally anchors the substrate to the SPAMA plate so the heat from the growth process is transferred to the reservoir, as shown in Figure 2.5. The temperature of the substrate is monitored by a thermocouple mechanically held in place by a screw to the back of the copper block. From run to run the temperature range in which the samples are grown is kept between -40C° and 25°C to minimize effects due to growth conditions. Should the temperature increase above this range, the guns are shut down and the system is allowed to cool.

The only modification to the cooling system concerned the source for liquid N_2. The two 30 liter dewars previously used were replaced with a single 100 liter pressurized dewar. A typical run required about 50 liters of liquid N_2, therefore the need to switch the 30 liter dewars in the middle of a run was eliminated. This prevented the possible release of impurities frozen out inside the chamber on the cooling ring.

2.6 Fabrication

Just before sputtering, the pressure is brought up to 2.5 mtorr, the ambient sputtering pressure during each run, by backfilling the chamber with high purity Ar (99.999%) gas. As a further protection against impurities, the Ar is passed through an oxygen scrubber and then through a liquid N_2 trap. The Ar pressure is held in dynamic equilibrium throughout the run by flowing Ar at a constant rate through each gun and then opening the gate valve just enough to maintain 2.5mtorr.

The run begins by turning on all the sputtering sources and letting them equilibrate which takes no more than 10 minutes. The target voltages and currents are fixed from run to run for each material so that the deposition rates are similar for samples made in different runs, this again helps minimize effects due to growth conditions. The deposition

rates

added

obtain

deposi

Table

metals

a The

b The

these

A t

rotating

source.

thereby

solder. w

rates are measured using quartz crystal film thickness monitors. A 3% correction is added to the measured rate, the result of comparing nominal bilayer thickness to those obtained from x-ray measurements. The values for target voltages, currents and deposition rates are listed in Table 2.1.

Table 2.1: Target voltages and currents and the resulting deposition rates for sputtered metals used in this study.

Metal	Target Voltage (V)	Target Current (A)	Deposition Rate (nm/s)
Ag	200	0.500	1.10±0.10[a]
Cu	400	0.700	1.30±0.10[a]
CuGe	400	0.700	1.07±0.02[b]
CuMn	400	0.600	1.13±0.01[b]
CuNi	500	0.800	0.90±0.05[a]
CuPt	400	0.700	0.80±0.05[a]
Cr	500	0.700	0.55±0.02[b]
Nb	600	1.010	0.80±0.05[a]
Co	500	0.800	0.85±0.05[a]
Fe	500	0.500	0.53±0.01[a]
FeV	500	0.700	0.45±0.02[b]
Py	500	0.800	0.80±0.05[a]

a The uncertainties represent fluctuations from run to run in deposition rate.
b The uncertainties represent fluctuations in the deposition rate during a run. Each of these metals is used in only one or two runs.

A two position shuttering system helps prevent cross contamination by manually rotating either a short open chimney or a short Al foil covered chimney above each source. The open chimney has a 5cm diameter hole cut in the Al foil covering the top, thereby narrowing the region exposed to the particle beam to just the desired substrate holder; while the covered chimney blocks the beam entirely. Note that the present system

either
current
Typ
each s
resistiv
runs. T
1. M
2. C
3. R
4. R
5. C
The tim
dependi
multila

2.7 Ta

Three
commerc
pure Cu
ordered
Angstrom
beyond th
only the
diameter a
dimension
EDM, by

either has all sources open or all sources blocked. A modification by Reza Loloee is currently underway to selectively open or block each source.

Typically in a single run, 6 CPP samples and 4 single layer 300nm films (one for each source) were produced. The 300nm films were done as checks to see if the resistivity and/or composition (in the case of alloys) significantly deviated from previous runs. The procedure for making a CPP sample was as follows:

1. Measure deposition rates for each material (masks closed).
2. Open mask for bottom Nb strip and deposit 350 nm of Nb.
3. Rotate to mask for sample and deposit the multilayer.
4. Rotate to mask for top Nb strip and deposit another 350 nm of Nb.
5. Close mask.

The time to deposit an entire CPP sample varied from approximately 30 to 60 minutes depending on the sample. The Nb strips each took roughly 7 minutes to deposit and the multilayer itself varied depending on the desired sample from 15 to 40 minutes.

2.7 Targets

Three different types of targets were used as sputtering sources: ready-made, commercially produced, in-house alloyed and in-house composite. Targets of 99.999% pure Cu, 99.999% pure Ag, 99.95% pure Co, 99.9% pure Fe and 99.95% pure Nb were ordered from Angstrom Scientific. Permalloy ($Ni_{81}Fe_{19}$) was also ordered from Angstrom Scientific because the melting temperatures of Ni-Fe alloys are above 1400°C, beyond the operational range of the quartz chamber on the induction furnace. Of these, only the Nb was received in the form required for immediate use, disks 5.72cm in diameter and 0.64 cm thick. The rest were received as bars and were cut to the final dimensions using the computer controlled traveling wire electrical discharge machine (EDM) by the staff of the physics shop at MSU.

All
made fr
and 99.9
1. T
2. C
sl
3. T
ba
4. M
ho
5. The
Some targ
to better
dimension
Compo
cutting sev
target with
made by pu
a screw thro
During
and thermal
copper base
targets are m
solder becau
source. Orig
for deposition
samples made

Alloyed targets of CuX were made in the rf induction furnace at MSU. These were made from 99.999% pure Cu and; 99.999% pure Pt, 99.999% pure Ge, 99.99% pure Ni and 99.9% pure Mn. The procedure listed below was followed :

1. The appropriate amount of each material was lightly etched in HNO_3.
2. Components were placed in a cylindrical, boron nitride coated, graphite crucible slightly larger than the intended 5.72cm target diameter.
3. The quartz chamber was pumped down to 10^{-6} torr for several hours and then backfilled with a gas mixture of 10% H_2 and 90% Ar to eliminate any oxidation.
4. Materials were heated until a good convection flow was observed, to ensure a homogeneous composition.

5. The target was allowed to cool for several hours before opening to the atmosphere.

Some targets such as the CuPt alloy were flipped over and remelted in a similar manner to better ensure homogeneity. The alloy target was then machined to the proper dimensions by the physics shop.

Composite targets were used for FeV and CoSm. The FeV target was constructed by cutting seven 1.28cm diameter holes (at the corners and center of a hexagon) in an Fe target with the EDM. Vanadium plugs were used to fill the holes. The CoSm target was made by putting a rectangular piece of Sm on a Co target. The Sm was held in place by a screw through the backside of the Co target.

During a run, the sources are water cooled to prevent overheating. For good electrical and thermal contact with the target, they are mounted on copper holders and bolted to the copper base through which the water flows. For good conductors such as Cu and Ag the targets are merely set on top of the holder. Magnetic targets must be held in place with In solder because of the strong magnetic fields needed to confine the plasma inside the source. Originally the Nb target was treated like a Ag or Cu target; but the power used for deposition heated the Nb target until it glowed. This limited the number of CPP samples made before shutting down to cool to just two. Soldering the Nb to the holder

with In

made b

with In provided much better thermal contact and allowed several CPP samples to be made before cooling down again.

S

Intro

This

on sput

composi

diffractic

were per

magnetic

The c

resistance

3.1 Co

Films

uniformity

Procedure

Chapter 3:

Sample Characterization and Experimental Procedures.

Introduction

This chapter lists and describes the results of sample characterization analyses done on sputtered multilayers made at MSU. These include a qualitative discussion of compositional studies using energy dispersive x-rays (EDX) and standard θ-2θ x-ray diffraction techniques at both low and high angles done by the author. Additional studies were performed by others using cross-sectional electron microscopy (XTEM) and nuclear magnetic resonance (NMR) provide more insight into the sample structure.

The chapter ends with a discussion of the different techniques used in measuring the resistance of a CPP sample, a CIP sample or a single layer thin film.

3.1 Compositional Analysis Using EDX

Films of alloyed targets were examined for both impurity concentration and uniformity of composition using energy dispersive spectroscopy (EDS or EDX). This procedure involves bombarding the sample films with electrons and analyzing the energy

spectrum of fluorescent x-rays. These studies were done at the Center for Electron Optics facility located here at MSU in the basement of the Pesticide Research Center. All EDX results were obtained using a JEOL JSM-35C Scanning Electron Microscope (SEM) equipped with a Tracor Northern x-ray detector. A dedicated PC running Noran Inc. commercial software performed the necessary calculations for the compositional analysis. Vivion Shull (now retired) and then Stan and Carol Flegler operated the SEM.

Fluorescent x-rays are produced after core electrons are ejected from various atoms within the sample via inelastic collisions with a beam of incident electrons from the SEM[1]. The core vacancies are then immediately filled by another higher level electron within each atom. These transitions release x-rays of a characteristic energy.

Since the electron energy levels depend on the atomic number, a characteristic x-ray spectrum exists for every element. This x-ray "fingerprint" can then be used to identify the constituent elements in the sample. The concentration is obtained by comparing the count rate of a particular transition series, either K_α or L_α, for each constituent element in the sample. Three factors must be taken into account before comparing the rates: (a) The element with higher atomic number has a larger cross section and will produce more x-rays (Z correction). (b) The probability an x-ray will be absorbed before it escapes the sample (A correction). (c) The probability an x-ray will create a secondary x-ray by fluorescence in the sample (F correction). Together these form the ZAF correction factor which is close to 1.0 for the materials studied here.

If the ZAF corrections are calibrated to scans of pure samples taken at the same electron energy then the accuracy of the concentration c for this method is ($c \pm 0.03c$). This calibration was not done so the error is approximately ($c \pm 0.07c$) for all impurities in this study [2]. Table 3.1 lists both the nominal and measured impurity concentrations for single layer sputtered 300nm films used for the work described in this thesis. The system is sensitive enough to detect impurities of less than 1 at.%, but low counting statistics make quantitative analysis difficult and generally unreliable. In all analyzed

films

is no

Tabl

Hos

‡ Targ

† Targ

= Fe i

cons

mult

films no detectable unintended impurities were seen. It should be noted that the detector is not sensitive to the lower Z elements from oxygen on down.

Table 3.1: Measured impurity concentrations of targets.

Host metal	impurity	nominal c (at.%)	measured c (at.%)	thickness (nm)
Cu	Ge‡	4	4.9±0.3	200
Cu	Mn†	7	7±0.5	200
Cu	Ni	6	5.9±0.4	300
Cu	Ni	14	13.7±1	300
Cu	Pt	6	5.9±0.4	300
Co	Sm	10	10.3±0.7	100
Fe	V	30	27±2	300
Ni	Fe¤	19	16±1	100-500

‡ Target made by M. Wilson.

† Target made by L. Hoines.

¤ Fe impurity concentrations of 19 at.% were measured in the purchased Py targets, consistent with manufacturer's specifications, however, Py films (both single and multilayered) repeatedly measured near 16 at.%.

3.2 X-rays

Multilayer properties are very sensitive to structure. Many very sophisticated methods such as XAFS, XTEM and NMR are used to probe the structure of multilayers at many different scales. Although results from more sophisticated studies done on samples made at MSU and studied by others will be reviewed, they are not the focus of this study. Simple θ-2θ x-ray diffraction (XRD) was used to probe the perpendicular structure of each multilayer. From these scans, the bilayer thickness and crystallographic orientation could be measured.

The sample spectra were obtained using the Rigaku rotating Cu anode diffractometer housed on the fourth floor of the Chemistry building at MSU. For a concise description of the setup used, see the dissertation of M.L. Wilson[3]. The divergence angle of the x-ray beam was limited to (1/6)° by a set of divergence slits placed before and after the sample. A graphite monochrometer placed between the sample and the detector ensured that only Cu-K_α radiation (0.15418nm) was detected. The sample alignment was good to ±0.1°, which may have introduced small errors in the peak positions for angles less than ~10°. This was of little consequence since most samples failed to produce any peaks in this region.

For reflected x-rays in the θ-2θ geometry, the momentum transfer vector is always perpendicular to the atomic planes in the sample and therefore only probes the structure along this direction. Peaks observed in these spectra correspond to periodicities along the sample's growth direction and give a measure of the lattice spacing of each material in the multilayer, the crystallite size and the bilayer spacing.

The Bragg condition describing the relationship between the diffraction spacing and the peak angle is given equation 3.1

$$m\lambda = 2d\sin\theta \qquad 3.1$$

where m is the order of the intensity peak, λ is the wavelength of the source (Cu-K_α radiation) and d is the spacing which produces the peak angle, θ. The largest repeated

spacing in each multilayer comes from the bilayer thickness, Λ. So for $d=\Lambda$, Bragg peaks should be seen at angles of less than ~ 10°. These peaks are almost never seen in the Co/Cu and Py/Cu samples used in this thesis. For rather thick bilayers, $\Lambda > 20nm$, this is understandable since the most intense peaks would be observed in the region where the detector is saturated by the beam line, however, peaks from thinner bilayers should still be detectable. A combination of similar electron density between the two materials and columnar growth could partially account for the absence of low angle superlattice peaks. At low angles the x-ray beam illuminates a larger area of the sample and therefore is very sensitive to the flatness of the illuminated area, Figure 3.1a. Although the interfaces within a column might be atomically flat, kinks form in the bilayer between neighboring columns which reduce the coherence of the scattered x-rays and may reduce the low angle superlattice peaks. If the column widths are much smaller than the illuminated area of the sample, then the x-rays would experience a large number of these kinks at low angles so that x-ray peaks from the bilayer spacing should be very hard to see. At high angles, where the x-rays begin to probe the lattice structure of the constituent materials, the kinks between neighboring columns are not as important since a greater portion of the x-ray beam may now sample the columns, themselves, Figure 3.1b.

At best however, this can only be a contributory factor, since others[4] have observed low angle peaks in similar sputtered Co/Cu samples.

a)

Lo
ser

Colu

Figure
incide

Hi
obser
since f
of the
<110>
consti
from th
additio

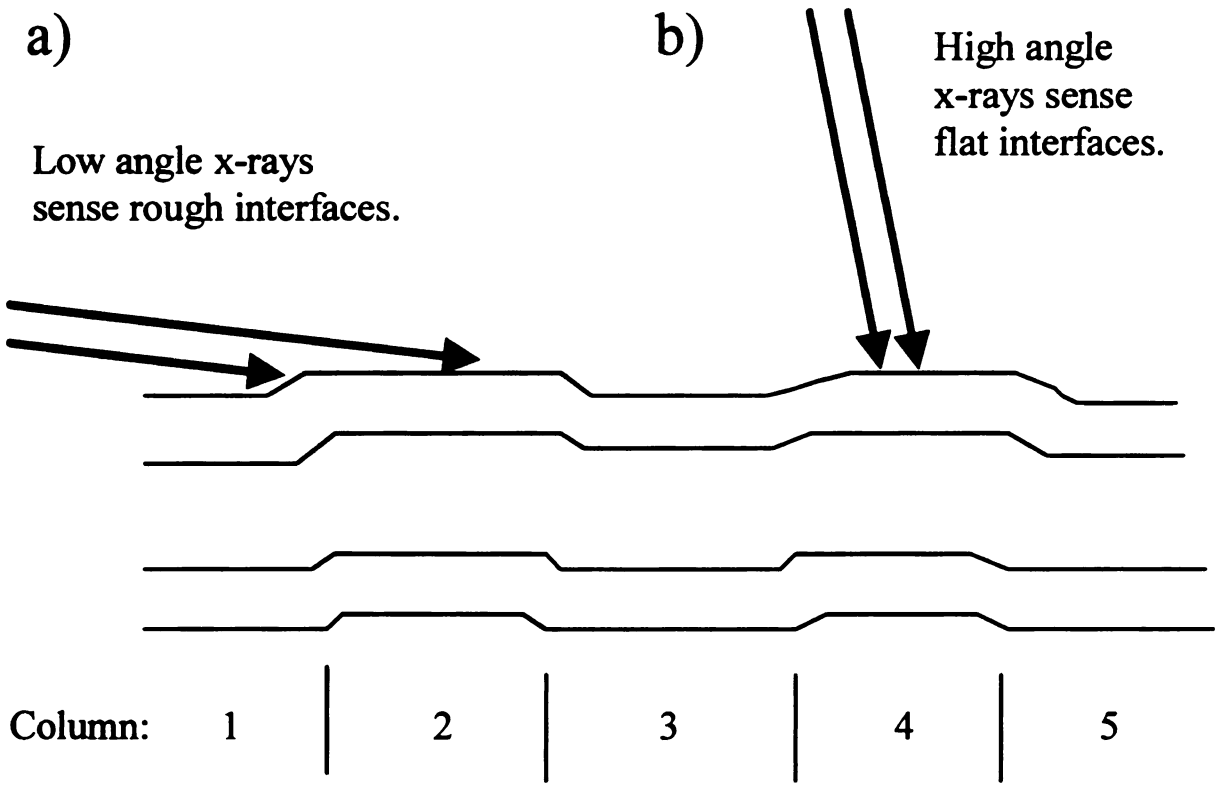

Figure 3.1: Schematic representation of both a) low angle and b) high angle x-rays incident on a multilayer exhibiting columnar growth.

High angle peaks are due to the lattice spacing of each constituent material. The observed structure peaks for each material is given in Table 3.2. These were expected since films grow with the most densely packed atomic planes oriented parallel to surface of the substrate in order to minimize energy. These planes are <111> for fcc lattices and <110> for bcc lattices. The side peaks next to the main lines of both multilayer constituents arise from a modulation of the constituent spectra by the spectra resulting from the bilayer thickness. The intensity of these satellites tends to be enhanced with the addition of heavy Z impurities into the spacer layer such as Pt, figures 3.2-3.4.

Table 3.2: Observed x-ray structure peaks.

Metal	Structure peak	θ-$2\theta^a$
Nb	110	38
Cu	111	43
Co	0001	48
Py	111	44

a Peak angle for a bulk film 300nm thick.

Crystallite size may be estimated from the structure peaks, although it is complicated by the presence of satellites in some cases. The average crystallite size perpendicular to the plane of the layers is given by Scherrer's equation:

$$S = \frac{K\lambda}{\beta \cos\theta} \qquad 3.2$$

where S is the crystallite size, β is the FWHM of the diffraction peak at angle θ and K is a constant related to the crystallite shape[5]. If K is taken to be unity then S becomes the volume average of the crystallite dimension normal to the reflecting planes, *hkl*[6]. The volume averaged crystallite size estimated from equation 3.2 ($K=1.0$) was approximately 30nm. For all but the thickest interlayers, this was greater than the bilayer thickness for each sample.

Not considered here is the effect of strain on the linewidth broadening of the lattice structure peaks. The lattice mismatch from one material to another undoubtedly strain each sample. Also, defects (both structural and chemical), which are inherit in sputtered samples, probably increase the amount of strain in a given multilayer.

Intensity (arbitrary units)

Figure
Cu(I

Intensity (arbitrary units)

Figure
SiO_2:Cu

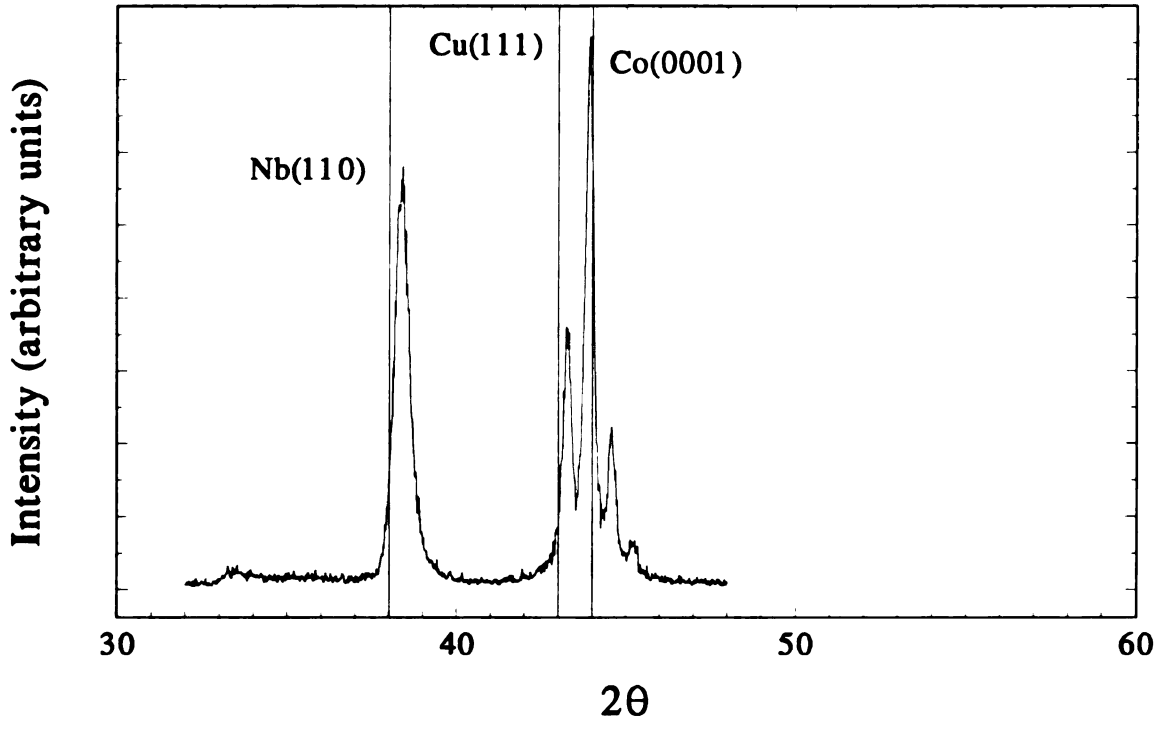

Figure 3.2. θ-2θ spectrum for *[Co(6.0nm)/Cu(9.0nm)]x48*. The bulk values of Nb (110), Cu(111) and Co(0001) are shown for comparison.

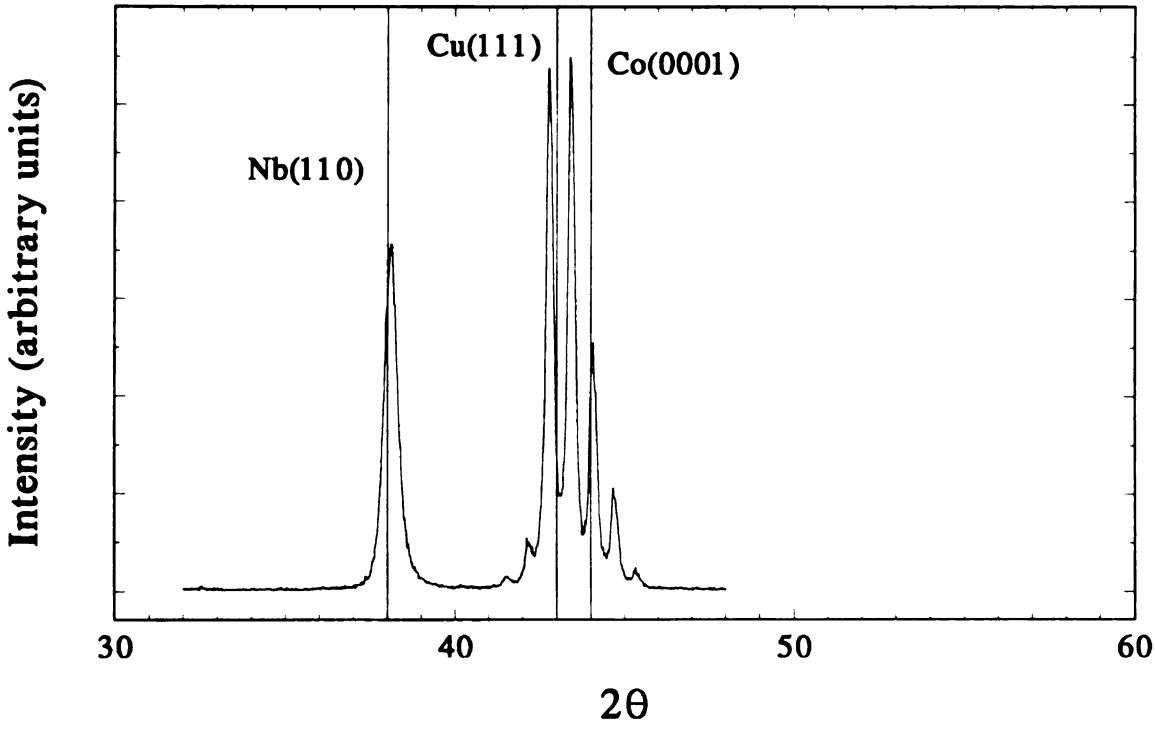

Figure 3.3. θ-2θ spectrum for *[Co(6.0nm)/CuPt(9.0nm)]x48*. The bulk values of Nb (110), Cu(111) and Co(0001) are shown for comparison.

Intensity (arbitrary units)

Figure 3
(110). Cu

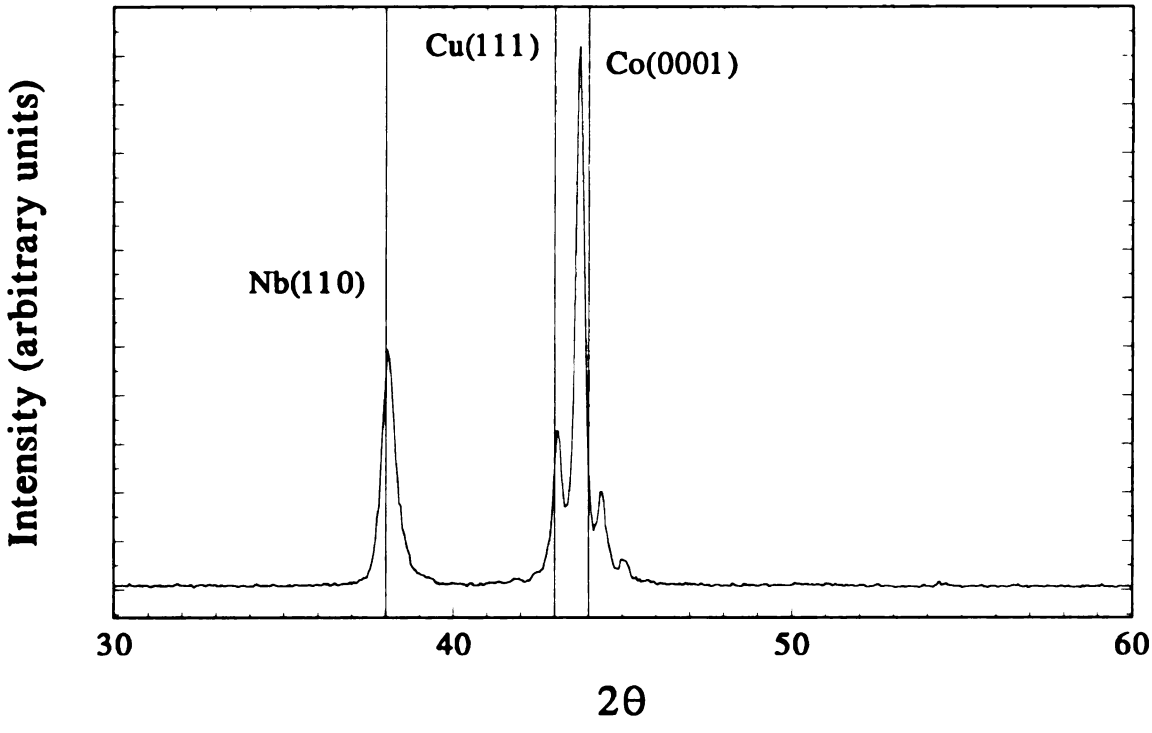

Figure 3.4. θ-2θ spectrum for *[Co(6.0nm)/CuNi14%(9.0nm)]x48*. The bulk values of Nb (110), Cu(111) and Co(0001) are shown for comparison.

3.3 Cross-sectional Analysis

Cross-sectional electron microscopy (XTEM) was used to study a limited number of samples. Studies at MSU were done on Co/Ag CPP samples by D. Howell *et al.*[7], while other XTEM studies were done on Co/Cu CIP multilayered films by P. Galtier *et al.*[8] at Thomson in Orsay, France. Results for NiFe/Cu and Co/Cu CPP samples are hard to analyze because the materials have similar atomic numbers so the Z contrast is rather poor. Galtier was able to image these materials by using a technique know as Fresnel contrast[9] which enhances the contrast between the materials by defocusing the electron beam. Some inferences can be made about the structural properties of NiFe/Cu and Co/Cu CPP samples by comparing the work done on Co/Ag with Galtier's on Co/Cu.

In the MSU studies, the layering is quite good for the first few bilayers, but thereafter dark-field micrographs show a columnar structure at least 20nm in width for the average column. Although layering is still uniform within each column, layering between neighboring columns does not always register and kinks form from one column to the next.

The Galtier study showed similar trends in the layering. However, the samples had a small number of thin bilayers so the layering was quite good, and although the beginnings of columnar growth are visible, well defined columns were not observed. Galtier did observe well defined columns for multilayered films sputtered in Orsay when the total sample thickness exceeded 50nm. The MSU samples he received had total thickness less than 50nm.

The Nb strip necessary for transport measurements in CPP samples had little effect on the smoothness of the layering within a column, but did seem to provide nucleation sites for the growth of columns. Dark-field micrographs show crystallites in the Nb at the Nb/ferromagnet interface correlating nicely with the columns in the multilayer.

Comparing the results of Galtier to those of Howell leads to the following conclusions about CPP NiFe/Cu and Co/Cu samples. They most likely have columnar growth

probe

with

samp

3.4

Nu

sputter

Alpher

Strasb

The

interfac

layers a

structur

thinnes

samples

The

thicknes

until a

structure

structure

Co layers

to 3 mon

comparis

consisten

probably nucleated by Nb crystallites near the Nb/ferromagnet interface. The layering within a column is probably quite good. The first few bilayers are smooth but as the sample grows the neighboring columns become mismatched.

3.4 Nuclear Magnetic Resonance

Nuclear magnetic resonance (NMR) studies were done on Co/Ag and Co/Cu samples sputtered at MSU and sent elsewhere for analysis. The Co/Ag series was studied by van Alphen *et al.*[10] in Eindhoven while samples of Co/Cu were studied by Mény *et al.*[11] in Strasbourg.

The Co/Ag results are detailed in the thesis of S.F. Lee[12]. By comparing the ratio of interface Co signal to bulk Co signal, this study[10] found that for $t_{Co}>1.0nm$ continuous Co layers are deposited in the sample. Below this value the Co layers consist of island-like structures. Behavior consistent with purely granular Co/Ag samples is seen for the thinnest Co thickness, 0.2nm. This will be important when considering the hybrid samples in Chapter 6.

The Co/Cu results[11] indicate that the structure of the Co layer depends upon the thickness of both Cu and Co. If the Cu thickness is held constant, the Co remains fcc until a $t_{Co}\sim3.0nm$. Near this thickness the Co contains a mixture of hcp and fcc structures. Further increases of t_{Co} will eventually lead to the detection of only the hcp structure. Increasing the Cu thickness will tend to increase the amount of fcc Co in the Co layers. Comparing the NMR data with interface models indicates that for thin Co up to 3 monolayers could be intermixed at the Co/Cu interfaces. For thicker Co, model comparison suggests only one intermixed layer. The thicker Co NMR spectra are also consistent with 9.0nm wide columnar grains.

3.4

both

the

tech

tech

circu

thick

i.e., i

3.3 is

In eq

where

the cu

Th

and c

failur

by pu

potent

Stress

potent

positi

3.5 Resistivity of Single Films

In most sputtering runs, single layer films of multilayer constituents were made as both a check of sample variability from run to run and as an independent measurement of the resistivity of each material. These films were measured using the van der Pauw technique[13].

The resistivity for films of arbitrary shape may be measured using the van der Pauw technique, if the film fulfills the following conditions: (1) The contacts are located on the circumference of the sample. (2) The contacts are sufficiently small. (3) The sample thickness is uniform over the entire sample. (4) The sample must be simply connected, i.e., it has no isolated holes within the film. When these conditions are satisfied, equation 3.3 is used.

$$\rho = \frac{\pi d}{\ln 2}\left(\frac{R_{ABCD} + R_{BCDA}}{2}\right) f\left(\frac{R_{ABCD}}{R_{BCDA}}\right) \qquad 3.3$$

In equation 3.3, d is the film thickness and f is a function of the ratio $R_{AB,CD}/,R_{BC,DA}$ where $R_{AB,CD}$ is the potential difference measured between contacts D and C divided by the current through contacts A and B. Values of f are tabulated in Ref. 13.

The resistivity of each film was measured by attaching the leads to the sample with In and cerralloy 117 solder. The holder was then slowly lowered into a dewar of liquid helium, the same environment in which CPP measurements are made. $R_{AB,CD}$ is obtained by putting 1.000 mA from a Kiethley 224 current source through leads A and B while the potential difference across leads C and D is measured with a Kiethley 181 nanovoltmeter. Similarly, $R_{BC,DA}$ is found by putting current through B and C while measuring the potential across A and D. The film thickness is measured using a Dektak IIA surface profilometer. The resistivity of the sample is then calculated using equation 3.3.

The uncertainty in the resistivity of these films is almost entirely due to measurement of the film's thickness, ±5-10%. Typically six different locations are scanned and averaged together for the film's height. Substrate curvature and discontinuities in the Nb strip profile can make determination of the film's height much harder.

3.6 Determination of CPP Area

The quantity of interest in the CPP geometry is the conductance per unit area, G/A. Experimentally it is easier to measure its inverse, AR, the product of the sample area and the total sample resistance. The effective sample area is the region of overlap between the crossed Nb strips, asi shown in Figure 1.5. This area is determined by the width of each Nb strip. A Dektak IIA surface profilometer[14] with horizontal and vertical resolutions of 50nm and 0.5nm, respectively, is used. Figure 3.5 shows a typical scan of a Nb strip.

The procedures followed for each scan are detailed in the thesis of S.F. Lee[12]. The only difference here is that all samples were deposited on Si <100> substrates which had no noticeable curvature compared to the sapphire substrates used by S.F. Lee. Here the width was always defined by finding the point 10nm above a sharp increase in the slope of the Nb profile on either side of the strip. Reasons for the 10nm given by S.F. Lee concern the suppression of T_C in thin superconducting films. The average width of the Nb leads was ~1.1mm making the sample area ~ 1.2mm^2. Uncertainties in the effective CPP areas were ±2-5%.

Height nm

Figure 3
vertical a

3.7 CI

Two d

The first v

CIP part o

current lea

resistance i

area. Typ

potentiome

was necessa

terminal mo

details see R

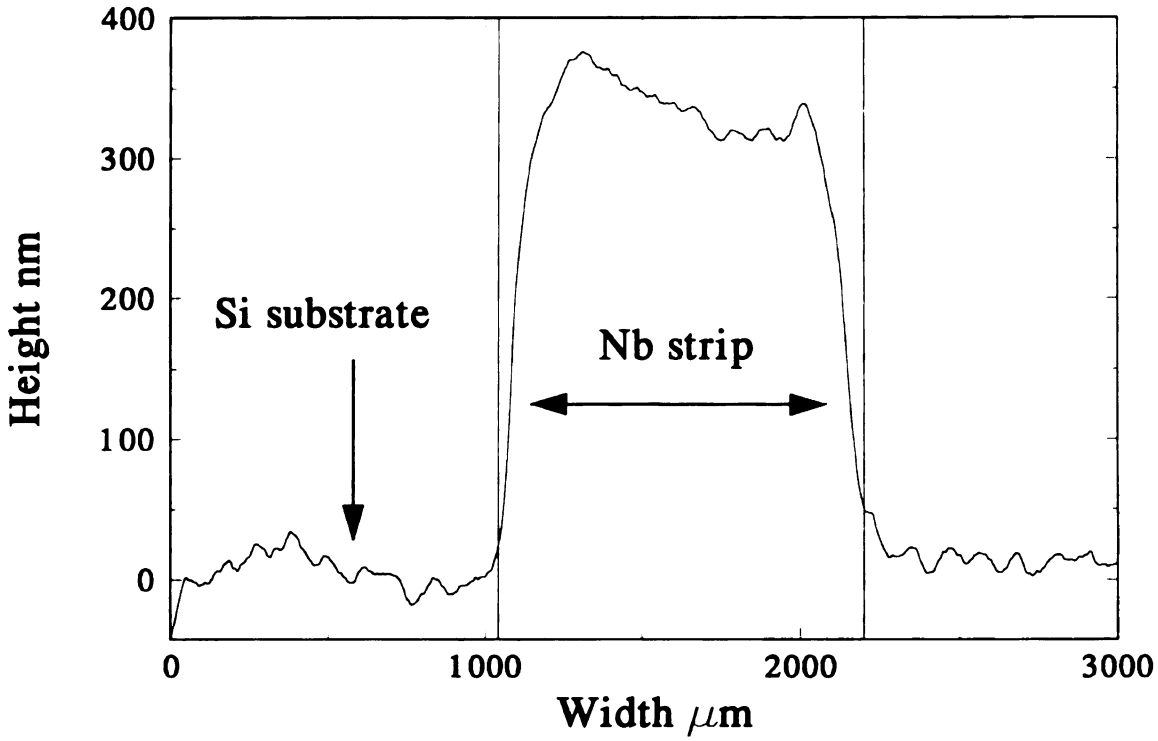

Figure 3.5. Nb strip profiled via Dektak, note the scale change from nm to mm for the vertical and horizontal, respectively.

3.7 CIP Measurements

Two different types of CIP measurements were made over the course of this study. The first will be designated as just CIP and will refer to those measurements made on the CIP part of the CPP samples, see Figure 1.5. For these measurements both voltage and current leads were soldered to each of the CIP pads on the sample. The sample's resistance is dominated by the two thin sections connecting the CIP pads to large circular area. Typically the sample's conductance was measured using a SHE model PCB potentiometric conductance bridge which has a range of 0.05Ω to 10Ω. Occasionally it was necessary to measure the resistance directly using a Fluke 8502A multimeter in four terminal mode which is capable of measuring resistances down to 0.01mΩ. For further details see Ref. 12.

The other type will be designated as a "CIP film" since these were multilayered films made without a mask (Figure 2.4a) and so only CIP resistances could be measured in these samples. The resistance of these samples is also measured using a four terminal method. For these CIP samples the leads are attached in a row along the sample using Ag paint as shown schematically in Figure 3.6. The samples were then loaded into a Quantum Design Magnetic Property Measurement System (MPMS) for temperature and field dependence studies. The computer controlled MPMS was interfaced with a Kiethley 224 programmable current source and a Kiethley 181 nanovoltmeter using the external device control (EDC) routines written by R. Loloee[15]. The potential difference between the inner leads is read while a 1.000mA current is put through the outside leads. Measurements for ±1.000mA are averaged together to eliminate any thermal EMFs.

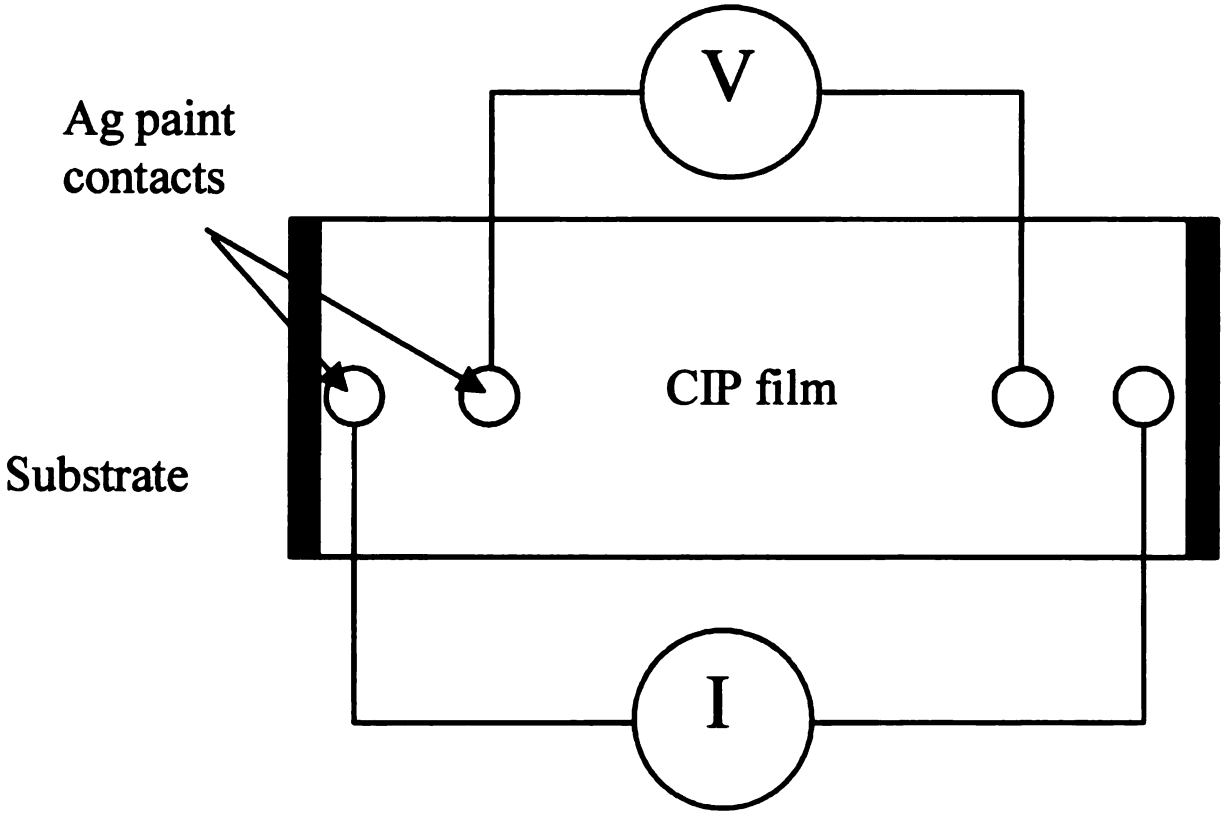

Figure 3.6: Schematic of CIP-MR measurement for CIP film. H is typically applied longitudinally, along the direction of the measuring current.

3.8 CPP Measurements

The apparatus used for measuring CPP resistances is based on the ability of a superconducting quantum interference device (SQUID) to detect extremely small voltages (~10^{-15}v). Three different SQUID based systems were used in the course of this study. The low field apparatus, described in S.F. Lee's thesis[12] and elsewhere[16], was used mainly to measure Co/Cu, Co/CuPt, Co/CuMn and Co/CuGe samples. The highest field achievable in this system was 1.0kG. The high field apparatus was built by S.F. Lee and is similar to the low field system except for the 5T superconducting magnet and the heavy Fe shielding around the SQUID. This system was seldom used except for samples with strong antiferromagnetic coupling which required 1-2T for saturation. The Quick Dipper (QD) system was designed and built by professor W.P. Pratt, Jr..

All three systems use the same basic design for the sensing circuit. The SQUID is used as a null detector to determine the ratio of sample current to reference current necessary to maintain the same potential drops across both the sample and the reference resistance. The SQUID is linked inductively to a circuit loop containing the sample and reference resistances, Figure 3.7. First a known current, I_S, is put through the sample side of the circuit loop. Since R_S and R_{ref} are in parallel, a small current will flow through the inductor next to the SQUID. The field generated by this inductor causes the SQUID to go out of balance. To null out this current (and hence the SQUID), another current, I_{ref}, is put through the reference side of the circuit loop. The reference current is increased until the potential across R_{ref} exactly balances the potential across R_S. As this happens, the current through the inductor decreases, reducing the flux through the SQUID loop bringing it back into balance. R_S is found using equation 3.4.

$$\frac{R_S}{R_{ref}} = \frac{I_S}{I_{ref}} \qquad 3.4$$

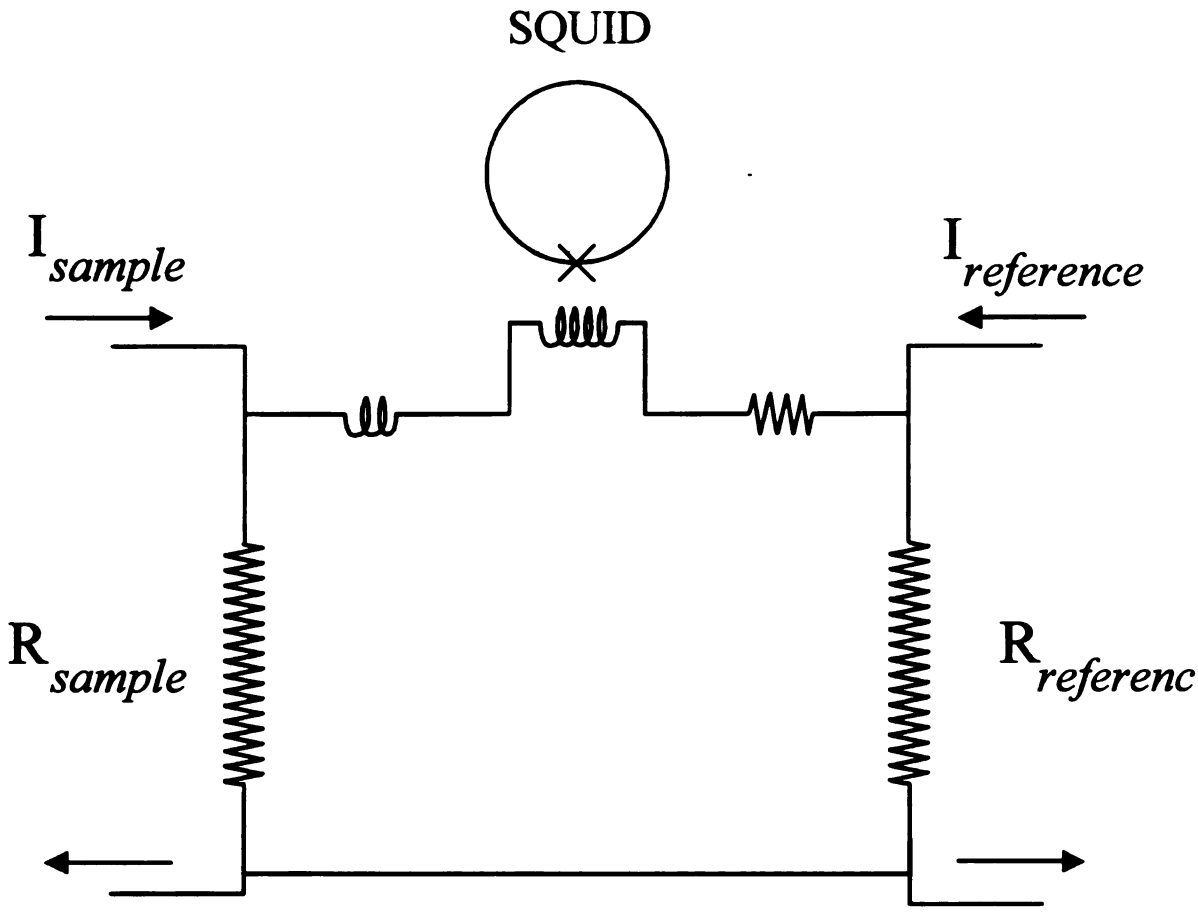

Figure 3.7: Schematic of SQUID measuring circuit.

The difference between the QD and the other two systems is that the SQUID controller for the QD has a feedback circuit in which I_{ref} is adjusted automatically; so that instead of manually adjusting and recording the current ratio I_S / I_{ref} through R_S and R_{ref}, only I_S and V_O, the feedback output voltage of the SQUID are measured. For the QD equation 3.5 is used.

$$R_S^* = 9.461\left(\frac{\Delta V_o}{\Delta I_s}\right) \qquad 3.5$$

where R_S^* is the effective sample resistance in nΩ and ΔV_O is the change in V_O measured in volts when I_S is changed by ΔI_S measured in Amps.

Superconducting wire is used for sample/reference circuit loop to eliminate any other resistive sources. Both the current leads and the two superconducting voltage leads are soldered to the Nb pads with In. The small contact resistance associated with these In solder joints is not important for the following reasons: (1) A constant current is maintained through the sample so a slightly higher resistance will not change I_S. (2) There is no current flow from the sample to the reference (and the reverse) when the circuit is balanced, so the In joints cannot drop any of the voltage. Also the In resistance is very small when compared with the 94.5μΩ reference resistor.

The magnet on the QD is a superconducting solenoid hand wound using multifilament NbTi (Cu matrix) wire. It is designed for a maximum of 30A, which gives ~1.6T of field. The calibration is given below in equation 3.6.

$$B = 0.05265 \times I \qquad 3.6$$

where B is the strength of the applied field in Tesla when a current of I Amps is put through the solenoid. The sample is always mounted in the same position with the current perpendicular to the applied field.

[1] I.A. Watt, "The Principles and Practices of Electron Microscopy", Cambridge University Press, Cambridge, U.K. (1985).

[2] L. Hoines Ph.D. Dissertation, Michigan State University (1994).

[3] M.L. Wilson, Ph.D. Dissertation, Michigan State University (1994).

[4] H. Holloway, private communication.

[5] H.P. Klug and L.E. Alexander, *X-Ray Diffraction Procedures For Polycrystalline and Amorphous Materials*, Wiley-Interscience, New York, NY (1974) p.659.

[6] *Ibid.* p. 657.

[7] D. Howell M.A. Crimp, unpublished.

[8] P. Galtier, unpublished.

[9] P. Galtier, T. Valet, O. Durand, J.C. Jacquet and J.P. Chevalier, Mat. Res. Soc. Symp. Proc., **313**, 47 (1993).

[10] E. A. M. van Alphen, P.A.A. van der Heijden and W.J.M. DeJonge, J. Appl. Phys. **76**, (1994).

[11] C. Mèny, P. Panissod and R. Loloee, Phys. Rev. B**45**, 12269 (1992).

[12] S.F. Lee, Ph.D. Dissertation, Michigan State University (1994).

[13] L.J. van der Pauw, Philips Research Reports 13, 1 (1958).

[14] Sloan Technology Corp., Santa Barbara, CA.

[15] R. Loloee, unpublished.

[16] D. Edmunds, W.P. Pratt Jr. and J.A. Rowlands, Review of Scientific Instruments 51, 1516 (1980).

Chapter 4:

Theory of CPP Transport in Magnetic Multilayers

Introduction

This chapter begins with a much simplified picture of spin dependent scattering. Then the two current model for electron transport in F/N multilayers is used to derive equations used in the analysis of CPP data given in chapters 5 and 6. This is followed by a discussion of the Valet and Fert equations which allow for finite spin diffusion lengths in both the F and N metals. Next the CPP phenomenon of spin accumulation at the F/N interface is examined along with spin flip scattering by spin orbit interactions. Finally the chapter closes with a section that theoretically shows GMR could either be positive or negative depending upon the spin asymmetry of adjacent F layers. For an introductory discussion of magnetism see Crangle[1]; for a more detailed discussion of magnetism see Bozorth[2], Chikazumi[3] or Cullity[4]. Also articles by J.E. Cooke[5] give results which include exchange interactions and spin waves in Co, Ni and Fe.

4.1 Spin Dependent Scattering - A Simplified Picture

This section is to give a crude idea of where spin dependent scattering arises. The spontaneous magnetic moments of Fe, Co and Ni are a result of the unpaired 3d electron spins. For isolated Co atoms the 3d orbital only contains 7 electrons out of the 10 that could be accommodated. Electron interactions favor an arrangement that maximizes the total spin, and so in accordance with Hund's Rules 5 electron spins point in the same direction while the remaining 2 electron spins point in the opposite direction. Since each electron may contribute one Bohr magneton (μ_B) to the macroscopic magnetization, the total magnetic moment of a Co atom is $3\mu_B$. For isolated atoms there is also a contribution from the orbital angular momentum of the electrons to the total magnetic moment, however, in a crystal the orbital moment is quenched and therefore will not be of concern here.

As atoms are brought close together to form a crystal electron orbitals overlap allowing electrons to hop from atom to atom. The electrons are no longer bound to a particular atom but are shared by all the atoms in the crystal. The *3d* and *4s* atomic levels spread into energy bands. The *4s* orbitals overlap much more than do the *3d* orbitals, which results in a wider *4s* band with mobile low effective mass electrons. The *3d* band does not overlap as much resulting in a narrow band of higher effective mass electrons. In a highly simplified *s-d* picture, the *4s* electrons are largely responsible for the transport properties of these metals, while the less mobile *3d* electrons are responsible for the magnetic properties. (This picture is oversimplified since massive hybridization occurs.)

The density of states $D_s(E)$ and $D_d(E)$ in the *s* and *d* bands of nonmagnetic transition metals are shown schematically in Figure 4.1a for both spin directions. The area under each D(E) curve equals the total number of states of each spin available to electrons. For a crystal with N atoms, this is N and 5N for *s* and *d* electrons, respectively. Since the d band is narrow (*d* electrons are less mobile) and must accommodate five times the number of electrons than the s band, $D_d(E) >> D_s(E)$.

Current propagating through a ferromagnet is mainly carried by equal numbers of spin up and spin down *4s* electrons. The resistivity depends on the amount of scattering the electrons undergo as they travel through the ferromagnet. This is proportional to the number of available states into which electrons can be scattered. This simplistic picture is shown schematically in Figure 4.1. As is done in the next section, one may define a resistivity for the spin up electrons, $\rho^{\uparrow}$, and similarly a $\rho^{\downarrow}$, for the spin down electrons. Each resistivity depends on the density of states near the Fermi surface. The metal shown in 4.1a has the same density of states for each spin, and therefore the scattering is independent of the electron's spin. Figure 4.1b shows the density of states for a ferromagnet which does depend on the electron spin. Here, $\rho^{\uparrow} \propto D^{\uparrow}(E)$ while $\rho^{\downarrow} \propto D^{\downarrow}(E)$ and at the Fermi surface $D^{\downarrow}(E_F) > D^{\uparrow}(E_F)$ which gives rise to an asymmetry in the scattering of spin up and spin down electrons. Therefore in Figure 4.1b, there is spin dependent scattering and $\rho^{\downarrow} / \rho^{\uparrow} > 1$.

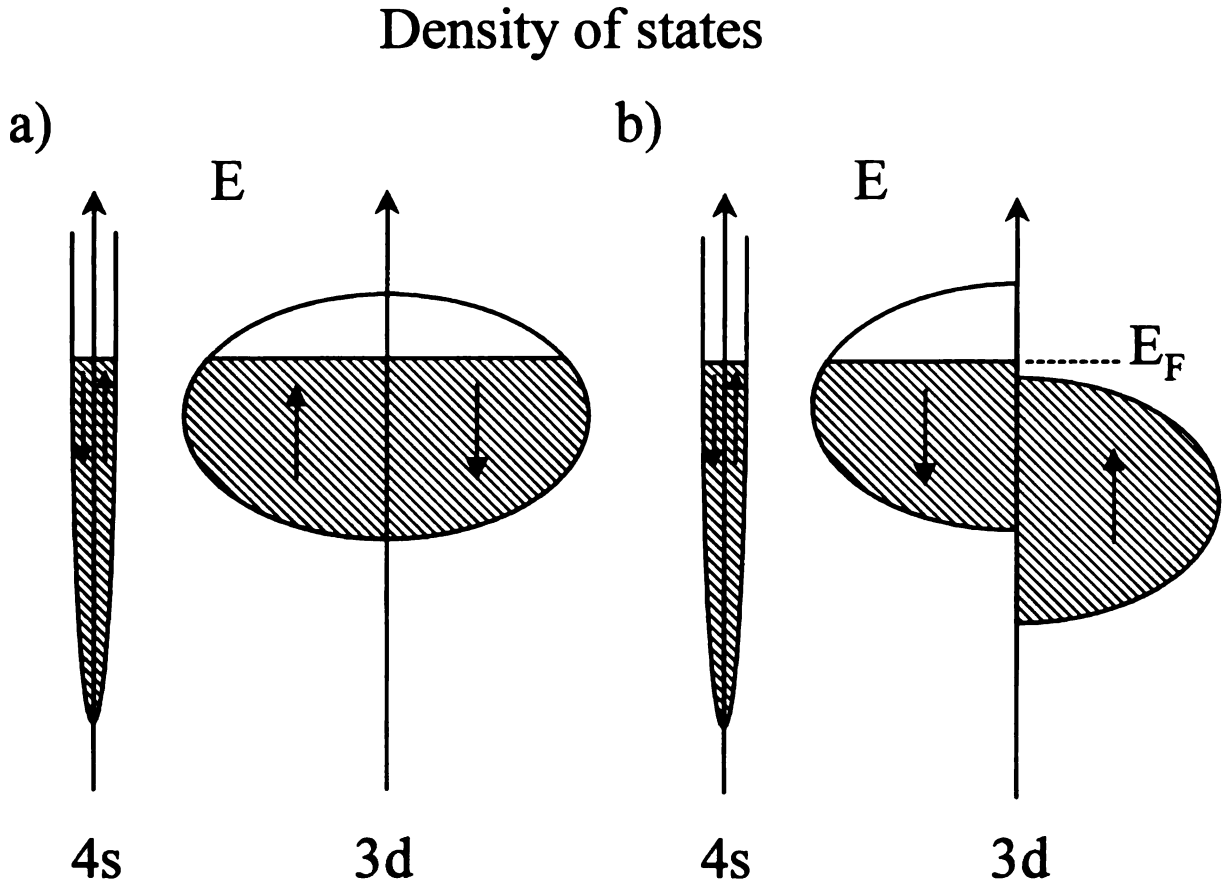

Figure 4.1: Schematic representation of the density of states for *3d* transition metals. In a) there are no unpaired spins so ferromagnetism would not be exhibited, however, b) does have a spin-split density of states in the *3d* band similar to Co which is a ferromagnet. (after Ref. 2)

4.

car

ele

hyr

the

-x c

dire

and

fer

cha

laye

a)

e

e

Figure
perpen
$\alpha = \rho$

4.2 The Two Current Model

Initially we assume there is no spin flip scattering. Then the current through a sample can be thought of as flowing through two independent channels defined by the spin of the electron relative to some defined axis. Consider a multilayer with the plane of the layers lying in the *xy* plane and a current, *J*, applied along the *z* axis (CPP geometry). Taking the magnetization of the ferromagnetic (F) layers as being in either the $+x$ direction or the $-x$ direction makes the *x* axis the spin quantization axis. This defines the absolute spin direction as + or -, where + electrons remain spin up as they pass through the multilayer and - electrons remain spin down as they pass through the multilayer. In each ferromagnetic layer one spin channel undergoes more scattering than the other spin channel. As the + electrons pass through the sample they undergo more scattering in F layers that have their magnetizations pointing down, schematically shown in Figure 4.2.

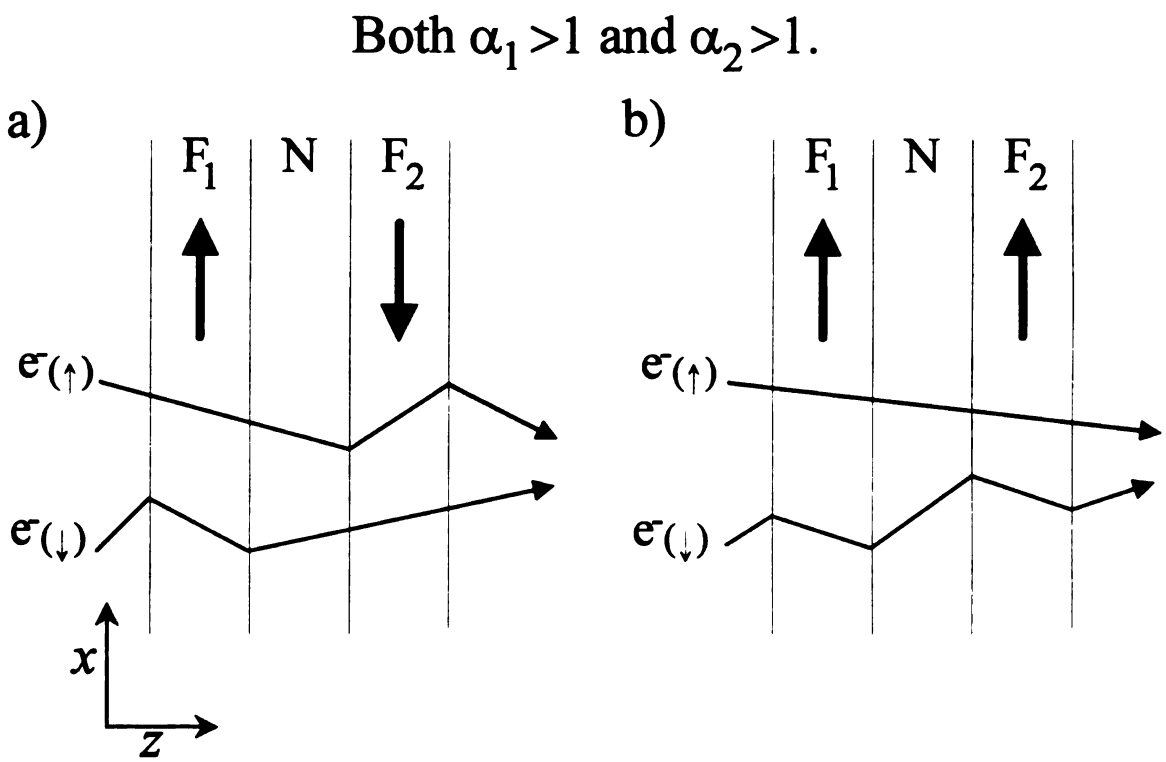

Figure 4.2: Schematic representation of electrons propagating along the z-axis, perpendicular to the layers for F_1 and F_2 a) antiparallel and b) parallel. Here, $\alpha = \rho^{\downarrow}/\rho^{\uparrow}$, is the same for all F layers.

Taking the concept of majority and minority carriers from electron transport in semiconductors, one may say that the + electrons are majority carriers for F layers in which the magnetization is in the + direction and minority carriers for F layers with the magnetization in the - direction. Similarly, for the other channel - electrons parallel to the F layer magnetization are majority carriers and are minority carriers for - electrons antiparallel to F layer magnetizations. The channels will carry current independently when the amount of spin-flip scattering in the sample is negligible. Figure 4.3 shows the equivalent circuit for the two channels. The resistance of each channel is a series combination of R_N, $R_{F/N}$, R_F and $R_{S/F}$ where these are the contributions to the resistance from the normal metal, F/N interfaces, ferromagnetic metal and S/F interfaces. We use the following definitions:

$$\begin{aligned}
\rho_F^{\uparrow} &= \frac{2\rho_F}{1+\beta} \\
\rho_F^{\downarrow} &= \frac{2\rho_F}{1-\beta} \\
R_{F/N}^{\uparrow} &= \frac{2R_{F/N}}{1+\gamma} \\
R_{F/N}^{\downarrow} &= \frac{2R_{F/N}}{1-\gamma} \\
\rho_N^{\uparrow} &= \rho_N^{\downarrow} = 2\rho_N \\
R_{S/F}^{\uparrow} &= R_{S/F}^{\downarrow} = 2R_{S/F}
\end{aligned} \qquad 4.1$$

Here $\rho_F^{\uparrow}$ ($\rho_F^{\downarrow}$) is the resistivity for an F layer with its local M_i parallel (antiparallel) to the electron spin. Similarly, $R_{F/N}^{\uparrow}$ and $R_{F/N}^{\downarrow}$ are the *F/N* interface resistances. ρ_F and ρ_N are the bulk resistivities of the F-metal and N-metal measured independently on thin films. β and γ are thus defined as the spin asymmetry parameters of the bulk F-metal and the F/N interface, respectively. $2R_{S/F}$ is the boundary resistance between the superconducting Nb and the ferromagnet (Co[6,7,8,9] or Py[10]) measured on a series of *S/F/S*

sandwiches. It is assumed that $R_{S/F}$ is the same for each spin channel and therefore makes no contribution to the change in a sample's resistance in going from an AP state to a P state.

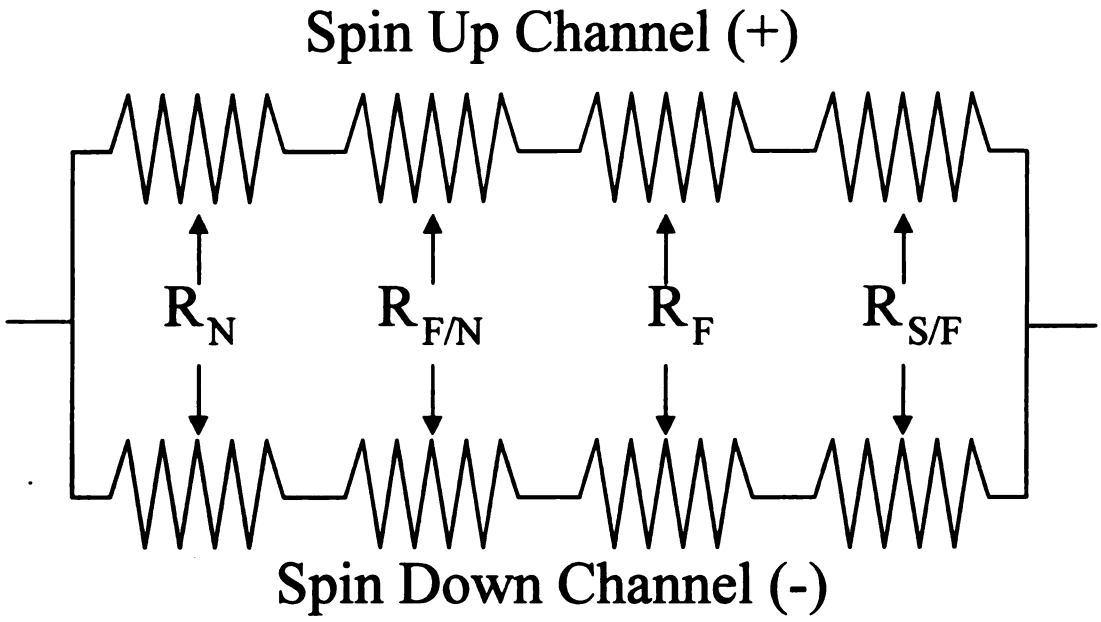

Figure 4.3: Equivalent circuit for the two channel model.

The resistances of the (+) and (-) channels are multilplied by the area, A, of the sample so that the bulk resistances may be directly compared with the interfacial resistances. The expression for adjacent F-layer magnetizations aligned antiparallel (AP) to each other is given by[11]:

$$AR_T^{(+)}(AP) = 2AR_{S/F}^{\uparrow} + \frac{N}{2}[\rho_F^{\uparrow} t_F + \rho_F^{\downarrow} t_F + \rho_N^{\uparrow} t_N + \rho_N^{\downarrow} t_N + 2AR_{F/N}^{\uparrow} + 2AR_{F/N}^{\downarrow}]$$

$$= 4AR_{S/F} + \frac{2N}{1-\beta^2}\rho_F t_F + 2N\rho_N t_N + \frac{2N}{1-\gamma^2}2AR_{F/N}$$

$$= AR_T^{(-)}(AP)$$

The parallel combination of $AR_T^{(+)}(AP)$ and $AR_T^{(-)}(AP)$ is just $AR_T(AP)$ given in equation 4.2:

$$AR_T(AP) = 2AR_{S/F} + N\rho_F^{*} t_F + N\rho_N t_N + N2AR_{F/N}^{*} \qquad 4.2$$

where $\rho_F^{*} = \rho_F/(1-\beta^2)$ and $R_{F/N}^{*} = R_{F/N}/(1-\gamma^2)$. If the total sample thickness, $T=N(t_F+t_N)$, is constant, equation 4.2 is linear in the bilayer number, N. The parameters for the slope and intercept of AR_T versus N are then given in terms of the ρ_F^{*} and $R_{F/N}^{*}$ instead of ρ_F and $R_{F/N}$.

The resistance of a sample that has adjacent F-layers parallel (P) to each other is straightforward to calculate but more complex since $AR_T^{(+)}(P) \neq AR_T^{(-)}(P)$. As in the derivation of equation 4.2 each channel is added in series first.

$$AR_T^{(+)}(P) = 2AR_{S/F}^{\uparrow} + N(\rho_F^{\uparrow} t_F + \rho_N^{\uparrow} t_N + 2AR_{F/N}^{\uparrow})$$

$$= 4AR_{S/F} + 2N\rho_N t_N + \frac{2N}{(1+\beta)}\rho_F t_F + \frac{2N}{(1+\gamma)}2AR_{F/N}$$

$$= 4AR_{S/F} + 2N\rho_N t_N + 2(1-\beta)N\rho_F^{*} t_F + 4(1-\gamma)NAR_{F/N}^{*}$$

Similarly, the resistance for (-) channel is obtained by replacing β and γ with $-\beta$ and $-\gamma$.

$$AR_T^{(-)}(P) = 4AR_{S/F} + 2N\rho_N t_N + 2(1+\beta)N\rho_F^{*} t_F + 4(1+\gamma)NAR_{F/N}^{*}$$

Adding $AR_T^{(+)}(P)$ and $AR_T^{(-)}(P)$ in parallel results in equation 4.3.

$$AR_T(P) = AR_T(AP) - \frac{\left[\beta N \rho_F^* t_F + \gamma 2 N A R_{F/N}^*\right]^2}{AR_T(AP)} \qquad 4.3$$

The spin asymmetry parameters may be extracted by first obtaining ρ_F^* and $R_{F/N}^*$ using equation 4.2. Then β and γ are obtained using equation 4.4. Rearranging terms in equation 4.3 gives a more useful quantity experimentally.

$$A\sqrt{R_T(AP)\left[R_T(AP) - R_T(P)\right]} = N\left[\beta \rho_F^* t_F + \gamma 2 A R_{F/N}^*\right] \qquad 4.4$$

This equation makes the interesting prediction that the square root should be independent of ρ_N, the normal metal resistivity. Results which confirm this prediction and thereby support the two channel model are presented later. In equation 4.4, quantities measured experimentally, the CPP resistances, are grouped on the left side. The right side of equation 4.4 may be used to determine β and γ by choosing two sets of data with t_F=*constant* and fitting the data to this equation. Choosing $t_F=t_N=T/2N$ gives equation 4.5 which has the bulk spin asymmetry independent of the number of bilayers.

$$A\sqrt{R_T(AP)[R_T(AP) - R_T(P)]} = \frac{\beta \rho_F^* T}{2} + N\gamma 2 A R_{F/N}^* \qquad 4.5$$

Plotting the $t_F=t_N$ data as a function of the bilayer number results in a positive intercept, proportional to the bulk spin asymmetry parameter, and a positive slope, proportional to the interface spin asymmetry parameter. In either case $t_F=t_N$ or t_F=*constant*, ρ_F^* and $R_{F/N}^*$ must be determined from fits of equation 4.2.

A commonly used asymmetry parameter may be defined by the ratio of the spin down resistivity to the spin up resistivity in the bulk F material and at the F/N interface, these are:

$$\alpha_F = \frac{\rho_F^{\downarrow}}{\rho_F^{\uparrow}}$$

$$\alpha_{F/N} = \frac{R_{F/N}^{\downarrow}}{R_{F/N}^{\uparrow}}$$

With the definitions given previously in equations 4.1, these spin asymmetry parameters may be related to the scattering parameters in the bulk, β, and at the interface, γ.

$$\alpha_F = \frac{1+\beta}{1-\beta}$$

$$\alpha_{F/N} = \frac{1+\gamma}{1-\gamma} \qquad 4.6$$

The expressions in 4.6 are used to relate β and γ to the asymmetry coefficients used extensively in the literature.

The two current model can also be used for more complex multilayer structures with two different magnetic components $F_1/N/F_2/N$. Here the AP state is produced by choosing ferromagnetic materials F_1 and F_2 with significantly different saturation fields, $H_{S1} >> H_{S2}$. The AP state is formed after saturating the sample at H_{S1} and then taking the field back through zero to just beyond $-H_{S2}$. The AR_T for each state (AP and P) is just the parallel combination of the spin up and spin down channels similar to that shown above.

$$AR^{(+)}(AP) = 4AR_{Nb/Co} + N[4\rho_N t_N + \rho_{Co}^{\uparrow} t_{Co} + 2AR_{Co/Ag}^{\uparrow} + \rho_{Py}^{\downarrow} t_{Py} + 2AR_{Py/Ag}^{\downarrow}] \quad 4.7a$$

$$AR^{(-)}(AP) = 4AR_{Nb/Co} + N[4\rho_N t_N + \rho_{Co}^{\downarrow} t_{Co} + 2AR_{Co/Ag}^{\downarrow} + \rho_{Py}^{\uparrow} t_{Py} + 2AR_{Py/Ag}^{\uparrow}] \quad 4.7b$$

Substituting the definitions listed in 4.1 into equations 4.7 gives AR in terms of β and γ for each ferromagnetic material. The resistance of the AP state for samples of Co/Ag/Py/Ag (where Py=$Ni_{84}Fe_{16}$) is obtained from the parallel addition of equations 4.7a and 4.7b. The P state for these samples is found in a similar fashion. A simplified expression for the AP state similar to that given in equation 4.2 for the AP state of the two component system does not exist for this three component system, since $AR^{(+)}(AP) \neq AR^{(-)}(AP)$.

4.3 Spin-flip Scattering for the CPP Geometry

In the previous section, it was assumed that the spin-flip scattering was negligible. Relaxing this condition leads to a very complicated set of equations derived by Valet and Fert[12]. In their theory, they showed that for multilayers the Boltzmann equation reduces to macroscopic transport equations if the spin diffusion length (a measure of the spin flip scattering length to be defined in equation 4.14) is much longer than the elastic mean free path (mfp), regardless of the ratio of the mfp to the layer thickness. They analyzed a two component system with single domain F-layers. Simplifying assumptions of: (1) single parabolic conduction bands, (2) same effective mass, m, and (3) same Fermi velocity, v_F, were made for each metal. The m and v_F simplifications may be relaxed without an essential change in their conclusions. They have included both spin dependent scattering in the bulk material and at the interfaces but limit themselves to low temperature to eliminate spin-flips from magnon-electron collisions. The spin-flip events they allow arise from spin-orbit interactions or exchange scattering associated with defects or impurities in either metal. The steady state spin dependent electrochemical potential (μ), electric field (F), and current densities (J) are found in each layer by matching the solutions to the transport equations at each interface. Continuity of the current across an interface leads to spin accumulation at each interface.

The Valet and Fert model give the following equations for finite spin diffusion lengths in both the F and N layers:

$$R(P,AP) = N[r_0 + 2r_{SI}^{(P,AP)}] \qquad 4.8$$

where

$$r_0 = (1-\beta^2)\rho_F^* + \rho_N^* t_N + 2(1-\gamma^2)r_b^* \qquad 4.9$$

equation 4.10

$$r_{SI}^{(P)} = \frac{\frac{(\beta-\gamma)^2}{\rho_N^*\ell_{sf}^N}\coth\left[\frac{t_N}{2\ell_{sf}^N}\right] + \frac{\gamma^2}{\rho_F^*\ell_{sf}^F}\coth\left[\frac{t_F}{2\ell_{sf}^F}\right] + \frac{\beta^2}{r_b^*}}{\frac{1}{\rho_N^*\ell_{sf}^N}\coth\left[\frac{t_N}{2\ell_{sf}^N}\right]\frac{1}{\rho_F^*\ell_{sf}^F}\coth\left[\frac{t_F}{2\ell_{sf}^F}\right] + \frac{1}{r_b^*}\left\{\frac{1}{\rho_N^*\ell_{sf}^N}\coth\left[\frac{t_N}{2\ell_{sf}^N}\right]\frac{1}{\rho_F^*\ell_{sf}^F}\coth\left[\frac{t_F}{2\ell_{sf}^F}\right]\right\}}$$

equation 4.11

$$r_{SI}^{(AP)} = \frac{\frac{(\beta-\gamma)^2}{\rho_N^*\ell_{sf}^N}\tanh\left[\frac{t_N}{2\ell_{sf}^N}\right] + \frac{\gamma^2}{\rho_F^*\ell_{sf}^F}\coth\left[\frac{t_F}{2\ell_{sf}^F}\right] + \frac{\beta^2}{r_b^*}}{\frac{1}{\rho_N^*\ell_{sf}^N}\tanh\left[\frac{t_N}{2\ell_{sf}^N}\right]\frac{1}{\rho_F^*\ell_{sf}^F}\coth\left[\frac{t_F}{2\ell_{sf}^F}\right] + \frac{1}{r_b^*}\left\{\frac{1}{\rho_N^*\ell_{sf}^N}\tanh\left[\frac{t_N}{2\ell_{sf}^N}\right]\frac{1}{\rho_F^*\ell_{sf}^F}\coth\left[\frac{t_F}{2\ell_{sf}^F}\right]\right\}}$$

In the limit where the spin diffusion length is much longer than the layer thickness, equations 4.8 to 4.11 will reduce to 4.2 for the AP state and 4.3 for P state shown in the previous section. If the spin diffusion length is approximately the layer thickness then the difference in the resistance between the AP and P states will be reduced by the spin-flipped conduction electrons, invalidating equations 4.2 and 4.3.

The effects of finite spin diffusion lengths are illustrated in Figures 4.4 and 4.5 where $\sqrt{[AR(AP)-AR(P)]AR(AP)}$ is plotted as a function of N, the bilayer number for the Valet-Fert equations (4.8-4.11). The deviation from infinite spin diffusion length is expected to be the greatest for smaller bilayer number when t_{Co} is held constant. In this region the normal metal interlayer is thicker so the ratio of t_N to ℓ_{sf}^N has the greatest

value. Comparing figures 4.4 and 4.5 reveals a greater sensitivity to ℓ_{sf}^{N} than to ℓ_{sf}^{F}. For further illustrations see Q. Yang's dissertation[13].

The Valet-Fert equations are valid only when $\ell_{sf}^{N} >> \lambda_{el}$. Recently Valet[14] has extended the analysis to second order in $\lambda_{el}^{N}/\ell_{sf}^{N}$ and found a correction term $\sim\frac{1}{4}\ell_{sf}^{N}(\lambda_{sf}^{N}/\ell_{sf}^{N})$. Further analysis must show if this correction holds to all orders.

Figu
bilay
^{45}Ca
720ns

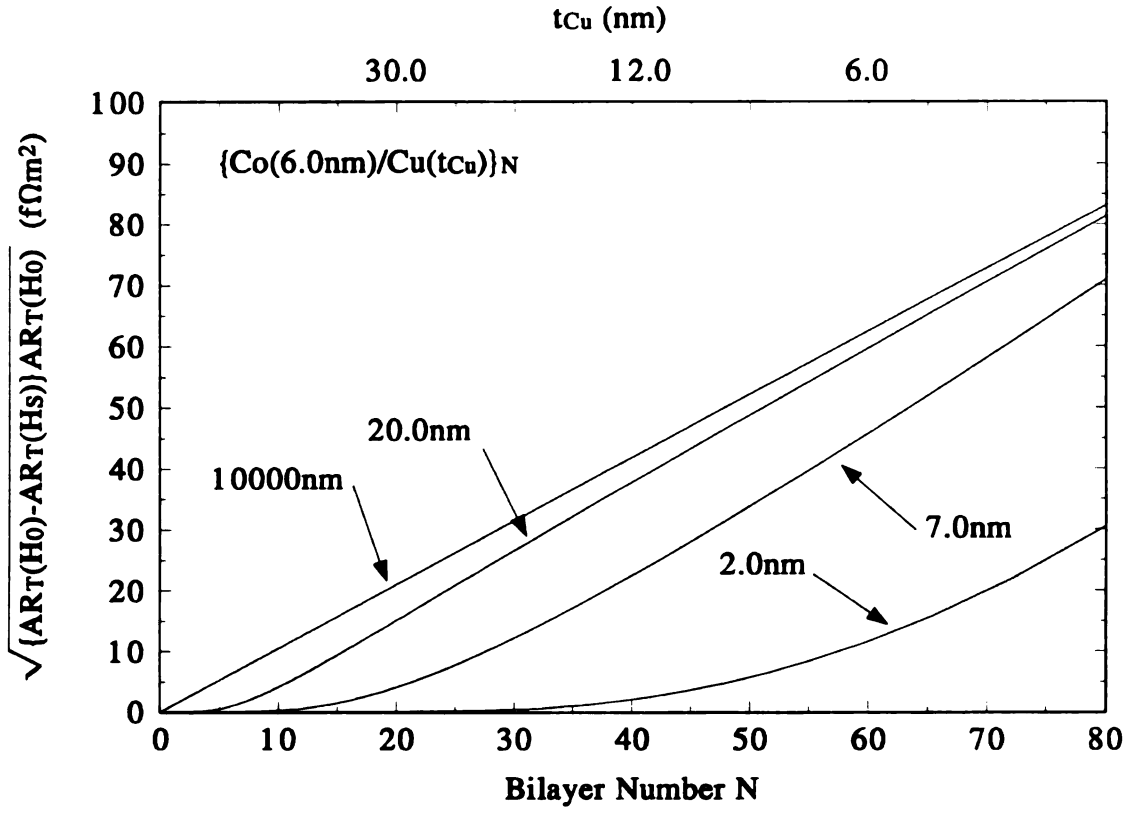

Figure 4.4: Theoretically predicted behavior of $\sqrt{AR(H_0)[AR(H_0)-AR(H_S)]}$ with the bilayer number, N, using the Valet-Fert model for $\ell_{sf}^{Co} = \infty$ and several different values of ℓ_{sf}^{Cu} listed in the Figure (ρ_{Cu}=10nΩm and ρ_{Co}=86nΩm). The total multilayer thickness is 720nm.

Figur
bilaye
f_{π}^{Co} 1
predic

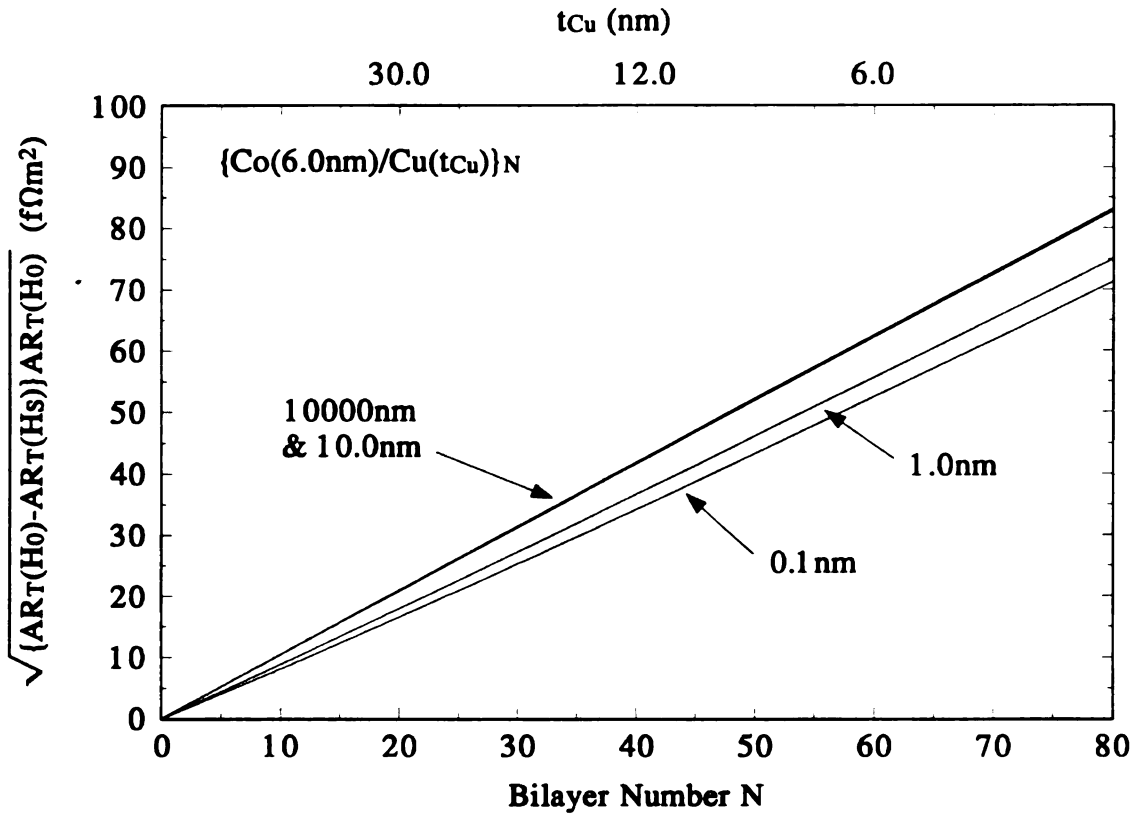

Figure 4.5: Theoretically predicted behavior of $\sqrt{AR(H_0)[AR(H_0)-AR(H_S)]}$ with the bilayer number, N, using the Valet-Fert model for $\ell_{sf}^{Cu} = \infty$ and several different values of ℓ_{sf}^{Co} listed in the Figure (ρ_{Cu}=10nΩm and ρ_{Co}=86nΩm). The 10000nm and 10nm predictions are nearly indistinguishable. The total multilayer thickness is 720nm.

4.4 Spin Accumulation in Magnetic Multilayers

Although spin-dependent scattering is responsible for both CIP-MR and CPP-MR, there are fundamental differences concerning the mechanisms through which the spin diffusion length (SDL) is manifested. The most important distinction between them comes from spin accumulation which occurs only in the CPP geometry. Spin accumulation refers to the buildup of a particular spin at an interface where the current of a given spin is suddenly forced to become smaller. Balancing spin accumulation are spin relaxation effects which relax the polarization of the electron spin.

To illustrate these effects on the transport properties at an interface, consider the boundary between two semi-infinite, identical ferromagnets (except for reversed magnetizations) shown in Figure 4.6. This closely follows the calculations of Fert, Valet and Barnas[15]. The current in each ferromagnet can be thought of as having two channels[16]. Here conduction electrons with spin parallel to the F_1 magnetization form the + spin channel while those with spin antiparallel to the F_1 magnetization form the - spin channel ($\alpha<1$ for both ferromagnets). For transport from F_1 to F_2, the + spin electrons (majority carriers) carry more of the current in F_1 than do the - spin electrons (minority carriers). After crossing the boundary into F_2 the spin channels switch roles because the magnetization is reversed, the - spin channel in F_1 is now the majority carrier in F_2. As a result, the flux of + spin electrons incident from the left of the interface is less than the outgoing flux of + spin electrons on the right. In effect the + spin electrons are being accumulated at the interface. This results in an out-of-equilibrium polarization and an increase in the chemical potential (μ) near the boundary for the + spin electrons. The opposite is true for the - spin electrons.

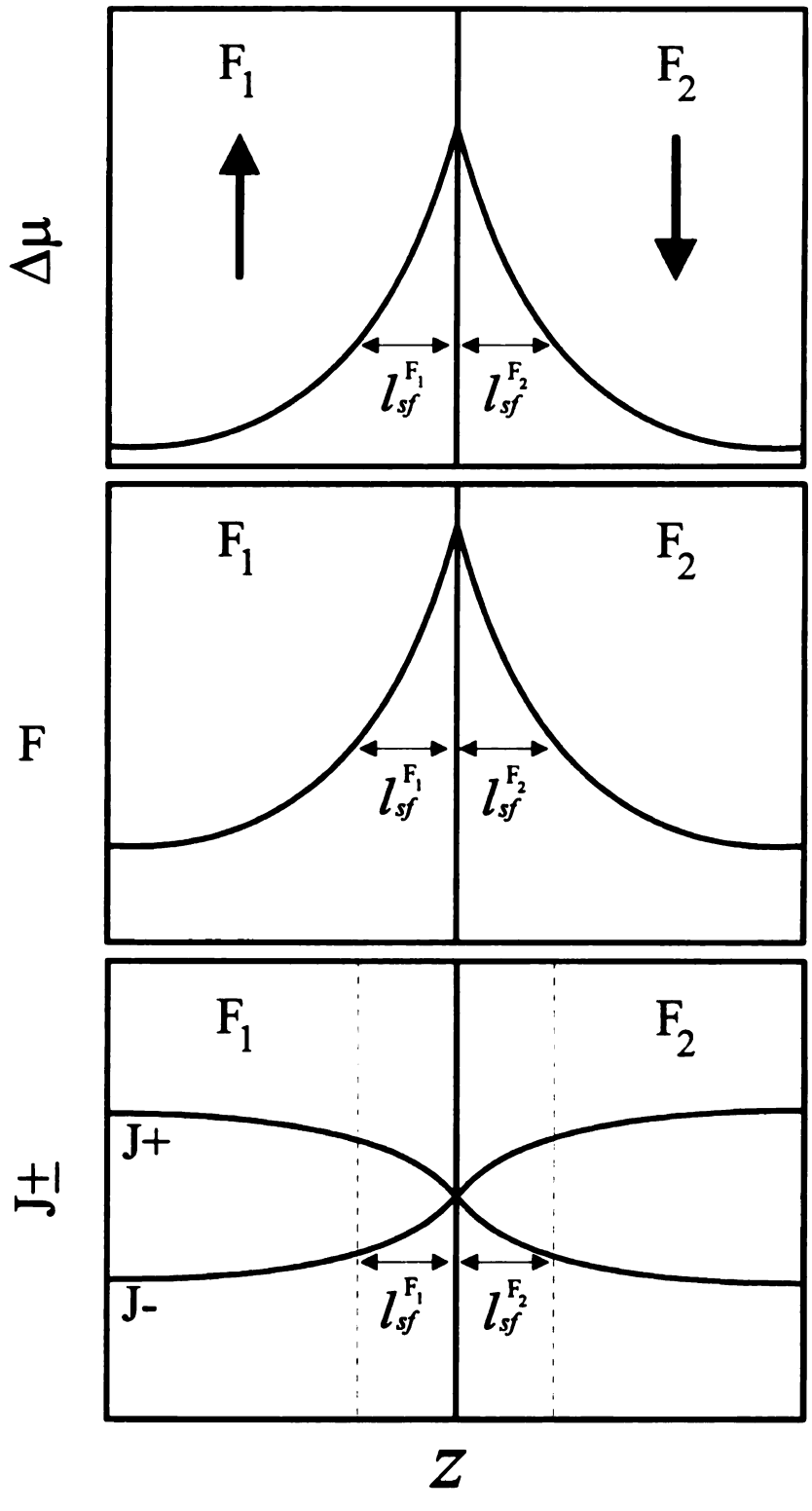

Figure 4.6: Effects of spin accumulation and relaxation at the interface of two ferromagnetic metal, F_1 and F_2 on the chemical potential, $\Delta\mu$, the pseudoelectric field, F, and the spin currents, J±, for an AP alignment of the moments of F_1 and F_2.

The

carrier

momen

distanc

modifie

followi

The so

differin

This sp

down a

it is als

been de

Son. *et*

Val

microsa

much l

where

diffusio

The spin relaxation process balances spin accumulation by allowing spins to change carrier channels. The spin relaxation time, τ_{sf}, is generally much longer than the momentum relaxation time, τ_s, and so spin accumulation will diffuse a significant distance away from the interface. The diffusion of the spins away from the interface modifies the chemical potential in this region. The potential difference now obeys the following diffusion equation.

$$\frac{(\mu_+ - \mu_-)}{\tau_{sf}} = D\frac{\partial^2}{\partial z^2}(\mu_+ - \mu_-) \qquad 4.12$$

The solution to 4.12 is a simple exponential provided the spin bands are symmetric, differing only in their scattering rates.

$$\mu_\uparrow - \mu_\downarrow = \Delta\mu_+ = Ae^{z/\ell_{sf}} \qquad z < 0$$

$$\Delta\mu_+ = Ae^{-z/\ell_{sf}} \qquad z > 0$$

This spatially changing potential (pseudoelectric field) will force + spin electrons to slow down and the - spin electrons to accelerate. Since the current is proportional to $\partial\mu/\partial z$, it is also modified by these interface effects as indicated in Figure 4.6. This problem has been dealt with macroscopically by Johnson and Silsbee[17] and also independently by van Son, *et al.*[18].

Valet and Fert[12] have justified this macroscopic picture by starting from the microscopic Boltzmann equations and taking the limit that the spin diffusion length is much longer than the mean free path. From Ref. 12:

$$J_s = \frac{\sigma_s}{e}\frac{\partial\mu_s}{\partial z}$$

$$\frac{e}{\sigma_s}\frac{\partial J_s}{\partial z} = \frac{(\mu_s - \mu_{-s})}{\ell_{sf}^2} \qquad 4.13$$

where for spin, s, the current density is J_s, the conductivity is $\sigma_s = n_s e^2\tau_s/m$ and the spin diffusion length (SDL) is ℓ_s defined by

$$\ell_s = v_F\left[\tau_{sf}(\tau_{sf}^{-1} + \tau_s^{-1})^{-1}/3\right]^{1/2} \approx v_F(\tau_{sf}\tau_s/3)^{1/2} \qquad 4.14$$

The equations

second says th

spin relaxation

for the chemic

the SDL of ea

in Ref. 18.

In the CIP

conduction ele

layer before it

critically on t

adjacent magn

though the SD

is the elastic

thickness bec

find it harder t

elastic mfp's

before their sp

This will seve

order of 1.0-

between adjac

electrons must

The equations in 4.13 give two simple expressions. The first is just Ohm's law. The second says that the spin accumulation due to the divergence of the current is balanced by spin relaxation through spin flips. Combining equations 4.13 gives the diffusion equation for the chemical potential in equation 4.12, if $D\tau_{sf}$ is replaced by ℓ_{sf}^2; which is related to the SDL of each spin channel by $\ell_{sf}^{-2} = \ell_{\uparrow}^{-2} + \ell_{\downarrow}^{-2}$, the kind of "average" SDL alluded to in Ref. 18.

In the CIP geometry, the elastic mfp determines the length scale. A spin polarized conduction electron must be able to travel from one magnetic layer to the next magnetic layer before its spin relaxes. For CIP, travel between adjacent magnetic layers depends critically on the elastic mfp. Electrons will tend to stay in a particular layer, isolating adjacent magnetic layers, if the layer thickness is much larger than the elastic mfp. Even though the SDL is typically at least one order of magnitude greater than the elastic mfp, it is the elastic mfp which determines where the electrons travel. Therefore as the layer thickness becomes on the order of the elastic mfp, spin polarized electrons in one layer find it harder to propagate directly to the adjacent magnetic layer. If the layers are several elastic mfp's then very few spin polarized electrons enter the adjacent magnetic layer before their spin relaxes, even though the layer thickness may be much less than the SDL. This will severely reduce the MR in CIP samples and limit layer thicknesses to of the order of 1.0-5.0nm for reasonable MR changes. In the CPP geometry, propagation between adjacent magnetic layers does not depend on the electron's elastic mfp since all electrons must travel through every layer. It is the SDL of the material that determines

whether or no

the main requi

In a multil

metal and fer

interface will

nature of a

hyperbolic ex

currents. Figu

in Ref. 12 fo

leads to the g

P magnetic cc

whether or not an electron will remain spin polarized relative to the next magnetic layer, the main requirement for GMR.

In a multilayer where the SDL is much longer than the thicknesses of both the normal metal and ferromagnetic metal, the spin accumulation and relaxation effects for each interface will interfere resulting in complex expressions for the resistance. The periodic nature of a multilayer modifies the simple exponential solutions given above to hyperbolic expressions for the chemical potential, the pseudoelectric field and the spin currents. Figure 4.7 gives a schematic representation of detailed calculations carried out in Ref. 12 for these three quantities. Matching the boundary conditions at the interfaces leads to the general expressions for the resistance of a CPP multilayer in both the AP and P magnetic configurations given in equations 4.8-4.11.

Figure 4.7: Sc
multilayer on t
$J_{\pm}$ for the AP s

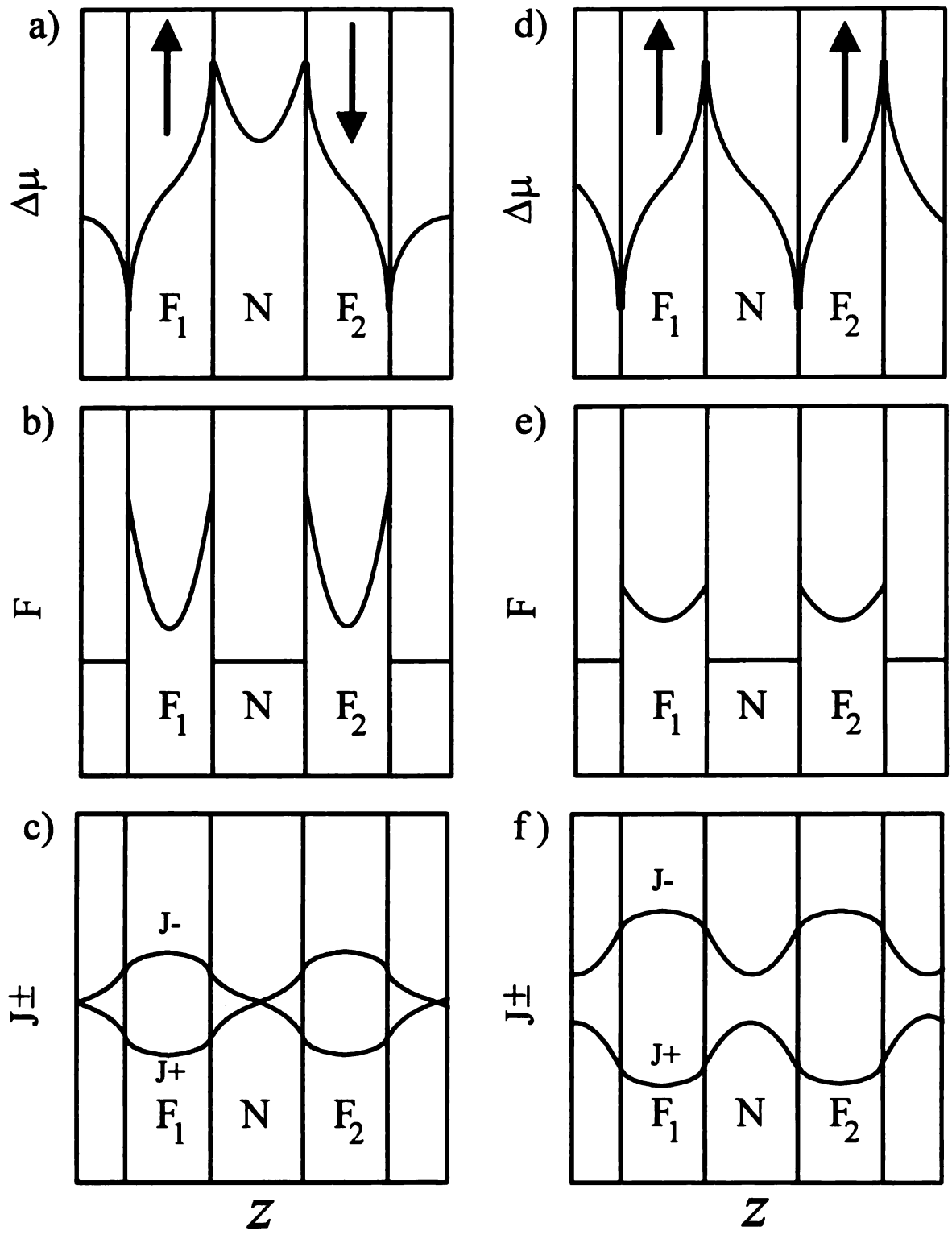

Figure 4.7: Schematic representation of spin accumulation and relaxation effects for a multilayer on the chemical potential, μ, the pseudoelectric field, F, and the spin currents, J± for the AP state, a), b) and c); and the P state, d), e) and f).

4.5 Spin

Increasin

MR of magn

impurities v

paramagneti

4.2K elimina

detailed desc

et al.[19]. Spi

Introduc

elements ad

Here τ_{sf}^{0} is t

impurities.

impurity ato

For trans

of the *4s* co

virtual boun

atom lie wit

would have

the conducti

in the *3d* in

states close

resonance is

in energy an

the *3d* impur

4.5 Spin Flip Scattering by Spin-orbit Interactions

Increasing the spin relaxation rate will significantly reduce the SDL and lower the MR of magnetic multilayers. Spin flips may result from three different sources: (a) from impurities with strong spin-orbit scattering, (b) from exchange interactions with paramagnetic impurities or (c) from electron-magnon collisions. Measurements made at 4.2K eliminate the electron-magnon interaction as a significant source of spin flipping. A detailed description of paramagnetic exchange interactions flipping spins is given by Fert *et al.*[19]. Spin-orbit interactions are considered here.

Introducing impurities with strong spin-orbit coupling such as Pt, Au or other *5d* elements adds an extra term, τ_{sf}^{I}, to the spin relaxation rate, τ_{sf}.

$$\frac{1}{\tau_{sf}} = \frac{1}{\tau_{sf}^{0}} + \frac{1}{\tau_{sf}^{I}}$$

Here τ_{sf}^{0} is the spin relaxation rate due to spin-orbit scattering by defects and residual impurities. The impurity term is proportional to the number of intentionally added impurity atoms per unit volume in the host metal.

For transition metal impurities, spin-orbit scattering is attributed to the hybridization of the *4s* conduction band states in the host with the *3d* states of an impurity atom. A virtual bound state is formed when empty electron states in the *3d* shell of an impurity atom lie within the conduction band of the host[20]. Normally the *3d* state of the impurity would have a specific energy and an infinite lifetime, but since the state now lies inside the conduction band it mixes with the conduction electron states. Therefore an electron in the *3d* impurity state is now able to escape into the continuum of conduction band states close to the energy of the *3d* impurity. The lifetime is no longer infinite and a resonance is seen in the density of states near the impurity state forming a state broadened in energy and extended in space. The width of the state depends on both the strength of the *3d* impurity potential and the degree of coupling with the conduction electron states.

To calcula

section. A sin

of the d state

number of d e

The spin flip c

where N_f is th

velocity. Equ

The spin diffu

Neglecting the

The spin diffu

spin channel[19]

in the ferroma

and in the ferro

Equations

polarized chann

To calculate the relaxation rate of the impurities, one must first find the spin flip cross section. A simple expression given by Yafet[21] relating the spin flip cross section in terms of the *d* state spin-orbit constant, λ_d, the width of the virtual bound state, Δ ($\approx$1eV), the number of *d* electrons, Z_d and the Fermi wave number, k_F, is

$$\sigma_{sf}^{I} = \frac{40\pi}{k_F^2}\left[\frac{\lambda_d}{\Delta}\right]^2 \sin^4\left(\pi\frac{Z_d}{10}\right) \qquad 4.15$$

The spin flip cross section is related to the spin flip relaxation by

$$\frac{1}{\tau_{sf}^{I}} = N_I v_F \sigma_{sf}^{I} \qquad 4.16$$

where N_I is the concentration per unit volume of impurity atoms and v_F is the Fermi velocity. Equations 4.15 and 4.16 are for nonmagnetic *3d* transition metal impurities. The spin diffusion length may be calculated once the spin relaxation time in known. Neglecting the residual term in equation 4.14 gives the spin flip mean free path as

$$\lambda_{sf} = v_F \tau_{sf}^{I} = \frac{1}{N_I \sigma_{sf}^{I}}$$

The spin diffusin length depends on the spin flip mfp, λ_{sf}, and the elastic mfp, λ, in each spin channel[19]. The elastic mfp in the nonmagnetic layer is the same in each channel but in the ferromagnetic layer this is not true. In the nonmagnetic layer the SDL is given by[19]

$$\ell_{sf}^{N} = \left[\frac{\lambda^N \lambda_{sf}^N}{6}\right]^{1/2} \qquad 4.17$$

and in the ferromagnetic layer by

$$\ell_{sf}^{F} = \left[\frac{\lambda_\uparrow \lambda_\downarrow \lambda_{sf}^F}{3(\lambda_\uparrow + \lambda_\downarrow)}\right]^{1/2} \qquad 4.18$$

Equations 4.17 and 4.18, together, define the length scales over which the spin polarized channels can exist as separate currents.

4.6 Positive and Negative Giant Magnetoresistance

Giant magnetoresistance refers to the change in electrical resistance with applied magnetic field brought about by spin dependent scattering of the conduction electrons. The difference between positive and negative GMR lies in the configuration of the multilayer with respect to the spin asymmetry coefficients of either the F layer, α_F , or at the F/N interface,$\alpha_{F/N}$, or both. A two component multilayer has one F component so that the spin asymmetry parameter is the same in every F layer and at every F/N interface, either all $\alpha>1$ or all $\alpha<1$. At zero field exchange forces between the F layers maintain an antiparallel state, which results in each channel undergoing the same amount of scattering as indicated in Figure 4.2a. Applying a field overcomes the exchange interaction and aligns adjacent F layer moments parallel to each other. This P state causes the same preferential scattering for one of the channels at every F layer leading to a shorting of the current by one of the channels, Figure 4.2b. This produces a negative GMR since the resistance drops as the field increases.

A multilayer with two ferromagnetic components, F_1 and F_2 , may be constructed in such a way that $\alpha_1>1$ for F_1 while $\alpha_2<1$ for F_2. In this way adjacent F layers will have reversed spin asymmetries. At zero field, exchange forces will again maintain an antiparallel alignment between F_1 and F_2. In the AP state a spin up electron weakly scattered in F_1 is also weakly scattered in F_2 because: (1) the magnetization of F_2 is antiparallel to that of F_1 and (2) the spin asymmetry has changed from $\alpha_1>1$ to $\alpha_2<1$, as indicated in Figure 4.8a. Applying a field to align F_1 with F_2 leads to a higher resistivity because now only the spin asymmetry is alternating from F_1 to F_2 so electrons from each channel now scatter the same amount, Figure 4.8b. This produces a positive GMR since the resistance increases with applied field.

Actually the exchange force is not essential to obtain a positive GMR. However, the ability to form AP and P states together with alternating spin asymmetries is required. Whether the AP state is formed by exchange forces or large differences in saturation

fields between F_1 and F_2 is not important. Positive GMR should be observable for both the CIP and CPP geometries .

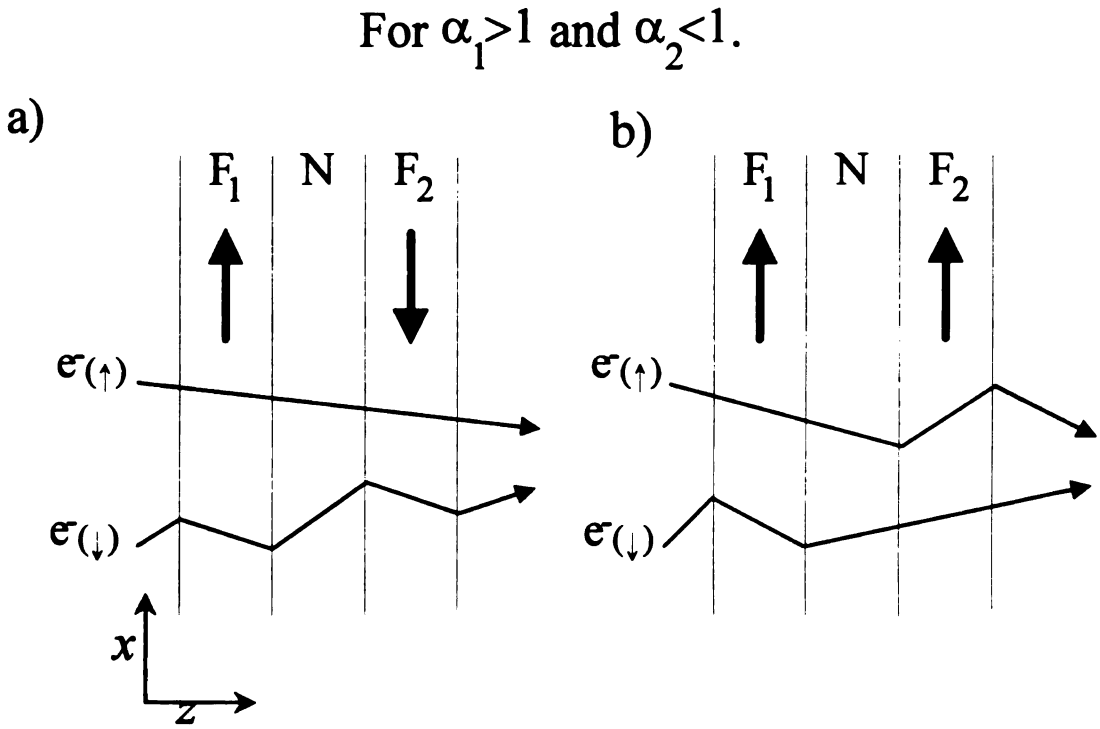

Figure 4.8: Spin dependent scattering of a) AP and b) P states for inverse (positive) GMR. Scattering is schematically represented as taking place only at the F/N interface for clarity.

[1] J. Crangle, *Solid State Magnetism*, Van Nostrand Reinhold, New York, NY (1991).

[2] R. M. Bozorth, *Ferromagnetism*, D. Van Nostrand, New York, NY (1951) p. 423.

[3] S. Chikazumi, *Physics of Magnetism*, Wiley, New York, NY (1964) p. 60.

[4] B.D. Cullity, *Introduction to Magnetic Materials*, Addison-Wesley, Reading, MA (1972) p. 117.

[5] J.F. Cooke,
[6] C. Fierz. *et al.*, Phys. Cond. Matt., **2**, 9701 (1990).

[7] C. Fierz. *et al.*, Physica B **165-166**, 4553 (1990).

[8] C. Fierz. *et al.* (unpublished).

[9] J.M. Slaughter, *et al.*, Proceedings of LT-18 [Jpn. J. Appl. Phys. **26**, Suppl. 26-3, 1451 (1987).

[10] P. Holody, *et al.* (unpublished).

[11] S.F. Lee, Ph.D. Dissertation, Michigan State University (1995).

[12] T. Valet and A. Fert, Phys. Rev. B **48**, 7099 (1993).

[13] Q. Yang, Ph.D. Dissertation, Michigan State University (1995).

[14] T. Valet (unpublished).

[15] A. Fert, T. Valet and J. Barnas, J. Appl. Phys. **75** (10), 6693 (1994).

[16] I.A. Campbell and A. Fert, in *Ferromagnetic Materials*, edited by E.P. Wohlfarth, (North Holland, Amsterdam, 1982), Vol.3, p. 769.

[17] M. Johnson and R.H. Silsbee, Phys. Rev. B **35**, 4959 (1987).

[18] P.C. van Son, H. van Kempen and P.Wyder, Phys. Rev. Lett. **58**, 2271 (1987).

[19] A. Fert, T. Valet and J.L. Duvail, Phys. Rev. B **52**, 6513 (1995).

[20] J.S. Dugdale, *The Electrical Properties of Metals and Alloys*, Edward Arnold (Publishers), London, England (1972) p.137.

[21] Y. Yafet, J. Appl. Phys. **39**, 853 (1968); J. Appl. Phys. **42**, 1564 (1971).

Ana

Introdu

For the CI

multilayers i

parameters.

Perpendicula

access to th

interfaces w

multilayers v

and Mn) by

to Cu based

Co/Cu and C

chapter will

multilayers.

Chapter 5:

Analysis of Co/Cu & Py/Cu Multilayers

Introduction

For the CIP geometry, derivation of the spin asymmetry parameters in magnetic multilayers is difficult and often requires one to appeal to a model with a few adjustable parameters. Measurement of the resistance of a multilayer with the Current applied Perpendicular to the Plane of the layers, the CPP geometry, allows one to gain direct access to the spin asymmetry parameters both in the bulk F layers and at the F/N interfaces without adjustable parameters[1,2,3,4,5,6]. An extensive study of Ag/Co CPP multilayers was done by S.F. Lee[7,8] and was further extended to AgX/Co (X=Pt, Au, Sn and Mn) by Q. Yang[9]. This study was done to extend the works of both Lee and of Yang to Cu based multilayers. In this chapter results for the first measurements done on CPP Co/Cu and CPP Py/Cu multilayers will be given and analyzed. Section 6.1 of the next chapter will explore the role that finite spin diffusion length (SDL) plays in Co/CuX multilayers.

5.1 Asyn

The Co C

fit the data.

(a) $AR_{Nb\,Co}$

Co Cu interfa

and (f) $\gamma_{Co\,Cu}$

were produce

both the Co a

A prelimi

fixed at 360n

bilayers. San

the presence

for samples w

that the Fe bu

Fe buffer wer

Co/Cu multil

oscillatory co

also provided

Measurements

were started b

of the CPP an

5.1 Asymmetry Parameters in Co/Cu Multilayers

The Co/Cu system was investigated by preparing three different series. To properly fit the data, equations 4.2 and 4.3 together require information about six quantities: (a)$AR_{Nb/Co}$, the Nb/Co interface resistance; (b)ρ_{Cu}, the Cu resistivity; (c)$AR^{*}_{Co/Cu}$, the Co/Cu interface resistance; (d)ρ^{*}_{Co}, the Co resistivity; (e)β_{Co}, the bulk spin asymmetry and (f)$\gamma_{Co/Cu}$, the Co/Cu interface spin asymmetry. Three different series of samples were produced, two with constant Co thickness and one which varied equal thicknesses of both the Co and Cu. The multilayer's total thickness was kept constant in each series.

A preliminary Co/Cu series was produced with t_{Co} held at 1.5nm and total thickness fixed at 360nm. The Cu layer was limited to thicknesses which gave integer numbers of bilayers. Samples were made with and without a 5nm Fe buffer. Parkin[10] showed that the presence of a Fe buffer layer increased the amount of coupling between the Co layers for samples with thin Cu spacer layers. Our experiments confirmed this, but also showed that the Fe buffer had little effect on samples with $t_{Cu}>5.0nm$. The samples without the Fe buffer were therefore used for the global fitting (to be described) to obtain β and γ for Co/Cu multilayers. A series of 1.5nm Co with an Fe buffer was made to verify the oscillatory coupling seen by others[11] for CIP samples of Co/Cu. We will see that this also provided valuable information on the magnetic state of the as prepared samples. Measurements of an extensive series of samples with t_{Cu} ranging from 0.7nm to 14nm were started by S.F.Lee and finished by the author. Figure 5.1 shows the field dependence of the CPP and CIP resistances and magnetization for a typical Co/Cu multilayer with the

field applied along the direction parallel to the layers. The resistance of each was measured by starting at zero field (H_0) and then increasing the field until the resistance saturates at H_S. The sample is then cycled once between H_S and $-H_S$. During this cycling the resistance peaks in two places, $\pm H_P$, near the coercive field of the multilayer, shown in Figure 5.1c. Comparing the figures in 5.1 reveals that the hysteresis loops in a), b) and c) are well correlated and features from each curve occur at approximately the same fields. Although the H_P state of the CPP in Figure 5.1a) is close to the coercive field, H_C of Figure 5.1c), a close examination of other samples shows that the H_P state of the CPP resistance is generally not identical to H_C. In fact, $M(H_P)$ may be an appreciable fraction of $M(H_S)$[12]. The H_S values are perhaps the most well defined states since saturation occurs when all the moments are aligned. The magnetoresistance is defined as:

$$MR(H) = \frac{R(H) - R(H_S)}{R(H_S)} \times 100\% \qquad (5.1)$$

where R(H) and $R(H_S)$ are the resistances at H and at H_S (the field at which the resistance saturates) respectively.

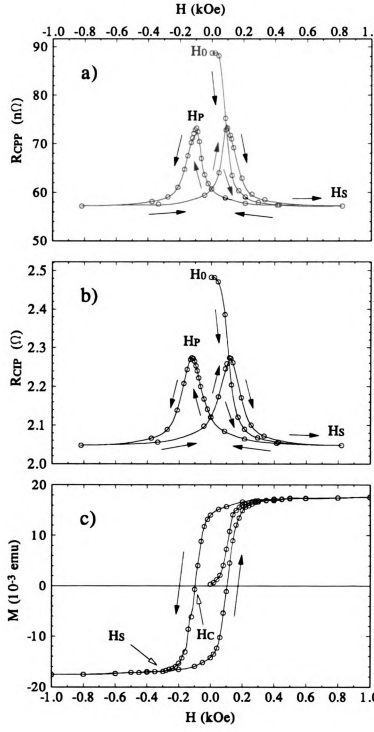

Figure 5.1: The field dependence of a) the CPP resistance, b) the CIP resistance and c) the magnetization of a *[Co(6.0nm)/Cu(6.0nm)]×60* multilayer.

Figure 5.2 shows the MR plotted as a function of Cu thickness. The CPP zero and peak data are plotted along with CIP peak data to show that the effect is generally doubled in the CPP geometry. The CIP data in Figure 5.2 are typical of those reported elsewhere[13]. Both the CPP and CIP samples exhibit oscillatory behavior in the MR.

The oscillatory behavior of the saturation field of CIP samples has also been observed by others[14]. The coupling constant can be calculated from the saturation field of an AF coupled sample. The oscillating saturation field therefore implies an oscillatory behavior in the strength of the coupling which is usually described as an oscillatory exchange interaction. In both MR and H_S measurements the oscillations decay with the Cu thickness until they become negligibly small for Cu thicknesses greater than 6.0nm. In this work the variation with Cu thickness is studied in the region $t_{Cu}>6.0nm$ where the analysis is uncomplicated by the presence of the oscillatory exchange field. The assumption is made that R(H=0)=R(AP). We will see some experimental evidence supporting this assumption and further note the prediction of Zhang and Levy[15] for the CPP geometry. Their work[15] predicts the same AP resistance for a CPP sample regardless of whether the F layer magnetizations are perfectly antiferromagnetically aligned or are collinear with a random, statistically uncorrelated (SU) configuration so long as the multilayer's total moment is zero, $\sum_i M_i = 0$, assuming that each F layer is a single domain.

Figure 5.2: M
for the copp
guides to the

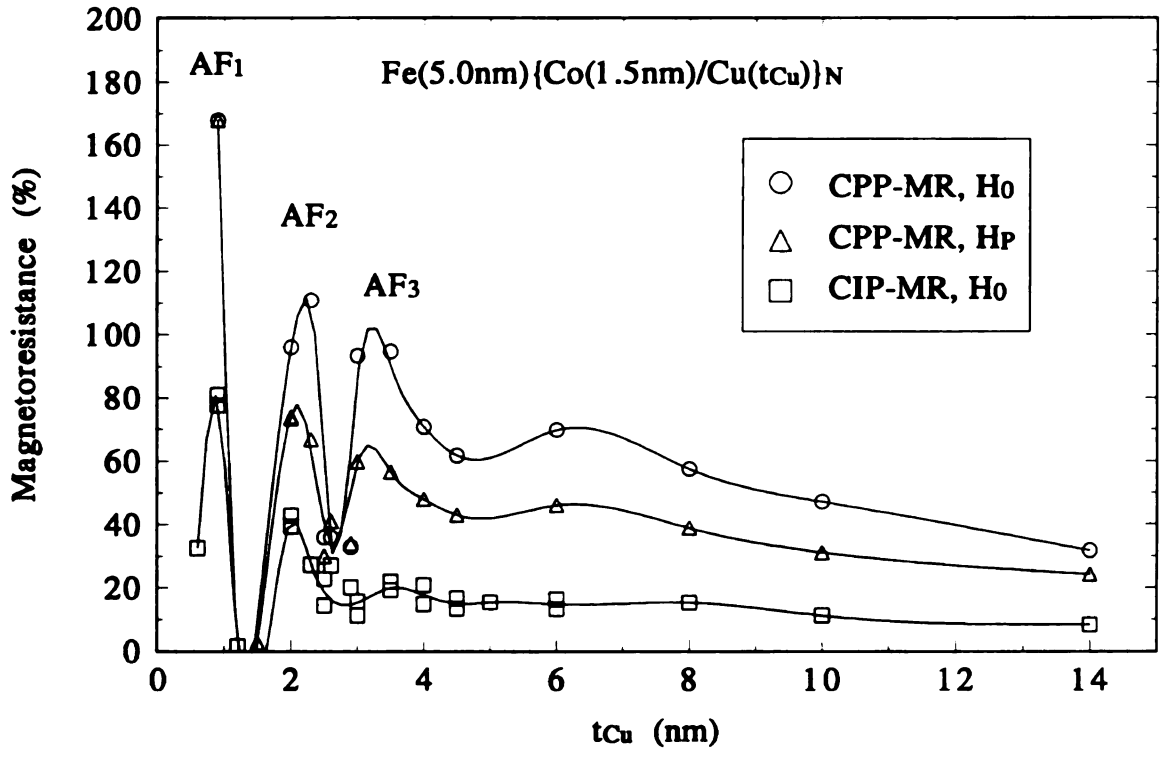

Figure 5.2: Magnetoresistance of *Fe(5nm)[Co(1.5nm)/Cu(t_{Cu})]×N* plotted as a function of t_{Cu}, the copper thickness. AF indicates antiferromagnetic coupling. The lines serve as guides to the eye.

Basis for S

Equa

AR_{SF}. B

thickness, a

where the s

used to dete

N-1 is on

superconduc

eliminates th

small but wi

next section.

Table 5.1: S

t_N and
t_F=c
t

The data

respectively, a

5.3a, 5.4a and

Basis for Separating Bulk and Interface Spin Dependent Parameters

Equation 4.2 gave $AR_T(AP)$ as a function of four quantities $\rho_F^*, \rho_N, AR_{F/N}^*$ and $AR_{S/F}$. By constraining the relationship between t_N and t_F, fixing t_T, the total sample thickness, and ignoring the differences between N and N-1, equation 4.2 becomes:

$$AR_T(AP) = Intercept + Slope \times N \qquad 5.2$$

where the slopes and intercepts are given Table 5.1 below. These relationships can be used to determine values for ρ_F^*, ρ_N, $AR_{S/F}^*$ and $AR_{S/F}$. The difference between N and N-1 is only important for small numbers of bilayers. It arises because the superconducting proximity effect in the Cu layer directly underneath the top Nb lead eliminates the resistance of one Cu layer and one Co/Cu interface. This correction is small but will be taken into account in the global fit of all three sets of Co/Cu data, in the next section.

Table 5.1: Slopes and intercepts for equation 5.2 above.

t_N and t_F relations	*Intercept*	*Slope*
t_F=constant	$2AR_{S/F} + \rho_N t_T$	$(\rho_F^* - \rho_N)t_F + 2AR_{F/N}^*$
t_F=t_N	$2AR_{S/F} + (\rho_F^* + \rho_N)t_T/2$	$2AR_{F/N}^*$

The data for t_{Co}=*1.5nm*, t_{Co}=*6.0nm* and t_{Co}=t_{Cu} are listed in Tables 5.2, 5.3 and 5.4, respectively, and are plotted as a function of the reduced bilayer number (N-1) in Figures 5.3a, 5.4a and 5.5a, respectively. The AR_T values for fields H_0, H_P and H_S are shown. In

each case there is a linear relation between AR_T and N-1. Assuming that the true AP state of a multilayer corresponds with the highest resistance, it would appear that the H_0 data approximate the AP state better and fits to $AR_T(AP)$ should use the H_0 data. According to Table 5.1 the slope of the t_N=t_F data directly measures $2AR^*_{F/N}$, the F/N interface resistance. The appreciable slope in Figure 5.5a clearly indicates this quantity contributes significantly to the overall resistance of each multilayer. The Nb/Co interface resistance was determined independently on series of Nb/Co/Nb sandwiches with varying t_{Co} [16]. Interestingly, the Nb/Co interface resistance remained the same for a series of sandwiches with the Co grown on a 5.0nm Fe buffer[17]. With knowledge of the Nb/Co interface resistance, the intercept of the fixed t_{Co} data is used to estimate the Cu resistivity which can then be compared with resistivity measurements done on 300nm thick Cu films. The value of ρ^*_F can then be determined from either of the remaining two relationships in Table 5.1. Table 5.5 lists the slopes and intercepts obtained from a least squares fitting of the H_0 data shown in Figures 5.3a, 5.4a and 5.5a.

Table 5.2: CPP and CIP values at H_0, H_P and H_S for *[Co(1.5nm)/Cu(t_{Cu})]×N*

Sample #	t_{Cu} nm	N	CPP AR (fΩm²)			CIP (Ω)		
			H_0	H_P	H_S	H_0	H_P	H_S
343-A1	28.5	12	20.71	19.32	17.40	1.4318	1.3968	1.3517
343-08	28.5	12	20.09	18.14	16.28	1.2207	1.1869	1.1416
343-04	18.5	18	27.09	23.61	20.01	1.6731	1.1869	1.5011
343-01	13.0	25	32.15	29.22	23.56	--------	--------	--------
357-07	10.5	30	41.61	34.47	26.74	2.5920	2.3883	2.1650
342-A2	8.0	38	47.40	39.37	28.59	3.1230	2.8217	2.4845
343-03	8.0	38	48.22	39.17	28.25	3.2852	2.9300	2.5760
342-05	6.0	48	59.67	49.21	34.34	4.0193	3.5817	3.0893

Table 5.3: CPP and CIP values at H_0, H_P and H_S for *[Co(6.0nm)/Cu(t_{Cu})]×N*

Sample #	t_{Cu} nm	N	CPP AR (fΩm²)			CIP (Ω)		
			H_0	H_P	H_S	H_0	H_P	H_S
357-01	54.0	12	30.96	29.26	27.27	0.3858	0.3840	0.3818
343-03	30.0	20	41.37	37.95	31.93	0.7426	0.7234	0.6982
357-03	24.0	24	45.69	40.71	33.86	0.9675	0.9628	0.8934
393-01	22.8	25	45.69	42.65	34.67	1.0196	0.9958	0.9474
325-05	20.0	28	51.54	47.29	37.74	0.9309	0.8979	0.8506
325-04	15.0	34	54.74	48.06	36.89	---------	0.7341	0.6908
325-03	12.0	40	65.01	57.20	42.77	1.1703	1.1208	1.0191
325-02	9.0	48	75.95	64.26	46.50	1.5873	1.4444	1.2783
434-06	7.1	55	91.61	74.66	52.69	1.6332	0.9360	0.7166
325-01	6.0	60	100.39	76.59	63.67	---------	2.2341	1.8663

Table 5.4: CPP and CIP values at H_0, H_P and H_S for *[Co(t_{Co}=t_{Cu})/Cu(t_{Cu})]×N*

Sample #	t_{Cu} nm	N	CPP AR (fΩm²)			CIP (Ω)		
			H_0	H_P	H_S	H_0	H_P	H_S
392-03	20.0	18	46.99	41.06	36.04	0.7894	0.7850	0.7728
342-04	18.0	20	51.96	46.27	39.84	1.1188	1.0770	1.0336
378-06	14.4	25	59.03	53.71	47.11	0.7144	0.7111	0.6984
319-04	12.0	30	66.24	57.50	48.99	1.4939	1.4522	1.3605
342-03	12.0	30	67.98	57.88	47.69	0.9741	0.7917	0.7704
342-02	9.0	40	76.47	64.62	50.47	0.6846	1.5473	1.4037
376-03	8.0	45	74.88	61.41	45.69	1.6375	1.4684	1.2660
342-01	7.2	50	88.42	76.49	59.73	2.3116	2.2170	2.0186
318-01	6.0	60	113.52	93.74	73.25	2.4826	2.2743	2.0475
328-01	6.0	60	104.27	79.74	64.87	2.2660	2.1820	1.9369

The quantities ρ_F^*, ρ_N, $AR_{S/F}^*$ and $AR_{S/F}$ may all be calculated using the values for the slopes and intercepts given in Table 5.5, but the values obtained this way give some inconsistent results depending on which pair of conditions are chosen from Table 5.1. In the next section a global fit using all three sets of H_0 data along with the H_S data which we now examine will be used to obtain more representative values.

Table 5.5: Slopes and intercepts of the three CPP Co/Cu series.

t_F	*Intercept* (fΩm^2)	*Slope* (fΩm^2)
1.5nm	7.9±0.5	1.06±0.02
6.0nm	13.5±1.4	1.32±0.5
t_F=t_N	24.6±1.5	1.29±0.04

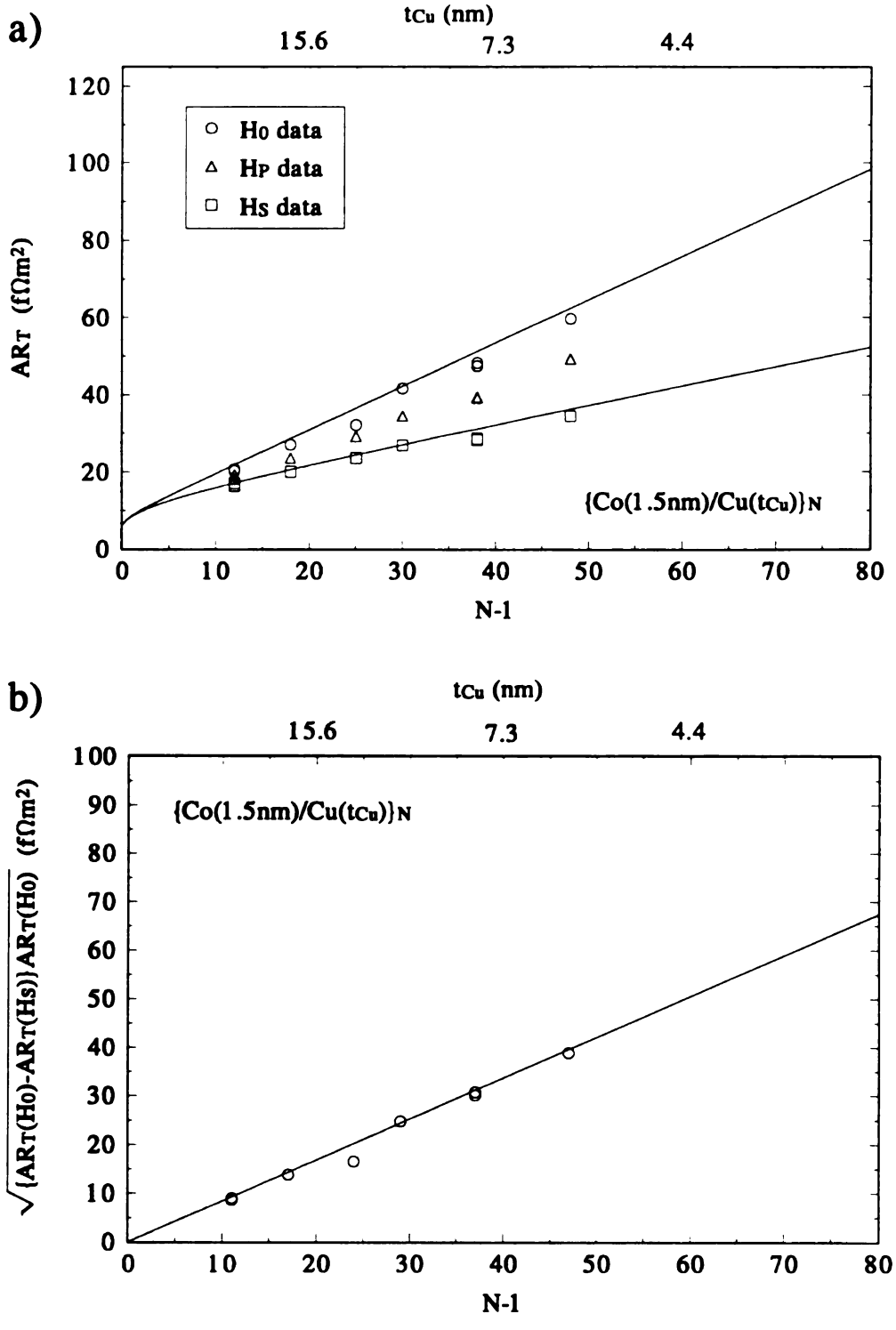

Figure 5.3: Plots of a) AR_T vs. *N-1* and b) $\sqrt{AR_T(H_0)[AR_T(H_0)-AR_T(H_S)]}$ vs. *N-1* for *[Co(1.5nm)/Cu(t_{Cu})]×N* multilayers. In a) the lines represent $AR_T(H_0)$ and $AR_T(H_S)$ and in b) the line represents $\sqrt{AR_T(H_0)[AR_T(H_0)-AR_T(H_S)]}$ using the parameters derived from the global fit to all three sets of data given in Table 5.6. Total sample thickness is 360nm.

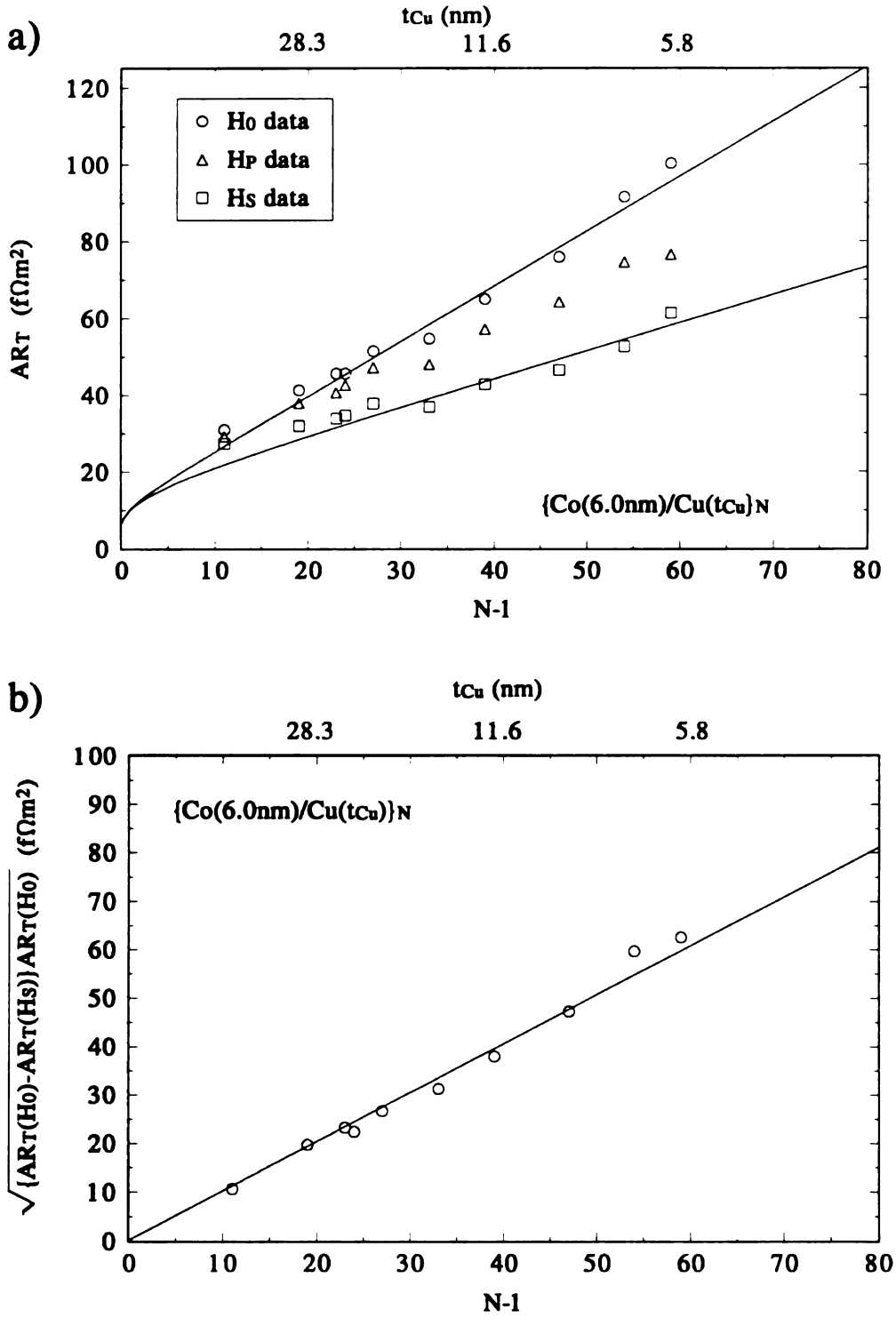

Figure 5.4: Plots of a) AR_T vs. *N-1* and b) $\sqrt{AR_T(H_0)[AR_T(H_0)-AR_T(H_S)]}$ vs. *N-1* for *[Co(6.0nm)/Cu(t_{Cu})]×N* multilayers. In a) the lines represent $AR_T(H_0)$ and $AR_T(H_S)$ and in b) the line represents $\sqrt{AR_T(H_0)[AR_T(H_0)-AR_T(H_S)]}$ using the parameters derived from the global fit to all three sets of data given in Table 5.6. Total sample thickness is 720nm.

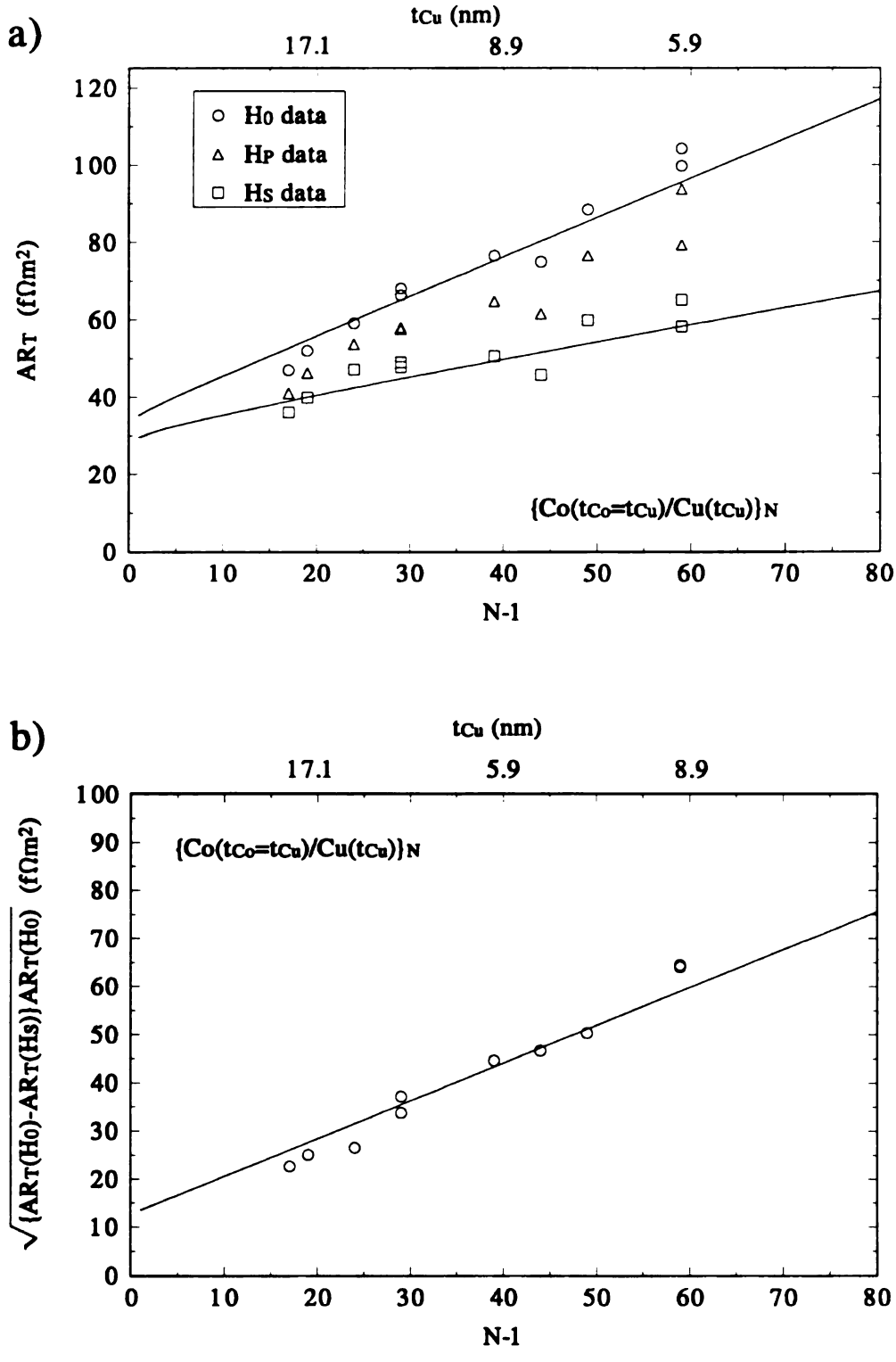

Figure 5.5: Plots of a) AR_T vs. *N-1* and b) $\sqrt{AR_T(H_0)[AR_T(H_0)-AR_T(H_S)]}$ vs. *N-1* for $[Co(t_{Co}=t_{Cu})/Cu(t_{Cu})]\times N$ multilayers. In a) the lines represent $AR_T(H_0)$ and $AR_T(H_S)$ and in b) the line represents $\sqrt{AR_T(H_0)[AR_T(H_0)-AR_T(H_S)]}$ using the parameters derived from the global fit to all three sets of data given in Table 5.6. Total sample thickness is 720nm.

The spin asymmetry parameters may be estimated once the resistivities are known. This is done by using equation 4.4 which is linear in the bilayer number and groups experimental quantities on the left and the two unknowns β and γ on the right. For fixed t_{Co} equation 4.4 becomes:

$$A\sqrt{R(H_0)[R(H_0)-R(H_S)]} = N[\beta\rho^{*}_{Co}t_{Co} + \gamma 2AR^{*}_{Co/Cu}] \qquad 5.3a$$

and for t_{Co}=t_{Cu}:

$$A\sqrt{R(H_0)[R(H_0)-R(H_S)]} = \beta\rho^{*}_{Co}t_T/2 + N\gamma 2AR^{*}_{Co/Cu} \qquad 5.3b$$

The slope of the right hand side of equation 5.3a (fixed t_{Co}) versus N contains both β and γ while equation 5.3b (t_{Co}=t_{Cu}) separates β and γ by intercept and slope. The data are displayed in Figures 5.3b, 5.4b and 5.5b.

Global Fit of the Co/Cu Data

Fitting all three sets of data simultaneously helps eliminate inconsistencies in the data. The same procedure used for the analysis done by S.F.Lee[3] on Co/Ag is applied here to Co/Cu. Analysis is now done for all the data at once.

The N-1 corrected versions of equations 5.2 for the AP state and equations 5.3 for the square root quantity are given below as equations 5.4 and 5.5, respectively.

For t_{Co}=*constant*:

$$AR_T^{AP} = 2AR_{Nb/Co} + \frac{N-1}{N}\rho_{Cu}t_T + \rho^{*}_{Co}t_{Co} + (N-1)[(\rho^{*}_{Co}-\rho_{Cu})t_{Co} + 2AR^{*}_{Co/Cu}] \qquad 5.4a$$

$$A\sqrt{R(H_0)[R(H_0)-R(H_S)]} = (N-1)[\beta\rho^{*}_{Co}t_{Co} + \gamma 2AR^{*}_{Co/Cu}] + \beta\rho^{*}_{Co}t_{Co} \qquad 5.4b$$

and $t_{Co}=t_{Cu}$:

$$AR_T^{AP} = 2AR_{Nb/Co} + (\rho_{Co}^* + \rho_{Cu})t_T - \rho_{Cu}t_{Cu} + (N-1)2AR_{Co/Cu}^* \quad 5.5a$$

$$A\sqrt{R(H_0)[R(H_0)-R(H_S)]} = \beta\rho_{Co}^* t_T/2 + (N-1)\gamma 2AR_{Co/Cu}^* \quad 5.5b$$

First $AR_{Nb/Co}$ is regarded as an independently determined quantity[8] and the three sets of H_0 data ($t_{Co}=1.5nm$, $t_{Co}=6.0nm$ and $t_{Co}=t_{Cu}$) are simultaneously fit[18] to equations 5.4a and 5.5a. The χ^2 for each data set is found and summed together. The total χ^2 is then minimized using ρ_{Co}^*, ρ_{Cu} and $AR_{Co/Cu}^*$ variable parameters. A similar fit is done for all three sets of square root data, $\sqrt{AR(H_0)[AR(H_0)-AR(H_S)]}$, to equations 5.4b and 5.5b to obtain the parameters $\rho_{Co}^*\beta$ and $\gamma 2AR_{Co/Cu}^*$. Now the spin dependent parameter β and γ can be determined using ρ_{Co}^* and $2AR_{Co/Cu}^*$ given by the H_0 fits.

The $t_{Co}=t_{Cu}=6.0nm$ samples have been listed as either belonging to the $t_{Co}=6.0nm$ set or the $t_{Co}=t_{Cu}$ set but not both which would weight them more heavily than the other points in the fit. The uncertainties quoted here have been adjusted so that the χ^2 is reduced to the number of degrees of freedom for each fit. The number of degrees of freedom is just the difference between the number of data points and the number of unknown parameters in the fit. There are 28 data points in both fits with 3 unknowns in the H_0 fit and 2 unknowns in the H_S fit. Therefore the H_0 fit has 25 degrees of freedom while the H_S fit has 26 degrees of freedom. The uncertainty of each data point is increased by a factor of $\sqrt{\chi^2/25}$ for H_0 and $\sqrt{\chi^2/26}$ for H_S. This procedure is based on the admission that there are uncertainties in the data whose nature is not known.

The results of the H_0 fit are given below:

$$\rho_{Cu} = 7 \pm 3 \text{ n}\Omega\text{m}$$
$$\rho^{*}_{Co} = 75 \pm 5 \text{ n}\Omega\text{m}$$
$$AR^{*}_{Co/Cu} = 0.51 \pm 0.02 \text{ f}\Omega\text{m}^2$$

The χ^2 was 83 for degrees of freedom 25, before uncertainties were adjusted.

The H_S fit gave:

$$\beta\rho^{*}_{Co} = 34 \pm 3 \text{ n}\Omega\text{m}$$
$$\gamma AR^{*}_{Co/Cu} = 0.39 \pm 0.01 \text{ f}\Omega\text{m}^2$$

The χ^2 was 250 for degrees of freedom 26, before uncertainties were adjusted. The spin asymmetry parameters may now be calculated. They are:

$$\beta = 0.46 \pm 0.05$$
$$\gamma = 0.77 \pm 0.04$$

Using $\rho_{Co} = \rho^{*}_{Co}(1-\beta^2)$ and $R_{Co/Cu} = R^{*}_{Co/Cu}(1-\gamma^2)$, the best values for the Co resistivity and interfacial Co/Cu resistance are:

$$\rho_{co} = 60 \pm 10 \text{ n}\Omega\text{m}$$
$$AR_{Co/Cu} = 0.20 \pm 0.02 \text{ f}\Omega\text{m}^2$$

The asymmetry ratio between the spin down channel and the spin up channel may be calculated using the following:

$$\alpha_{Co} = \frac{\rho^{\downarrow}_{Co}}{\rho^{\uparrow}_{Co}} = \frac{(1+\beta)}{(1-\beta)} = 2.7 \pm 0.3$$
$$\alpha_{Co/Cu} = \frac{R^{\downarrow}_{Co/Cu}}{R^{\uparrow}_{Co/Cu}} = \frac{(1+\gamma)}{(1-\gamma)} = 7.7 \pm 1.3$$

Comparing the resistance ratios of the spin down to spin up channels for bulk Co and Co/Cu interfaces gives a measure of which contributes more to the MR of the system. The resistance of the Co/Cu interface gives the same resistance as 7.0nm of Co. For

Co/Cu samples with t_{Co}=*7.0nm* the α's calculated above indicate that the interface contribution to the spin dependent scattering is 2.8 times more than the contribution from bulk Co. Therefore the spin dependent scattering most responsible for GMR must be located near the Co/Cu interface.

Although the H_0 state seems to be more representative of the true AP state, it suffers from the fact that once the saturation field is applied the H_0 state can never be recovered. More will be said in the Py/Cu section about trying to recover the original H_0 measurement. The H_P (and H_S) measurements are quite stable and very reproducible with both field cycling and thermal cycling. In the same measurement run, the H_P and H_S data for the initial field cycle are identical to H_P and H_S values obtained in later cycles. Thermal cycling between room temperature and 4.2K produces little difference between the original H_P and H_S values and those taken after cooling to 4.2K again. Even measurements of the same sample taken months apart agree within mutual uncertainties, demonstrating that oxidation is not a problem.

The N-1 correction changes the relations in Table 5.1 in two way. (a) First, the equations are now linear in N-1 (if N is large) and the resistance of the extra (N^{th}) Co layer is added to each of the intercepts. (b) Second, the Cu term, $\rho_{Cu}t_T$, in each intercept is no longer a constant, but proportional to (N-1)/N. In Figures 5.3a, 5.4a and 5.5a the observed curvatures in the fits are attributed to this non-linear Cu term. For large N the Cu term becomes nearly constant since (N-1)/N≈1 and the fits appear linear in N-1. As N→1, the Cu term goes to zero resulting in a lower intercept than that expected from an extrapolation from the high N data. For the t_{Co}=*6.0nm* series $\rho_{Cu}t_T$ = 4.3 fΩm^2 (half that

for the other two series). Since $\rho_{Cu}t_T$ is small, we are unable to attribute any curvature in our data to this non-linearity.

Table 5.6: Summary of fitted H_0 parameters (see text for fit description) and independent measurements. A $2AR_{Nb/Co}$ of 6.1fΩm^2 was assumed in the fit.

	independent measurements	H_0 fit	units
$2AR_{Nb/Co}$	6.1±0.6		fΩm^2
ρ_{Cu}	6±1	7±3	nΩm
ρ_{Co}	60±10	60±10	nΩm
ρ^*_{Co}		75±5	nΩm
β		0.46±0.05	
α_{Co}		2.7±0.3	
$AR_{Co/Cu}$		0.20±0.02	fΩm^2
$AR^*_{Co/Cu}$		0.51±0.02	fΩm^2
γ		0.77±0.04	
$\alpha_{Co/Cu}$		7.7±1.3	

To determine whether or not the parameters in Table 5.6 (obtained from fitting data in the uncoupled region of Figure 5.2) are consistent with the strongly AF-coupled Co layers at the AF_1, AF_2 and AF_3 peaks of Figure 5.2, a plot of $AR_T(H_0)$ and $AR_T(H_S)$ as a function of the corrected bilayer number for the *Fe(5.0nm)[Cu(t_{Cu})/Co(1.5nm)]×N* series is compared with the values based on the fitted parameters from Table 5.6. This is shown in Figure 5.6. The fitted parameters describe the H_0 data quite well near the 1st and 2nd AF peaks (t_{Cu}=*0.9nm* and *2.1 nm*). The 3rd AF peak in Figure 5.6 is somewhat below the

H_0 fit. Since the coupling is stronger for thinner Cu layers, the first AF peak should be the closest to a perfect AP state. However, the strong AF coupling here is extremely sensitive to fluctuations in the Cu thickness[19] so it is hard to determine whether or not the sample is completely AF or contains some F coupled regions. The second AF peak is less sensitive to Cu layer thickness fluctuations and so easier to use for precisely locating the peak AF coupling. Since the H_0 fit directly connects AF_1 and AF_2 with the uncoupled region, one may conclude that either: a) The as-deposited state of the F layer magnetizations for samples in the uncoupled region must be aligned antiparallel, possibly by magnetostatic interactions between the Co layers which may arise from the layering or thickness fluctuations in the sample. b) The as-deposited configuration of the F layer magnetizations is random in accordance with the theoretical prediction of Zhang and Levy[2]. For the CPP geometry, they predict the AP resistance of multilayers with a random arrangement of F layer magnetizations is equivalent to the AP resistance for strongly AF coupled multilayers. Figure 5.6 may provide experimental evidence supporting the theoretical prediction of Zhang and Levy[2], however, further experiments must be done to eliminate magnetostatic interactions as the cause of possible AP ordering in the H_0 state.

The H_S fit represents the uncoupled H_S data well but lies consistently above the H_S data in the coupled region. Some samples in the coupled region (near F_1 and F_2 in Figure 5.6) have their H_0 data lying slightly above the H_S fit which is an indication that these samples are strongly F-coupled.

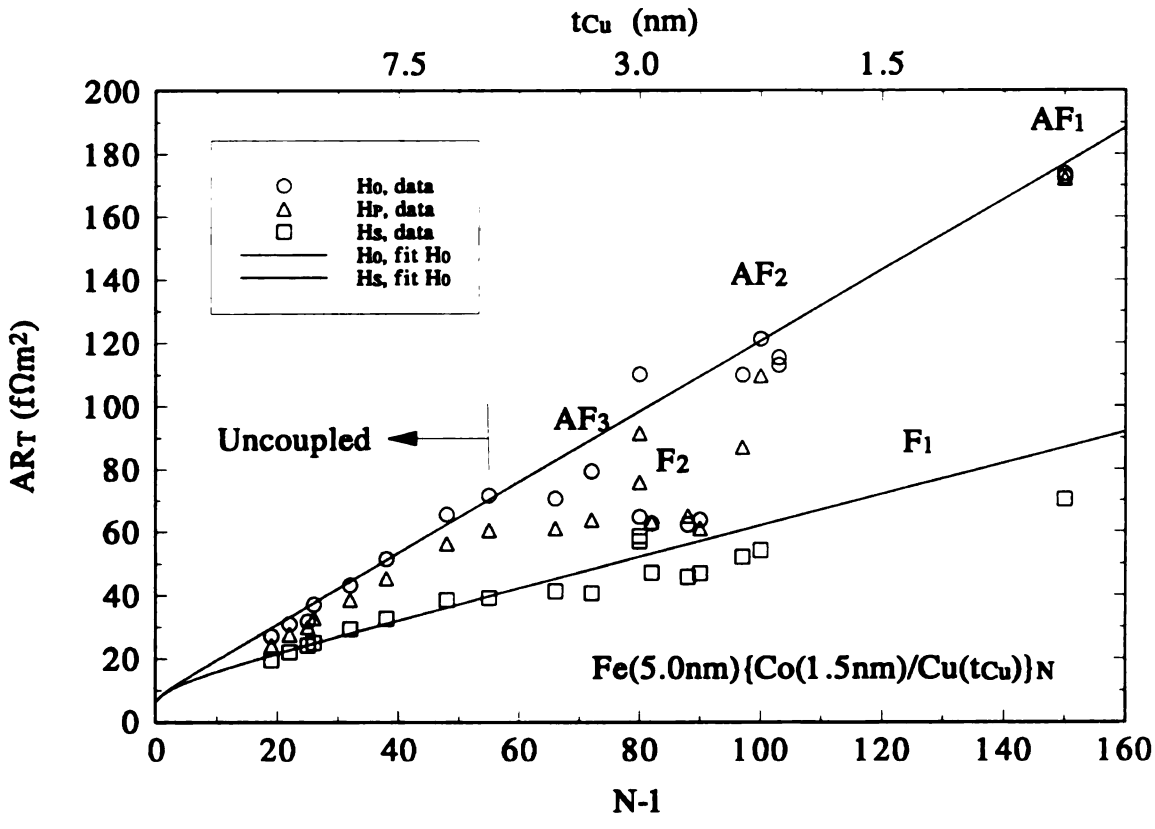

Figure 5.6: AR_T vs. the bilayer number N-1 for the *Fe(5nm)[Co(1.5nm)/Cu(t_{Cu})]×N* system. The lines represent AR_T^{AP} and AR_T^{P} using the parameters derived from the global fit to all three sets of data given in Table 5.6 with H_0 as the AP and then H_P as the AP state.

As a side note, the first AF peak has both H_0 and H_P points overlapping, indicating that the AF coupling is same for both states. The second AF peak shows a significant difference between the H_0 and H_P resistances. The weaker AF coupling might be unable to overcome pinning forces which cause some F layers to remain parallel to each other after saturation.

To summarize, Co/Cu multilayers were analyzed in terms of the two channel model. The spin asymmetry parameters for both bulk Co and the Co/Cu interface were estimated by globally fitting three separate series of H_0 and H_S data. Results from this fit are given in Table 5.6. It was found that the Co/Cu interfaces contribute significantly to the multilayers' total resistance, one Co/Cu interface resistance is equivalent to the resistance of 7.0nm of Co. In addition, $\alpha_{Co/Cu} = 7.7 > \alpha_{Co} = 2.7$ meaning that the Co/Cu interface contribution to the spin dependent scattering is almost a factor three greater than the contribution from bulk Co. Experimental evidence supporting the equivalence of statistically uncorrelated and antiparallel states is given in Figure 5.6.

---

[1] S.F. Lee, W.P. Pratt Jr., Q. Yang, P. Holody, R. Loloee, P.A. Schroeder and J. Bass, J. Magn. Magn. Mater. **118**, L1 (1993).

[2] H.E. Camblong, S. Zhang and P.M. Levy, Phys. Rev. B **47**, 4735 (1993).

[3] W.P. Pratt Jr., S.F. Lee, P. Holody, Q. Yang, R. Loloee, J. Bass and P.A. Schroeder, J. Magn. Magn. Mater. **126**, 406 (1993).

[4] G.E.W. Bauer, Phys. Rev. Lett. **69**, 1676 (1992).

[5] Y. Asano, A. Oguri and S. Maekawa, Phys. Rev. B **48**, 6192 (1993).

[6] H. Itoh, J. Inoue and S. Maekawa, Phys. Rev. B **51**, 342 (1995).

[7] S.F. Lee, Ph.D. Dissertation, Michigan State University (1994).

[8] S.F. Lee, Q. Yang, P. Holody, R. Loloee, J. H. Hetherington, S. Mahmood, B. Ikegami, K. Vigen, L.L. Henry, P.A. Schroeder, W.P. Pratt Jr. and J. Bass, Phys. Rev. B **52**, 15426 (1995).

[9] Q. Yang, Ph.D. Dissertation, Michigan State University (1995).

[10] S.S.P. Parkin, Z.G. Li and D.J. Smith, Appl. Phys. Lett. **58**, 2710 (1991).

[11] D.H. Mosca, A. Barthélémy, P. Etienne, A. Fert, P.A. Schroeder, W.P. Pratt Jr. and R. Loloee, J. Magn. Magn. Mater. 94, L1 (1991).

[12] P.A. Schroeder, S.F. Lee, P. Holody, R. Loloee, Q. Yang, W.P. Pratt Jr. and J. Bass, J. Appl. Phys. **76**, 6610 (1994).

[13] S.S.P. Parkin, R. Bhadra and K.P. Roche, Phys. Rev. Lett. **66**, 2152 (1991).

[14] S.S.P. Parkin, Phys. Rev. Lett. **67**, 3598 (1991); S.S.P. Parkin, N. More and K.P. Roche, Phys. Rev. Lett. **64**, 2304 (1990).

[15] S. Zhang and P. Levy, Phys. Rev. B **47**, 6776 (1993).

[16] C. Fierz, S.F. Lee, J. Bass, W.P. Pratt Jr. and P.A. Schroeder, J. Condens. Matter **2**, 9701 (1990); Physica B **165-166**, 453 (1990); J.M. Slaughter, J. Bass, W.P. Pratt Jr., P.A. Schroeder and H. Sato, Jpn. J. Appl. Phys. **26**, Suppl. 26-3, 1451 (1987).

[17] P. Holody, et al., unpublished.

[18] S.L. Meyer, *Data Analysis for Scientists and Engineers*, Wiley, NY, New York (1986).

[19] F. Giron, P. Boher, P. Houdy, P. Beauvillian, K. Le Dang and P. Veillet, J Magn. Magn. Mater. **121**, 318 (1993).

5.2 Spin Asymmetry Parameters in Py/Cu Multilayers

To gain further insight into the differences between bulk and interface spin dependent scattering in magnetic multilayers, three series of Py/Cu ($Py=Ni_{84}Fe_{16}$) multilayers similar to those prepared for the Co/Cu study were made. Unlike Co/Cu where the impurities are concentrated near the F/N interface, a layer of permalloy will have Fe atoms evenly distributed over the entire thickness of each Py layer, so that impurity scattering (Fe in Ni) now takes place throughout the Py layers, which suggests that a large bulk spin asymmetry will exist. Fert and Campbell[1] have shown that $\alpha = \rho^{\downarrow} / \rho^{\uparrow}$ for impurities of Fe in a Ni host is large for dilute alloys. One might therefore expect that $\alpha_{Py} > \alpha_{Co}$. Furthermore if one considers the Py/Cu interface to approximate an alloy of Ni in Cu, then the much lower α for Ni in Cu suggests that perhaps $\alpha_{Py} > \alpha_{Py/Cu}$. Part of the motivation in performing measurements on Py/Cu was to see if these crude predictions would be correct.

Measurement of the CPP resistance for a series of Py/Cu multilayers is the best way of accessing the relative amounts of interface and bulk scattering in this system. Three separate series of Py/Cu samples were made; two with constant t_{Py} (1.5nm and 6.0nm) and another with $t_{Py}=t_{Cu}$. Unlike the Co series all samples were limited to a total thickness of 360nm in an effort to minimize the waviness of the layered structure[2] which may correlate with H_C[3].

The field dependence of the MR for a typical Py/Cu multilayer is shown Figure 5.7 along with the magnetization. The peaks in both CPP and CIP MRs after saturation occur

near but not at the coercive field in the magnetization curve. The range of field over which the resistance changes is much smaller than that for Co/Cu in Figure 5.1. The average H_P is 20Oe for $t_{Py}=1.5nm$ and 6.0 Oe for $t_{Py}=6.0nm$, more than a factor of 20 smaller than the average H_P for Co/Cu. The saturation fields are nearly 10 times smaller in Py/Cu than in Co/Cu.

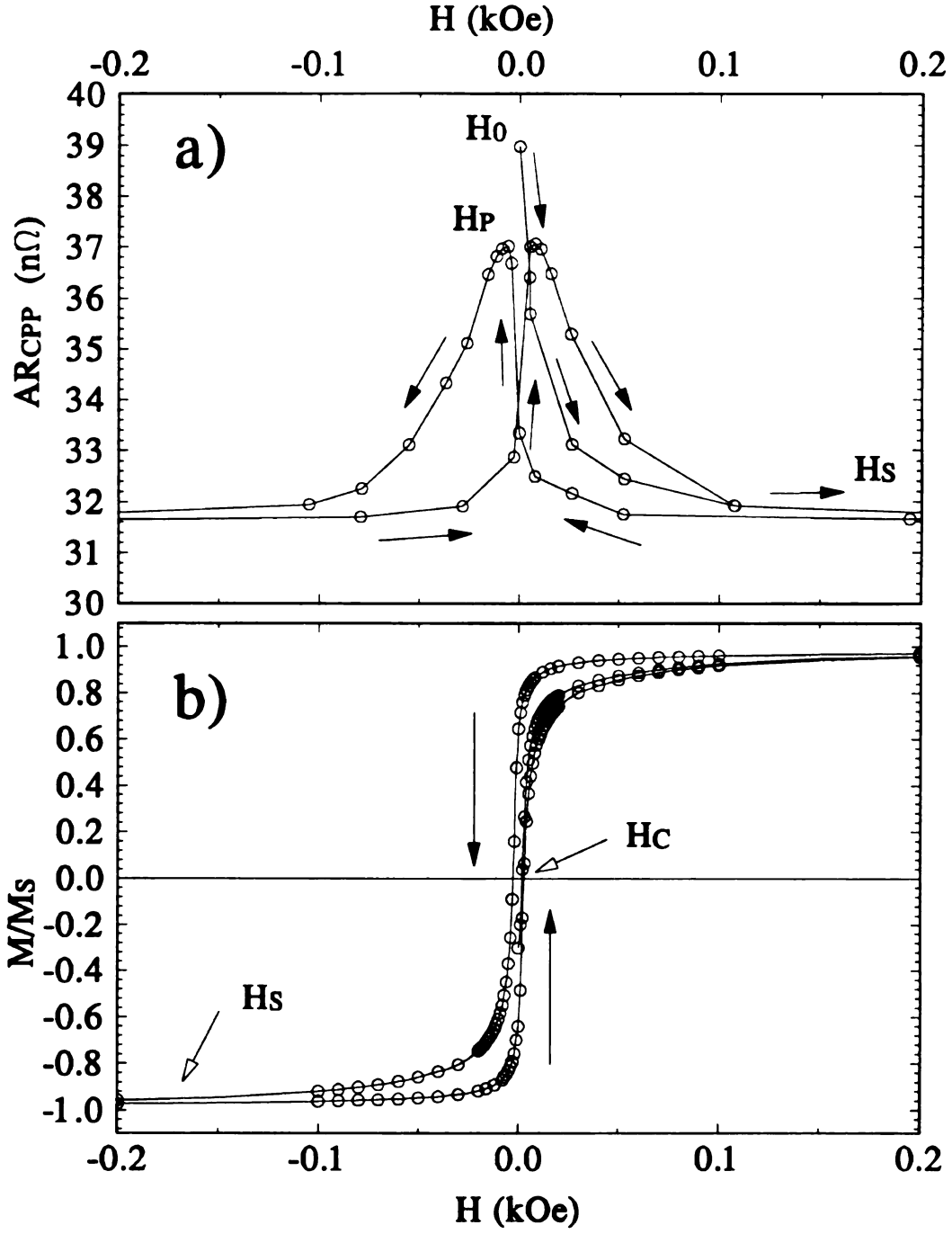

Figure 5.7: The field dependence of a) the CPP resistance and b) the magnetization for a *[Py(6.0nm)/Cu(8.4nm)]×25* multilayer. Note that the resistance changes over a much smaller field range then for the Co/Cu multilayer shown in Figure 5.1.

The data for each Py/Cu series, $t_{Py}=1.5nm$, the $t_{Py}=6.0nm$ and $t_{Py}=t_{Cu}$, is presented in Tables 5.7, 5.8 and 5.9, respectively. As will be shown the Py/Cu system proved to be much more difficult to analyze than the Co/Cu system for the following reasons: (a) The scatter of the experimental points is much greater in the Py/Cu system than in the Co/Cu. (b) The coupling between Py layers extends out to thicker Cu layers than did the coupling between Co layers in Co/Cu. (c) The largest resistance measured for the Py/Cu system was not always the H_0 resistance as it was for Co/Cu.

Oscillations in the CIP-MR for Py/Cu multilayers were first reported by S.S.P. Parkin[4]. The MR (defined in equation 5.1) for our $t_{Py}=1.5nm$ samples is plotted in Figure 5.8 as a function of the Cu thickness. The CPP-MR and CIP-MR peaks occur at the same Cu thickness and both MR's exhibit the same oscillation length of 1.2nm. Peaks in both the CIP-MR and CPP-MR indicate strong AF coupling between Py layers. The three antiferromagnetic peaks seen by Parkin[4] are also given in Figure 5.8 for comparison. Evidence for the oscillatory coupling extending out to $t_{Cu}=6.0nm$ is seen in Figure 5.8 but the 3rd, 4th and 5th AF peaks are somewhat diminished indicating that a significant portion of the sample is F-coupled. Only the 1st and 2nd AF peaks can be identified as having strong AF-coupling. As was the case for Co/Cu, Figure 5.2, the CPP-MR is roughly twice that of the CIP-MR. Samples with $t_{Cu}>10.0nm$ have a monotonically decreasing H_0 CPP-MR, and therefore these samples are considered to be uncoupled. The region between $t_{Cu}=6.0nm$ and $t_{Cu}=10.0nm$ has MR's which are significantly lower than both the strongly AF samples for thin Cu layers and the uncoupled samples with thick Cu layers. Several samples in this region also show the H_P CPP-MR higher than the

H_0 CPP-MR. Unlike the Co/Cu system, the crossover from oscillating MR to monotonically decreasing MR is not well defined in the Py/Cu system. However, cutting off the data at a Cu thickness in which the CPP-MR is clearly monotonically decreasing with Cu thickness will allow a direct comparison of α_{Py} and $\alpha_{Py/Cu}$ with α_{Co} and $\alpha_{Co/Cu}$, the major point in this study.

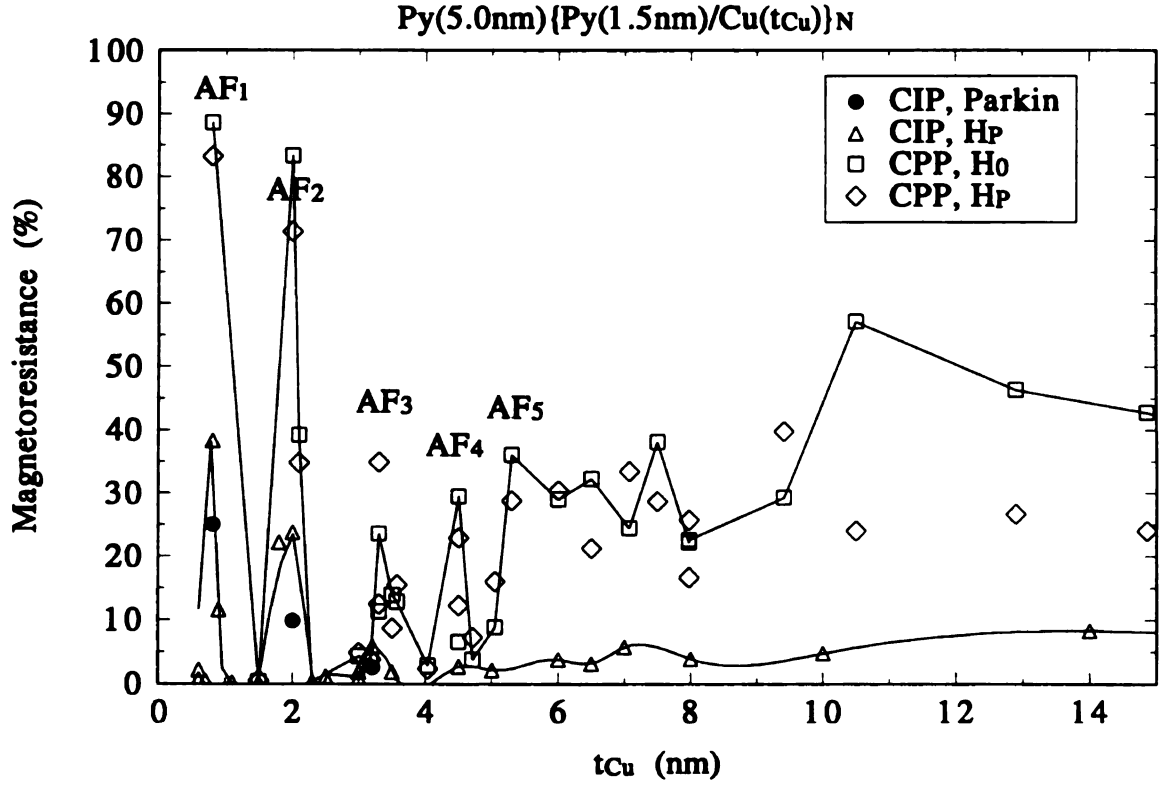

Figure 5.8: The CPP-MR for H_0 (squares) and H_P (diamonds) is plotted for the *Py(5.0nm)[Py(1.5nm)/Cu(t_{Cu})]×N* series. The CIP-MR for H_P (triangles) is plotted for the slightly different *Py(5.0nm)[Py(1.5nm)/Cu(t_{Cu})]×14* series to compare with Parkin[4] (filled circles). Measurements were made at 4.2K except for Parkin's which were done at 300K.

Table 5.7: CPP values at H_0, H_P, H_S and H_D for the *[Py(1.5nm)/Cu(t_{Cu})]×N* series. The data above the blank row were used in Fits A and B, given later.

Sample #	t_{Cu} nm	N	Area mm^2	CPP-AR(H) $f\Omega\text{-}m^2$			
				H_0	H_P	H_S	H_D
432^{02}	435	8	1.304	18.11	16.65	14.35	
410^{01}	345	10	1.253	20.29	19.34	17.11	
417^{06}	285	12	1.276	22.00	20.38	17.07	
417^{05}	225	15	1.261	25.80	23.64	20.38	25.44
409^{02}	185	18	1.306	29.94	28.07	22.56	
425^{02}	149	22	1.416	31.92	27.72	22.35	31.77
403^{05}	129	25	1.272	41.38	35.83	28.27	
432^{03}	105	30	1.174	44.18	34.86	28.10	
425^{01}	94	33	1.175	41.42	40.78	32.02	
377^{02}	80	32	1.327	37.48	37.97	30.13	
378^{01}	80	38	1.259	43.95	45.08	35.84	
509^{05}	75	40	1.209	36.66	38.66	30.03	41.49
504^{01}	70	42	1.323	37.39	40.12	30.04	
425^{08}	65	45	1.181	46.06	42.20	34.81	
377^{03}	60	48	1.225	46.95	47.47	36.38	
509^{02}	57	50	1.327	43.58	47.12	37.38	49.88
417^{07}	53	53	1.326	49.48	46.84	36.35	
544^{04}	51	55	1.313				
544^{06}	47	58	1.288	56.76	58.68	54.72	60.81
403^{06}	45	60	1.293	54.36	57.27	51.03	58.17
544^{07}	45	60	1.293				
377^{01}	40	65	1.261	49.63	49.37	48.26	
425^{03}	36	71	1.183	46.02	47.10	40.79	
432^{04}	35	72	1.126	47.02	44.88	41.29	
509^{06}	33	75	1.347	48.70	53.19	39.41	54.85
544^{01}	33	75	1.145	56.99	57.60	51.20	60.55
544^{02}	32	77	1.323	52.75	52.90	50.97	53.80
503^{01}	30	80	1.466	63.12	63.42	60.50	
491^{03}	20	100	1.625	102.25	99.00	73.43	
509^{01}	20	103	1.242	121.03	113.17	66.02	
509^{04}	15	120	1.391	60.91	61.04	60.74	
503^{02}	8	157	1.405	158.01	153.48	83.76	

Table 5.8: CPP values at H_0, H_P, H_S and H_D for the *[Py(6.0nm)/Cu(t_{Cu})]×N* series. The data above the blank row were used in the Fits A and B, given later.

Sample #	t_{Cu} nm	N	Area mm^2	CPP-AR(H) $f\Omega\text{-}m^2$			
				H_0	H_P	H_S	H_D
432^{05}	540	6	1.411	18.77	17.24	15.58	
699^{01}	454	7	1.284	24.24	24.32	21.53	25.54
425^{05}	340	9	1.282	24.67	23.16	19.70	
409^{03}	300	10	1.369	28.11	27.73	21.64	
613^{02}	267	11	1.461	31.08	28.80	21.20	31.02
417^{01}	240	12	1.212	38.09	30.35	28.01	
580^{04}	240	12	1.250	33.13	24.63	21.96	32.50
433^{02}	217	13	1.335	33.06	29.82	25.96	
699^{02}	217	13	1.186	29.71	30.97	23.98	35.15
580^{02}	197	14	1.393	37.01	31.40	28.31	41.97
699^{03}	180	15	1.312	30.32	31.45	23.87	34.31
417^{02}	180	15	1.321	40.00	31.36	29.24	
580^{06}	165	16	1.285	48.93	33.51	32.07	48.06
424^{05}	165	16	1.234	51.93	48.20	40.64	
378^{05}	150	17	1.185	36.26	32.77	27.60	
613^{03}	140	18	1.554	40.62	40.00	30.21	42.49
403^{07}	130	19	1.300	43.46	45.02	33.06	
378^{04}	110	21	1.181	33.07	32.04	29.65	
613^{05}	92	23	1.285	37.62	35.31	32.50	39.68
417^{03}	84	25	1.211	46.35	45.46	42.40	
578^{04}	84	25	1.580	36.41	37.06	31.64	39.98
613^{01}	78	26	1.613	36.82	34.89	32.83	36.71
377^{06}	60	30	1.339	39.64	39.84	37.50	
613^{04}	49	33	1.293	40.73	40.95	39.28	41.52
377^{04}	40	36	1.151	43.20	43.18	42.51	
425^{07}	40	36	1.251	40.01	40.03	39.02	
425^{06}	35	38	1.195	43.32	43.27	42.77	
403^{08}	30	40	1.265	53.49	-	53.42	
510^{04}	30	40	1.356	40.02	40.05	39.52	40.05
510^{02}	20	45	1.305	47.76	47.86	47.44	47.98
510^{03}	15	48	1.210	46.20	46.15	46.04	
510^{01}	8	53	1.258	73.75	72.77	56.80	73.24

Table 5.9: CPP values at H_0, H_P, H_S and H_D for the *[Py(t_{Py}=t_{Cu})/Cu(t_{Cu})]×N* series. The data above the blank row were only used in Fit B, given later.

Sample #	t_{Cu} nm	N	Area mm^2	CPP-AR(H) fΩ-m^2			
				H_0	H_P	H_S	H_D
628^{01}	360	5	1.422	32.08	32.65	27.79	31.13
424^{01}	300	6	1.135	35.63	34.31	31.81	38.07
627^{01}	300	6	1.289	30.42	31.20	26.00	31.61
424^{03}	225	8	1.173	30.58	32.01	28.88	32.70
628^{03}	200	9	1.304	33.33	35.03	29.26	38.02
433^{03}	180	10	1.218	40.05	37.65	35.63	
438^{01}	180	10	1.390	40.87	37.60	35.55	42.35
628^{05}	164	11	1.513	33.71	33.32	27.42	35.40
424^{02}	150	12	1.350	35.32	35.94	31.57	38.11
627^{04}	150	12	1.640	35.59	34.82	30.70	37.74
424^{04}	180	10	1.327	53.94	53.40	50.93	
403^{01}	120	15	1.382	40.15	39.36	37.28	41.73
438^{02}	90	20	1.274	39.26	38.44	36.97	40.89
628^{04}	90	20	1.517	34.25	33.03	30.01	35.22
404^{02}	75	24	1.246	42.16	39.87	39.30	41.76
438^{05}	67	27	1.212	37.24	37.35	36.31	
403^{02}	60	30	1.241	44.62	43.56	42.15	
628^{07}	60	30	1.427	37.47	36.53	33.64	38.06
433^{06}	56	32	1.274	38.02	37.98	36.92	
404^{01}	45	40	1.427	49.81	49.57	48.63	
417^{08}	45	40	1.194	43.54	-----	42.58	
403^{03}	36	50	1.258	45.62	45.46	44.79	
509^{04}	15	120	1.391	60.91	61.04	60.74	

As was argued previously, the H_0 state is the best approximation to the AP state for Co/Cu. For Py/Cu, the situation is less clear because of greater variability between samples. In many cases the H_P resistance may equal or even surpass the as deposited, H_0 resistance. A direct comparison of H_0 and H_P resistances may be made by defining the ratio, Π, as follows:

$$\Pi = \frac{MR(H_0)}{MR(H_P)} = \frac{R(H_0) - R(H_S)}{R(H_P) - R(H_S)} \qquad 5.5$$

The Π ratio is used to determine whether or not the H_0 resistance is significantly higher than the H_P resistance. Having $\Pi>1.0$, i.e. between 1.5 to 2.0, indicates that the H_0 resistance is significantly larger than the H_P resistance. In cases where $\Pi\approx1.0$, it is unclear which resistance best approximates the true AP resistance of the sample, since $AR(H_0)\approx AR(H_P)$. While $\Pi<1.0$, i.e. below 0.90, indicates the H_P resistance is significantly higher than the H_0 resistance.

The ratio Π is plotted as a function of N in Figure 5.9 for each Co/Cu series. In these multilayers Π is well defined and varies little for all three series: $\Pi=1.81\pm0.20$ for $t_{Co}=1.5nm$, $\Pi=1.71\pm0.32$ for $t_{Co}=6.0nm$ and $\Pi=1.86\pm0.21$ for $t_{Co}=t_{Cu}$. For Co/Cu the values of Π for each sample indicates that the H_0 resistance is always significantly larger than the H_P resistance.

For each Py/Cu series, the Π values do not stay within a narrow range. The data for Py/Cu are given in Figure 5.10. For the moment we concentrate on the unfilled H_0 points. The average of the $t_{Py}=1.5nm$ series is $\Pi=1.68\pm0.32$ for samples with $t_{Cu}>10.0nm$. As shown in Figure 5.10a, the Π values steadily decrease for samples with

t_{Cu}<*10.0nm*. The average of the t_{Py}=*6.0nm* series has Π=1.45±0.66 for samples with t_{Cu}>*16.0nm*, neglecting extreme values (Π>3.0). Again as the Cu spacer becomes thinner (t_{Cu}<*16.0nm*), the Π values steadily decrease as seen in Figure 5.10b. However for the t_{Py}=t_{Cu} series, the Π values are fairly constant at Π=0.99±0.40 over the whole range of Cu thickness shown in Figure 5.10c.

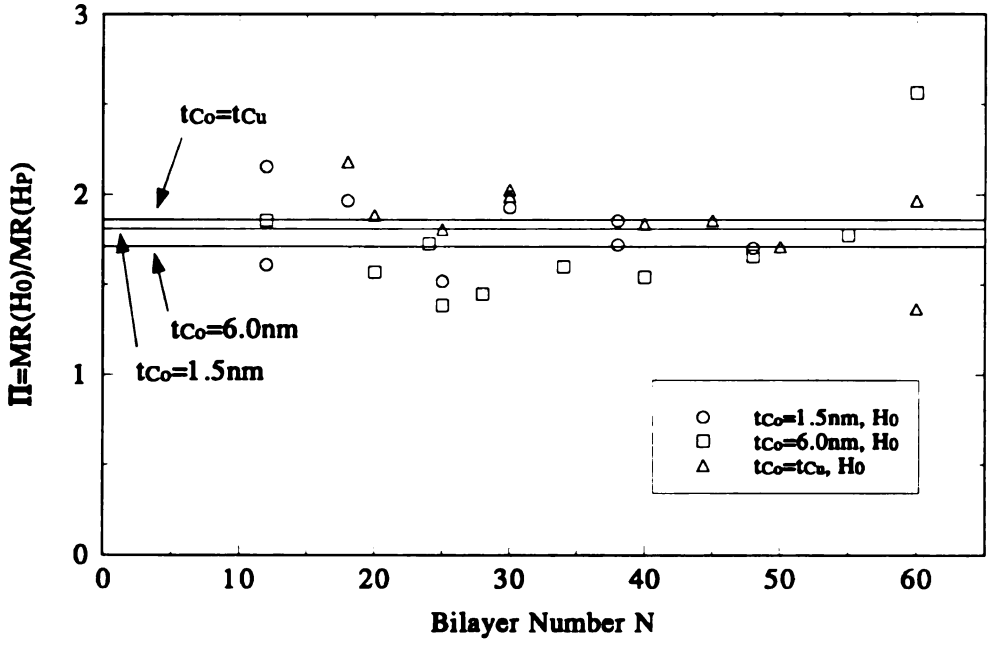

Figure 5.9: The Π values for Co/Cu all three multilayers series. The lines indicate the average Π value for each series.

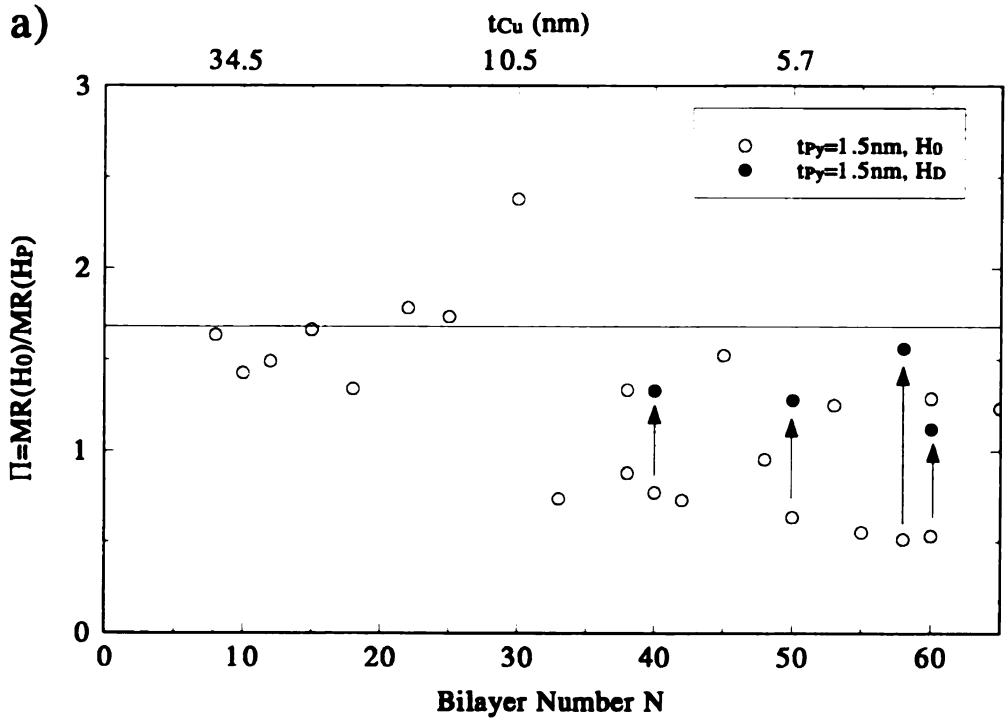
a)
tCu (nm)
34.5
10.5
5.7
tPy=1.5nm, H0
tPy=1.5nm, HD
Π=MR(H0)/MR(HP)
Bilayer Number N

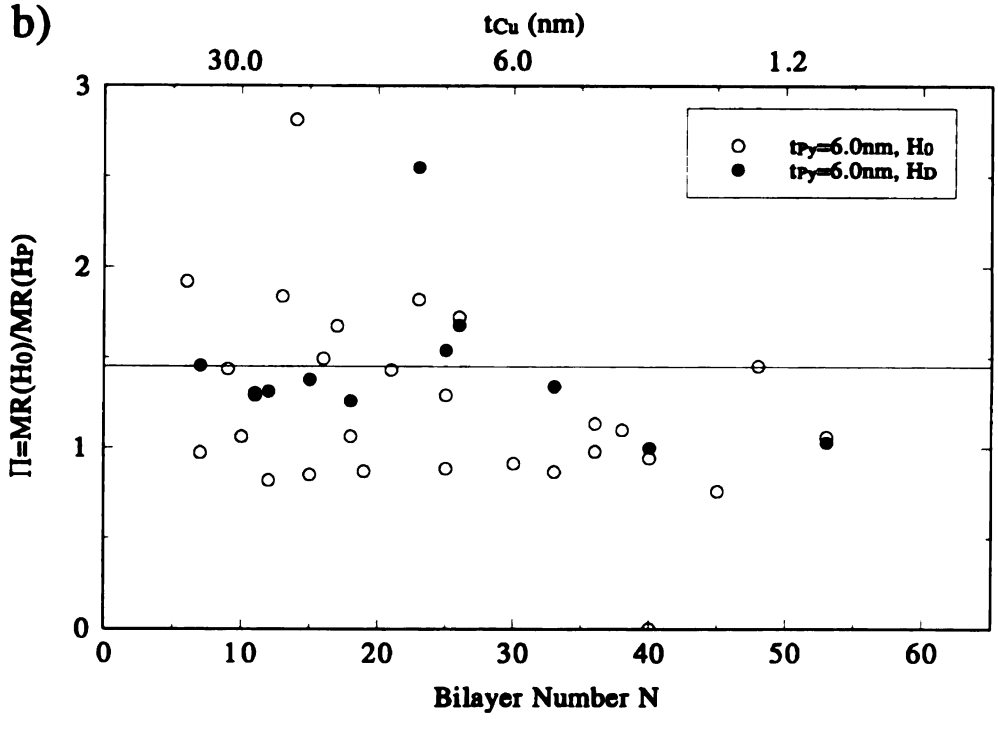
b)
tCu (nm)
30.0
6.0
1.2
tPy=6.0nm, H0
tPy=6.0nm, HD
Π=MR(H0)/MR(HP)
Bilayer Number N

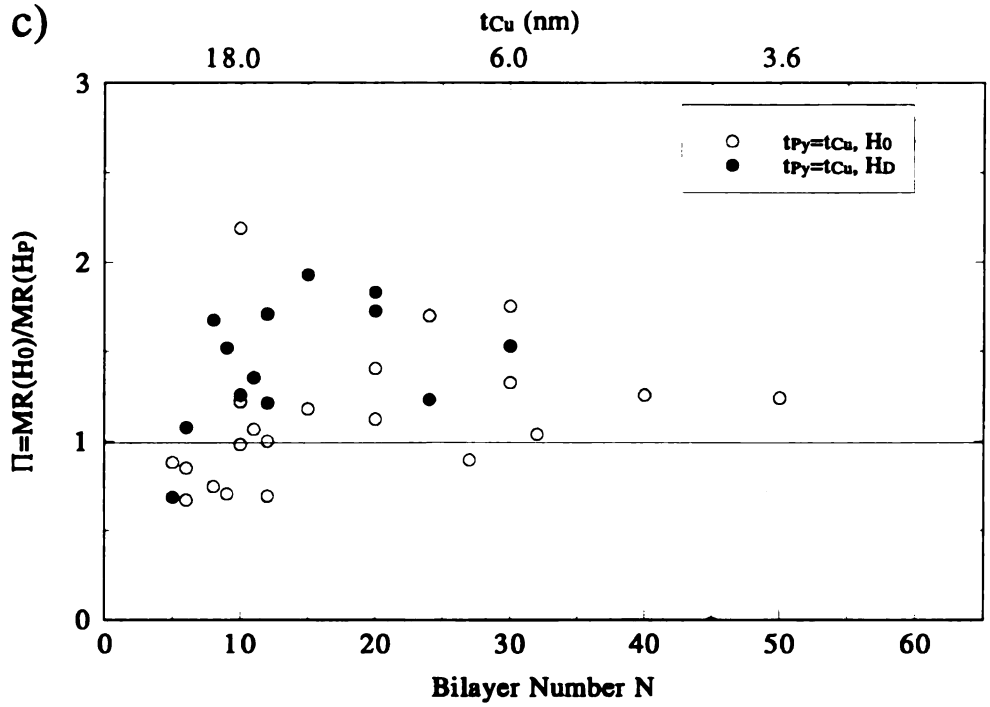

Figure 5.10: The ratio Π plotted as function of the bilayer number, N for a) the t_{Py}=*1.5nm* series, the t_{Py}=*6.0nm* series and the $t_{Py}=t_{Cu}$ series. Unfilled symbols are H_0 values and filled symbols are H_D values. Generally Π_D points are directly above the Π_0 values for the same sample. This is indicated in Figure 5.10a by arrows for a few representative samples.

The Co/Cu data clearly suggest that the H_0 resistance is always the largest measured for any sample independent of the thickness of either Co or Cu. The Py/Cu data only suggest this is true when t_{Py} is relatively thin (1.5nm or 6.0nm) and is fairly thick. There seems to be a fundamental difference between the H_0 resistances measured for the $t_{Py}=t_{Cu}$ data and the H_0 resistances measured for the constant t_{Py} data.

The ambiguity between the H_0 and H_P resistances for the $t_{Py}=t_{Cu}$ samples lead to a search for another resistance state; one in which the magnetization was also nearly zero after the sample had been exposed to a saturating field. Experimentally it is possible to approach a state of zero magnetization after saturation by cycling the sample through the hysteresis loop several times, progressively lowering the applied field with each cycle. This cycling randomizes the domains in the magnetic layers leaving the magnetization of the final state close to zero. Samples were demagnetized at 4.2K by starting at saturation and cycling at least 12 times, each time reducing the field. Nearly one third of the cycling was done inside the peak field of each sample. The resulting resistance state of the sample is labeled, H_D, the demagnetized resistance. Π ratios substituting H_D for H_0 in equation 5.5 will be denoted by Π_D.

In Co/Cu multilayers, the H_D resistances for a few representative samples[5] always fell between the H_0 and H_P resistances. For these samples the H_D resistances resulted in an average Π_D ratio of 1.3. Clearly the H_0 state for Co/Cu multilayers is a unique state which is irreversibly changed once a saturating field is applied.

In Figure 5.10 Π_D values are shown by filled symbols. For the $t_{Py}=1.5nm$ multilayers with $\Pi\approx1.6$, the H_D resistance was larger than the H_P resistance but smaller than the H_0 resistance. These points are not recorded in Figure 5.10a. Figure 5.10a does show that those $t_{Py}=1.5nm$ multilayers with $\Pi\approx1.0$ increased to $\Pi_D\approx1.3$. For the $t_{Py}=6.0nm$ multilayers with $\Pi\approx1.45$, the H_D resistance was also between H_P and H_0 resistances. Those $t_{Py}=6.0nm$ samples (Figure 5.10b) with $\Pi\approx1.0$ increased to $\Pi_D\approx1.5$. The $t_{Py}=6.0nm$ samples with thin Cu thickness showed little change in their Π values upon

demagnetizing, possibly because these sample are in the region of strong coupling. Nearly every demagnetized $t_{Py}=t_{Cu}$ sample in Figure 5.10c showed $\Pi_D>\Pi$ for the H_D resistance.

Since a majority of the $t_{Py}=t_{Cu}$ samples have $\Pi\approx1.0$, it seems likely that the H_0 and H_P resistances are related to each other. As noted earlier, H_P for the 1.5nm and 6.0nm Py data becomes smaller as the Py thickness increases. Since H_P roughly corresponds to the coercive field, this is equivalent to the coercive field decreasing with increasing Py thickness. This is confirmed by magnetization experiments. Figure 5.11 shows the hysteresis curve of a *[Py(30.0nm)/Cu(30.0nm)]×6* sample. The sample has a coercive field of 1.7Oe, much smaller than samples from the other two Py/Cu series with comparable Cu thickness. The small coercive field suggests that the magnetic configuration of the Py layers for $t_{Py}=t_{Cu}$ samples with thicker Py layers is very sensitive to small magnetic fields. Samples are exposed to small stray fields during sputtering. Powerful magnets used to confine the plasma during the sputtering process are not completely shielded from the sample and expose it to a field possibly as high as 3.0Oe during growth. As Figure 5.11 shows, this small field could produce a significant portion of the saturation magnetization for this sample. Therefore, the measured H_0 resistances of $t_{Py}=t_{Cu}$ samples are similar to their H_P resistances because the samples have been partially saturated before measurements were made.

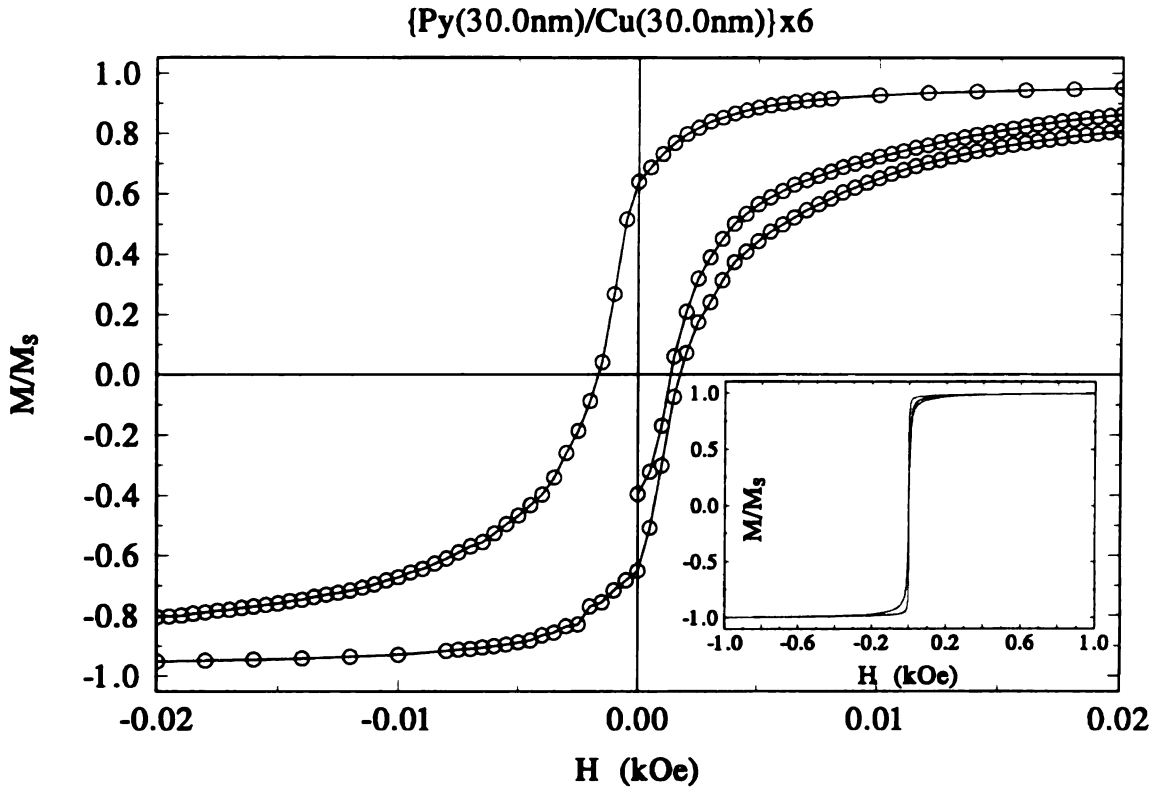

Figure 5.11: The magnetization hysteresis curve for a multilayered sample with *[Py(30.0nm)/Cu(30.0nm)]×6* at T=5K. The coercive field for this sample was 1.7Oe. The insert shows that the sample saturates quickly.

Global Fit of the Py/Cu Data

Preliminary results based on a partial analysis of the t_{Py}=*1.5nm and 6.0nm* are published elsewhere[6,7]. These results will be commented on later. The analysis done here represents a complete analysis of our Py/Cu data in the limit that $\ell_{sf}^{Py} >> t_{Py}$. In these fits, for a given sample, the larger of $AR(H_0)$ and $AR(H_D)$ was used for $AR_T(AP)$. In Figures 5.12-5.14 all the data are plotted using this criterion. The data for all three sets of Py/Cu multilayers were globally fit following the same procedure outlined in the

previous section for Co/Cu multilayers. At first a fit was done using all the data in Tables 5.7-5.9 above the cutoff (blank row), to minimize the effect of coupled Py layers. This fit of the Py/Cu data resulted in values for ρ^*_{Py}, ρ_{Cu} and $AR_{Py/Cu}$ which poorly represented all three series. To properly fit the H_0 data for the $t_{Py}=t_{Cu}$ series, required $\rho^*_{Py} \approx 140n\Omega m$ much smaller than was required for either the 1.5nm or 6.0nm Py H_0 data. The previous section also showed that it is difficult to interpret the H_0 data of the $t_{Py}=t_{Cu}$ series as being the closest approximation to an AP state. Because of the ambiguity of the H_0 state in the $t_{Py}=t_{Cu}$ samples, two different fits to the Py/Cu data were done.

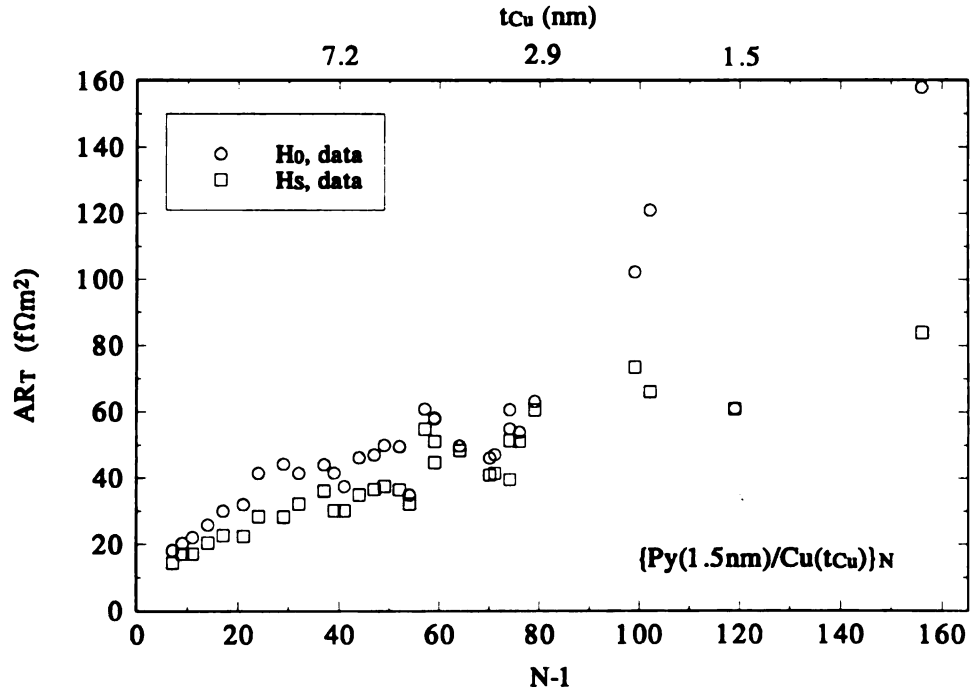

Figure 5.12: The H_0 and H_S data for the *Py(5.0nm)[Py(1.5nm)/Cu(t_{Cu})]×N* series.

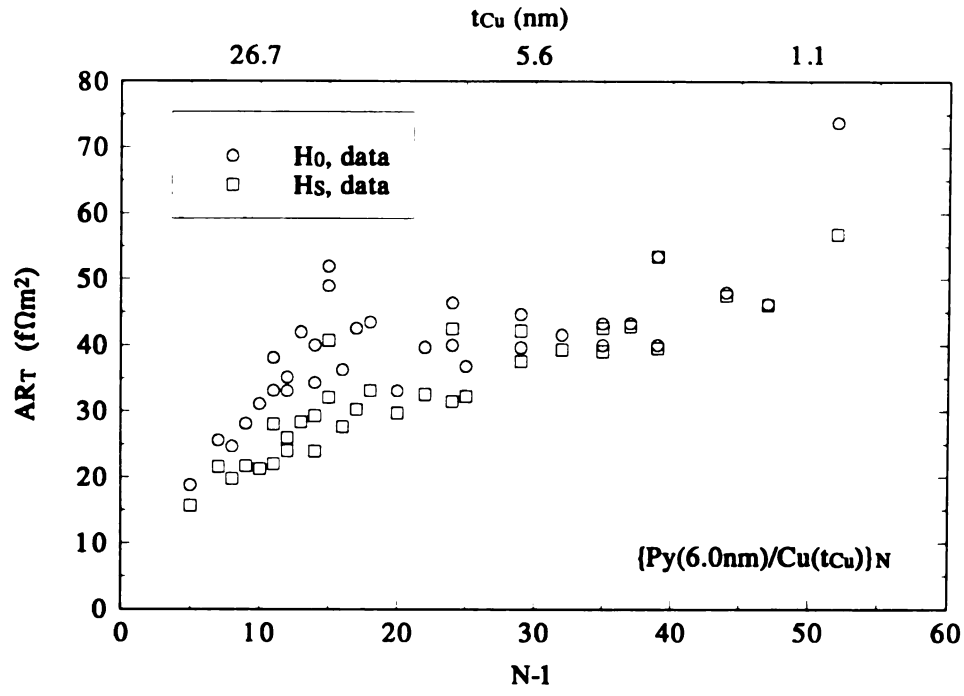

Figure 5.13: The H_0 and H_S data for the *[Py(6.0nm)/Cu(t_{Cu})]×N* series.

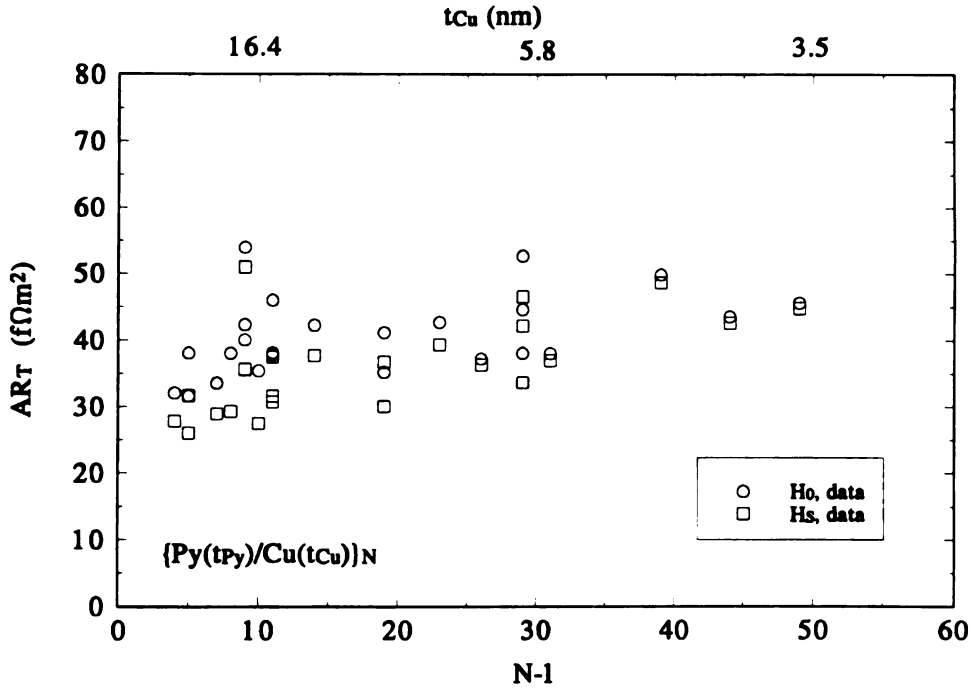

Figure 5.14: The H_0 and H_S data for the *[Py(t_{Py}=t_{Cu})/Cu(t_{Cu})]×N* series.

Fit A

Fit A only includes the 1.5nm and 6.0nm Py data given in Tables 5.7 and 5.8 above their indicated cutoffs. With only four sets of data, the H_0 and H_S data for t_{Py}=*1.5nm* and *6.0nm*, the fitting procedure now treated ρ^*_{Py}, $AR^*_{Py/Cu}$, β and γ as the only free parameters. The Nb/Py boundary resistance and the Cu resistivity were constrained to independently measured values. A Cu resistivity of $\rho_{Cu} = 5.0 \pm 1.0 n\Omega m$ was determined by measuring 300nm thick Cu films made along with the multilayers during the various runs. The Nb/Py boundary resistance of $2AR_{Nb/Py} = 6.5 \pm 1.0 f\Omega m^2$ was determined by fitting the resistance of a series of Nb/Py(t_{Py})/Nb trilayers as a function of the Py thickness. The intercept of the best fit line through the trilayer data is a direct measurement of the Nb/Py boundary resistance. Similarly to the Co/Cu data , the Py/Cu data is fit in a two step process: (a) First the H_0 data for t_{Py}=*1.5nm* and *6.0nm* series is fit to equation 4.2 to obtain ρ^*_{Py} and $AR^*_{Py/Cu}$. (b) Second both the H_0 and H_S data are used to fit equation 4.4 to obtain values for β and γ. The results for fitting procedure A are listed in Table 5.10. The columns labeled Set 1 and Set 2 contain the best parameters for slightly different cutoffs in the data. The cutoff for the t_{Py}=*1.5nm* data is the same for both Set 1 and Set 2. The cutoff choice for the t_{Py}=*6.0nm* H_0 data is less clear. The square root data peaks at N-1=15, so data beyond N-1=15 are likely to be affected by coupled Py layers. The samples with N=16 may be suspect because it is not known whether they are on the coupled side or the uncoupled side of this peak. One of the N=16 samples is eliminated from Set 1 and Set 2 since the H_S resistance is much larger than the

H_S values of the neighboring points in Figure 5.13. The other N=16 point of Figure 5.13 is included in Set 1 but not in Set 2.

Table 5.10: Summary of fitted parameters for Fit A. A $2AR_{Nb/Py}$ of 6.5fΩm^2 and a ρ_{Cu} of 5.0nΩm were assumed for each fit. The uncertainties in Set 1 and Set 2 have adjusted so that the χ^2 will match the degrees of freedom for each fit, see the text.

	independent measurements	Fit A		units
		Set 1	Set 2	
$2AR_{Nb/Py}$	6.5±1.0			fΩm^2
ρ_{Cu}	5.0±1.0			nΩm
ρ_{Py}	137±35	147±22	140±22	nΩm
ρ^*_{Py}		218±19	211±19	nΩm
β		0.57±0.07	0.58±0.07	
α_{Py}		3.7±0.3	3.8±0.3	
$AR_{Py/Cu}$		0.16±0.06	0.17±0.06	fΩm^2
$AR^*_{Py/Cu}$		0.45±0.04	0.44±0.04	fΩm^2
γ		0.79±0.08	0.79±0.08	
$\alpha_{Py/Cu}$		8.7±0.7	8.4±0.7	

The uncertainties in the parameters (under Fit A for columns 3 and 4) in Table 5.10 have been adjusted so that the χ^2 will equal the number of degrees freedom for the fit, N_A-2. (Here N_A is the number of data points used in fit A and 2 is the number of adjustable parameters.) Comparing Set 1 and Set 2 in Table 5.10 reveals only minor differences in all the parameters. For the fit of the H_0 data, Set 1 of Fit A had a χ^2 of 71 and with N_A=21 for Set 1 the uncertainties in ρ^*_{Py} and $AR^*_{Py/Cu}$ were increased by a factor of $\sqrt{\chi^2/(N_A-2)} = 1.93$. For Set 2 of Fit A the H_0 fit resulted in a slightly smaller χ^2 of 60,

and with N_A=20 the uncertainties in ρ^*_{Py} and $AR^*_{Py/Cu}$ were increased by a factor of $\sqrt{\chi^2/(N_A-2)} = 1.83$. It is fair to say that both Set 1 and Set 2 give reasonable fits to the H_0 data of the 1.5nm and 6.0nm Py data. The χ^2 per degree of freedom is only slightly less for the choice of Set 2. The fit of the square root data, $A\sqrt{R(H_0)[R(H_0)-R(H_S)]}$, resulted in a χ^2 of 239 for Set 1. The uncertainties in β and γ are increased by a factor of $\sqrt{\chi^2/(N_A-2)} = 3.54$ for Set 1. Similarly for Set 2, the χ^2 of the square root fit is 209 and the uncertainties in β and γ are increased by a factor of $\sqrt{\chi^2/(N_A-2)} = 3.41$. Again for Fit A both Set 1 and Set 2 fit the data reasonably well, with the reduced χ^2 for Set 1 being slightly greater than that for Set 2 (12.6 to 11.6, respectively).

The largest difference between Set 1 and Set 2 occurs for the Py resistivity. The value of ρ^*_{Py} for both sets differs by less than 5%, which considering the uncertainty in ρ^*_{Py} for each choice, makes them more or the less the same. The value of $AR^*_{Py/Cu}$ in Set 1 and Set 2 are even closer, differing by only 2.2%. All other parameters in Table 5.10 for Set 1 and Set 2 are virtually identical, especially when taking into account their uncertainties.

Fit B

Fit B uses the same 1.5nm and 6.0nm Py data as Fit A along with the H_S data above the cutoff from the $t_{Py}=t_{Cu}$ series. Although the H_0 resistance state of the $t_{Py}=t_{Cu}$ data may be significantly altered by the magnetic field of the sputtering system, keeping the H_S data of the $t_{Py}=t_{Cu}$ set seems justifiable in that the saturation state of a sample has the same magnetic configuration (and therefore the same resistance) each time the sample is saturated. However, keeping only the H_S data will only affect the Py spin asymmetry parameters, β and γ, since the H_0 data is used to fit ρ^*_{Py} and $AR^*_{Py/Cu}$. The Fit B procedure is as follows: (a) First, the H_0 data for $t_{Py}=1.5nm$ and $6.0nm$ series is fit to equation 4.2 to obtain ρ^*_{Py} and $AR^*_{Py/Cu}$. (b) Second, the H_0 data for the $t_{Py}=1.5nm$ and $6.0nm$ series are used to estimate H_0 values for the $t_{Py}=t_{Cu}$ series. (c) Third, the H_0 and H_S data for the $t_{Py}=1.5nm$ and $6.0nm$ series along with the estimated H_0 values and H_S data for the $t_{Py}=t_{Cu}$ series are fitted to equation 4.4 to obtain values for β and γ. The results for fitting procedure B are listed in Table 5.11. The columns labeled Set 1 and Set 2 have the same meanings as in Fit A. The estimated H_0 resistances for the $t_{Py}=t_{Cu}$ series are based on the fitted values of ρ^*_{Py} and $AR^*_{Py/Cu}$ determined by fitting the H_0 1.5nm and 6.0nm Py data. In Fit B the Cu resistivity and the Nb/Py boundary resistance are also constrained to the same values given previously in Fit A.

Table 5.11: Summary of fitted parameters for Fit B. A $2AR_{Nb/Py}$ of 6.5fΩm^2 and a ρ_{Cu} of 5.0nΩm were assumed for each fit. The uncertainties in Set 1 and Set 2 have adjusted so that the χ^2 will match the degrees of freedom for each fit, see the text.

	independent measurements	Fit B		units
		Set 1	Set 2	
$2AR_{Nb/Py}$	6.5±1.0			fΩm^2
ρ_{Cu}	5.0±1.0			nΩm
ρ_{Py}	137±35	116±22	114±21	nΩm
ρ^*_{Py}		218± 19	211±19	nΩm
β		0.68±0.07	0.68±0.07	
α_{Py}		5.3±0.4	5.2±0.3	
$AR_{Py/Cu}$		0.22±0.05	0.22±0.05	fΩm^2
$AR^*_{Py/Cu}$		0.45±0.04	0.44±0.04	fΩm^2
γ		0.71±0.07	0.72±0.07	
$\alpha_{Py/Cu}$		6.0±0.4	6.2±0.4	

The uncertainties in the parameters (under Fit B for columns 3 and 4) in Table 5.11 have been adjusted so that the χ^2 will equal the number of degrees freedom (the difference in the number of data points and the number of adjustable parameters, N_B-2) for the fit. Comparing Set 1 and Set 2 in Table 5.11 reveals only minor differences in all the parameters. In fitting the H_0 data, the same data points used in Fit A are used in Fit B, therefore the values of the parameters, ρ^*_{Py} and $AR^*_{Py/Cu}$, and their uncertainties listed in Table 5.11 for Fit B are the same as those given in Table 5.10 for Fit A. The fit of the square root data, $A\sqrt{R(H_0)[R(H_0)-R(H_S)]}$, includes the H_S data of ten t_{Py}=t_{Cu} samples in addition to the points used in Fit A. This resulted in a χ^2 of 370 for Set 1. The uncertainties in β and γ are increased by a factor of $\sqrt{\chi^2/(N_B-2)} = 3.57$ for Set 1,

N_B=31. Similarly for Set 2, the χ^2 of the square root fit is 322 and the uncertainties in β and γ are increased by a factor of $\sqrt{\chi^2/(N_B-2)} = 3.39$, N_B=30. Again for Fit B both Set 1 and Set 2 fit the data reasonably well, with the reduced χ^2 for Set 1 being slightly greater than that for Set 2, 12.8 to 11.5, respectively.

The largest difference between Set 1 and Set 2 in Fit B also occurs for the Py resistivity. The values of ρ^*_{Py} and $\delta\rho^*_{Py}$ for both sets are the same as those in Fit A, since the same H_0 data is used in both Fit A and Fit B. All other parameters listed for Set 1 and Set 2 in Table 5.11 are virtually identical, especially when taking into account their uncertainties.

Comparison of Fits A and B

As has been shown above choosing Set 1 or Set 2 within either Fit A or Fit B makes no difference in the value of the fitted parameters. However, comparing the parameters derived with Fit A to those obtained with Fit B do show some significant differences, even though the same ρ^*_{Py} and $AR^*_{Py/Cu}$ values are used in each fit. In comparing the remaining parameters for Fit A and Fit B, the parameters only overlap at the extremes of their uncertainties, with the exception of the α's which do not overlap at all. Clearly the t_{Py}=t_{Cu} series has an appreciable effect in modifying the parameters β and γ. The α's for Fits A and B show the largest disparities. In Fit A, $\alpha_{Py/Cu}$ is more than a factor of two larger than α_{Py} for either Set 1 or Set 2, while Fit B gives $\alpha_{Py/Cu}$ and α_{Py} approximately

equal for Set 1 and Set 2. Fit B suggests that the bulk Py contribution to spin dependent scattering is on par with the Py/Cu interface contribution to spin dependent scattering. Fit A indicates that the bulk Py contribution to spin dependent scattering is only half the Py/Cu interface contribution to spin dependent scattering.

The 1.5nm Py data is shown in Figure 5.15 and 5.16 along with lines representing the parameters given in Tables 5.10 and 5.11. Figure 5.15a compares Set 1 values for both Fit A and Fit B, while Figure 5.15b compares the Set 2 value for both fits. In each figure, the H_0 fits are identical, since the same ρ^*_{Py} and $AR^*_{Py/Cu}$ values are obtained in both fits. The curvature of the fits can be explained by the nonlinearity of the Cu term as N approaches zero, see page 91. The H_S fits differ slightly with Fit B lying below Fit A. The 1.5nm Py square root data is plotted in Figures 5.16a and 5.16b along with lines representing the various values given in Tables 5.10 and 5.11. Differences between Figure 5.16a and 5.16b are nearly impossible to distinguish.

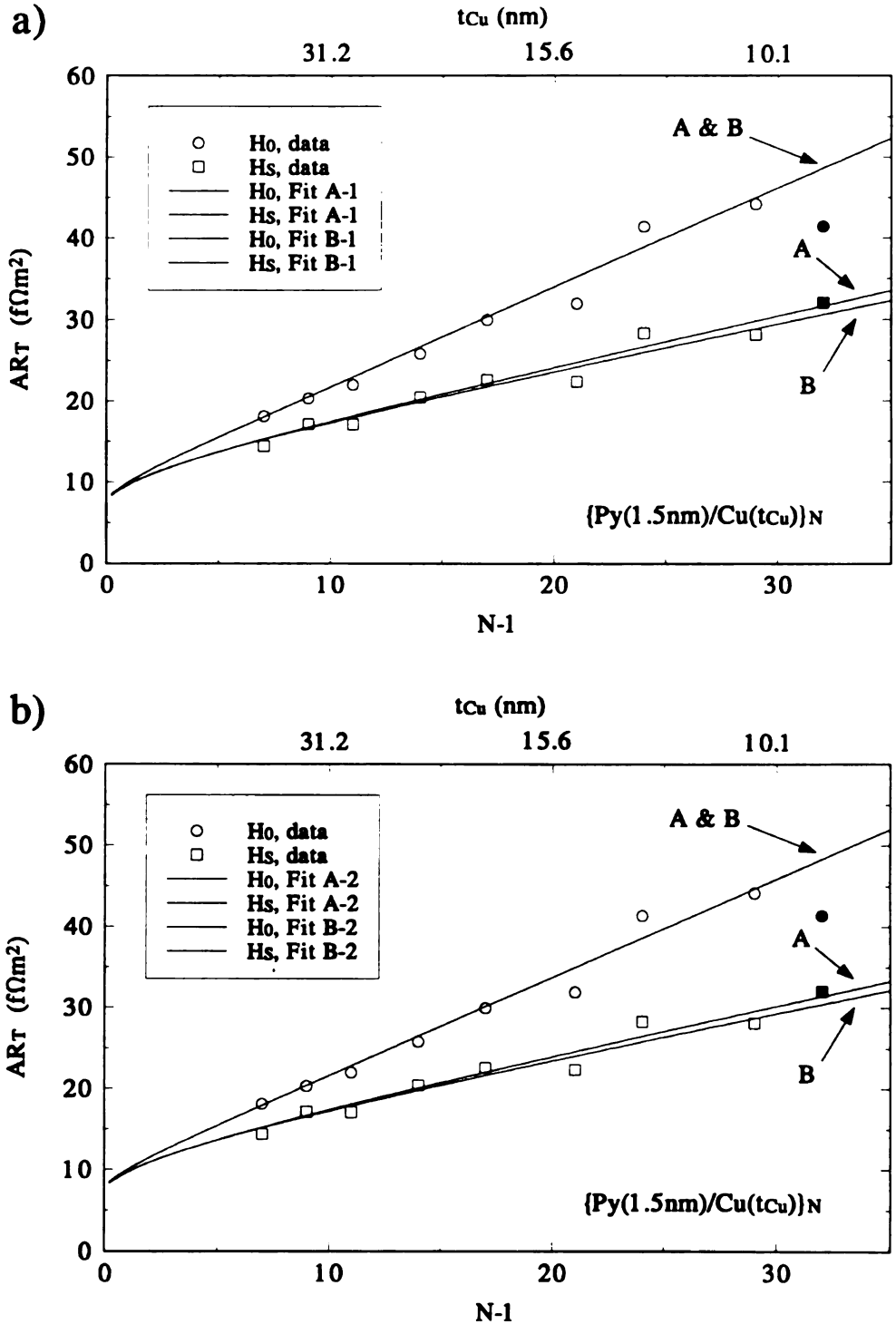

Figure 5.15: $AR_T(H_0)$ and $AR_T(H_S)$ plotted as a function of the corrected bilayer number, N-1 for the *Py(5.0nm)[Py(1.5nm)/Cu(t_{Cu})]×N*. Total sample thickness is held constant at 360nm. Fits A and B in a) use Set 1 parameters listed in Table 5.10s and 5.11, while Fits A and B in b) use Set 2 parameters from Tables 5.10 and 5.11. Points with filled symbols were not used in fits.

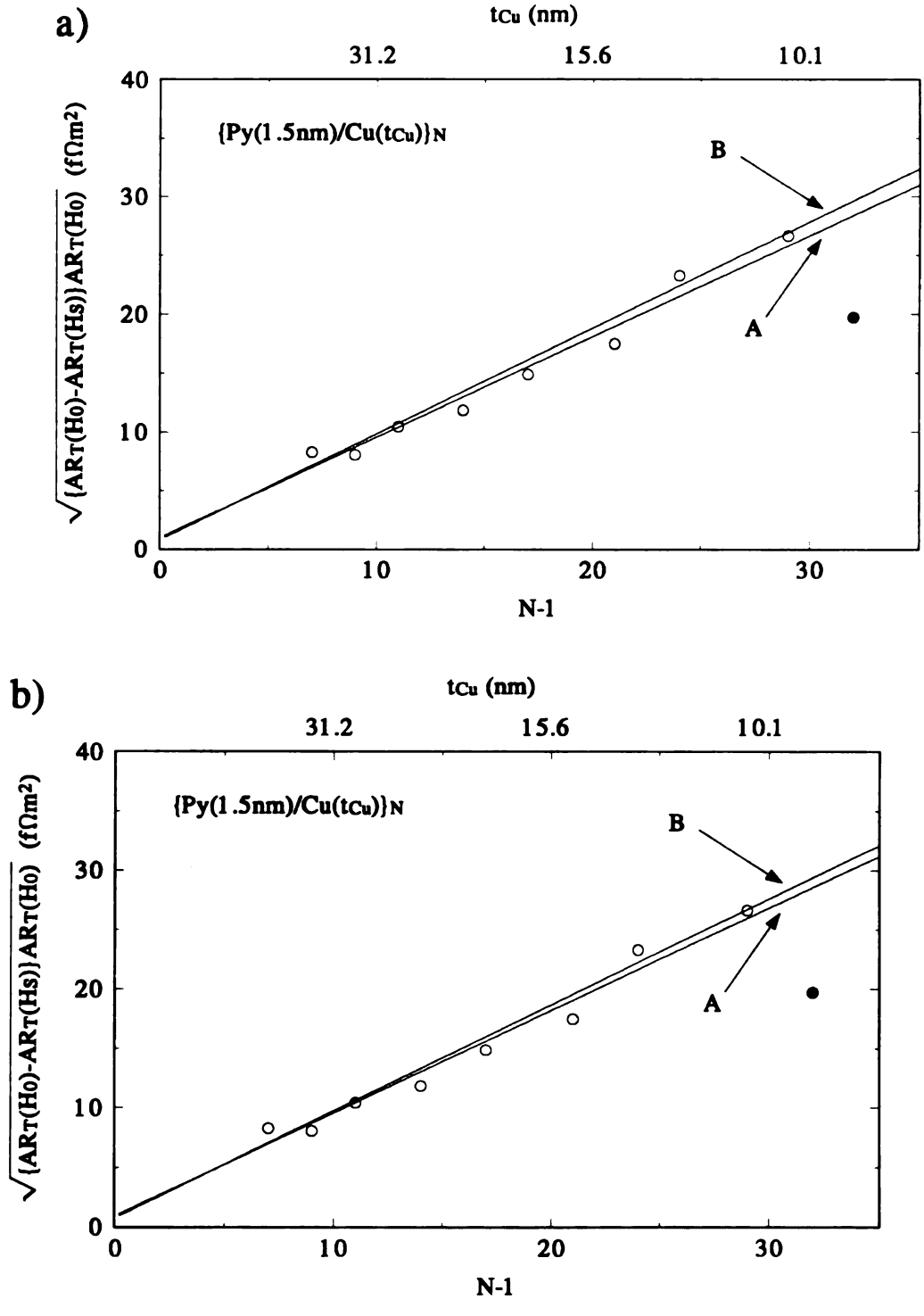

Figure 5.16: The square root data plotted as a function the reduced bilayer number, N-1 for the *Py(5.0nm)[Py(1.5nm)/Cu(t_{Cu})]×N*. Total sample thickness is held constant at 360nm. Fits A and B in a) use Set 1 parameters listed in Tables 5.10 and 5.11, while Fits A and B in b) use Set 2 parameters from Tables 5.10 and 5.11. Points with filled symbols were not used in fits.

The 6.0nm Py data is shown in Figures 5.17 and 5.18 along with lines representing the various fits. The $AR_T(H_0)$ and $AR_T(H_S)$ data and Set 1 parameters for Fits A and B are plotted in Figure 5.17a while the Set 2 parameters for Fits A and B are plotted in Figure 5.17b. The differences between the Set 1 parameters in Figure 5.17a and those of Set 2 shown in Figure 5.17b are barely perceptible. In each figure the H_0 fits are identical, while the H_S Fit A parameters give values for $AR_T(H_S)$ slightly above those obtained from Fit B parameters. The 6.0nm Py square root data is plotted in Figure 5.18 along with the square root fits.

The $t_{Py}=t_{Cu}$ $AR_T(H_0)$ and $AR_T(H_S)$ data is plotted in Figure 5.19 along with the various fits. The differences between the fits using the Set 1 parameters in Figure 5.19a and those using the Set 2 parameters in Figure 5.19b are small but noticeable. In both figures the H_0 fits are identical and both Fits A and B are well above the H_0 data. This is not too surprising given that the H_0 data was not used in either of Fits A and B because their Π ratios in Figure 5.10c were approximately 1.0. The $AR(H_S)$ obtained with Fit B parameters differ markedly from those obtained using Fit A parameters. Although both Fits A and B lie above the best fit line through the H_S data, the parameters of Fit B come significantly closer to describing the H_S data. It is a little surprising that Fit B does not do a better job of fitting the $t_{Py}=t_{Cu}$ saturated data, but in fitting the H_S data one must know the values of the actual H_0 data. For these data the H_0 values were assumed, based on fits to the Py 1.5nm and 6.0nm H_0 data. One could argue that the 1.5nm and 6.0 data have been weighted more heavily than the $t_{Py}=t_{Cu}$ data in Fit B since 1.5nm and 6.0 H_0 data are

effectively acting as the H_0 data for the $t_{Py}=t_{Cu}$. series. This would in effect skew the H_S values of Fit B closer to the H_S values of Fit A. Fit B in both Figure 5.19a and 5.19b lies roughly half way in between the H_S data and the H_S values obtained from Fit A.

The square root data for the $t_{Py}=t_{Cu}$ series is plotted in Figure 5.20. The AR(H_0) data has been estimated from the parameters for ρ^*_{Py} and $AR^*_{Py/Cu}$ given in Tables 5.10 and 5.11. Although the data is quite scattered, the Set 1 parameters for both Fits A and B represent the square root data better than the Fits using the Set 2 parameters.

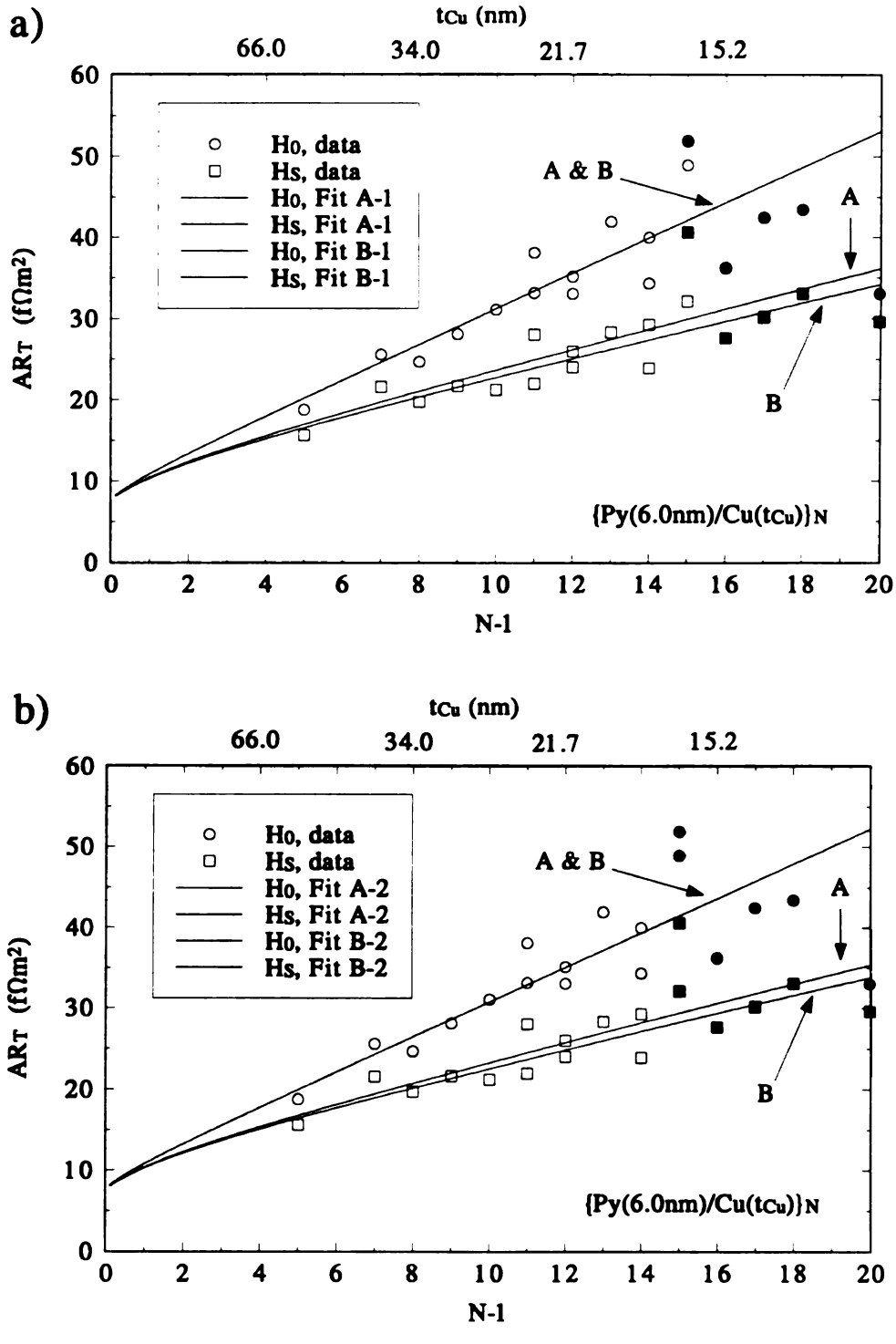

Figure 5.17: $AR_T(H_0)$ and $AR_T(H_S)$ plotted as a function of the corrected bilayer number, N-1 for the *[Py(6.0nm)/Cu(t_{Cu})]×N*. Total sample thickness is held constant at 360nm. Fits A and B in a) use Set 1 parameters listed in Tables 5.10 and 5.11, while Fits A and B in b) use Set 2 parameters from Tables 5.10 and 5.11. Points with filled symbols were not used in fits.

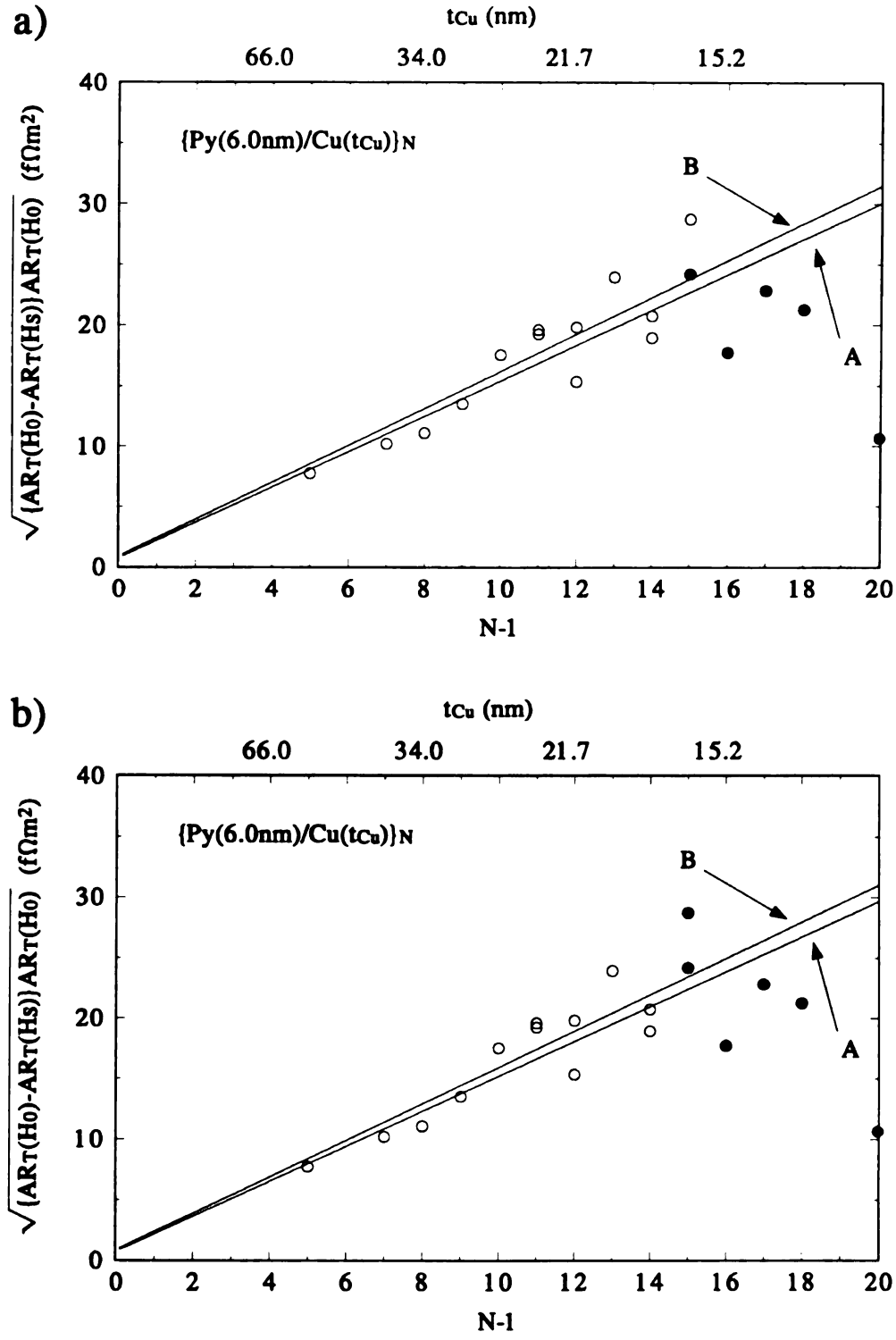

Figure 5.18: The square root data plotted as a function the reduced bilayer number, N-1 for the *Py(5.0nm)[Py(1.5nm)/Cu(t_{Cu})]×N*. Total sample thickness is held constant at 360nm. Fits A and B in a) use Set 1 parameters listed in Tables 5.10 and 5.11, while Fits A and B in b) use Set 2 parameters from Tables 5.10 and 5.11. Points with filled symbols were not used in fits.

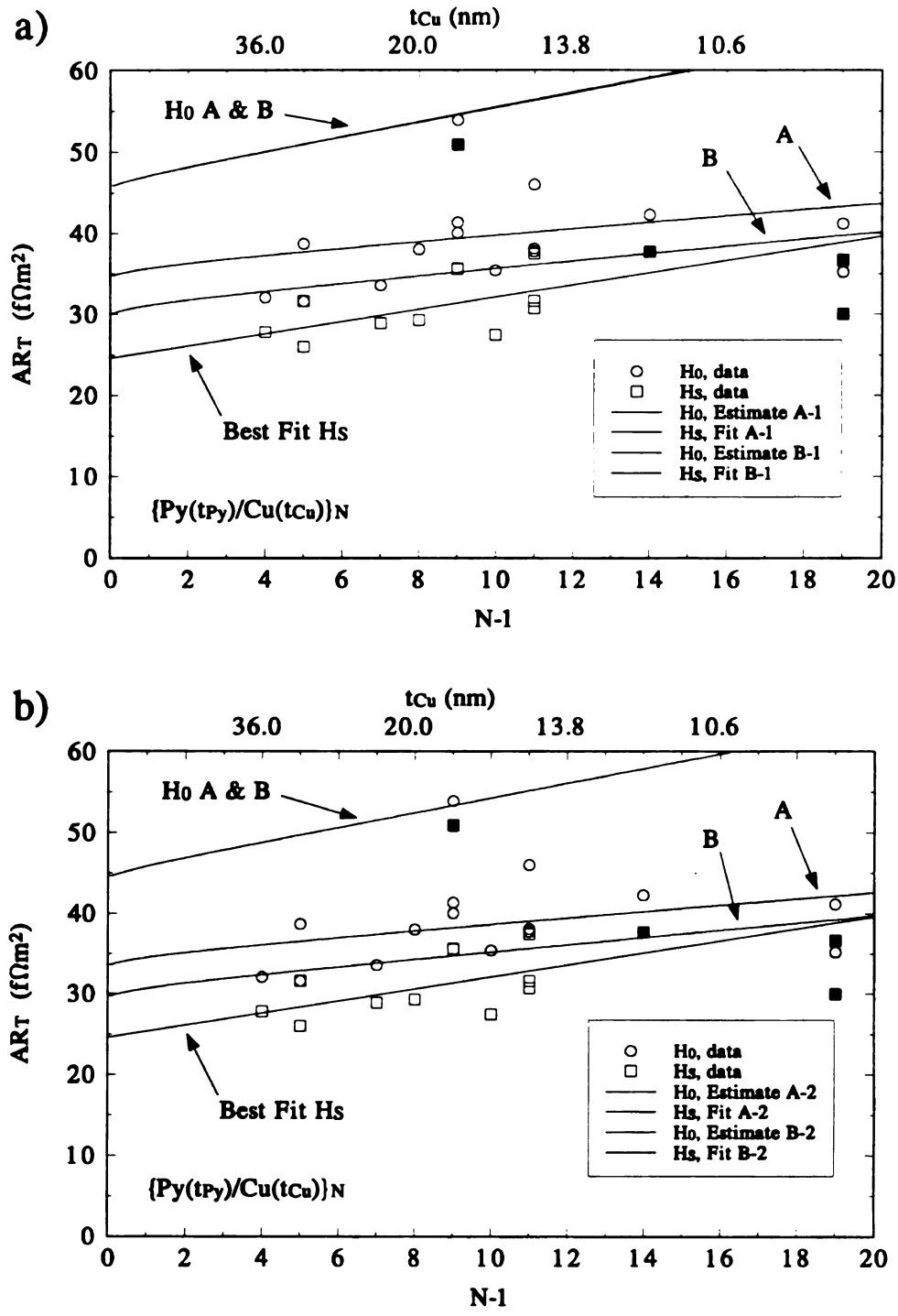

Figure 5.19: $AR_T(H_0)$ and $AR_T(H_S)$ plotted as a function of the corrected bilayer number, N-1 for the $[Py(t_{Py}=t_{Cu})/Cu(t_{Cu})]\times N$. Total sample thickness is held constant at 360nm. Fits A and B in a) use Set 1 parameters listed in Tables 5.10 and 5.11, while Fits A and B in b) use Set 2 parameters from Tables 5.10 and 5.11. The Best Fit H_S line is a least squares fit to the H_S data. Points with filled symbols were not used in fits. H_0 data was not used in either fit.

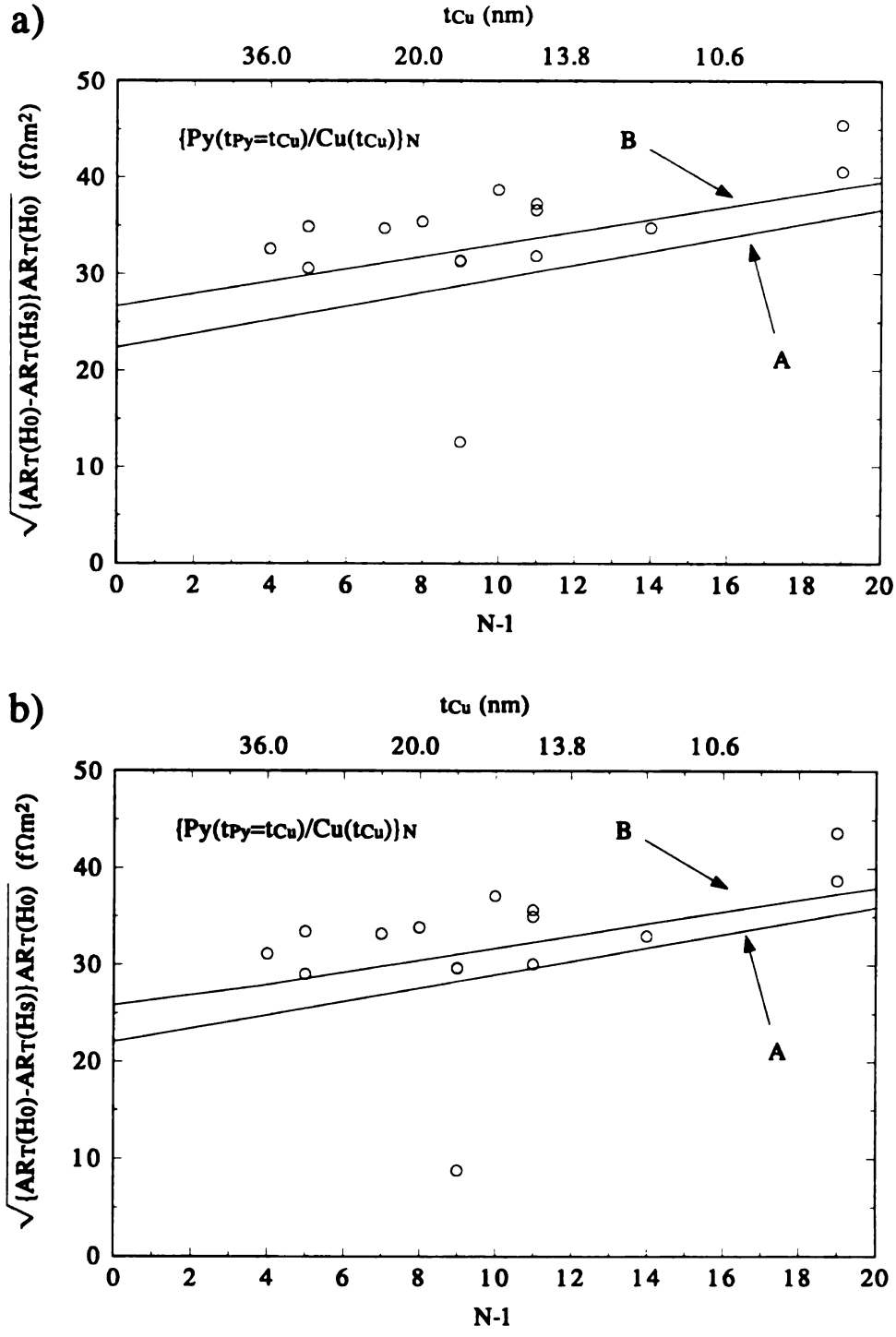

Figure 5.20: The square root data plotted as a function of the corrected bilayer number, N-1 for the $[Py(t_{Py}=t_{Cu})/Cu(t_{Cu})]\times N$. Total sample thickness is held constant at 360nm. Fits A and B in a) use Set 1 parameters listed in Tables 5.10 and 5.11, while Fits A and B in b) use Set 2 parameters from Tables 5.10 and 5.11. The Best Fit H_S line is a least squares fit to the H_S data. H_0 data was not used in either fit.

To choose the best set of parameters from those in presented Tables 5.10 and 5.11 a comparison with independently measured values of the permalloy resistivity is necessary. Table 5.12 lists the resistivities of Py films 100-300nm thick, made in several runs along with the CPP samples. Some of the films were masked to provide a set four terminal geometry from sample to sample, others were measured using the Van der Pauw technique described in chapter 3. An average value for the Py resistivity was obtained by weighting each measurement of ρ_{Py} by the associated uncertainty in its geometry, typically ±5%. This gave $\rho_{Py} = 137 \pm 9$ nΩm. However, the uncertainty in ρ_{Py} did not reflect the amount of scatter in the resistivity measurements which resulted in a reduced χ^2 of 14.3. Adjusting the ρ_{Py} uncertainties to bring the reduced χ^2 to 1.0 gave the value listed in Tables 5.10 and 5.11, $\rho_{Py} = 137 \pm 35$ nΩm which reflects the range of Py resistivites that were mearsured.

The parameters from Fit A-2 come the closest to the independently determined value for ρ_{Py} at 140±22nΩm. Fit A-1 gives a value for ρ_{Py} slighly higher than the independently determined value, but well within the uncertainties. Both sets of parameters from Fit B are somewhat low when compared to the 137nΩm value but the uncertainty of each overlaps with the independent measurement.

As previously mentioned a partial analysis of the Py/Cu data have been published elsewhere[6,7]. The analysis found in Ref. 6 represents our initial estimates for β and γ (or α_{Py} and $\alpha_{Py/Cu}$). At the time of these estimates only samples with t_{Py}=*1.5nm* and *6.0nm* were being examined. The parameters given in Ref. 7 are also results of an analysis done

only on samples with t_{Py}=*1.5nm* and *6.0nm*. While this analysis uses the same t_{Py}=*1.5nm* data, about one third of the t_{Py}=*6.0nm* samples used in Fits A and B were made after this analysis was done.

Table 5.12: Py resistivity measurements on films made along with CPP samples in several runs.

Sample #	M/V[a]	t_{Py} (nm)	ρ (nΩm)	±δρ (nΩm)
431-01	M	950±3	142	5
431-04	M	900±6	123	8
431-06	M	900±12	120	16
431-07	M	109± 6	148	8
438-06	M	84±1	133	2
438-07	M	85±3	113	4
438-08	M	94±3	151	24
438-09	M	114±18	177	5
569-06	V	244± 25	107	11
570-09	V	298±12	126	5
571-10	V	280±16	115	7
605-10	V	324±3	144	2
613-07	V	277±20	102	7

a M signifies a masked film and V signifies Van der Pauw measurement.

Comparison with Co/Cu Multilayers

Based on resistivity measurements of impurity scattering in dilute ferromagnetic alloys done by Campbell and Fert[1], one might expect that permalloy would have a larger α than Co. CPP-MR measurements done on Co/Cu multilayers in section 5.1 and Py/Cu multilayers in section 5.2 show that this expectation is justified. The value of α_{Co} given in Table 5.6 is lower than the α_{Py} values given in Tables 5.10 and 5.11. At the extreme of their uncertainties the Fit A value for α_{Py}=3.7±0.3 does not quite overlap with α_{Co}=2.7±0.3, while the Fit B value of α_{Py}=5.3±0.4 is well above α_{Co}. The interface parameters are less clear. The value of $\alpha_{Co/Cu}$=7.7±1.3 lies between the Fit A value for $\alpha_{Py/Cu}$=8.7±0.7 and the Fit B value for $\alpha_{Py/Cu}$=6.0±0.4. However, in comparing the ratio of the contributions to the spin dependent scattering from the bulk F metal to that from the F/N interface, one finds that the ratio of interface to bulk is larger for Co/Cu. Values in Table 5.6 give $\alpha_{Co/Cu}/\alpha_{Co}$=2.9 whereas $\alpha_{Py/Cu}/\alpha_{Py}$ is 2.4 for Fit A and 1.1 for Fit B, both smaller than the Co ratio.

The resistivity of the Py is more than double that of the Co. This is expected since the sputtered Py layers are most likely forming a disordered random alloy of Ni and Fe with concentrations similar to the sputtering target. However, somewhat surprisingly the interface resistances of Co/Cu, $AR_{Co/Cu}$, and Py/Cu, $AR_{Py/Cu}$, are quite similar. One might expect the Co/Cu interface resistance to be higher since Co prefers the hcp structure, while Cu and Py both prefer fcc. However, NMR studies[8] on Co/Cu multilayers show

that the Co is fcc for Co layers less than 3.0nm thick, therefore the Co/Cu interfaces are probably similar structurally to the Py/Cu interfaces.

---

[1] I.A. Campbell and A. Fert, in *Ferromagnetic Materials*, edited by E.P. Wohlfarth, (North Holland, Amsterdam, 1982), Vol. **3**, p.769.

[2] XTEM pictures show good layering throughout the sample thickness, however, beyond 100nm the layers begin undulating. P. Galtier, T. Valet, O. Durand, J.C. Jacquet and J.P. Chevalier, Mat. Res. Soc. Symp. Proc., Vol. **313**, p. 47 (1993).

[3] R.D.K. Misra, T. Ha, Y. Kadmon, C.J. Powell, M.D. Stiles, R.D. McMichaels and W.F. Egelhoff Jr., in *Magnetic Ultrathin Films: Multilayers and Surfaces*, edited by E.E. Marinero, B. Heinrich, W.F. Egelhoff Jr., A. Fert, H. Fujimori, G. Guntherodt and R.L. White, MRS Symposium Proceedings Vol. **384**, Material Research Society, Pittsburgh, PA., p.373 (1995).

[4] S.S. P. Parkin, Appl. Phys. Lett. **60**, 517 (1992).

[5] P.A. Schroeder, S.F. Lee, P. Holody, R. Loloee, Q. Yang, W.P. Pratt, Jr. and J. Bass, J. Appl. Phys., **76**, 6610 (1994).

[6] P.A. Schroeder, J. Bass, P. Holody, S.F. Lee, R. Loloee, W.P. Pratt Jr. and Q. Yang, Mat. Res. Soc. Symp. Proc. Vol. **313**, 47 (1993).

[7] Q. Yang, P. Holody, R. Loloee, L.L. Henry, W.P. Pratt Jr., P.A. Schroeder and J. Bass, Phys. Rev. **B51**, 3226 (1995); J. Bass, P.A. Schroeder, W.P. Pratt Jr., S.F. Lee, Q. Yang, P. Holody, L.L. Henry, R. Loloee, Mater. Sci. Eng. **B31**, 77 (1995).

[8] C. Meny, P. Panissod and R. Loloee, Phys. Rev. **B45**, 12269 (1992).

Chapter 6:

Complex Magnetic Multilayers

This chapter will focus on multilayer systems that are more difficult to analyze. First, Co/CuX multilayers, where CuX is a Cu based alloy, will be seen to exhibit finite spin diffusion length effects in CPP-MR. Second, a system that uses two F-metals, Co and Py, will show how GMR can be attained without relying on strong AF-coupling. The last part will investigate attempts at producing a reversed GMR, one in which the AP state corresponds with the sample's lowest resistance.

6.1 Finite Spin Diffusion Length Effects in Multilayers of Co and Cu Alloys.

To better understand the transport properties of magnetic multilayers, it is necessary to see how different types of scattering effect the resistance of a sample. In chapter 5 the resistance of Co/Cu and Py/Cu multilayers was successfully described by a simple two channel model. In this model, the electrons are divided into two parallel spin channels,

for each of which the resistances are summed in series. Inherent in this model is the assumption that each spin channel carries current independently and therefore an electron in the spin up channel will not flip spin and join the spin down channel along the way. Spin flip events are enhanced by spin-orbit scattering from impurities, exchange scattering by paramagnetic impurities and by electron-magnon scattering. Spin flips may be characterized by two different length scales, ℓ_{sf}, the spin diffusion length and l_{sm}, the spin mixing length. The spin diffusion length is the distance an electron travels before flipping its spin, without transfer of momentum. The spin mixing length is the distance the electrons travel before the two spin currents are mixed by scattering that simultaneously flips an electron's spin and transfers momentum. The effects of electron-magnon scattering producing spin flips may be neglected for measurements made at 4.2K. Electron Spin Resonance (ESR) measurements[1] of the spin flip cross section attributed to intrinsic defects in Cu indicate that the infinite spin diffusion length assumed in the two channel model analysis of the Co/Cu multilayers of chapter 5 was justified.

The Valet-Fert[2] theory described in chapter 4 predicts measurable deviations from the linearity of $\sqrt{AR(H_0)[AR(H_0)-AR(H_S)]}$ and *N-1*, as the spin diffusion length (SDL) approaches the layer thickness. This theory showed that a Boltzmann equation model reduces to macroscopic transport equations for spin diffusion lengths much longer than the mean free path of the conduction electrons. Equations 4.8-4.11 are the Valet-Fert results for the two channel model when finite SDL effects are taken into account for both the F and N metals.

A systematic study of SDL effects in magnetic multilayers of the form Co/CuX where X=Pt, Mn, Ni or Ge was begun. Each Co/CuX series was characterized by both high and low angle diffraction. As was shown in chapter 3, these spectra revealed no change in the lattice structure of the multilayer with the additions of each impurity. One difference between the original Co/Cu series and each Co/CuX series exhibited here is the addition of an extra "capping" layer of Co before the top Nb lead is deposited. This modification to the multilayer structure now leaves a Co layer next to each Nb lead. The ferromagnetic Co layers are intended to suppress the superconducting proximity effect in the multilayers thus eliminating possible complications concerning whether or not the CuX layer next to the Nb will become superconducting. To examine the sample variability from sputtering run to sputtering run, two $[Co(6.0nm)/Cu(t_{Cu})]\times N$ samples with $t_{Cu}=9.0$ and $30.0nm$ ($N=20$ and 48) were sputtered along with the Co/CuX samples. These Co/Cu samples were fabricated before the CuX source was turned on preventing possible contamination by the CuX gun.

Co/CuPt(6%) Samples

Introducing a small amount of Pt into the Cu layers of the multilayer should considerably shorten the SDL of the normal metal layer by providing an impurity with strong spin-orbit scattering[3]. A dilute alloy containing 6 at.% Pt was chosen as a compromise between substantial altering of the normal metal properties and being able to reliably measure an effect. Multilayers of $[Co(6.0nm)/CuPt(t_{CuPt})]\times N$ were made for

comparison with the *[Co(6.0nm)/Cu(t_{Cu})]×N* series previously made for the Co/Cu study in chapter 5. The total sample thickness of the CuPt samples was held constant at 720nm. To avoid complications with the alloy modifying the coupling between magnetic layers[4], only samples with $t_{CuPt} \geq 6.0nm$ were made. The data for the Co/CuPt(6%) series is given in Table 6.1.

Table 6.1: CPP values at H_0, H_P and H_S for the *[Co(6.0nm)/CuPt(t_{CuPt})]×N* series. The total sample thickness is 720nm.

Sample #	t_{Cu} nm	N	Area mm^2	CPP-AR(H) fΩ-m^2		
				H_0	H_P	H_S
490^{02}	600	11	1.233	115.34	115.34	115.27
484^{04}	300	20	1.381	124.92	124.92	124.26
490^{03}	300	20	1.284	128.90	128.81	128.24
490^{07}	300	20	1.380	118.89	118.81	118.20
508^{07}	300	20	1.234	108.08	108.03	107.69
484^{08}	180	30	1.253	120.35	120.23	118.53
484^{03}	90	48	1.591	147.07	145.52	138.03
490^{06}	90	48	1.260	128.02	123.52	118.17
508^{05}	90	48	1.305	114.30	114.30	109.25
484^{02}	60	60	1.432	160.46	147.50	138.62

Co/CuMn(7%) Samples

A second series of multilayers that had a shortened SDL was made by alloying Cu and Mn. For Mn the spin-orbit relaxation is small[3] and can be neglected so that the primary source of spin flip scattering at low temperatures is attributed to an exchange scattering which does not directly relax the spin accumulation to the lattice but transfers it to the paramagnetic impurity system[5] which then relaxes to the lattice. This leads to an exchange scattering relaxation term in addition to the spin-orbit contribution. A series of samples doped with 7 at.% Mn in Cu was made similarly to the aforementioned Co/Cu series. The resistances of the *[Co(6.0nm)/CuMn(t_{CuMn})]×N* series are given in Table 6.2, the total thickness was held at 720nm.

Table 6.2: CPP values at H_0, H_P and H_S for the *[Co(6.0nm)/CuMn(t_{CuMn})]×N* series. The total sample thickness is 720nm.

Sample #	t_{Cu} nm	N	Area mm^2	CPP-AR(H) fΩ-m^2		
				H_0	H_P	H_S
478^{07}	600	11	1.251	199.43	199.43	199.41
478^{03}	300	20	1.204	196.17	196.19	196.17
479^{02}	180	30	1.305	217.38	217.36	217.33
479^{03}	120	40	1.423	186.95	186.79	186.42
478^{02}	90	48	1.366	185.79	185.32	184.76
478^{04}	60	60	1.326	177.28	174.35	172.01

The data for the above three systems Co/CuPt, Co/CuMn and Co/Cu are shown in Figure 6.1. The Co/Cu samples made during the Co/CuX runs have the additional Co "capping" layer and are denoted by the open circles in Figures 6.1, 6.3 and 6.4. These newer Co/Cu agree, generally within the scatter of the data, with the Co/Cu samples studied previously. Large departures from linearity similar to those predicted by Fert and Valet are seen for the Co/CuPt and Co/CuMn samples. One further step is necessary to confirm these departures are indeed explained by the Valet-Fert theory.

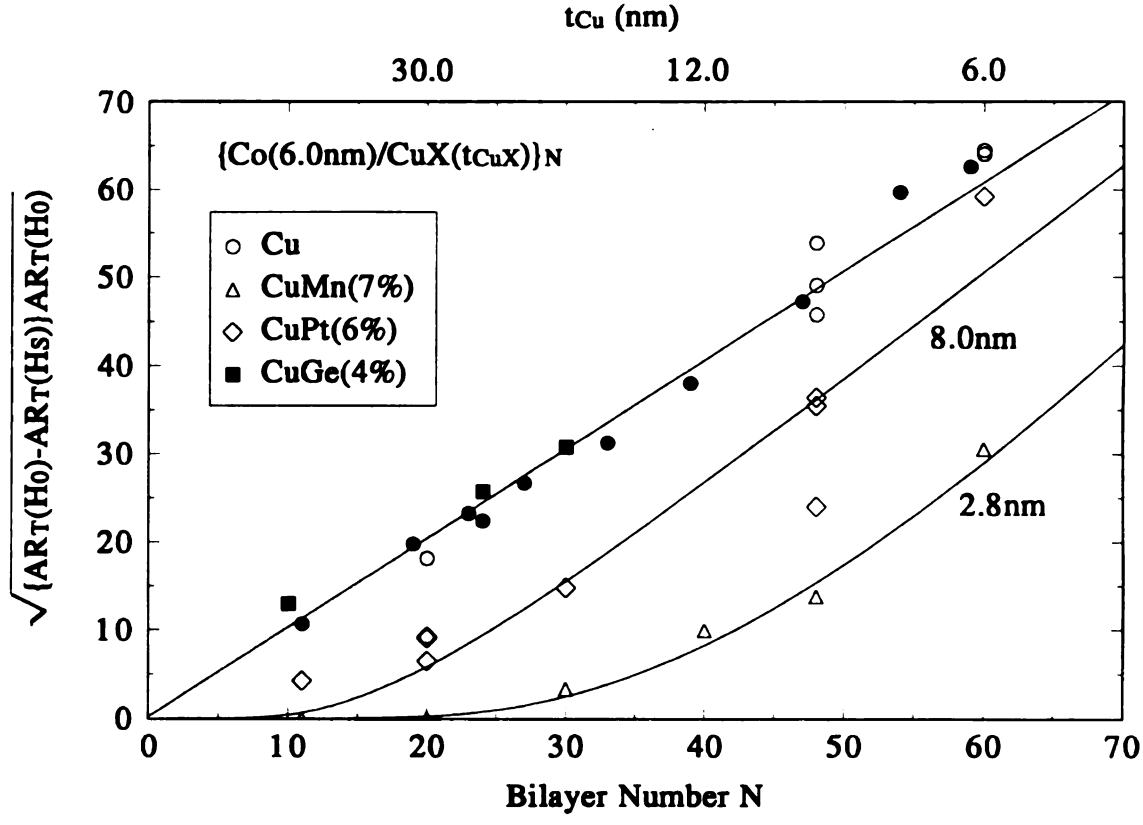

Figure 6.1: Plotted are both the measured and predicted values using the Valet-Fert theory for the quantity $\sqrt{AR(H_0)[AR(H_0)-AR(H_S)]}$ as a function of N, the bilayer number. The Valet-Fert predictions use $\ell_{sf}^{Co}=\infty$ and $\ell_{sf}^{CuX}=2.8\text{nm}$, 8.0nm and ∞ with the appropriate ρ_{CuX}, given in Table 6.4. The Co/CuGe samples have a total thickness 360nm, while all other samples are 720nm thick. The filled symbols have different CuX thickness than those indicated on the top axis.

The normal metal resistivity does not enter explicitly into equation 4.4 reproduced here with corrections for the extra Co layer.

$$\sqrt{AR(H_0)[AR(H_0)-AR(H_S)]} = N[\beta\rho^{*}_{Co}t_{Co}+\gamma 2AR^{*}_{Co/Cu}]+\beta\rho^{*}_{Co}t_{Co}$$

Even so, the resistivity of the CuPt(6%) and CuMn(7%) is substantially higher than for Cu, more than a factor of 20. To test whether the departures from linearity are caused by the shortening of the SDL or the increase in the resistivity (which depends upon the elastic mfp) a third series of Co/CuGe multilayers was made. An alloy of 4 at.% Ge in Cu has roughly 20 times the resistivity of Cu but has a very small spin flip cross section[3] and therefore a large SDL≈61nm. If the Co/CuGe samples behave like the Co/Cu data then it is the shortening of the SDL by the Pt and Mn impurities that cause the deviation from equation 4.4. Significant departures of the Co/CuGe data from the Co/Cu data would have indicated that elastic mfp effects play a more fundamental role in CPP electron transport than was previously thought. The resistances of the *[Co(6.0nm)/CuGe(t_{CuGe})]×N* series are given in Table 6.3, the total sample thickness is only 360nm because the CuGe(4%) sputtering target was thin. The results plotted in Figure 6.1 for the Co/CuGe(4%) samples clearly indicate that the direct effect of increased resistivity can only be a very minor effect.

Table 6.3: CPP values at H_0, H_P and H_S for the *[Co(6.0nm)/CuGe(t_{CuGe})]×N* series. The total sample thickness is 360nm.

Sample #	t_{Cu} nm	N	Area mm^2	CPP-AR(H) fΩ-m^2		
				H_0	H_P	H_S
445^{02}	300	10	1.313	82.70	80.98	80.67
445^{06}	60	30	1.271	87.39	81.66	76.56
445^{03}	90	24	1.227	94.15	90.79	87.11

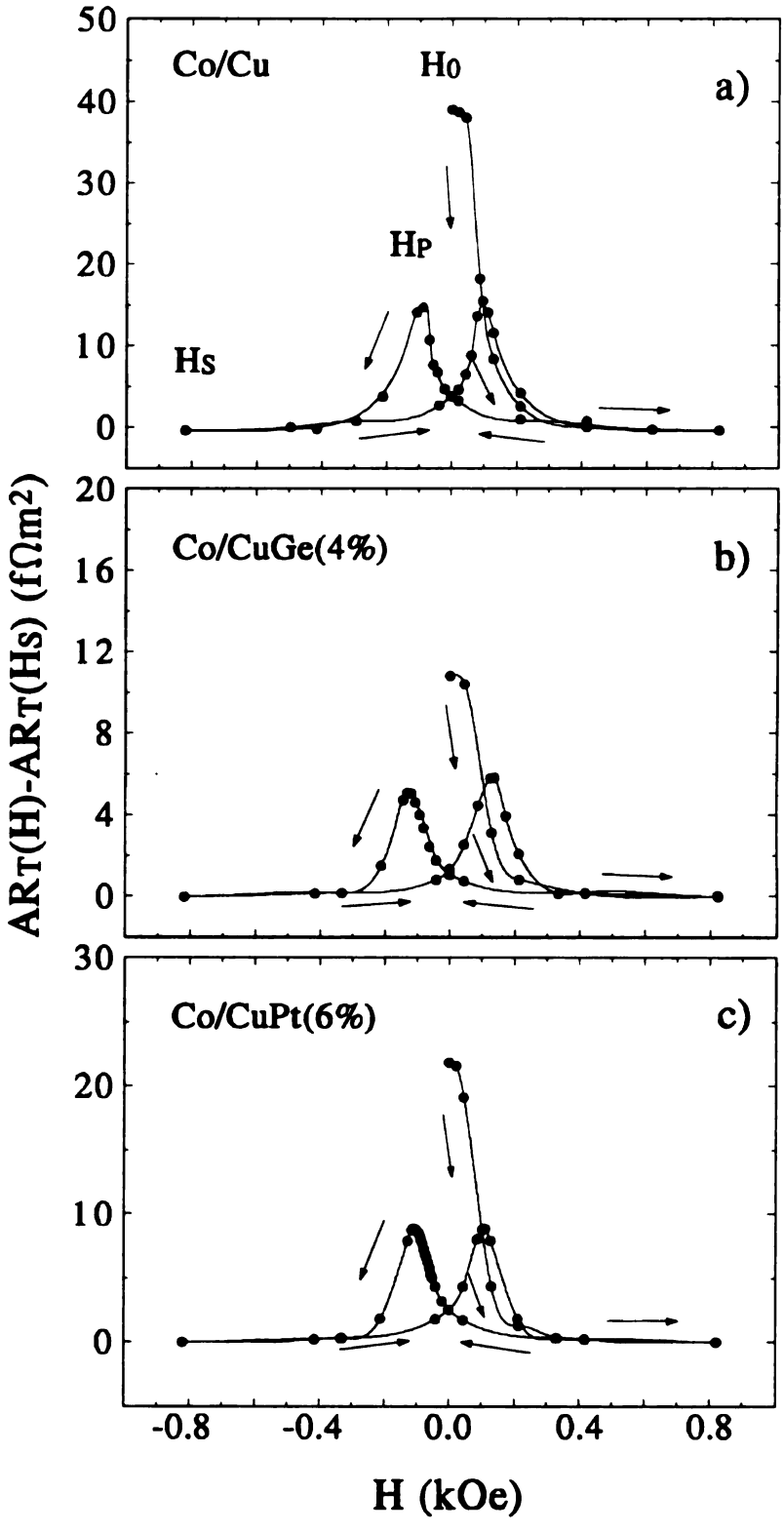

Figure 6.2: A comparison of $AR_T(H)$-$AR_T(H_S)$ versus H for samples with the same nominal bilayer thickness a) *[Co(6.0nm)/Cu(9.0nm)]×48*, b) *[Co(6.0nm)/CuGe(9.0nm)]×24* and c) *[Co(6.0nm)/CuPt(9.0nm)]×48*. The lines are guides to the eye.

Before finally comparing the data with the Valet-Fert theory, we consider evidence that no major changes occur in the coupling of the system. If the coupling between Co layers remains weak with the addition of impurities into the Cu spacer layer, then a similar field dependence of AR_T should be seen for samples of Co/CuX and Co/Cu with the same spacer thickness. Figure 6.2 shows the field dependence of $AR_T(H)$-$AR_T(H_S)$ for similar multilayers of Co/Cu, Co/CuGe(4%) and Co/CuPt(6%). All three multilayers in Figure 6.2 exhibit similar field dependent behavior. The as-deposited H_0 resistance has the largest value for each sample. Each sample saturates well before 1.0 kOe. The H_P resistance of each also occurs at approximately the same field, near the coercive field. The magnitudes of $AR_T(H)$-$AR_T(H_S)$ are also quite similar for each multilayer in Figure 6.2. (To correctly compare the magnitude of $AR_T(H)$-$AR_T(H_S)$ for the Co/CuGe(4%) sample to first order, the difference must be doubled since the total thickness of the CuGe(4%) samples is half that of the other series.) The similarities in forms and magnitudes of the samples shown in Figure 6.2a, 6.2b and 6.2c allows one to conclude that introducing Pt and Ge impurities into the Cu spacer layer does not modify the coupling between Co layers such that these multilayers are no longer considered uncoupled. As a further check, the ratio Π (defined by equation 5.5) is calculated for each Co/CuX sample and plotted in Figure 6.3. The values for Π fluctuate about 1.7 for every series except Co/CuPt(6%). This suggests that the impurities also do not greatly modify the relationship between $AR_T(H_0)$ and $AR_T(H_P)$. The Π values for a majority of the Co/CuPt(6%) data are closer to 1.2. Although this signifies a smaller difference

between the H_0 and H_P resistances, the H_0 resistance is still the largest and therefore should be used for the AP state[6].

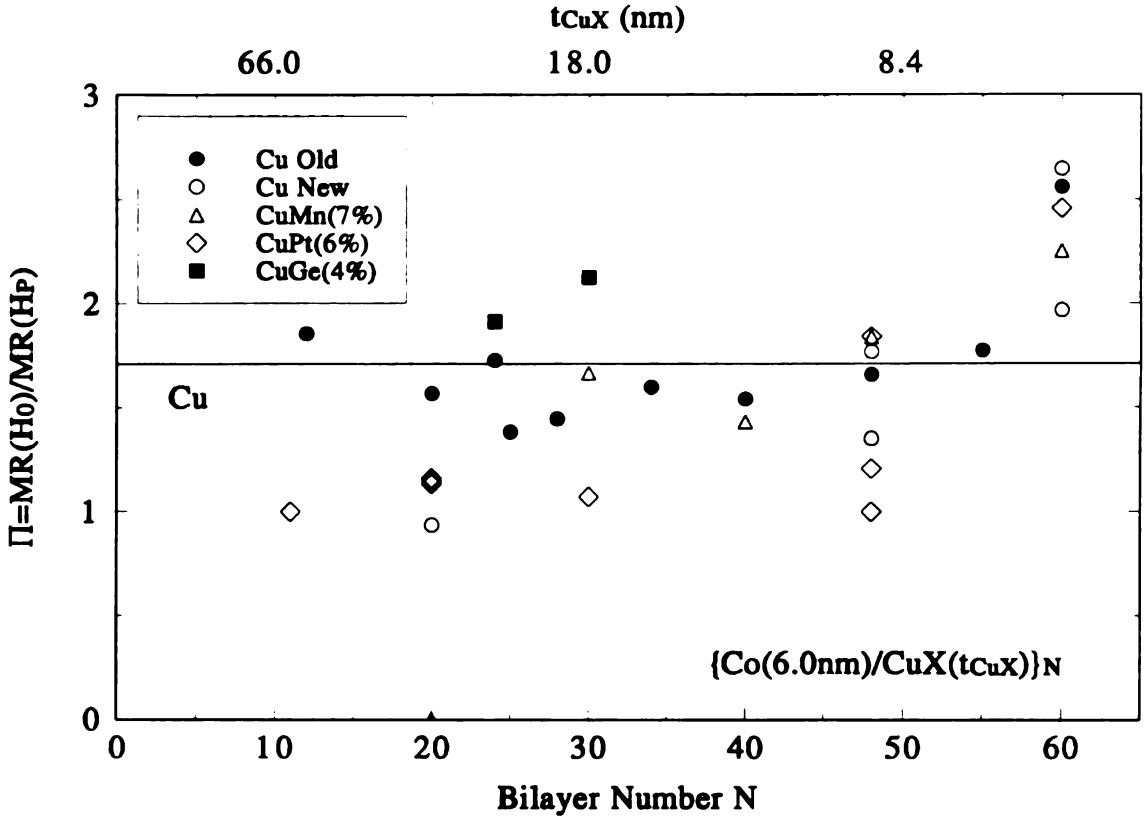

Figure 6.3: Plotted are Π ratios as a function of the N, the bilayer number for Co/Cu, Co/CuMn, Co/CuPt and Co/CuGe samples with t_{Co}=*6.0nm*. The filled symbols have t_{CuX} different from those indicated on the top axis. The solid line represents the average Π ratio for the Co/Cu series.

Comparison with Valet-Fert Theory

For the constant 6.0nm Co data, a straight line through the origin is expected for normal metals with SDL much larger than the layer thickness. This behavior was

observed for the constant Co series shown in Figures 5.3b and 5.4b of chapter 5. Deviations from this behavior are attributed to spin flips in the normal metal layer. The largest deviations are observed for the Co/CuMn(7%) data. The Co/CuPt(6%) data show a smaller but still measurable effect. The three Co/CuGe(4%) samples are well within the scatter of the Co/Cu series and therefore must have a long SDL.

The data of each Co/CuX series were fitted to the Valet-Fert equations (4.8-4.11) assuming $\ell_{sf}^{Co} = \infty$ and using ℓ_{sf}^{N} as a fitting parameter. These fits used the same parameters derived from the analysis of the three Co/Cu series examined in the previous chapter. The only exception was that ρ_{Cu} was replaced by measured values of ρ_{CuX} made on 300nm CuX films fabricated in each sputtering run with the CPP multilayers. Table 6.4 lists the parameters used in the analysis along with independent estimates of ℓ_{sf}^{N}.

Table 6.4: Estimated parameters for Cu alloys.

Metal or Alloy[a]	ρ_N^c (nΩm)[b]	ρ_N^m (nΩm)[c]	λ_{el}^N (nm)[d]	λ_{sf}^N (nm)[e]	ℓ_{sf}^N (nm) (nm)[f]
Cu	---	5.5±1	110	11000	450
CuMn(7%)	310	270±30	2.1	24(6)	3(1.5)
CuPt(6%)	120	130±10	5.5	50	7
CuGe(4%)	162	182±20	4.0	5700	61
CuNi(14%)	185	180±30	3.5	250	12
CuNi(6%)	85	88±15	7.7	580	27

[a] Impurity concentrations in atomic %.
[b] Calculated from intended impurity concentrations and known resistivities per atomic % impurity[7].
[c] Measured on sputtered films 300-500nm thick. Uncertainties are the largest deviations from the average values.
[d] Calculated from ρ_N^c (ρ_N^m for Cu) and free electron equations[8].
[e] The sputtered Cu value assumes a defect content of ≈1% and a spin-orbit cross section of 1×10^{-18} cm^2. The CuPt value was calculated from a free electron conversion of ESR

cross sections[3,8]. The CuMn value was estimated by Fert[5] from available information about exchange coupling in this alloy, parenthetical value was calculated from a cross section measured by Starr, *et al.*[9] using weak localization.

[f] Calculated using equation, 4.17 $\ell_{sf}^{N} = \sqrt{(\lambda_{sf}^{N}\lambda_{el}^{N})/6}$ also given in[2,5,10].

The data support the estimates for ℓ_{sf}^{N} given Table 6.4. The CuMn(7%) and CuPt(6%) data both clearly lie below the straight line representing $\ell_{sf}^{N}=\infty$ in Figure 6.1, with the CuMn(7%) showing the bigger effect. The best fit curve through the CuMn(7%) data yields $\ell_{sf}^{CuMn} = 2.8$nm, in good agreement with the estimate of 3.0nm listed in Table 6.4. The best fit curve through the CuPt(6%) data gives $\ell_{sf}^{CuPt} = 8.0$nm close to the calculated value of 7.0nm.

Because both the Co/CuGe(4%) and Co/Cu data lie near the infinite SDL line (Figure 6.1), one can eliminate the differences in the elastic mfp as the cause of the reduction in CPP-MR. The reduction in the CPP-MR for the CuMn(7%) and CuPt(6%) multilayers must arise from something other than the reduced elastic mfp. The CuGe(4%) samples also show that changing the total thickness of the multilayer by half does not have a measurable effect.

Co/CuNi(14%) Samples

The possibility of spin flip scattering at the interfaces of Py/Cu multilayers has been mentioned in several papers[11,12] on GMR in these samples. This could profoundly affect the applicability of the $\ell_{sf} = \infty$ Valet-Fert theory. To investigate this possibility, in Py/Cu multilayers a series of Co/CuNi(14%) samples was measured. The magnetic properties of CuNi alloys are well documented[13]. Cu has a filled *3d* band and a half filled *4s* conduction band, while Ni has vacancies in both the *3d* and *4s* bands. The unpaired spins in the *3d* band are responsible for ferromagnetism in Ni. Since Cu and Ni form a solid solution over the entire concentration range, it is possible to make alloys of any concentration. As Cu is added to Ni, it is energetically favorable for the *4s* Cu electrons to fill in the *3d* Ni band. Adding the proper amount of Cu will kill the ferromagnetism of the CuNi alloy. This happens at 60 at.% Cu concentrations. With higher Cu content the alloy becomes a Pauli paramagnet. Unlike Mn in Cu, the Ni atoms do not form magnetic ions with the Cu host. The absence of a local magnetic moment should rule out spin flip scattering via the exchange interaction with paramagnetic impurities, leaving spin orbit coupling as the mechanism for reducing the SDL.

A series of $[Co(6.0nm)/CuNi(t_{CuNi})]\times N$ samples with total thickness 720nm was measured at 4.2K and compared with similar Co/Cu samples described earlier. A 14 at.% Ni concentration was chosen so that the resistivity of the alloy would be similar to the other Cu based alloys in Table 6.4. The data are listed in Table 6.5 and plotted in Figure

6.4 with $\sqrt{AR(H_0)[AR(H_0)-AR(H_S)]}$ as a function of N, the bilayer number, for both Co/Cu and Co/CuNi(14%).

Table 6.5: CPP values at H_0, H_P, H_S and H_D for the *[Co(6.0nm)/CuNi(t_{CuNi})]×N* series. The total sample thickness is 720nm.

Sample #	t_{Cu} nm	N	Area mm^2	CPP-AR(H) fΩ-m^2			
				H_0	H_P	H_S	H_D
637[05]	60.0	11	1.208	122.80	122.79	122.76	
633[03]	30.0	20	1.190	128.98	128.66	128.17	128.78
637[04]	30.0	20	1.205	118.56	118.27	117.81	118.37
644[06]	30.0	20	1.309	98.46	97.86	96.87	98.04
644[03]	18.0	30	1.272	104.04	101.90	98.34	102.55
644[04]	12.0	40	1.259	108.30	104.32	98.77	105.62
633[02]	9.0	48	1.153	136.12	130.74	124.60	132.19
637[03]	9.0	48	1.187	144.07	139.22	132.46	140.02
644[05]	9.0	48	1.339	117.64	111.98	103.74	113.92
633[04]	6.0	60	1.201	134.99	124.90	116.23	126.81

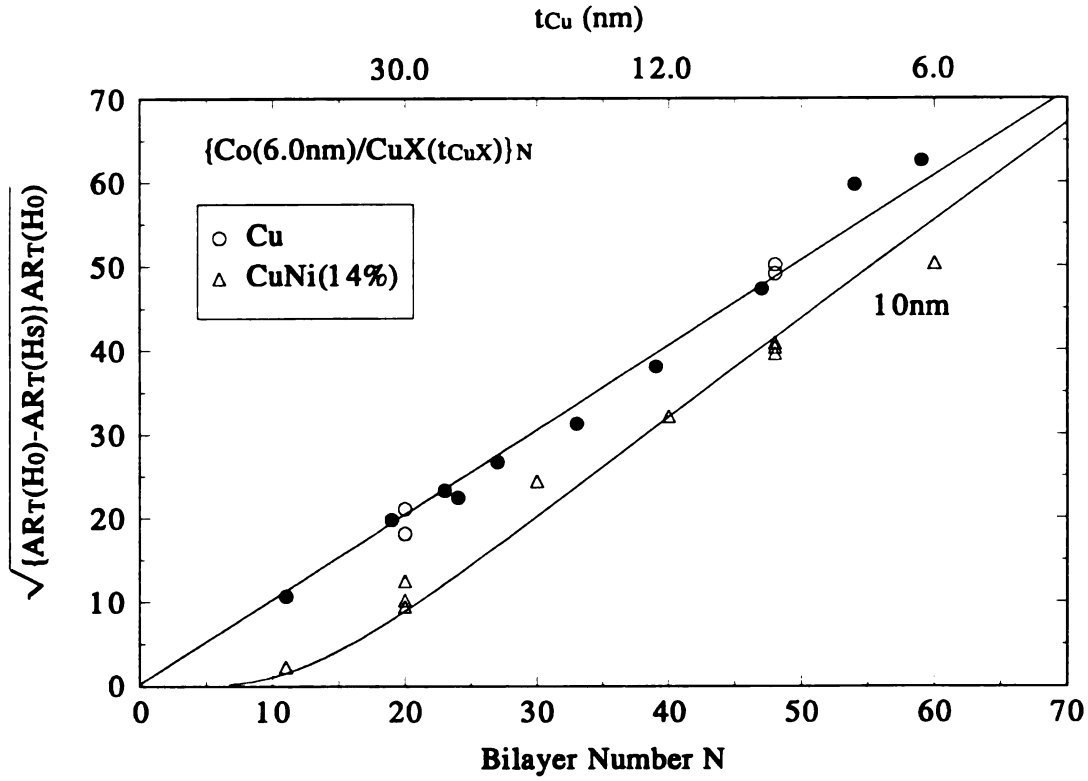

Figure 6.4: Plotted are both the measured and predicted values using the Valet-Fert theory for the quantity $\sqrt{AR(H_0)[AR(H_0)-AR(H_S)]}$ as a function of N, the bilayer number. The Valet-Fert predictions use $\ell_{sf}^{Co}=\infty$ and $\ell_{sf}^{CuX}=10\text{nm}$ and ∞ with the appropriate ρ_{CuX}, given in Table 6.4. The total thickness of multilayers from both series is 720nm. The filled symbols have different Cu thickness than those indicated on the top axis.

In Figure 6.4, the Co/CuNi(14%) samples clearly fall below the line representing infinite SDL, therefore the spin diffusion length is shortened by the addition of Ni to the Cu spacer layer. The open symbols in Figure 6.4 are Co/Cu samples made prior to the

Co/CuNi(14%) samples in the same sputtering run. The field dependence of the Co/CuNi(14%) samples was similar to those shown in Figure 6.2 in both form and magnitude, so any modification in the coupling between Co layers by the Ni impurities is small[4,14]. The ratio Π is plotted as a function of N in Figure 6.5. Both sets of data are evenly scattered about 1.7 over the whole bilayer range, indicating that the relationship between the H_0 and H_P resistances is the same for each series.

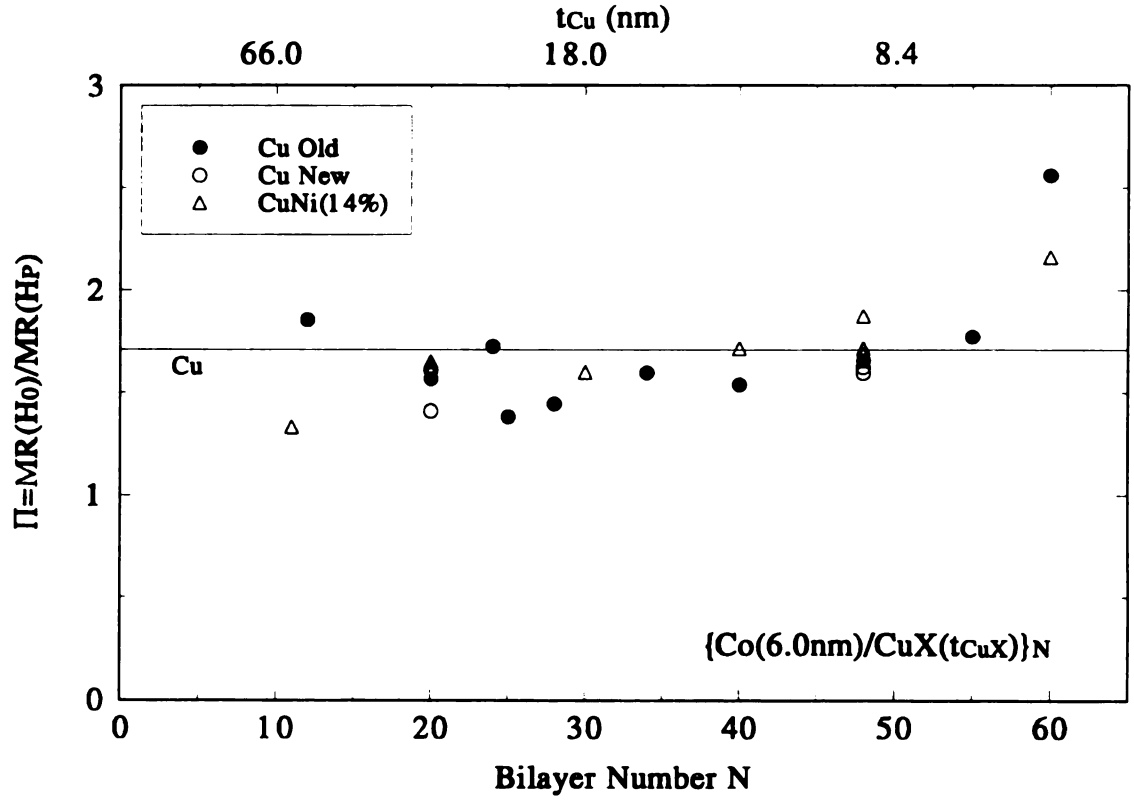

Figure 6.5: Plotted are Π ratios as a function of the N, the bilayer number for Co/Cu and Co/CuNi samples with t_{Co}=*6.0nm*. The filled symbols have t_{Cu} different from those indicated on the top axis. The solid line represents the average Π ratio for the Co/Cu series.

Spin orbit scattering is suspected as the mechanism for flipping spins for two reasons. First, the CuNi(14%) data are consistent with the Valet-Fert model using $\ell_{sf}^{CuNi} = 10\text{nm}$, close to the predicted value in Table 6.4 based on the spin orbit cross section of Ni. Second, comparing the CuNi(14%) data with the CuPt(6%) data reveals that the Pt impurities are much better at spin flip scattering than are the Ni impurities. The Ni concentration is more than double the Pt concentration, and yet has a longer spin diffusion length. This is consistent with ESR data[3] which show that *3d* transition metals, such as Ni, are much less efficient at spin orbit scattering than are *5d* metals, like Pt. Furthermore, preliminary results for similar experiments on Co/CuNi samples currently carried out at MSU by S.Y. Hsu[15], in which the Ni concentrations are varied from 5% to 20%, show that the measured SDL for each Ni concentration agrees with calculated values of the SDL based on spin orbit scattering.

Another possible mechanism for spin flip scattering in Co/CuNi is the formation of tiny Ni clusters in the Cu layer which possess a local magnetic moment. Electrons scattering off these clusters would likely undergo spin flips, reducing the SDL of the material. The possibility of Ni cluster formation in Cu is unlikely because Cu and Ni form a solid solution at all concentrations. Also, the CuNi layers are sputtered from a homogeneous target of CuNi(14%) at rates of 1.0nm/s, presumably forming a random alloy. Magnetic measurements on 300nm films of CuNi(14%) showed no evidence of magnetic clusters forming in the film.

Reconsideration of the Co/Cu Data

The scatter in the Co/Cu data presented in Figure 6.1 means that we cannot distinguish between the $\ell_{sf}^{CuGe} = 61\text{nm}$ and $\ell_{sf}^{N} = \infty$ in the normal metal. In these samples, it was assumed that $\ell_{sf}^{Co} >> t_{Co} = 6.0\text{nm}$. However for samples with thicker Co layers one might expect to see the square root data deviate from a fit based on this assumption. Figure 5.5b shows small deviations between the square root t_{Co}=t_{Cu} data and the fit based on the two channel model (where $\ell_{sf}^{Cu} = \infty$ and $\ell_{sf}^{Co} = \infty$ are assumed). In Figure 5.5b the low N data lie noticeably below the fit. By assuming $\ell_{sf}^{Cu} = \infty$, justified by the Co/Cu data in Figure 6.1, a fit using the Valet-Fert model to the t_{Co}=t_{Cu} data could give a possible lower bound on the SDL in Co. The square root data for the t_{Co}=t_{Cu} series is plotted in Figure 6.6 along with predictions using the Valet-Fert model for finite SDL. Figure 6.6 shows the extreme cases for SDL's in both the Cu and Co needed to explain the slight curvature in the t_{Co}=t_{Cu} data. As shown in Figure 6.6b, for $\ell_{sf}^{Cu} = \infty$, a Co SDL of 2.5nm could explain the curvature[16] in the t_{Co}=t_{Cu} data as the Co thickness increases (N decreases). Alternatively, these deviations could be explained by assuming $\ell_{sf}^{Co} = \infty$ and a SDL of 75nm in the Cu as seen in Figure 6.6a. The two extremes put a lower bound of $\ell_{sf}^{Co} = 2.5\text{nm}$ and $\ell_{sf}^{Cu} = 75\text{nm}$. The lower bound on the SDL in Cu is a factor of 6 smaller than the 450nm given in Table 6.4 which is based on a measurement of the spin orbit cross section attributed to defects in Cu[3,17]. The agreement between the estimated values of ℓ_{sf}^{N} and the fitted values of ℓ_{sf}^{N} for each Co/CuX series implies that the SDL in Cu is

probably closer to 450nm than 75nm. Therefore the curvature in the low N t_{Co}=t_{Cu} data is probably due to a finite SDL in Co greater than 2.5nm.

Looking closely at Figures 6.6a and 6.6b one notices that the infinite fit crosses the fits for finite SDL. This discrepancy is attributed to the handling of the Nb/Co boundary resistance in each model. In the two channel model presented in chapter 4, the Nb/Co boundary resistance is included by adding $4AR_{Nb/Co}$ to the + channel and the - channel before the + and - channels are added in parallel. For the case with finite SDL, the Valet-Fert model has yet to be rigorously extended to multilayers with superconducting Nb contact layers, and therefore the Nb/Co boundary resistance, $2AR_{Nb/Co} = 6.1 \text{f}\Omega\text{m}^2$, is added in series to equation 4.8. Simply adding the Nb/Co boundary resistance to the Valet-Fert predictions is only an approximation of the real resistance and as Figure 6.6 shows there are small inconsistencies. Fortunately they exist at a level below our ability to measure.

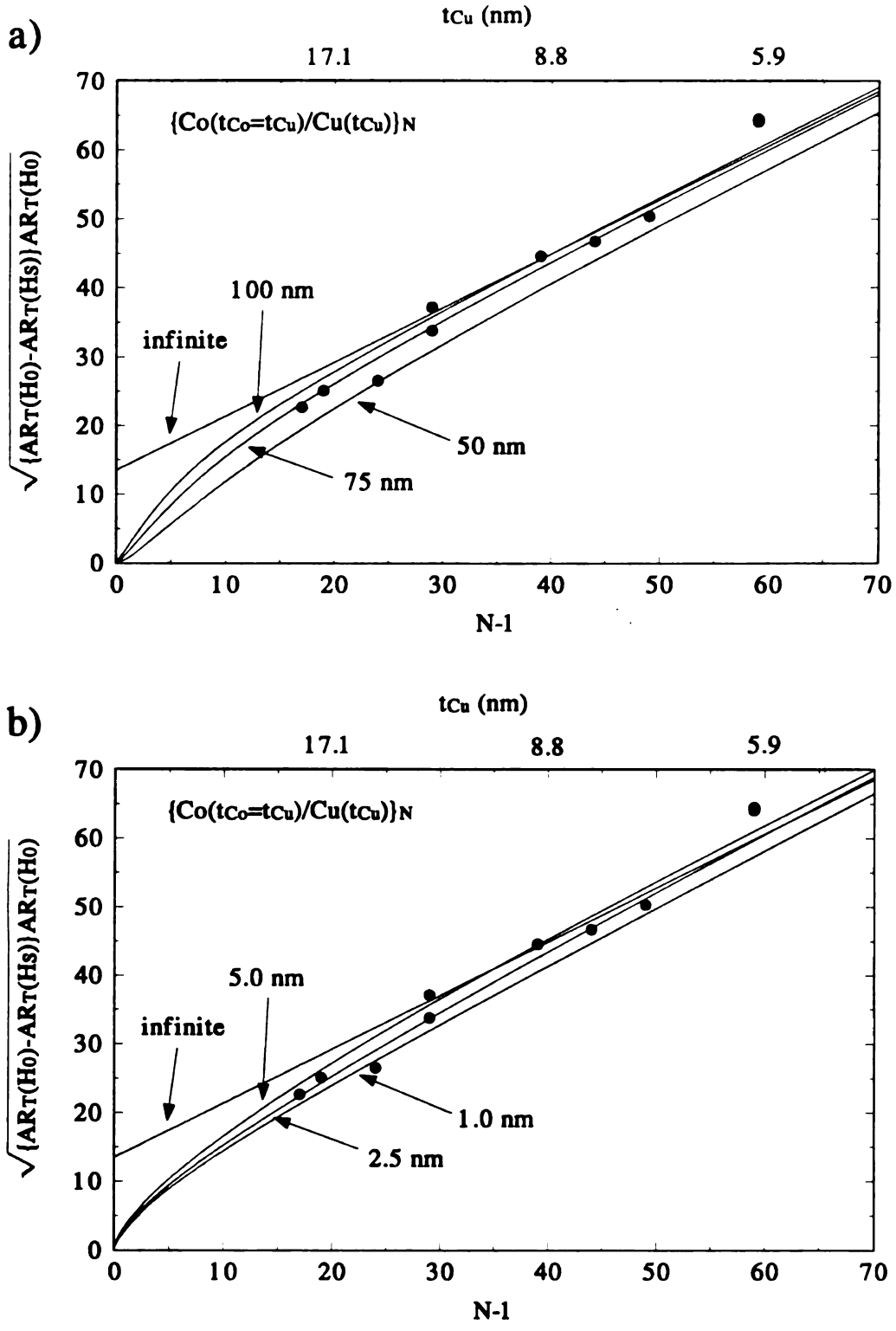

Figure 6.6: Valet-Fert predictions for the $[Co(t_{Co}=t_{Cu})/Cu(t_{Cu})]\times N$ series using the Co/Cu parameters from Table 5.6 together with a) assumed values of $\ell_{sf}^{Co}=\infty$ and $\ell_{sf}^{Cu}=50$nm, 75nm, 100nm and ∞ ; and with b) assumed values of $\ell_{sf}^{Cu}=\infty$ and $\ell_{sf}^{Co}=1.0$nm, 2.5nm, 5.0nm and ∞ .

[1] F. Beuneu and P. Monod, Phys. Rev. **B 13** (1976) 3424.

[2] T. Valet and A. Fert, Phys. Rev. **B 48**, 7099 (1993).

[3] P. Monod and S. Schultz, J. Phys. (Paris) **43**, 393 (1982).

[4] S.S.P. Parkin, C. Chappert and F. Herman, Europhys. Lett. **24**, 71 (1993).

[5] A. Fert, J.L. Duvail and T. Valet, Phys. Rev. **B 52**, 6513 (1995).

[6] Demagnetizing a few representative Co/CuPt(6%) samples show that the $AR(H_D)$ is less than the H_0 resistance. The ratio Π_D is less than 1.2.

[7] J. Bass, in *Metals: Electronic Transport Phenomena*, edited by K. H. Hellwege and J. L. Olsen, Landolt-Börnstein, New Series, Group 3, Vol. 15 Pt.a (Springer-Verlag, Berlin, 1982).

[8] N. W. Ashcroft and N. D. Mermin, *Solid State Physics* (W. B. Saunders, Philadephia, 1976).

[9] A. F. Starr, A. Nishida and S. Schultz (unpublished).

[10] T. Valet [illegible] A. Fert, J. Magn. Magn. Mater. 121, 378 (1993).

[11] B. Dieny, J. Magn. Magn. Mater. 136, 335 (1994).

[12] V.S. Speriosu, J.P. Nozieres, B.A. Gurney, B. Dieny, T.C. Huang and H. Lefakis, Phys. Rev. **B 47**, 11579 (1993).

[13] R.M. Bozorth, *Ferromagnetism*, D. Van Nostrand, New York, NY (1951) p. 308.

[14] J.F. Bobo, L. Hennet and M. Piecuch, Europhys. Lett. 24, 139 (1993).

[15] S.Y. Hsu, *et al.*, to be published.

[16] Data in S.F. Lee, Ph.D. Dissertation, Michigan State University (1994) show deviations from the fitted quantities in similar multilayers of Co/Ag for $t_{Co}>15.0nm$ with more significant deviations for $t_{Co}>20.0nm$. MR and magnetization studies on these thick Co samples show complex magnetic behavior.

[17] A. C. Gossard, T. Y. Kometani and J. H. Wernick, J. Appl. Phys. **39**, 849 (1968).

6.2 Giant Magnetoresistance in Hybrid Multilayers.

Fundamental to large changes in a magnetic multilayer's resistance is the ability to form two very different magnetic states, where the moments of adjacent magnetic layers are aligned either parallel or antiparallel to each other. In the previous chapter samples with very thin Cu spacer layers exhibited an oscillatory MR. Peaks in the MR corresponded to strong AF exchange coupling between F layers which formed the AP resistance. Samples in the uncoupled region still behaved as if the adjacent F layers were aligned antiparallel. (This could be explained by magnetostatic interactions between the F layers or a random configuration of the F layer magnetizations.) However, in this section the alignment of the magnetic layers is governed by the differences in the coercive forces between adjacent magnetic layers.

The term "hybrid" refers to a multilayer containing two distinct magnetic components. Here the materials Py and Co are used to provide the magnetic contrast necessary to produce an AP state. As mentioned in chapter 5, for the same thickness, the coercive fields of Co are more than 20 times larger than those of Py. This large difference in coercivity results in large resistance changes in the sample at low fields. This section is divided into two parts: The first deals with CIP-MR and magnetic measurements on both Ag and Cu based hybrid systems. The second deals exclusively with CPP transport measurements made on a series of Ag based hybrids in which the Py thickness is varied.

In most of this section the magnetic contrast between discontinuous layers of ultra-thin Co and thicker continuous layers of Py is used to produce the AP state necessary for

GMR. Prior measurements on Co/Ag multilayers indicated poor MR for Ag thicknesses less than 5.0nm[1] when thick continuous layers of Co were used. However, if the Co thickness was reduced to less than 1.0nm then large MR's were observed[2,3]. These ultra-thin Co samples exhibited larger saturation fields for both the resistance and magnetization than those required for multilayers with thicker Co layers. NMR studies by van Alphen *et al.*[4] described in section 3.4 indicated that the Co existed as clusters below nominal Co layer thicknesses of 1.0nm. As will be described, it is believed that the clustering of the Co layers reduces the effect of pinholes thereby improving the MR. In addition to improving the MR, samples with clustered Co layers exhibit larger coercive and saturation fields than samples with continuous layers of Co of comparable thickness. These properties are utilized in the hybrid structures that follow.

The magnetic properties of a system of ferromagnetic clusters can be somewhat sensitive to temperature. Very simply, at low T, a cluster behave ferromagnetically. However, as the thermal energy approaches the magnetic energy of a cluster, the cluster begins to behave paramagnetically. This crossover from ferromagnetism to paramagnetic behavior is sometimes referred to as superparamagnetism. Properties such as the coercive field of a system of clusters are reduced to zero as T increases. A more detailed discussion of the temperature dependence of ferromagnetic clusters is given later.

CIP-MR in hybrid multilayers.

Although CIP-MR measurements are hard to interpret without complicated models with several adjustable parameters[5], this geometry is important technologically since it allows MR measurements on samples with resistances of a few Ω, instead of the ≈nΩ encountered in the CPP direction[6]. All of the resistance studies were carried out by L.B. Steren in Orsay, France. The magnetic studies were done at MSU using Quantum Design magnetometers. The studies were done independently on the same sample; after sputtering, each half inch square substrate was cleaved into two equal parts. One half was kept here for the magnetic measurements while the other was sent to Orsay for the resistance studies.

The resistance and magnetization of each multilayer are well correlated. Figure 6.7 shows the field dependence of both the magnetization and the resistance of a *[Co(0.4nm)/Ag(4.0nm)/Py(4.0nm)/Ag(4.0nm)]×10* sample at 4.2K. The field dependence is typical for most hybrid samples. In the low resistance state, the applied field aligns both the Py and Co moments. As the field is lowered the resistance stays roughly the same until a small negative field in reached. The small rise in the resistance after saturation as the field is reduced may be attributed to some of the more anisotropic clusters. The Co clusters will tend to orient themselves along their easy axes at low field minimizing their energy with respect to the applied field; so that although the Co layer magnetization points in a specific direction, the individual cluster moments are actually distributed over some range of angles. As the field is swept through H_C for Py, the Py magnetization flips and a large change in the resistance is observed. The resistance levels

off after the Py layers are saturated forming a small plateau. Sweeping the field further in this direction begins to flip the Co layer bringing the sample back into the low resistance state. The initial H_0 resistance is much smaller than the H_P resistance because the Co clusters have not yet been polarized along the field direction. Therefore only half the Co clusters have moments antiparallel to the adjacent Py layers, creating a resistance state which is definitely not an AP state. The magnetization plot for the same sample shows a similar field dependence as the field is swept through the Py H_C. In these hybrids, most of the Py flips with a change in field of only 5-15Oe. The MR associated with the flip of the Py is about 30% giving slopes ($\Delta R/\Delta H$) as high as 6%/Oe, much more field sensitive than MR devices now used in hard drives[7].

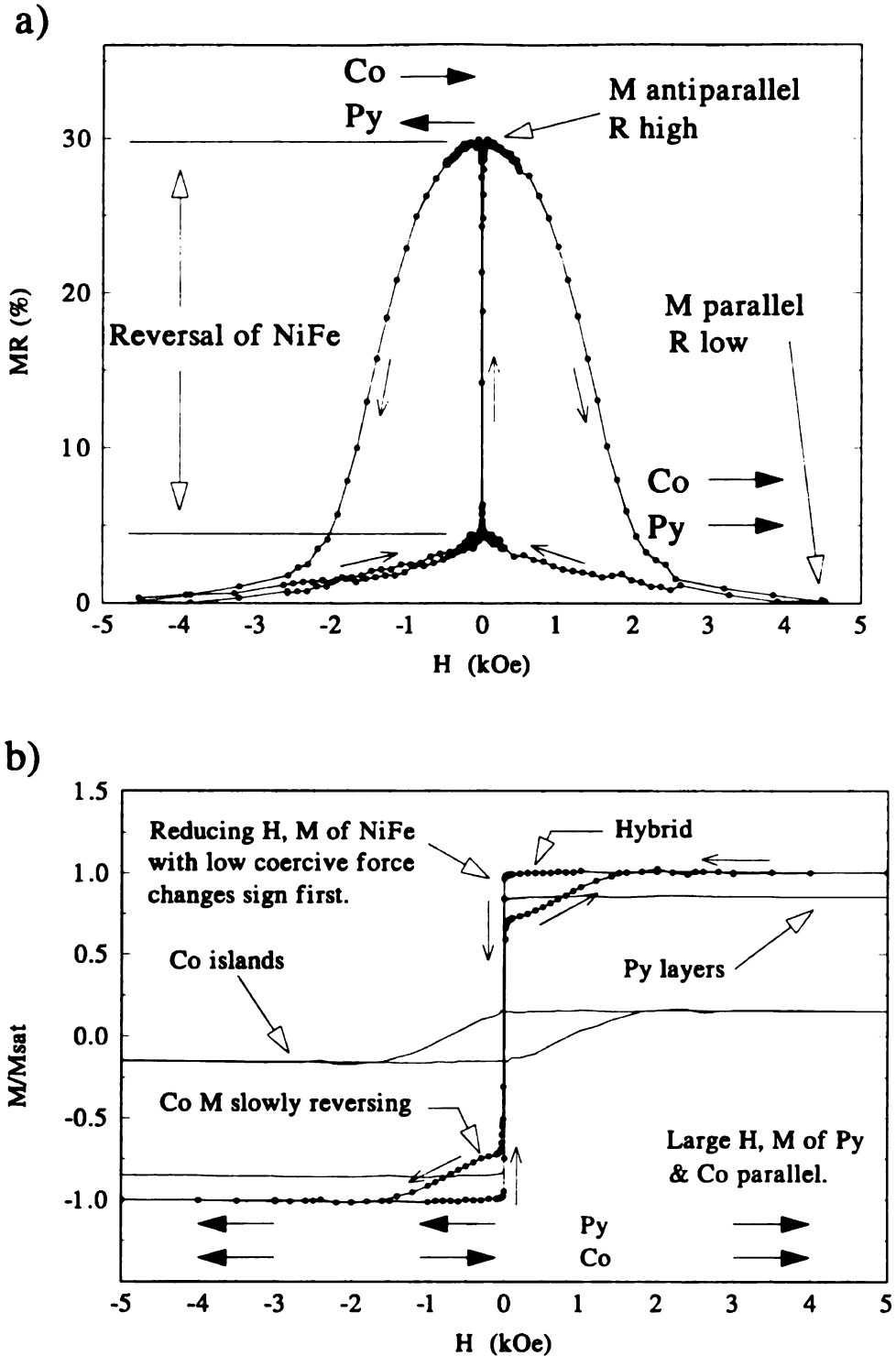

Figure 6.7: The field dependence for a *[Co(0.4nm)/Ag(4.0nm)/Py(4.0nm)/Ag(4.0nm)]×10* sample of a) the CIP-MR and b) the magnetization at 4.2K. In b) the hysteresis of the Co and Py is shown schematically. The curve label hybrid in b) is an actual measurement.

The thickness of each layer is chosen to be smaller than the elastic mfp of each material. The thin 0.4nm Co layers are not thick enough to form a continuous layer, NMR measurements by van Alphen *et al.*[4] indicate complete layers of Co form after 1.0nm of Co has been deposited. There are two advantages in having a layer of island-like clusters of Co in these samples. Studies have shown that multilayers made with a Ag spacer layer less than 5.0nm and continuous Co layers[1,8,9,10] exhibit poor MR. This is usually ascribed to ferromagnetic bridging (pinholes) between F layers. Further inquiries showed large oscillatory MR effects in Co/Ag with ultra-thin Co layers[2,5]. The first advantage is that the layer of Co clusters is then, less sensitive to ferromagnetic bridging by pinholes or defects. Figure 6.8 illustrates that a pinhole connecting a Co cluster to a Py layer, will only ferromagnetically couple a cluster near the bridging site, leaving the rest of the Co layer uncoupled from the Py layer.

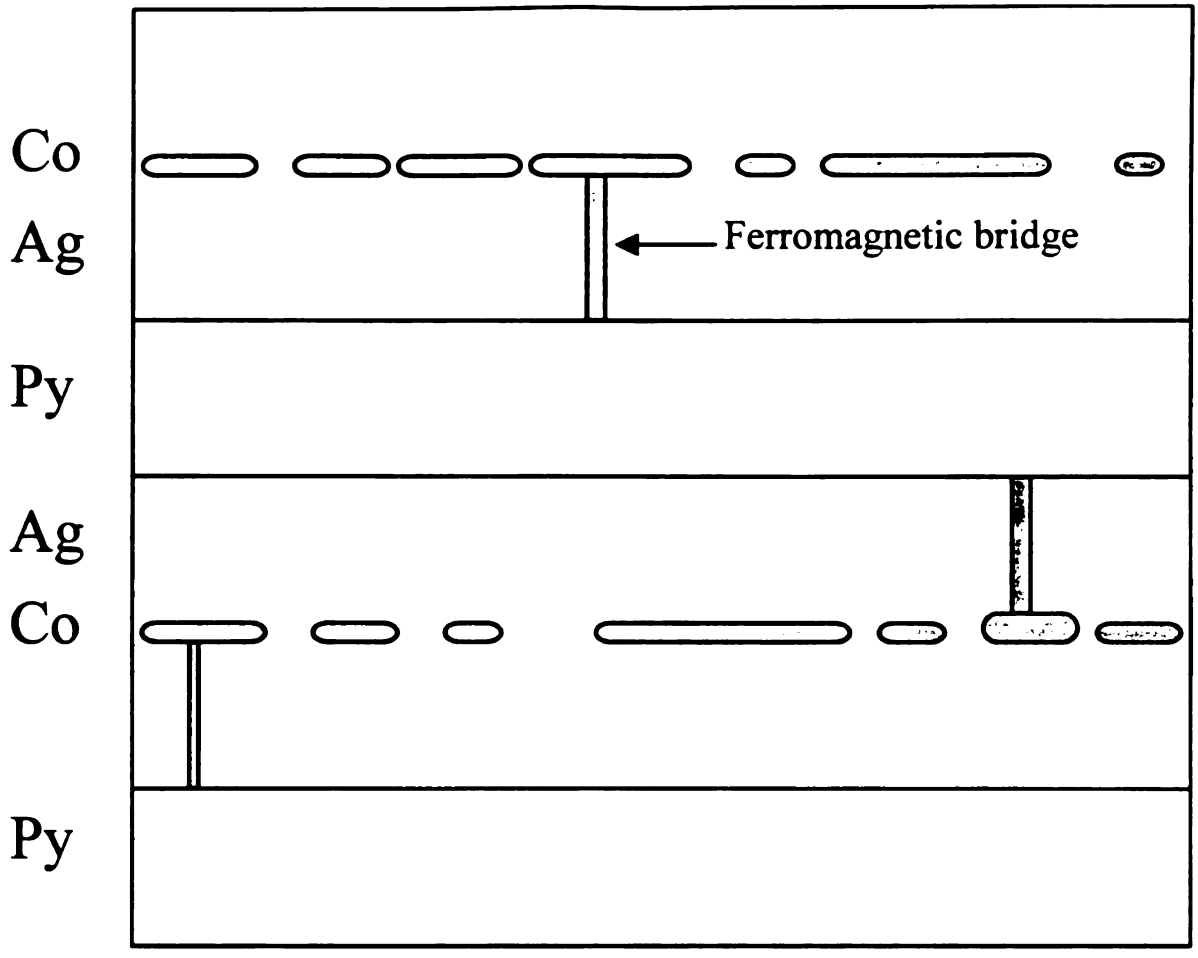

Figure 6.8: Schematic illustration of a pinholes bridging Py and Co. With island-like Co clusters only a small fraction of the Co ferromagnetically couples to the Py layers.

The second advantage is an enhancement in the magnetic contrast between Co and Py. Within a layer of island-like ferromagnetic clusters, magnetostatic interactions between the clusters increase the hysteresis and saturation field of this layer, relative to a similar continuous layer[9]. Therefore a layer of Co clusters is magnetically harder than a comparably thick continuous Co layer. Also, the actual volume of Co present in these hybrid structures is so small that the bipolar fields produced by the Co clusters have only

the sligh

the Py[11].

hybrids [

to Cu and

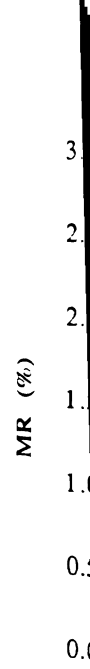

Figure 6.9
[Co(0.4nm
clusters ha

the slightest effect on the Py coercive properties, very effectively decoupling the Co from the Py[11]. The Py layers also have a lower H_C in the Ag based hybrids than in Cu based hybrids [12,13,14] which may be attributed to the weaker miscibility of Ag and Py compared to Cu and Py[15].

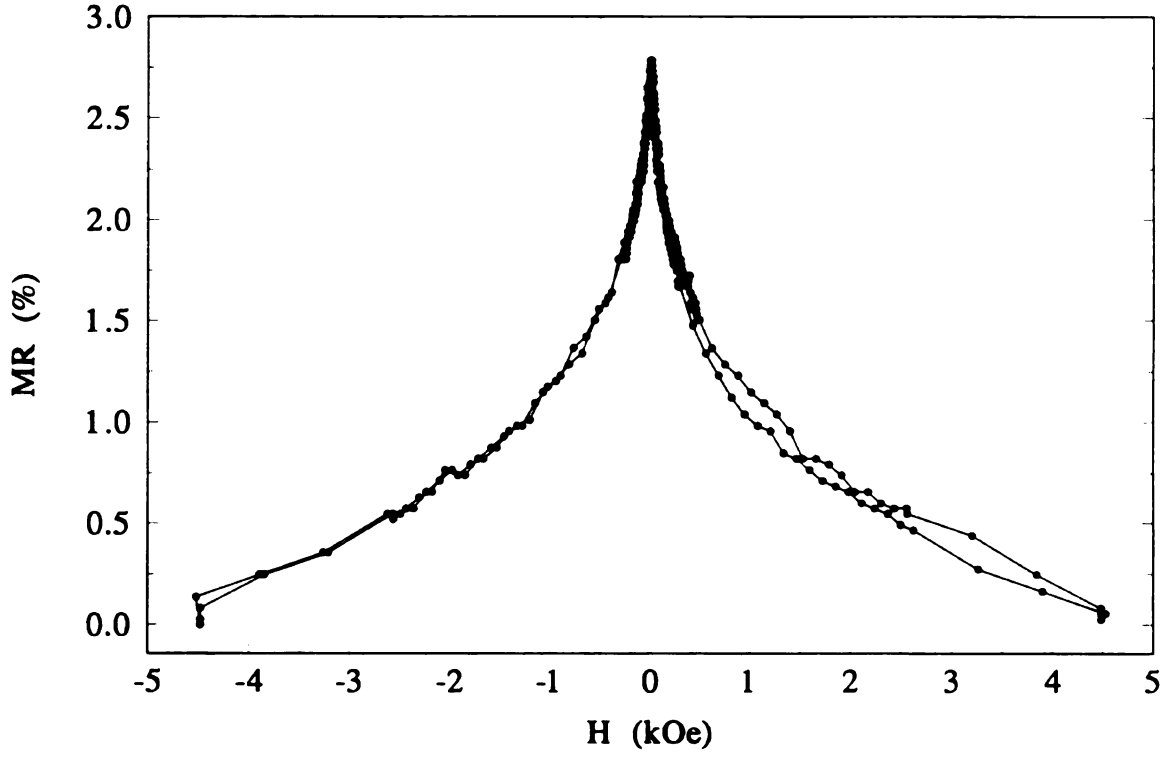

Figure 6.9: The field dependence of the CIP-MR at 300K for a hybrid sample with *[Co(0.4nm)/Ag(4.0nm)/Py(4.0nm)/Ag(4.0nm)]×10.* Superparamagnetism of the Co clusters has drastically reduced the MR observed at 4.2K (compare with Figure 6.7a).

The

sensitivity

as the te

Evidence

that shov

temperatu

distributi

Co cluste

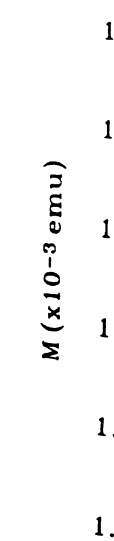

Figure 6.1

[Co(0.6nm)

field (ZFC

cooled (FC

curve defin

The disadvantage of using Co clusters is the degradation of both the MR and sensitivity with increasing temperature as shown in Figure 6.9. The reduction of the MR as the temperature increases is attributed to superparamagnetism in the Co clusters. Evidence for this is observed in temperature dependent magnetization measurements like that shown in Figure 6.10. Cooling the sample in zero field (ZFC) from room temperature to 5K, freezes the moment of Co clusters in a certain (presumably random) distribution. A small 100Oe field is applied which saturates the Py layers but leaves the Co clusters in their ZFC orientations.

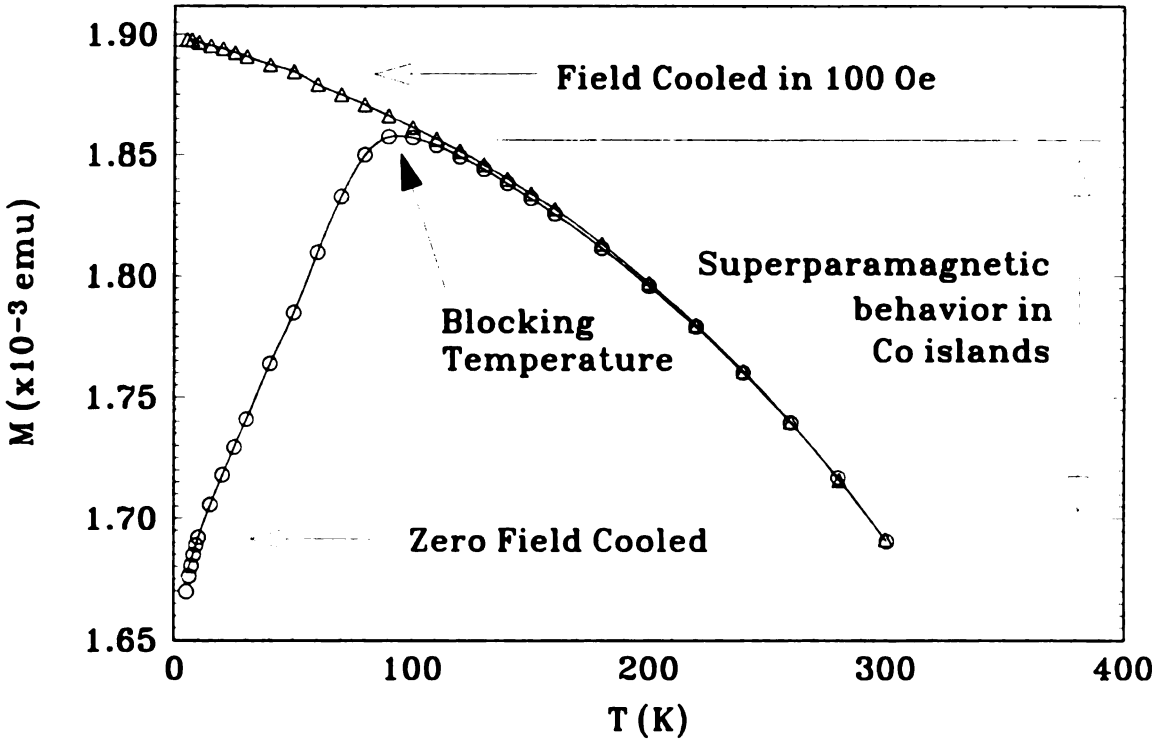

Figure 6.10: The temperature dependence of the magnetization is plotted for the hybrid *[Co(0.6nm)/Ag(4.0nm)/Py(4.0nm)/Ag(4.0nm)]×10*. Initially the sample is cooled in zero field (ZFC) and then a 100Oe field is applied to saturate the Py layers. For the field cooled (FC) curve the sample is allowed to cool in the 100Oe field. The peak in the ZFC curve defines the blocking temperature.

Blocking

The depe

measured

giving th

Since the

amount o

than the e

magnetic

to as the

be expres

crystal ax

change in

The di

anisotropy

the <100>

the anisotr

of the crys

between th

Blocking Temperature and Magnetic Anisotropy

The dependence of a material's magnetic properties on the direction in which they are measured is known as the magnetic anisotropy. When measuring a sample, the direction giving the lowest saturation field in known as the easy direction or axis of the material. Since the saturation field is small along the material's easy direction only a minimal amount of energy is required for saturation. To saturate the material in a direction other than the easy axis requires additional energy to overcome the anisotropy. Generally, the magnetic anisotropy energy possesses the crystal symmetry of the material and is referred to as the magnetocrystalline anisotropy. For a cubic system, this anisotropy energy can be expressed in terms of the direction cosines of the magnetization with respect to the crystal axes. The two lowest order terms are given in equation 6.1, where E_a is the change in energy as the magnetization is rotated through some angle, θ.

$$E_a = K_1(\alpha_1^2\alpha_2^2 + \alpha_2^2\alpha_3^2 + \alpha_3^2\alpha_1^2) + K_2(\alpha_1^2\alpha_2^2\alpha_3^2) + \cdots \qquad 6.1$$

The direction of the easy axis for cubic systems is complicated and depends on the anisotropy constants K_1 and K_2 for a particular material. For bcc Fe the easy axis is in the <100> direction and in fcc Ni the easy axis is the <111> direction. The expression for the anisotropy energy of an hcp system is simpler since the easy axis lies along the *c* axis of the crystal. In this case, the anisotropy energy depends only on a single angle, θ, between the *c* axis and the magnetization.

$$E = K_1 \sin^2\theta + K_2 \sin^4\theta + \cdots \qquad 6.2$$

The mag

magnetic

even dor

For

the easy

poles at

than alo

produce

ferroma

geome

magne

Where

oblate

anisot

Which

There

magn

appro

In

treatm

The magnetocrystalline anisotropy is intrinsic to the material but other extrinsic forms of magnetic anisotropy may contribute to a sample's anisotropy energy and in some cases even dominates the magnetocrystalline anisotropy of the sample.

For example the geometry of a ferromagnetic material will also affect the direction of the easy axis. Demagnetizing fields within the material act to limit the number of free poles at the surface of the material. A demagnetizing field along a short axis is stronger than along a long axis. Therefore, a field applied along a short axis must be stronger to produce the same true field inside the specimen. For example: (a) a long needle like ferromagnet has its easy axis along the axis of the needle; whereas, (b) a thin disk geometry will have the easy axis in the plane of the disk. The demagnetizing fields of a magnetized sample have an associated magnetostatic energy which is given by

$$E = \tfrac{1}{2} H_d M = \tfrac{1}{2} N_d M^2$$

Where H_d=$N_d M$ is the demagnetizing field and N_d is the demagnetizing factor. For an oblate spheroid with semi-major axes c > semi-minor axis a and magnetization M_S, the anisotropy energy becomes:

$$E_{shape} = \tfrac{1}{2}(N_a - N_c) M_S^2 \sin^2 \theta \qquad 6.3$$

Which is of the same form as the first term in equation 6.2 with $K_S = \tfrac{1}{2}(N_a - N_c) M_S^2$. Therefore the shape ansiotropy of an oblate spheroid is dependent upon both the magnetization of the sample and the ratio of the c axis to the a axis. With $c>>a$ this approximates a thin disk.

In many materials it is possible to induce anisotropy by special preparation or treatment of the sample. As will be shown later, it is possible to induce a permanent easy

axis in a sample by depositing the sample in a strong magnetic field. The induced anisotropy is similar to other uniaxial anisotropies listed previously.

$$E = K_u \sin^2 \theta$$

Where K_u is the anisotropy constant and θ is the angle between the magnetization and the direction of the field applied during growth.

The magnetization of a small, single domain particle will tend to point along its easy axis in order to minimize its internal energy. In general the direction of the easy axis for a small particle depends on both crystal structure and the macroscopic dimensions of the particle and their relative orientations. Table 6.6 gives some values for the shape anisotropy of an oblate spheroid of Co for comparison with K_1=6.8×10^{6}erg/cm^3.

Table 6.6: Values of shape anisotropy for oblate spheroids of Co (M_S=1422 emu/cm^3).

c/a	N_a-N_c	K_S *(10^6 erg/cm^3)*
1.0	0	0
1.1	0.472	0.477
1.5	1.892	1.913
5.0	5.231	5.289
10.0	5.901	5.966
20.0	6.165	6.233
∞	2π	6.353

At low temperatures and in zero applied field, the anisotropy energy of the particle, *KV*, will dominate in holding its magnetization in place. (Here *K* represents the total

strength of the anisotropy which could be a complex function of the magnetocrystalline and shape anisotropies.) As the temperature increases, the particle's internal energy increases by an amount, $k\Delta T$. At a certain temperature, the particle's thermal energy becomes of the order of the particle's anisotropy energy and the particle's magnetization no longer points in a particular direction. The temperature at which $kT \approx KV$ is called the blocking temperature, T_B. When the particle's anisotropy can no longer keep its magnetization from spontaneously reversing then the particle acts paramagnetically. The magnetization of paramagnets is governed by a Langevin Law which describes the competition between thermal fluctuations and an applied field. The particle's moment will tend to align with an applied field while the thermal fluctuations will tend to disalign the moment and field. The major difference between a normal paramagnetic material and one with clusters of magnetic atoms is magnitude of the magnetic moment. The magnetic moment per atom of a paramagnetic material is just a few μ_B while ferromagnetic particles above T_B have moments of 10^3 μ_B. For example a spherical Co particle only 5.0nm in diameter has a moment of $\approx 10000\mu_B$. These types of particles are said to behave superparamagnetically because of their large moments and their paramagnetic behavior above T_B.

To determine the blocking temperature of an assembly of superparamagnetic particles one must examine the time required to relax the magnetization. The rate of decrease in the magnetization is proportional to the initial magnetization of the system and the probability that a particle has enough thermal energy to overcome the energy gap

presented by the anisotropy energy, $\Delta E=KV$. The probability is given by the Boltzmann factor $e^{-KV/kT}$. Therefore,

$$-\frac{dM}{dt} = f_0 M e^{-KV/kT} = \frac{M}{\tau} \qquad 6.4$$

Where $f_0 \approx 10^{-9} sec^{-1}$ is called the frequency factor. The constant τ is the relaxation time of the magnetization and is given in equation 6.5.

$$\frac{1}{\tau} = f_0 e^{-KV/kT} \qquad 6.5$$

Since the temperature and the volume appear in the exponential, they are rather insensitive to the choice of the relaxation time. An appropriate choice for the relaxation is 100 sec. This is roughly the amount of time it takes to make a measurement of the magnetization. Using this estimate for τ one may estimate the blocking temperature of the system.

$$T_B \approx \frac{KV}{25k_B} \qquad 6.6$$

As will be done later, the volume of the average superparamagnetic particle may also be estimated using equation 6.6 if their anisotropy constant is known.

The nature of the MR above the blocking temperature is completely different from that at 4.2K (compare Figure 6.7a with Figure 6.9). Above T_B, the Co magnetization is governed by a Langevin Law and the Co clusters lose their remanent magnetization, or alternatively, H_C for the Co layer goes to zero[2]. With no remanent magnetization, the Co clusters are randomly oriented near zero field. Therefore in small fields where the Py magnetization flips, the relative orientation between the Co clusters and the Py layers

does not change; both before and after the Py flips, roughly half the moments of the Co clusters are parallel and half antiparallel. Since the relative orientation between the Py and the Co is not changed, minimal change in the resistance is observed. As the field is increased, the Co clusters gradually become polarized, parallel to the Py layers, in the direction of the applied field. Since some of the Co was antiparallel to the Py near zero field, a small drop in the resistance is seen. The MR drops an order of magnitude within 20K of $T_B \approx 60K$ for $t_{Co}=0.4nm$.

Raising the Blocking Temperature (a) Variation with t_{Co}

For commercial application, it is necessary to increase T_B to above room temperature. Three different studies were done to investigate how T_B could be varied. The first set of experiments varied the Co thickness in both Ag and Cu based hybrids to study what happens as the island-like Co layer becomes a continuous Co layer. NMR data by van Alphen, *et al.*[4] showed that continuous Co layers formed when the nominal thickness reached ~1.0nm in Co/Ag multilayers. Magnetic measurements by R. Loloee[2] also indicated clustering in both Co/Cu and Co/Ag systems for $t_{Co}<1.0nm$, with T_B in the Cu samples almost four times that of the Ag ones.

Table 6.7a gives measurements of the magnetic properties due to the Co layers in the $[Co(t_{Co})/Ag(4.0nm)/Py(4.0nm)/Ag(4.0nm)]\times 10$ samples. The MR and sensitivity of these samples at room temperature and 4.2K are given in Table 6.7b. Similar measurements for the $[Co(t_{Co})/Cu(4.0nm)/Py(4.0nm)/Cu(4.0nm)]\times 10$ series are given in Tables 6.8a and

6.8b. The blocking temperatures for both series are shown in Figure 6.11 as a function of the Co thickness. Both series show an increase in T_B with t_{Co} less than 1.0nm. If the strength of the anisotropy changes little with the volume, then a higher T_B means that the increased anisotropy energy (KV) is a result of larger average cluster volumes as the Co thickness increases. The Cu hybrids show T_B a factor of two greater than the Ag hybrids, consistent with the findings of Loloee[2].

Table 6.7a: Magnetic quantities for *[Co(t_{Co})/Ag(4.0nm)/Py(4.0nm)/Ag(4.0nm)]×10* attributed to the Co clusters.

t_{Co}(nm)	T_B (K)	M_S (emu/cm^3)	K (erg/cm^3)[a]	V (nm^3)[b]
0.4	50		6.8×10^6	25
0.6	90	1137	6.8×10^6	46
0.7	80		6.8×10^6	41
0.85	140	1154	6.6×10^6	73
1.0	120	1189	6.7×10^6	62
1.15	120	1000	6.7×10^6	62
1.3	140	1325	6.6×10^6	73

a From Reference 16.
b Calculated using equation 6.6.

Table 6.7b: CIP Magnetoresistance and sensitivity measurements at both liquid He and room temperatures for the *[Co(t_{Co})/Ag(4.0nm)/Py(4.0nm)/Ag(4.0nm)]×10* series.

t_{Co} (nm)	MR (%)[a]	S (%/Oe)[a]	MR (%)[b]	S (%/Oe)[b]
0.4	25.6	0.95	3.20	0
0.6	30.7	2.30	3.40	0
0.7	33.5	2.40	3.50	0
0.85	28.8	4.90	3.70	0.36
1.0	29.0	3.80	3.98	0.22
1.15	29.1	3.08		0.21
1.3	28.9	2.72	3.15	0.10

a Measurement made at 4.2K.
b Measurement made at 300K.

Table 6.8a: Magnetic quantities for *[Co(t_{Co})/Cu(4.0nm)/Py(4.0nm)/Cu(4.0nm)]×10* attributed to the Co clusters.

t_{Co}(nm)	T_B (K)	M_S (emu/cm^3)	K (erg/cm^3)[a]	V (nm^3)[b]
0.4	180	1150	6.2×10^6	100
0.6	200	1110	5.8×10^6	120
0.8	260	1240	5.3×10^6	170
1.0	270	1133	5.1×10^6	180
1.3	280	1050	4.9×10^6	200
1.6	290	985	4.4×10^6	230
2.0	335	999	3.9×10^6	300

a From Reference 16.
b Calculated using equation 6.6.

Table 6.8b: CIP Magnetoresistance and sensitivity measurements at both liquid He and room temperatures for the *[Co(t_{Co})/Cu(4.0nm)/Py(4.0nm)/Cu(4.0nm)]×10* series.

t_{Co} (nm)	MR (%)[a]	S (%/Oe)[a]	MR (%)[b]	S (%/Oe)[b]
0.4	24.7	1.50	3.80	0.38
0.6	29.1	1.40	4.50	0.35
0.8	27.8	2.42	5.90	0.67
1.0	28.6	2.34	6.30	0.41
1.3	25.4	0.78	6.20	0.39
1.6	25.6	1.10	6.50	0.53
2.0	23.1	1.11	5.85	0.23

a Measurement made at 4.2K.
b Measurement made at 300K.

As the Co thickness increases beyond 1.0nm, T_B in each series levels off which indicates a crossover to continuous Co layers. The volume of the average Co cluster may be estimated from equation 6.6 using the measured values of T_B and the temperature dependent values of K_1 given for bulk Co in Cullity[16]. The average cluster volume is given in Tables 6.7a and 6.8a. The Cu hybrids show significantly larger Co cluster sizes approximately twice the volume of the Ag hybrids. TEM studies have revealed that the layering in thin-Co/Cu multilayers is much better than in thin-Co/Ag samples of comparable nominal thickness[17]. The lattice parameter similarity and surface energy considerations[18] between Co and Cu suggest Co/Cu has a more stable superlattice structure than Co/Ag.

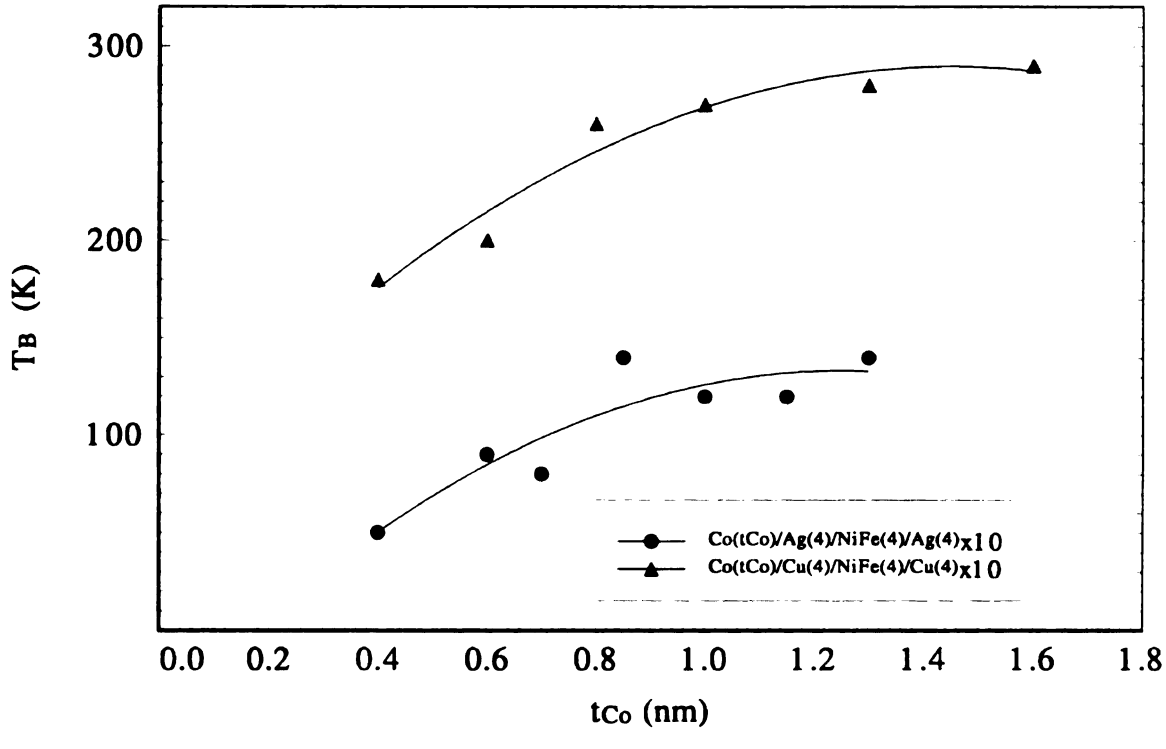

Figure 6.11: The blocking temperature, T_B, is plotted for *[Co(t_{Co})/NM/Py(4.0nm)/NM]×10* samples with *NM=Ag(4.0nm)* or *Cu(4.0nm)* as function of t_{Co} for both series. The lines are guides to the eyes.

The MR dependence on t_{Co} is similar to that for the T_B data for both types of hybrids. Figure 6.12 plots both the MR and sensitivity (S in %/Oe) for both series at 4.2K and at 300K. At low temperatures, the Ag hybrids show much more sensitivity to field than do the Cu ones, even though the overall MR of both is nearly the same. This supports the idea that the Py layers in the Ag hybrids[14] are softer than in the Cu hybrids[11,12,13,14]. At room temperature, it is the Cu hybrids which show a better field sensitivity. T_B for the thicker Co samples is close to room temperature so that some of the larger Co clusters in these samples have not yet become superparamagnetic. The reduction in the MR at 300K is an order of magnitude in the Ag hybrids while the Cu hybrids are reduced only a factor of 4. Similar reductions are observed in the sensitivity data. Interestingly, all the data in Figure 6.12 exhibit features at $t_{Co} \approx 0.8nm$. All the Ag data show peaks near or at 0.8nm of Co. For $t_{Co} < 0.8nm$ the MR and hence the sensitivity increase as t_{Co} increases, presumably because the larger Co islands present a greater area for the electrons to scatter from. Thicker than 0.8nm, the Co forms continuous layers and ferromagnetic bridging by pinholes decreases the MR and sensitivity. The same is true for the Cu samples except that bridging is less of a problem with Cu.

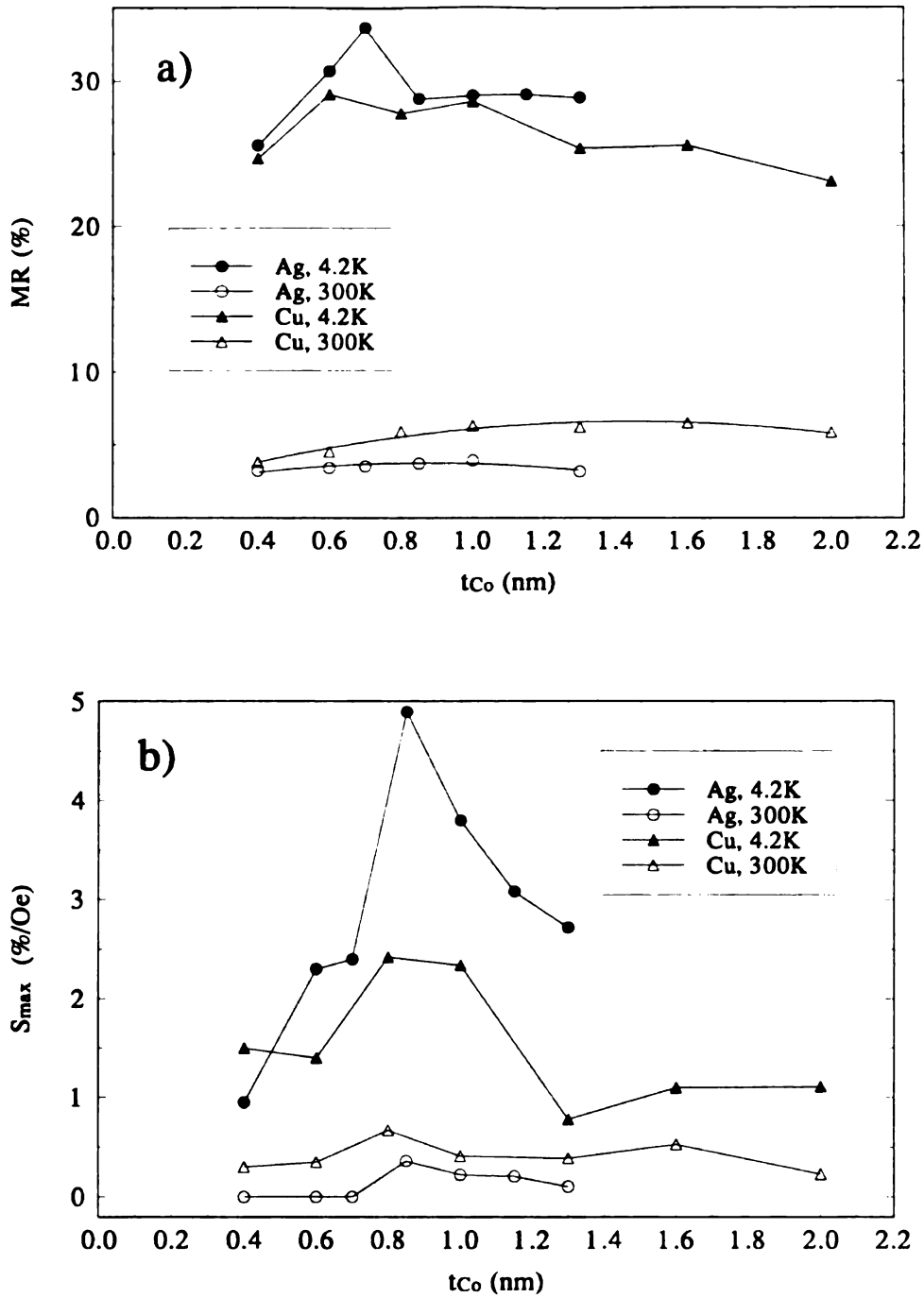

Figure 6.12: The a) CIP-MR and b) the maximum slope, $S = \Delta R / \Delta H$, of the CIP-MR are plotted as a function of t_{Co} for samples of *[Co(0.6nm)/NM/Py(4.0nm)/NM)]×10* with *NM=Ag(4.0nm)* or *Cu(4.0nm)*. The lines are guides to the eye.

Angular

The la

multilayer

magnetiza

conductio

Spin depe

the botto

between e

Vedyayev

between c

adjacent m

observed

predicted

$k_F^{\uparrow} k_F^{\downarrow} \neq$

A stud

conductiv

magnetic l

as spin val

Angular Dependence of MR

The large difference in coercive fields of Co clusters and Py layers makes the hybrid multilayer an ideal system for studying the dependence of MR on the angle between layer magnetizations. The mechanism for GMR is attributed to spin dependent scattering of the conduction electrons and/or spin dependent potential barriers between successive layers. Spin dependent potential barriers are due to the difference in Fermi energy with respect to the bottom of the conduction band between adjacent materials. Exchange splitting between electron subbands can cause the barriers to be spin dependent[19]. Calculations by Vedyayev, *et al.*[20] show that GMR varies linearly with $\sin^2(\varphi/2)$, where φ is the angle between consecutive magnetic layers, only when there are no potential barriers between adjacent materials. Alternatively, the linear variation of the conductivity with $\sin^2(\varphi/2)$ is observed when $k_F^{\downarrow} = k_F^{\uparrow}$. Large deviations from the linear behavior in $\sin^2(\varphi/2)$ are predicted by Vedyayev[20] for ratios of the Fermi momentum different from one, $k_F^{\uparrow}/k_F^{\downarrow} \neq 1$.

A study[21]by Fert's group using our samples showed that the variation in the sample's conductivity, σ, was proportional to $\sin^2(\varphi/2)$, where φ is the angle between consecutive magnetic layers. Similar experimental results have been observed in other systems such as spin valves of Py/Cu/Py/FeMn[22], Py/Cu/Co trilayers[23] and Fe/Cr/Fe sandwiches[24].

Measurement of Coupling Fields

Despite the effective decoupling of the Py layers from the Co layers, a small easily measurable coupling field does exist between Co and Py. It is calculated by comparing major and minor hysteresis loops in either the resistance or the magnetization[21]. In each case the sample is taken to saturation and then cycled through a minor loop which only flips the Py relative to the Co. In Figure 6.13 the half-width of the minor loop is just the coercive field of the Py, while the distance that the center of the minor loop is shifted from zero represents the coupling field. Note that the sample coercive field and the Py coercive field are different.

Table 6.9 contains the calculated values of the coupling field, H_C^{Py}, and the coercive field, H_C of Py. The coupling is shown in Figure 6.14 as a function of Co thickness for both Ag and Cu based hybrid systems. The values in Figure 6.14 for the coupling field obtained from magnetization measurements (filled symbols) are in good agreement with those based on the resistance measurements (open symbols). The coupling field is positive for almost every sample, indicative of ferromagnetic coupling between the Co and Py. For both Cu and Ag based series the coupling field increases with t_{Co}. For multilayers of Co/Cu and Py/Cu, a Cu thickness of 4.0nm lies within a weakly ferromagnetically coupled region for these multilayers, so it is not surprising that the Co/Cu/Py/Cu samples are slightly F-coupled. A smaller ferromagnetic coupling field is observed for the Ag based hybrids. The small coupling field slightly complicates the angular dependence analysis but is easily corrected[21].

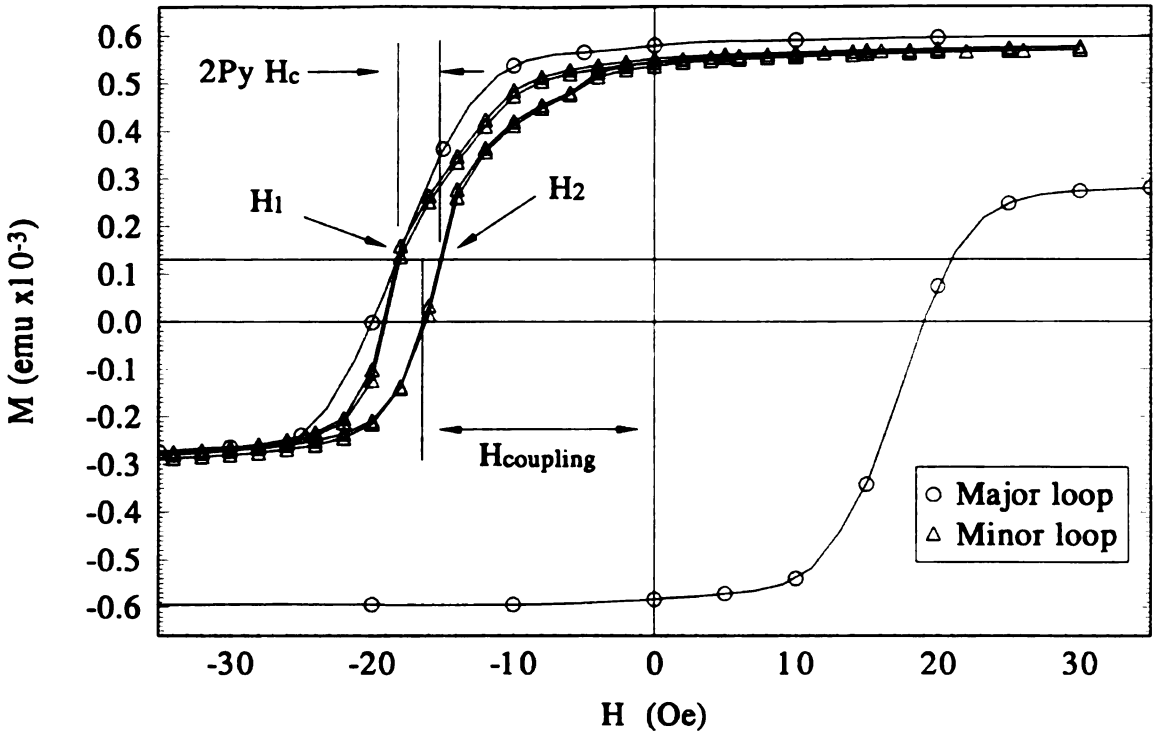

Figure 6.13: Comparing major and minor hysteresis loops of the magnetization shows a weak coupling field between the Py layers and the Co clusters. The minor loop extends ≈±45Oe from the Py coercive field. The displacement of the minor loop from H=0 represents the coupling field. Here the coupling is ferromagnetic. These hysteresis loops are for *[Co(0.4nm)/Ag(4.0nm)/Py(4.0nm)/Ag(4.0nm)]×10.*

Also shown in Figure 6.14 is the Py coercive field for each sample. The H_C of the Py layers is constant for both hybrid series which is expected since every sample has the same nominal Py thickness. The Py of the Cu based hybrids has $H_C \approx 5.0Oe$, more than three times larger than the 1.5Oe for the Py of the Ag based hybrids. The agreement between the magnetization (filled symbols) and resistance (open symbols) measurements in Figure 6.14 for the H_C of Py is quite good.

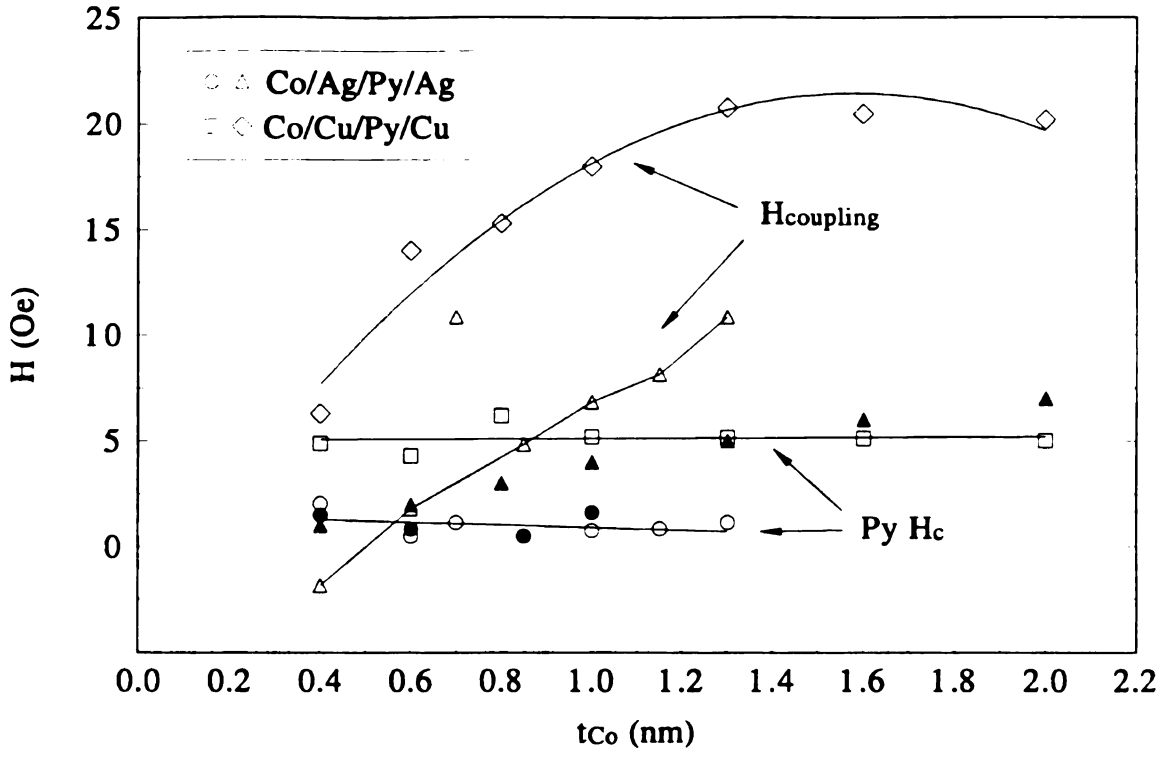

Figure 6.14: The coupling fields for samples of $[Co(t_{Co})/NM/Py(4.0nm)/NM]\times 10$ plotted as a function of t_{Co}, where *NM=Ag(4.0nm)* or *Cu(4.0nm)*. The open (filled) symbols are measurements of the coupling taken from resistance (magnetization) hysteresis loops. Nearly every sample shows ferromagnetic coupling. Plotted along with the coupling fields is the Py coercive field for each sample.

Table 6.9: Measurements of the Py coercive field, H_C, and the coupling field, H_C^{Py}, between the Co and Py layers for the $[Co(t_{Co})/NM/Py(4.0nm)/NM]\times 10$ series.

NM=Ag(4.0nm)			*NM=Cu(4.0nm)*				
t_{Co} *(nm)*	H_C^{Py}*(Oe)*[a]	H_C *(Oe)*[a]	t_{Co} *(nm)*	H_C^{Py}*(Oe)*[a]	H_C *(Oe)*[a]	H_C^{Py}*(Oe)*[b]	H_C *(Oe)*[b]
0.4	4.90	6.3	0.4	2.05	-1.85	1.50	-2.10
0.6	4.30	14.0	0.6	0.50	1.80	0.83	3.65
0.8	6.20	15.3	0.7	1.15	10.85		
1.0	5.20	18.0	0.85	0.50	4.85	0.48	5.00
1.3	5.15	20.8	1.0	0.75	6.85	1.60	6.40
1.6	5.10	20.5	1.15	0.80	8.14		
2.0	5.08	20.2	1.3	1.15	10.85		

a Measurement made using hysteresis loops in the resistance.

b Measurement made using hysteresis loops in the magnetization.

Raising the Blocking Temperature (b) Addition of Sm

To raise the blocking temperature of the Co islands, it is necessary to increase the anisotropy energy. In the last section, this was done by making the Co layer thicker thereby creating larger Co islands. However, giving the Co islands a stronger anisotropy would also accomplish this task. Adding Sm to Co enhances the uniaxial anisotropy of Co by up to two orders of magnitude[25] in single crystals of Co_5Sm. Sputtered films[26] of CoSm several μm thick have shown anisotropies of 5×10^7 erg/cm^3, much larger than the magnetocrystalline anisotropy of Co.

Sputtering from a composite target resulted in a 10 at.% Sm concentration. Results for a *[CoSm(t_{CoSm})/Cu(4.0nm)/Py(4.0nm)/Cu(4.0nm)]×10* series of samples are given in Tables 6.10a and 6.10b. The field dependence of the MR and magnetization, shown in Figure 6.15, have similar forms to the Co/Ag/Py/Ag samples shown in Figure 6.7.

Comparing the CoSm/Cu/Py/Cu and Co/Cu/Py/Cu systems reveals several differences between the two Cu based hybrid systems. The MR measured at both 4.2K and 300K for the CoSm samples is roughly half of that measured in similar Co samples as shown in Figure 6.16. This reduction in the MR also lowers the sensitivity by a factor of two. Both the saturation and coercive fields measured for the CoSm hybrids are nearly double those of the Co multilayers. This enhances the contrast between the Py and the CoSm clusters, resulting in a broader and more easily defined region in which the Py moments are antiparallel to the CoSm cluster moments. Minor loop measurements showed that the CoSm clusters exhibit a weaker coupling to the Py layers than the Co

clusters. Surprisingly, the blocking temperature for the CoSm clusters is not much different from the Co clusters as shown in Figure 6.17.

The anisotropy of the CoSm clusters was not measured, however the CoSm blocking temperatures indicate that the anisotropy energies for the CoSm/Cu/Py/Cu series and the Co/Cu/Py/Cu series are approximately the same. There are two possibilities one can infer from the T_B measurements for CoSm and Co. (a) The CoSm clusters have nearly the same volume as the Co clusters which means their values for K are nearly the same. (b) The CoSm clusters are smaller than the Co clusters ($V_{CoSm}<V_{Co}$) which means $K_{CoSm}>K_{Co}$ such that $K_{CoSm}V_{CoSm}\approx K_{Co}V_{Co}$.

Table 6.10a: Magnetic quantities for *[CoSm(t_{CoSm})/Cu(4.0nm)/Py(4.0nm)/Cu(4.0nm)]×10* attributed to the CoSm clusters.

t_{CoSm} (nm)	T_B (K)	M_S (emu/cm^3)
0.4	115	1050
0.6	180	753
0.8	215	1010
1.0	250	1020
1.3	280	879

Table 6.10b: CIP Magnetoresistance and sensitivity measurements at both liquid He and room temperatures for the *[CoSm(t_{CoSm})/Cu(4.0nm)/Py(4.0nm)/Cu(4.0nm)]×10* series.

t_{CoSm} (nm)	MR (%)[a]	S (%/Oe)[a]	MR (%)[b]	S (%/Oe)[b]
0.4	14.9	1.25	1.30	
0.6	15.5	2.00	1.64	
0.8	13.3	0.97	2.80	0.22
1.0	10.5	1.93	3.67	0.73
1.3	14.3		3.45	0.71

a Measurements made at 4.2K.
b Measurements made at 300K.

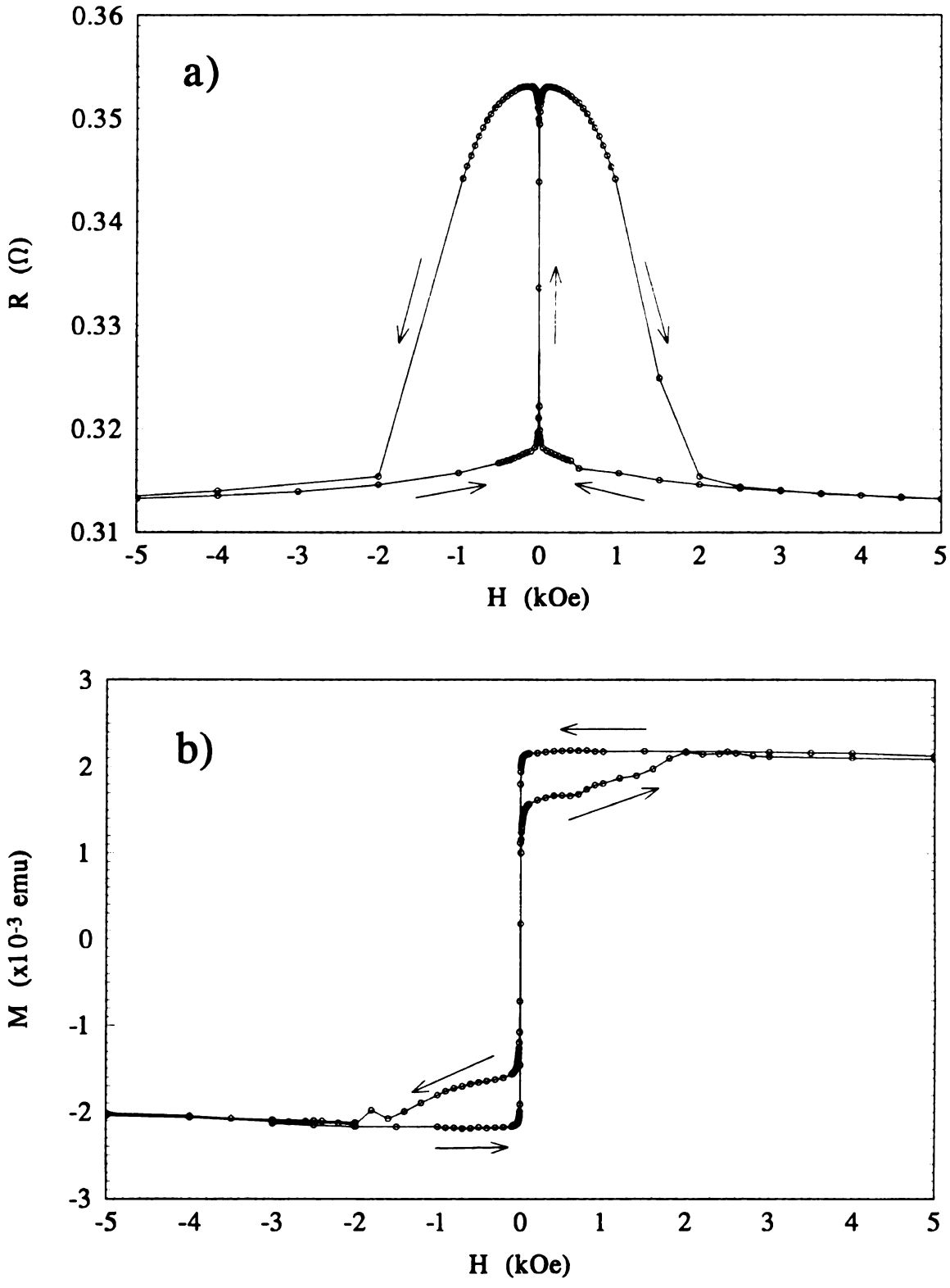

Figure 6.15: The field dependence of a) the CIP-MR and b) the magnetization at 4.2K for a *[CoSm(0.6nm)/Cu(4.0nm)/Py(4.0nm)/Cu(4.0nm)]×10* sample.

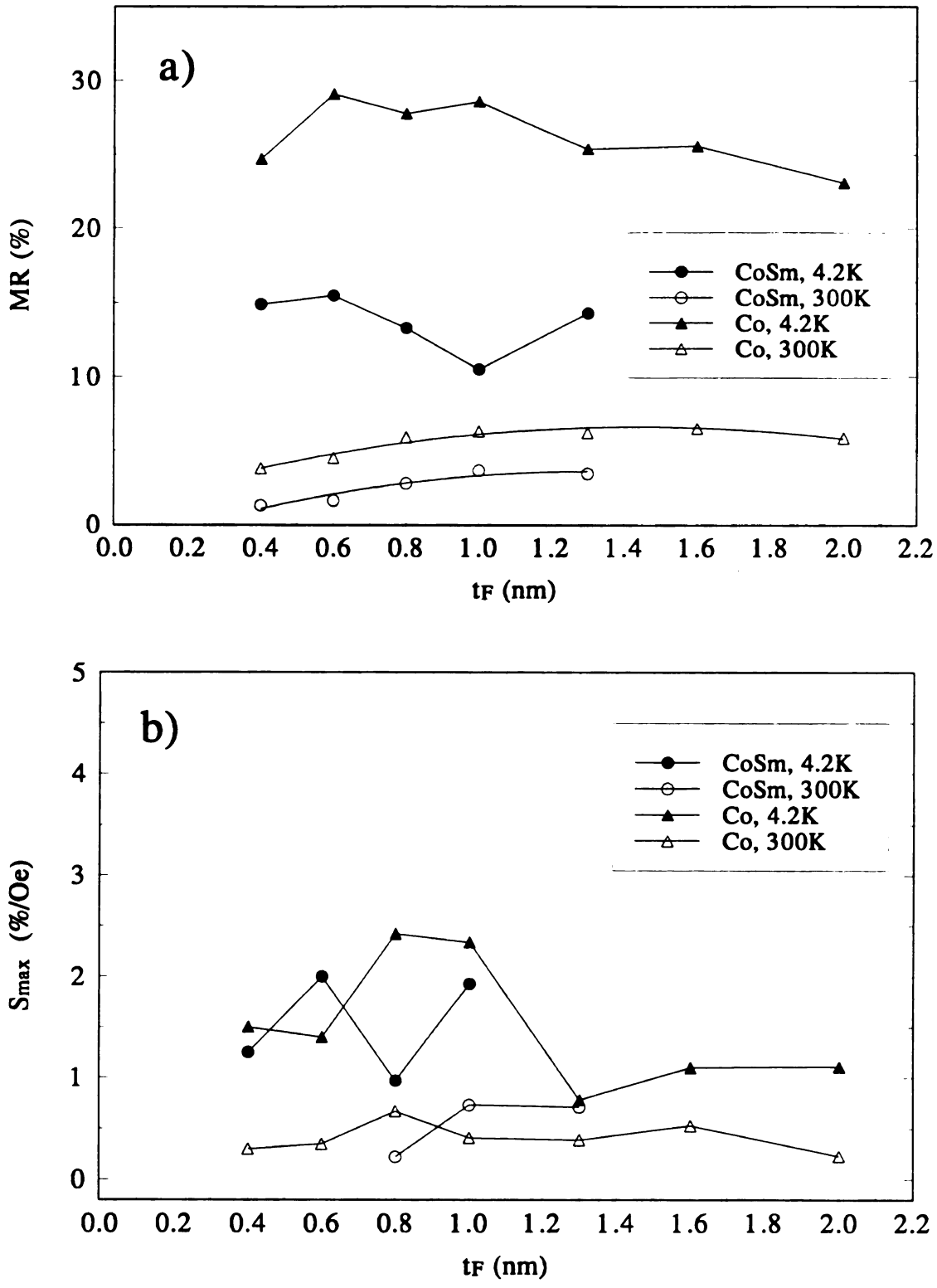

Figure 6.16: The a) CIP-MR and b) the maximum slope, $S = \Delta R / \Delta H$, of the CIP-MR are plotted as a function of t_F for samples of $[F(t_F)/Cu(4.0nm)/Py(4.0nm)/Cu(4.0)]\times 10$, where *F=Co* or *CoSm*. Lines are guides to the eye.

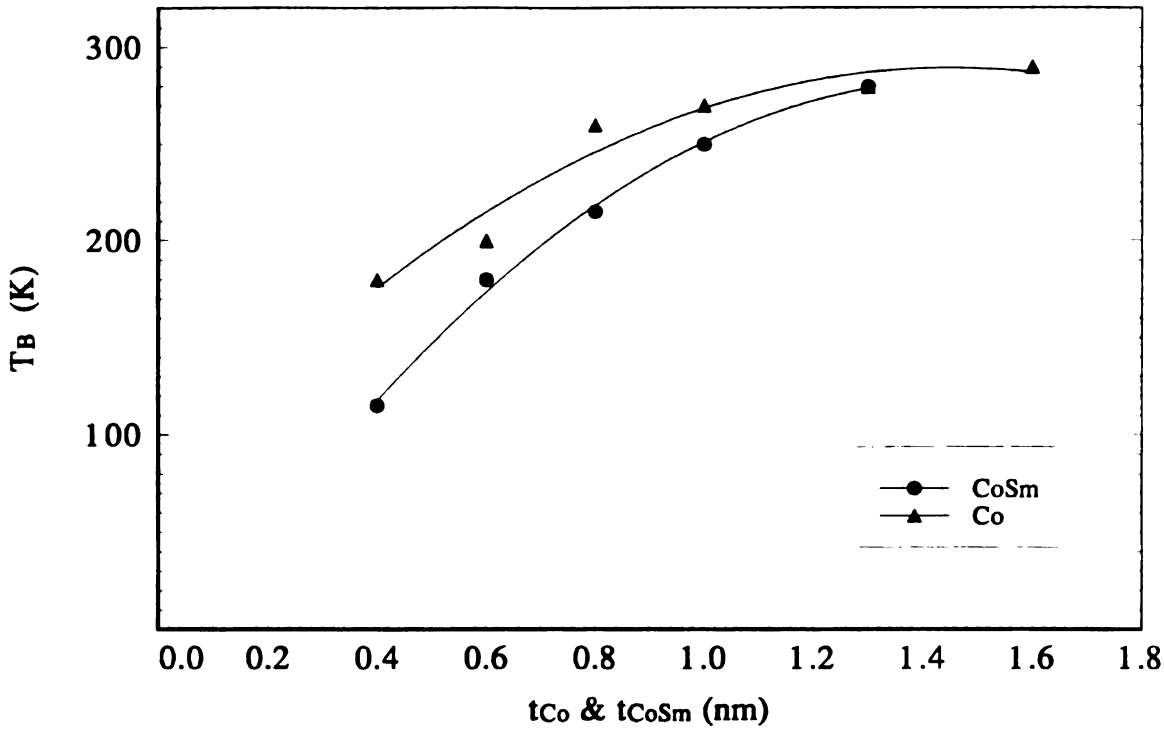

Figure 6.17: The blocking temperatures of *[F(t_F)/Cu(4.0nm)/Py(4.0nm)/Cu(4.0)]×10* samples plotted as function of t_F, where *F=Co* or *CoSm*. Lines are guides to the eye.

Studies[27,28,29] have shown that the size of CoSm cystallites is related to the structure of the underlying material. Typically, a grain size about 5nm is observed for CoSm with a 100nm underlayer of Cr[27,28,29]. XTEM pictures[27,28] show that columns formed in the Cr layer continue smoothly into the CoSm layer. However, no distinguishable columnar structure was observed in CoSm for 100nm Cu underlayers[28]. Furthermore, the absence of a CoSm peak in x-ray diffraction measurements showed that CoSm was amorphous in these samples. Although anisotropies can be large[30,31] for amorphous CoSm, they are about the same order of magnitude as the magnetocrystalline anisotropy of Co.

Columnar growth has been observed in multilayer systems made here at MSU. It seems likely that columnar growth in the Co/Cu/Py/Cu samples would be similar to columnar growth in the CoSm/Cu/Py/Cu samples which are sputtered under nearly identical conditions. This would tend to make the volume of the Co clusters and the CoSm clusters similar. This along with blocking temperature data from Tables 6.8a and 6.10a implies that $K_{Co} \approx K_{CoSm}$ and that adding the Sm did not increase the anisotropy of the Co clusters significantly.

Raising the Blocking Temperature (c) Growth in a Magnetic Field

Another way to change the anisotropy of the Co clusters is to grow the films in the presence of a strong magnetic field. During growth the presence of a strong magnetic field induces a strong uniaxial anisotropy in the multilayer along the direction parallel to the field (see Figure 2.4c). Presented here are preliminary studies done on samples with anisotropies induced during growth for multilayers with Py and for multilayers with Co.

In the same sputtering run, samples of *[Py(4.0nm)/Ag(4.0)nm]×20* were deposited with and without an induced easy axis. The samples with an induced easy axis were subjected to a magnetic field of approximately 2.6 kOe during growth. Figure 6.18 shows the magnetization of these samples with the measuring field applied both perpendicular and parallel to the induced easy axis in the plane of the film. The multilayer without the induced easy axis was rotated 90° with the applied field in the plane of the film. This sample shows the same magnetization curve for both orientations

with respect to the film, implying that the sample has no preferred direction in the plane of the film. The field grown sample does show an easy axis along the direction of the field. The magnetization along the induced axis flips rapidly near the H_C for Py (≈0.5Oe), reversing itself completely in just 1.0 Oe. The in-plane magnetization normal to the easy axis shows very little hysteresis, passes through the origin and completely reverses its direction in nearly 20Oe. These are indications that the Py layers are being coherently rotated away from induced easy axis. The induced in-plane anisotropy is calculated by finding the area between the magnetization curves along and normal to the easy axis. This gives $K=2.08\times10^3$ emu/cm^3, of the order of Py's magnetocrystalline anisotropy.

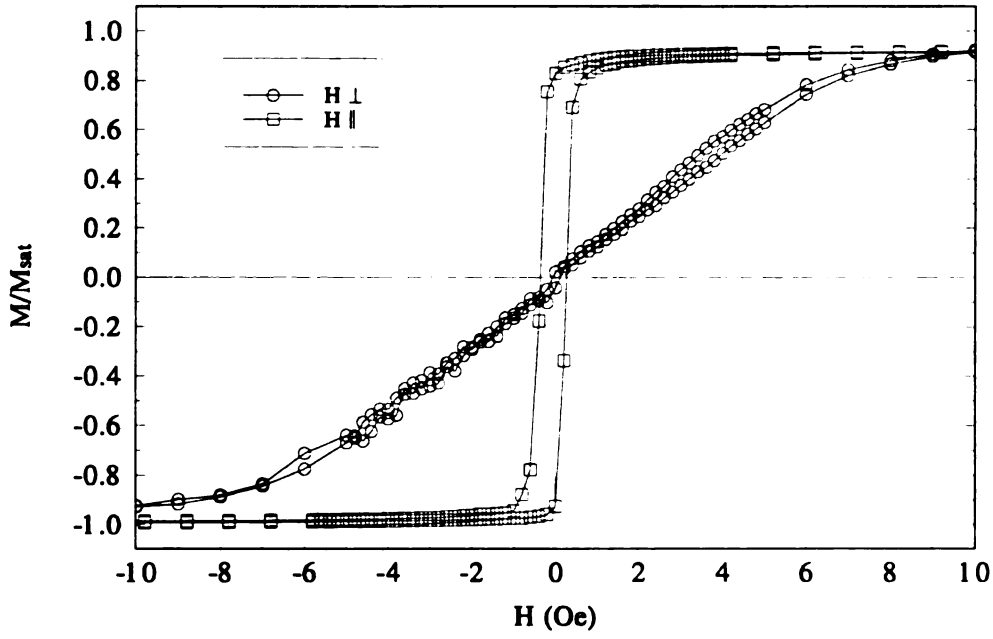

Figure 6.18: The magnetization hysteresis curves along (squares) and normal (circles) to the in-plane easy axis for a multilayer of *[Py(4.0nm)/Ag(4.0nm)]×20* at T=5.0K. The direction of the induced easy axis in the Py layers was defined during growth by a 2.6kOe magnetic field (see Figure 2.4c).

Samples of Co/Ag were also field grown to induce an easy axis in the plane of the film. Results for samples of *[Co(6.0nm)/Ag(6.0nm)]×20* are shown in Figure 6.19. The large hysteresis present in the in-plane, normal curve implies that the reversal of the magnetization is due to both coherent rotation and domain wall motion. There is a very noticeable difference between both in-plane curves. The one along the easy axis is much more square and reverses much faster than does the curve normal to the induced axis. The induced anisotropy for this sample is $K_f \approx 2.0 \times 10^4 erg/cm^3$, an order of magnitude less than the magnetocrystalline anisotropy of Co.

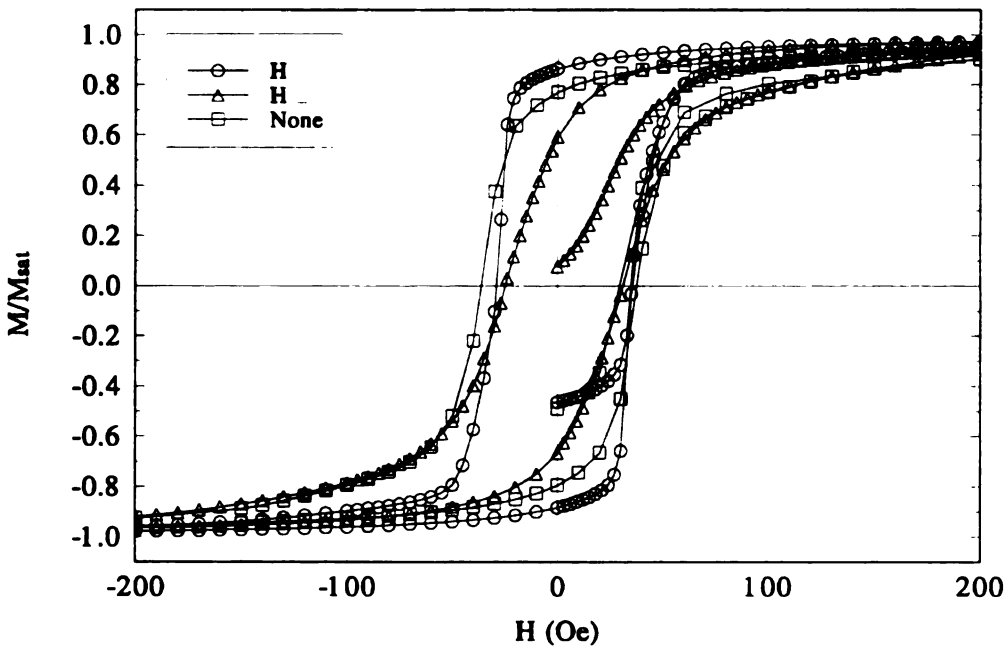

Figure 6.19: The magnetization hysteresis curves along (circles) and normal (triangles) to the in-plane easy axis for a multilayer of *[Co(6.0nm)/Ag(6.0nm)]×20* at T=5.0K. The direction of the induced easy axis in the Co layers was defined during growth by a 2.6kOe magnetic field (see Figure 2.4c). A similar sample without an induced anisotropy is also shown for comparison (squares).

It was hoped that inducing an anisotropy during a sample's growth would increase the anisotropy energy of the Co clusters so that T_B would be raised above room temperature. However, several samples exhibited T_B well below those samples made without an induced axis. This suggested a reduced Co volume. Both high and low angle X-ray diffraction measurements confirmed this suspicion. The samples made with the induced easy axis showed a smaller bilayer thickness. The magnets used to induce the easy axis must be changing the sputtering conditions of the plasma, resulting in a slower than expected rate of deposition. Careful monitoring of the target voltages and currents revealed a 10% drop in each when the magnets rotated over the sputtering source. The problem was dealt with by increasing the target voltages and currents 10% above that required to produce the desired deposition rate in zero field. However, it is unclear just how fast the sputtering sources adjust to the presence of the magnets when they are rotated over a source. X-ray diffraction measurements done on samples with this correction showed a bilayer thickness closer to the nominal value.

Although evidence for an induced in-plane anisotropy was observed in Co/Ag multilayers with thin discontinuous Co layers, it was unclear whether or not the anisotropy energy has increased. The lower T_B measurements indicate smaller Co cluster volumes, so that even if the clusters are harder magnetically (via the induced anisotropy), the reduced volume of the clusters could still shift T_B to lower temperatures.

The goal of increasing the blocking temperature of the Co clusters by inducing an anisotropy during growth was not realized. The inducing magnetic field slowed the rate of deposition producing smaller than expected Co clusters. The smaller cluster volumes

complicated our attempts to increase the anisotropy energy, KV, of the Co. However, the field does induce an anisotropy in magnetic multilayers. This should increase the magnetic contrast between the Co and Py in two ways. (a) The induced easy axis increased the remanent magnetization in the Co layers, as shown in Figure 6.19 for Co/Ag samples. (b) The induced easy axis caused the Py magnetization to completely reverse itself in just 1.0 Oe as shown in Figure 6.18 for Py/Ag samples. Combining these characteristics in a hybrid sample should increase the sensitivity of these multilayers.

GMR in CPP hybrid Multilayers

Experiments with a series of Ag based hybrids in which the Py thickness was varied were done to estimate the α for bulk Py. The samples were made in the usual CPP fashion, section 2.6, with superconducting Nb leads on top and bottom. A series of $[Co(0.4nm)/Ag(4.0nm)/Py(t_{Py})/Ag(4.0nm)]\times 20$ multilayers was measured at 4.2K. A 2.0nm layer of Co was deposited between the multilayer and each Nb lead to eliminate the proximity effect. The field dependence of the CPP resistance of a typical hybrid sample is shown in Figure 6.20. Comparing with Figure 6.7 one immediately sees that the CPP-MR is double the CIP-MR for the hybrid system, similar to the simpler Co/Ag[1,32], Co/Cu[33] and Py/Cu[34] systems. It was expected that the sensitivity of the hybrids in the CPP direction would also be doubled. However, the slope ($\Delta R/\Delta H$) where the Py flips actually *appeared* to be greater for the CIP part of the sample, for the following reason.

The field necessary to saturate the Co layers in these samples is ≈3-5kOe, about 5 times larger than any field applied to the Co/Cu, Co/CuX or Py/Cu systems studied previously. At 4.2K the Nb leads stay superconducting until a field of 10kOe is applied. The Nb/Co boundary resistance increases slightly as the field approaches 10kOe, after

which a rapid rise in the resistance is observed. However, before the transition from the superconducting state to normal state, flux penetration occurs for type II superconductors[35] like Nb. Flux penetration in the Nb leads is thought to be a problem only when the applied fields are much greater than 1.0kOe. Therefore the previous CPP studies are unaffected. The high fields necessary to saturate the hybrid samples with thin Co layers are well above this critical field. Lowering the applied field from 6-7kOe, traps the penetrating flux inside the sample. As the applied field is reversed both the trapped field and the coercive field of the Py must be overcome, to reorient the Py magnetization. Since the CIP resistance is dominated by the two narrow strips well away from the CPP sample (see Figure 1.5), the trapped field only affects the CPP data resulting in a CIP sensitivity which is apparently greater than the CPP sensitivity.

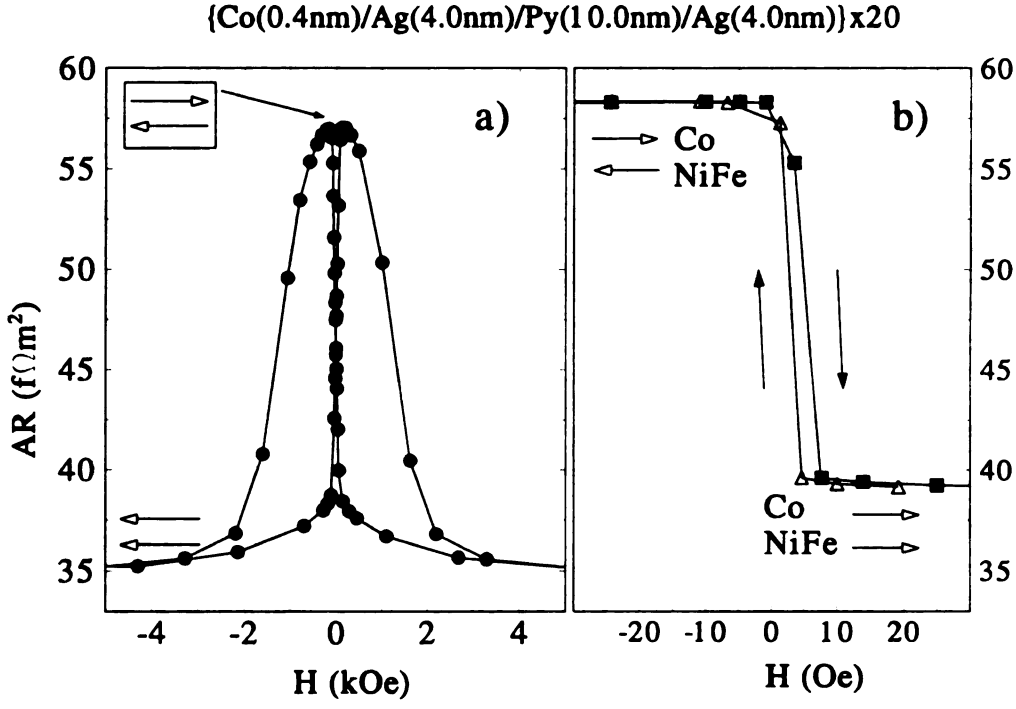

Figure 6.20 : In a) AR(H) for *[Co(0.4nm)/Ag(4.0nm)/Py(10.0nm)/Ag(4.0nm)]x20* is plotted. The large saturation field is indicative of island-like Co layers. Plotted in b) is AR(H) in the vicinity of the flipping Py moments after the trapped flux has been released (see text). The slope, $\Delta R/R$, is a factor of 10 greater in b) than in a) the region where the Py flips.

Experiments to test this hypothesis were done. After the sample is taken through one complete cycle and brought back to zero field, the temperature of the multilayer is raised to just above the T_C of the superconductor, ≈8K in sputtered Nb films. Above T_C the Nb is normal and the trapped field is released. The T_B of the Co islands is about 5 times greater than the T_C for Nb, so that the increased temperature will not thermally reorient a significant number of the Co clusters. After releasing the trapped field, the sample is cooled to 4.2K and resistance measurements are made over the range of $\pm H_S$ for Py. This improved the slope of the CPP part to 10%/Oe, nearly double that of the CIP part. This is consistent with the doubling of the MR from the CIP to CPP geometries since the MR of each occurs for the same change in field. Figure 6.20b shows the field dependence of the resistance when cycled at low field after the trapped field is expelled.

The two channel model for electron transport in CPP multilayers is used to analyze this system. The parameters, β and γ, describing the scattering in the hybrid system are much more difficult to ascertain because $AR^{+}(AP) \neq AR^{-}(AP)$. As a consequence $AR_T(AP)$ calculated from the equivalent resistance circuit, becomes a much more complex quantity and the previous method of obtaining β and γ no longer applies. Therefore, the resistance measurements are compared with calculated AR_T values based on the parallel combination of equations 4.7a for the AP state and 4.7b for the P state. Figure 6.21 shows both measured and calculated values of $AR(H_p)$ and $AR(H_S)$ as the Py thickness is varied. The H_p resistance is chosen for comparison with the calculated AP state because this resistance is the highest for each sample.

The model used for comparison purposes adds in series the resistivity of each metal: Ag, Co and Py along with the interface resistances of Co/Ag and Py/Ag for each spin channel in equations 4.7. The parameters used for the calculated resistances are given in Table 6.11. The parameters for Co and Co/Ag were derived from a detailed study of Co/Ag multilayers done by S.F. Lee[36] . Those listed as Py/Ag parameters are estimates not based on a detailed study of Py/Ag multilayers. They are based on the assumption that

the values $AR_{Py/Ag}$ and $\gamma_{Py/Ag}$ are not very different from those of Py/Cu, which was studied in detail in chapter 5. There is some justification for this rather gross assumption in that a comparison of the Co/Cu and Py/Cu parameters in Tables 5.6 and 5.10 reveals fairly similar interface values for both systems. In addition, Lee's[36] Co/Ag interface values differ only slightly from those of Co/Cu in chapter 5. It would seem that the F/N interface parameters are somewhat insensitive to which normal metal is used, Cu or Ag. Therefore using the Py/Cu values in place of the Py/Ag ones may not be completely without merit[37].

Table 6.11: Parameters used in fitting the CPP *[Co(0.4nm)/Ag(4.0nm)/Py(t_{Py})/Ag(4.0nm)]×20* samples.

$2AR_{S/F}$	6.1	fΩm^2
ρ^*_{Co}	100	nΩm
ρ_{Ag}	10	nΩm
β_{Co}	0.56	
γ_{Co}	0.79	
$AR^*_{Co/Ag}$	0.60	fΩm^2
ρ^*_{Py}	164	nΩm
β_{Py}	0.46	
γ_{Py}	0.81	
$AR^*_{Py/Ag}$	0.46	fΩm^2

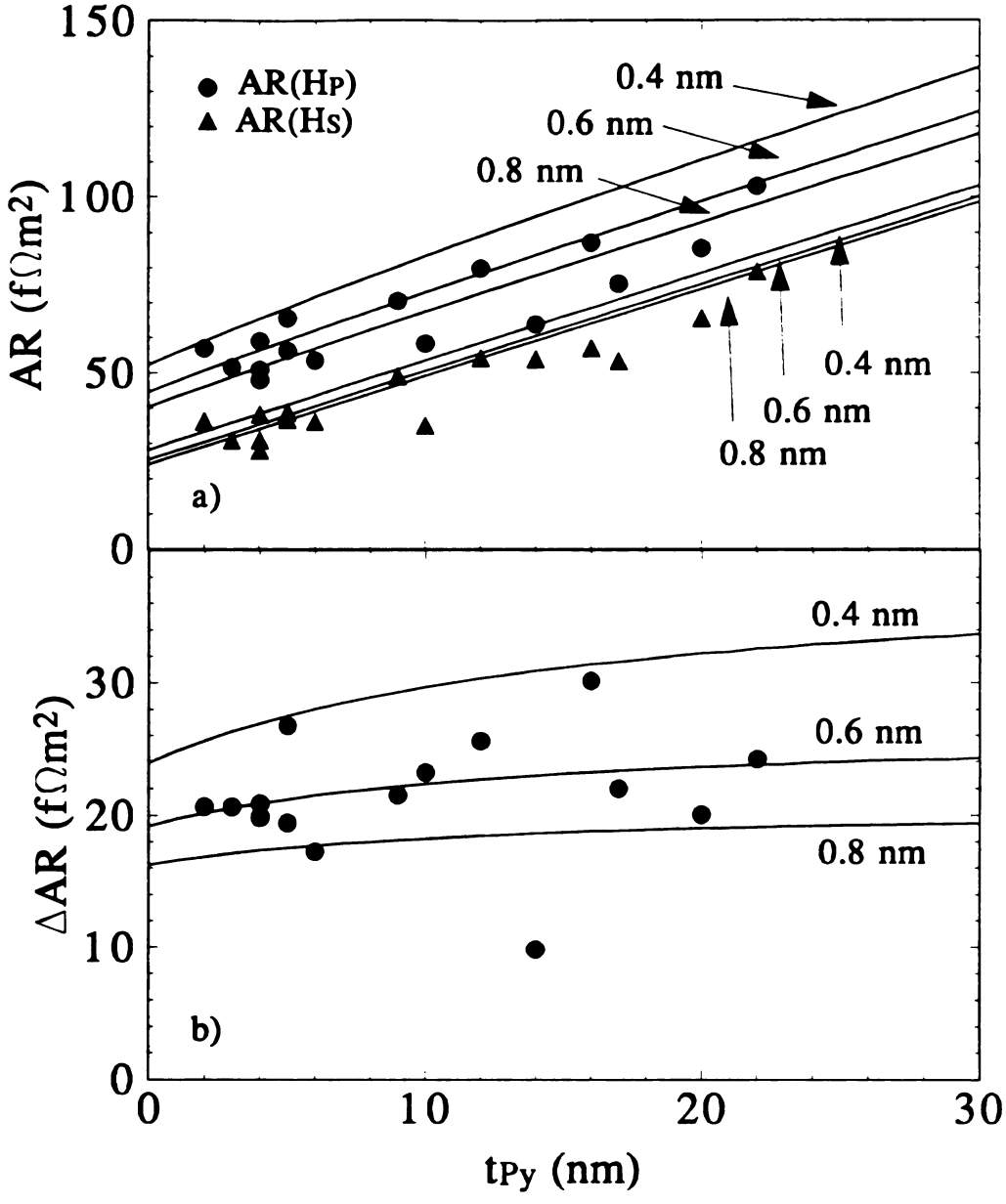

Figure 6.21: In a) $AR(H_P)$ and $AR(H_S)$ are plotted as a function of t_{Py}. Plotted in b) as a function of t_{Py} is $\Delta AR=(H_P)-AR(H_S)$. In both a) and b) the lines represent the values predicted by the two channel model assuming $t'_{Co} = 0.4$, 0.6 and 0.8nm along with $\ell_{sf}^{Py} = \infty$.

More problematic to the analysis of this CPP hybrid system is the thin Co layer. A 0.4nm layer of Co is definitely not continuous[2,3,4,14]. This must affect the transport properties of the sample, since a thin discontinuous Co layer provides regions in which the electrons may pass from one Py layer to the next Py layer without being scattered by the Co layer. Since the Py magnetizations are pointing in the same direction, a portion of the sample acts as if it is never in the AP state no matter what the relative orientation of the Co and Py magnetizations. As a crude way of compensating for this, equations 4.7 have been modified in the following way. First it is assumed that the total volume of Co in each Co layer is that of a nominally complete 0.4nm thick layer without clumping. To allow for Co islands, the thickness of the Co layers is increased while at the same time the area of these layers is reduced, keeping the total Co volume constant. These modified equations are given below.

$$AR_{AP}^{(+)} = 2N[R_{Co}^{(+)} + 2\rho_{Ag}t_{Ag} + \rho_{Py}^{*}t_{Py}(1-\beta_{Py}) + 2AR_{Py/Ag}^{*}(1-\gamma_{Py})] \qquad 6.7a$$

$$AR_{AP}^{(-)} = 2N[R_{Co}^{(-)} + 2\rho_{Ag}t_{Ag} + \rho_{Py}^{*}t_{Py}(1+\beta_{Py}) + 2AR_{Py/Ag}^{*}(1+\gamma_{Py})] \qquad 6.7b$$

where

$$R_{Co}^{(+)} = \rho_{Co}^{*}t_{Co}^{'}(1+\beta) + 2AR_{Co/Ag}^{*}(1+\gamma)t_{Co}/t_{Co}^{'}$$
$$R_{Co}^{(-)} = \rho_{Co}^{*}t_{Co}^{'}(1-\beta) + 2AR_{Co/Ag}^{*}(1-\gamma)t_{Co}/t_{Co}^{'}$$

$R_{Co}^{(\pm)}$ represent the effective Co resistance due to the clusters. The Co/Ag interface resistance is scaled by $t_{Co}^{'}$, the effective Co thickness. A in the last term is modified by the factor $t_{Co}/t_{Co}^{'} <$. A parallel combination of equations 6.7 models the resistance of the AP state. Similarly the P state resistance is modeled by a parallel combination of equations 6.8.

$$AR_{P}^{(+)} = 2N[R_{Co}^{(+)} + 2\rho_{Ag}t_{Ag} + \rho_{Py}^{*}t_{Py}(1-\beta_{Py}) + 2AR_{Py/Ag}^{*}(1-\gamma_{Py})] \qquad 6.8a$$

$$AR_P^{(-)} = 2N[R_{Co}^{(-)} + 2\rho_{Ag}t_{Ag} + \rho_{Py}^{*}t_{Py}(1+\beta_{Py}) + 2AR_{Py/Ag}^{*}(1+\gamma_{Py})] \qquad 6.8b$$

where

$$R_{Co}^{(+)} = \rho_{Co}^{*}t_{Co}^{'}(1-\beta) + 2AR_{Co/Ag}^{*}(1-\gamma)t_{Co}/t_{Co}^{'}$$
$$R_{Co}^{(-)} = \rho_{Co}^{*}t_{Co}^{'}(1+\beta) + 2AR_{Co/Ag}^{*}(1+\gamma)t_{Co}/t_{Co}^{'}$$

This model for the hybrid CPP resistance assumes that $\ell_{sf} = \infty$ for all three components, Ag, Co and Py. This is a valid assumption for the relatively thin Co and Ag layers, but as the thickness of the Py increases one might expect to see finite SDL effects occur in the Py layers. The Valet-Fert theory for finite SDL effects in magnetic multilayers has not been completed for systems containing two different magnetic components[38], however, the extreme case of $\ell_{sf}^{Py} = 0$ is easy to model. For this case the series resistor model shown in Figure 4.3 is modified so that in each Py layer the two spin currents mix together, resulting in the equivalent resistor network for a single unit cell shown in Figure 6.22. Multiplying the equivalent resistance in Figure 6.22 by the number of unit cells (N=20) and then adding on the Nb/Co boundary resistance gives the total calculated resistance necessary for comparison with the measured values of AR_T.

The calculated values in figures 6.21 and 6.23 are based upon equations 6.7 and 6.8 for both ℓ_{sf}^{Py} limits. The $AR(H_P)$ and $AR(H_S)$ data show some scatter but are generally below the values predicted by both ℓ_{sf}^{Py} limits for complete 0.4nm Co layers. The data seem most consistent with an effective Co thickness of 0.6nm for the average Co island. Figures 6.21b and 6.23b plot ΔAR, the difference between $AR(H_P)$ and $AR(H_S)$, as a function of t_{Py}. This is done to eliminate errors common to both the AP and P states. Although the ΔAR data was scattered, agreement appears to be better with the $\ell_{sf}^{Py} = \infty$ model since all the data fall below the fit which assumed a continuous Co layer nominally 0.4nm thick. Whereas for the $\ell_{sf}^{Py} = 0$ model shown in Figure 6.23b, a significant fraction of the ΔAR data are well above the 0.4nm prediction. For the model to fit these points

the interfacial scattering would have to be increased and the bulk scattering reduced (to keep the Co volume constant). This seems to be contrary to the NMR structural studies done on Co/Ag by van Alphen *et al.*[4] which showed a significant bulk signal down very thin Co layers. Furthermore, the $\ell_{sf}^{Py} = \infty$ model is more sensitive to small fluctuations in the Co thickness than is the $\ell_{sf}^{Py} = 0$ model. Only a fluctuation of 0.4nm in the Co thickness describes all the data in Figure 6.21b, whereas a number of points lie outside this fluctuation in the Co thickness in Figure 6.23b.

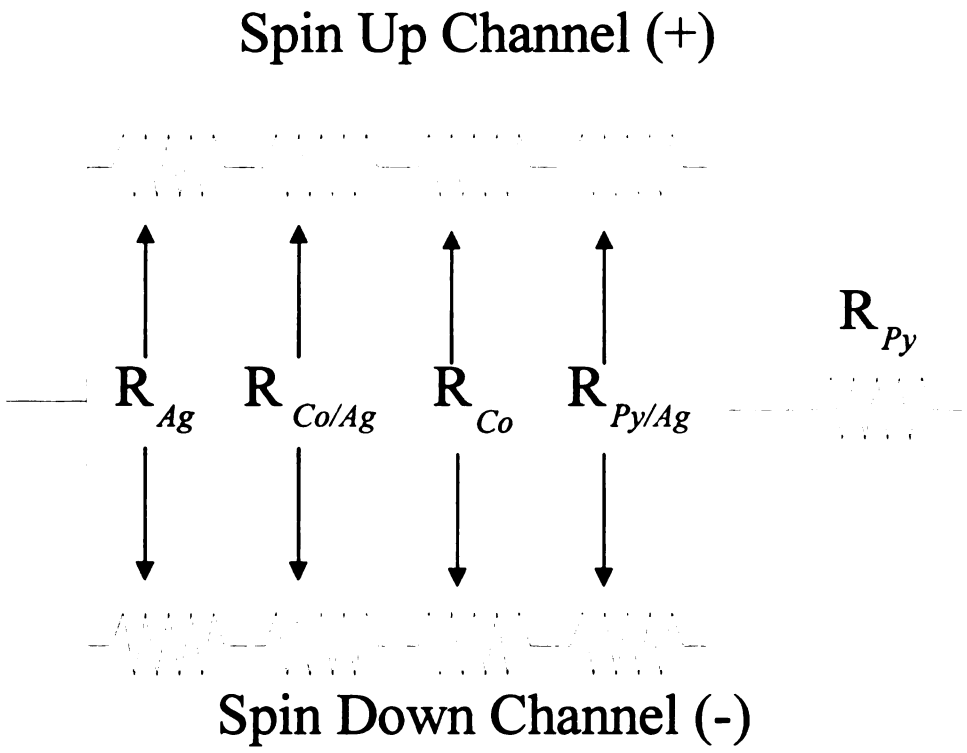

Figure 6.22: Equivalent resistor model for $\ell_{sf}^{Py} = 0$.

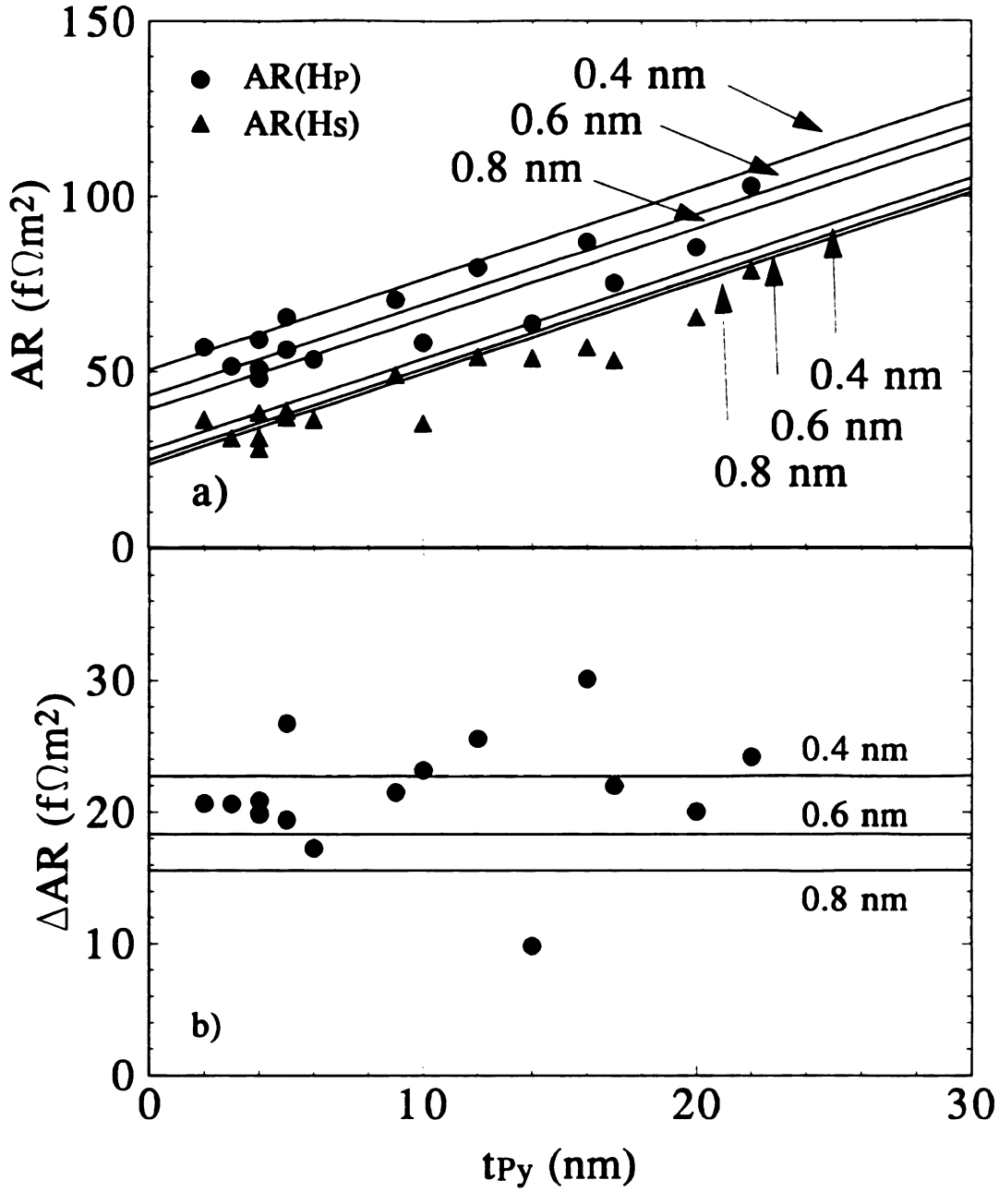

Figure 6.23: In a) $AR(H_P)$ and $AR(H_S)$ are plotted as a function of t_{Py}. Plotted in b) as a function of t_{Py} is $\Delta AR=AR(H_P)-AR(H_S)$. In both a) and b) the lines represent the values predicted by the two channel model assuming $t_{Co}^{'} = 0.4$, 0.6 and 0.8nm along with $\ell_{sf}^{Py} = 0$.

Samples with extremely thick layers of Py were made to see if the SDL effects were discernible on a larger scale. Figure 6.24 includes these two data points along with the predictions for both models with an effective Co thickness of 0.6nm. Both these points are lower than the 0.6nm prediction for the $\ell_{sf}^{Py} = \infty$ model. This suggests a slight finite SDL effect but when the 0.8nm prediction is considered these two points are consistent with an infinite Py SDL. In Figure 6.24a the $AR(H_P)$ and $AR(H_S)$ data for the thick Py samples deviates strongly from the linear behavior of the $AR(H_P)$ and $AR(H_S)$ data for thinner Py samples. Neither SDL limit predicts such curvature as the Py becomes thicker. Some other mechanism, possibly a structural change in the sample for larger Py thickness must be causing the lower than expected resistances.

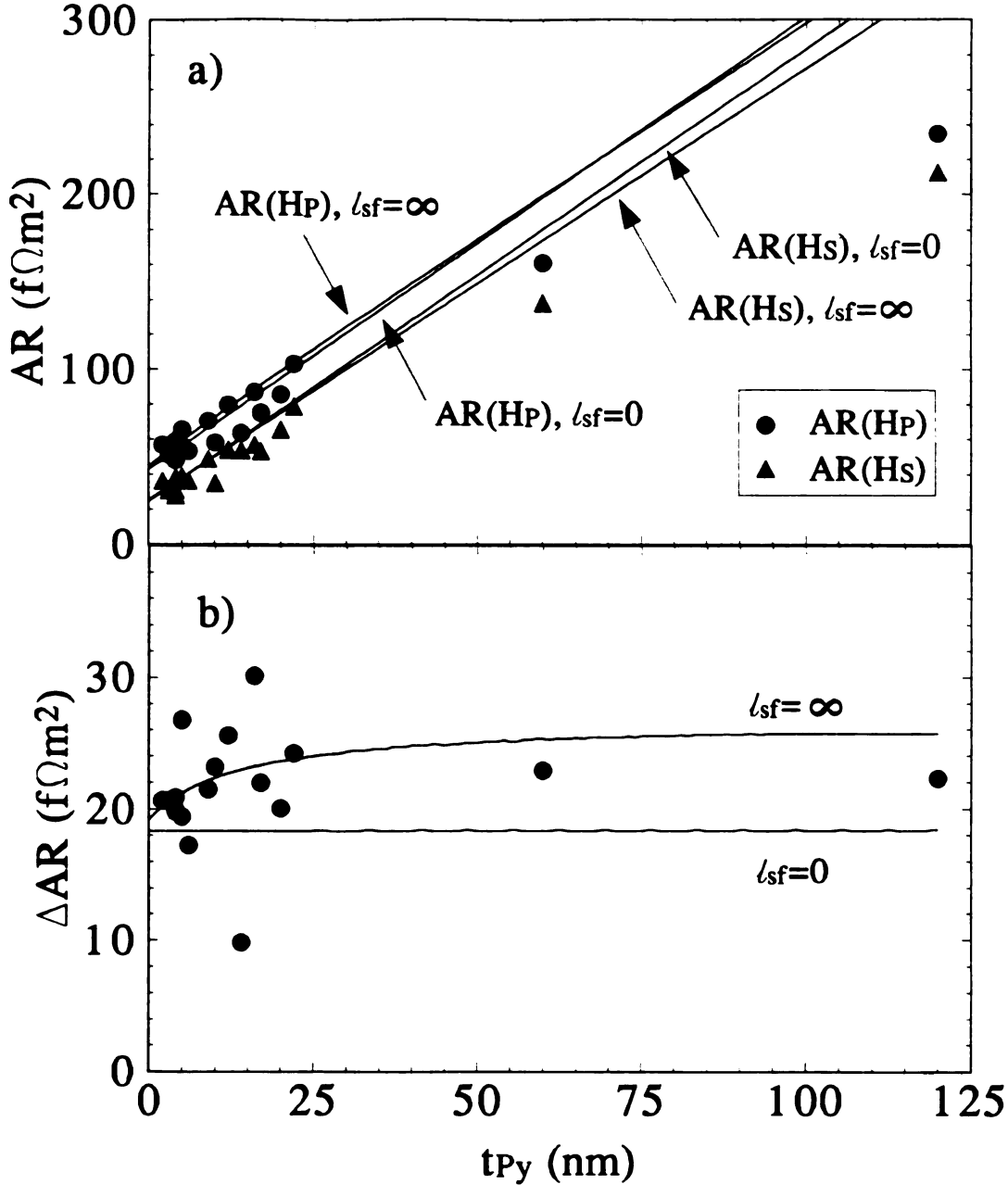

Figure 6.24: In a) $AR(H_P)$ and $AR(H_S)$ are plotted as a function of t_{Py}. Plotted in b) as a function of t_{Py} is $\Delta AR=AR(H_P)-AR(H_S)$. In both a) and b) the lines represent the values predicted by the two channel model assuming $t'_{Co} = 0.6$nm and either $\ell_{sf}^{Py} = 0$ or $\ell_{sf}^{Py} = \infty$.

Table 6.12: CPP-AR values for the *[Co(0.4nm)/Ag(4.0nm)/Py(t_{Py})/Ag(4.0nm)]×20* series.

Sample #	t_{Py} (nm)	Area (mm^2)	AR(H_P) ($f\Omega m^2$)	AR(H_S) ($f\Omega m^2$)
558^{01}	2.0	1.194	56.95	36.32
558^{02}	4.0	1.295	59.09	38.22
558^{03}	9.0	1.545	70.50	49.00
558^{04}	16.0	1.459	87.12	56.98
558^{05}	4.0	1.584	48.01	28.09
559^{02}	20.0	1.429	87.12	65.50
559^{03}	6.0	1.540	53.56	36.30
559^{04}	12.0	1.433	79.71	54.16
559^{05}	3.0	1.590	51.58	30.96
559^{06}	4.0	1.514	50.85	31.04
571^{02}	22.0	1.481	103.08	78.86
571^{03}	5.0	1.254	65.59	38.85
571^{04}	17.0	1.584	75.32	53.33
571^{05}	14.0	1.375	63.73	53.90
605^{01}	60.0	1.312	161.0	138.1
605^{02}	5.0	1.326	56.30	36.89
605^{04}	10.0	1.260	58.30	35.12
617^{01}	120.0	1.431	235.0	212.7

6.3 Inverted Giant Magnetoresistance

All previous studies presented here have been done on systems in which the resistance drops with the application of a magnetic field. This type of GMR is sometimes referred to as Giant *negative* Magnetoresistance since the resistance decreases as the field increases. Systems which exhibit an increase in resistance upon saturation have a *positive* GMR. As a historical note, the term inverted or reversed is also used for positive GMR systems since the effect was first discovered in multilayers exhibiting negative GMR. The reason why negative GMR is the most common can be seen from the crude band pictures in Figure 4.1. For any of these band models $D^{\uparrow}>D^{\downarrow}$ which means $\rho^{\uparrow}>\rho^{\downarrow}$ and $\alpha=\rho^{\downarrow}/\rho^{\uparrow}<1$. Clearly to obtain a positive GMR one needs detailed band structures with $D^{\downarrow}>D^{\uparrow}$ or spin dependent scattering at the interface which gives a positive MR.

The inverted GMR systems differ from the normal GMR systems in that α is not the same for all magnetic layers throughout the multilayer. Normal MR samples have all magnetic layers with either $\alpha>1$ or $\alpha<1$, whereas an inverted sample has magnetic layers which alternate α between $\alpha>1$ and $\alpha<1$. (See Figure 4.8.) The alternating α's should produce a short circuiting of the current for the AP state, leading to a lower resistance in the AP state than in the P state.

CIP-MR measurements were performed at room temperature with the usual four point probe technique on multilayers of $[M_1/Cu(t_{Cu})/M_2/Cu(t_{Cu})]\times 5$, where M_1 is itself a sandwich of *Fe(1.2nm)/Cr(0.4nm)/Fe(1.2nm)* and M_2 is a single *Fe(1.5nm)* layer as

illustrated in Figure 6.25. The Fe/Cu interfaces are believed to have $\alpha > 1$ from electronic structure arguments[39,40]. The trilayer of Fe and Cr that forms M_1 is believed to have $\alpha < 1$ by analogy with measurements made for Cr impurities in Fe[41] and also by electronic structure arguments[40]. The thin 0.4nm Cr thickness is chosen so that the two 1.2nm Fe layers will be strongly ferromagnetically coupled together, essentially behaving as a single magnetic entity.

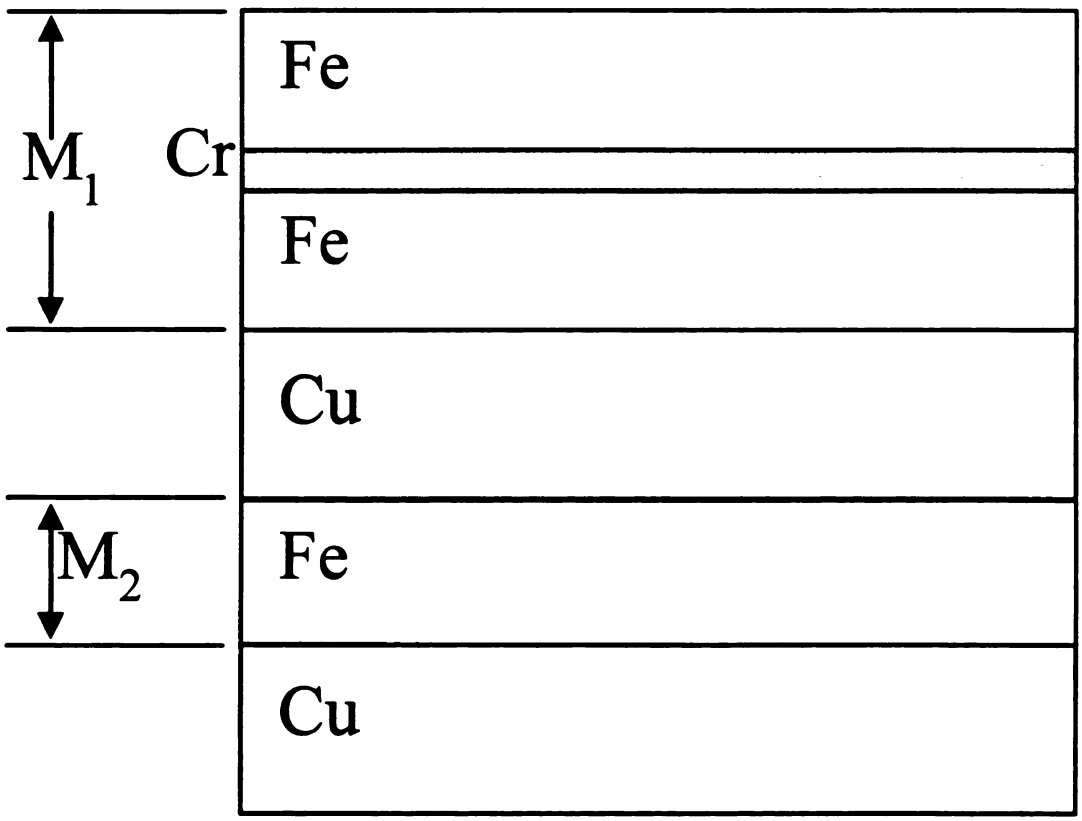

Figure 6.25: Schematic representation of the structure of $[M_1/Cu(t_{Cu})/M_2/Cu(t_{Cu})]\times 5$ where M_1=*Fe(1.2nm)/Cr(0.4nm)/Fe(1.2nm)* and M_2=*Fe(1.5nm)*.

The AP state of these multilayers is brought about by antiferromagnetic exchange coupling through the Cu layer. Experimental results for sputtered Fe/Cu multilayers[42,43] indicate a maximum in the AF coupling at $t_{Cu}=1.4nm$. Samples with t_{Cu} ranging from 1.0nm to 2.0nm were made to find the thickness of Cu which gives the maximum AF coupling between M_1 and M_2.

A positive MR was observed in several samples similar to the one shown in Figure 6.26. The maximum inverted MR is seen for $t_{Cu}=1.6nm$, close to the 1.4nm expected from the Fe/Cu data[42,43]. The MR curves in Figure 6.26a are similar for fields in the plane of the film, applied both parallel and perpendicular to the current direction. This demonstrates that the observed MR is not attributable to the anisotropic magnetoresistance, (AMR), resulting from the spontaneous resistivity anisotropy of ferromagnets[44,45]. The AMR measured in these samples is less than 0.2%, an order of magnitude below those shown in Figure 6.26a.

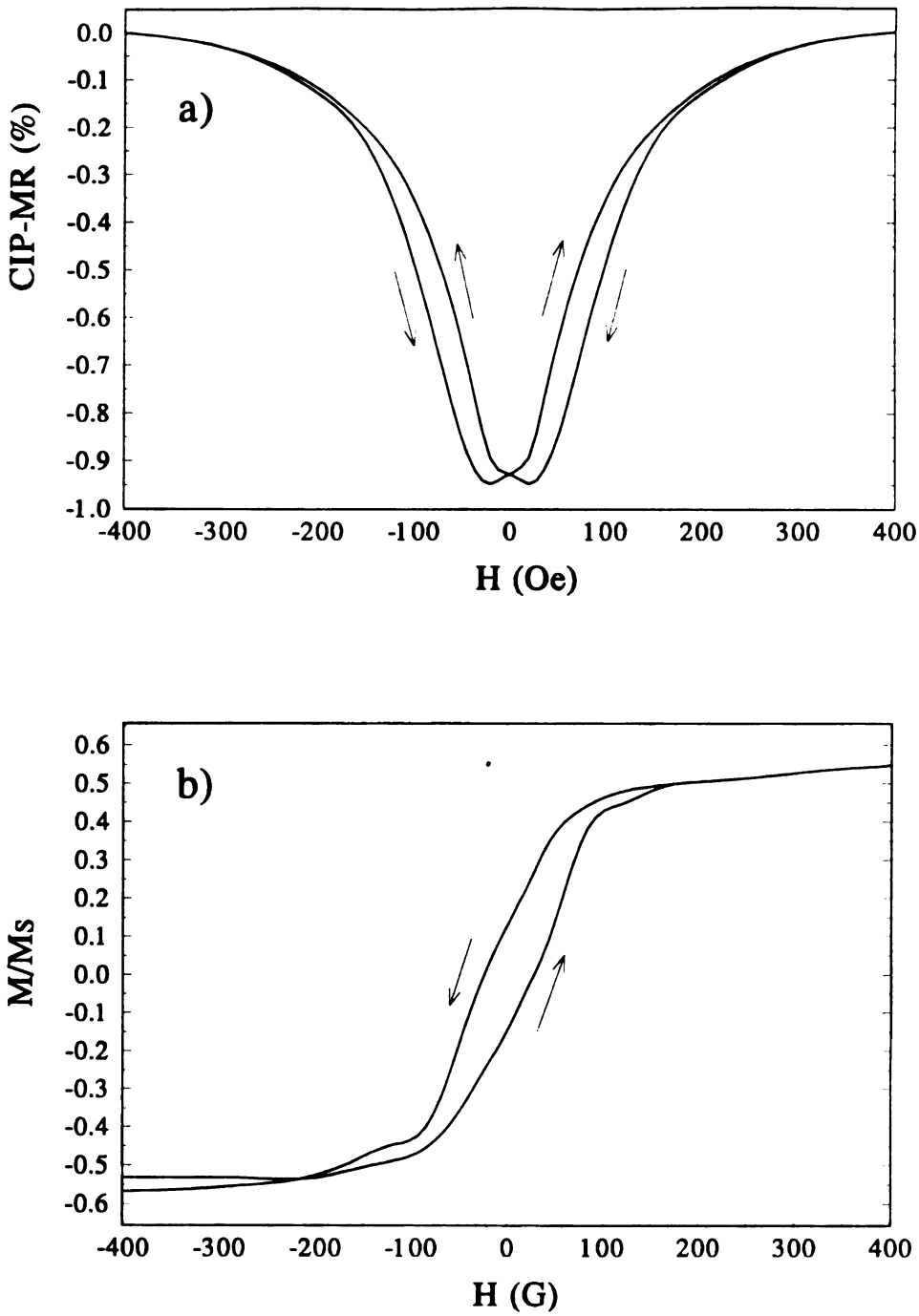

Figure 6.26: The low field behavior at 300K of a) the CIP-MR and b) the magnetization for $[M_1/Cu(1.6nm)/M_2/Cu(1.6nm)]\times 5$.

The magnetization curve for the $t_{Cu}=1.6nm$ sample given in Figure 6.26b provides indications that AF coupling is present in the sample. The remanent magnetization is only 14% of the magnetization at saturation, typical of AF coupling in multilayers. The low saturation field ≈ 150Oe is also typical of relatively weak AF coupling in Fe/Cu[42,43]. The usual correlations between the field dependence of the resistivity and the magnetization are noted. The saturation fields are both close to 150Oe and the minima in the MR curve are close to the coercive fields of the multilayer. Further evidence supporting AF coupling between the Fe/Cr/Fe trilayers and the Fe layers through the Cu spacer layer is found in the inverted MR's dependence on the Cu thickness. In Figure 6.27b the inverted MR is plotted as a function of the Cu spacer thickness. Although the inverted MR is much smaller than that of the Fe/Cu system, Figure 6.27a, both systems exhibit an oscillatory MR with the spacer thickness. Peaks in the MR are attributed to strong AF exchange coupling through that particular thickness of the normal metal spacer layer[6,46]. Both systems in Figure 6.27 couple Fe layers through a Cu spacer layer, so it is reasonable to expect that each system should have a maximum in the magnitude of the MR at about the same Cu thickness, 1.4nm.

Careful examination of Figure 6.26 reveals that although the hysteresis of both the MR and magnetization curves disappear by 150Oe, both are slowly changing with field. Finally at 10kOe both the magnetization and the MR become completely saturated. However, the MR curve of Figure 6.28a now shows that the small inverted effect seen at low field sits atop a very strongly coupled normal effect, which is double the inverted MR. This slow increase in the magnetization was also observed in separate Fe/Cr/Fe

samples similar to M_1 in the inverted system. The magnetization data for both the simple Fe/Cr/Fe samples and the more complex M_1/Cu/M_2/Cu systems suggest that the coupling across the Cr layer is not perfectly ferromagnetic but a mixture of AF and F coupling which is inducing a tilt[47] between the Fe layer on either side of the Cr layer. A straightforward calculation shows that an average tilt of 59° corresponds to the intermediate saturation step of 70% of M_S, derived by a linear extrapolation to zero field in Figure 6.28b.

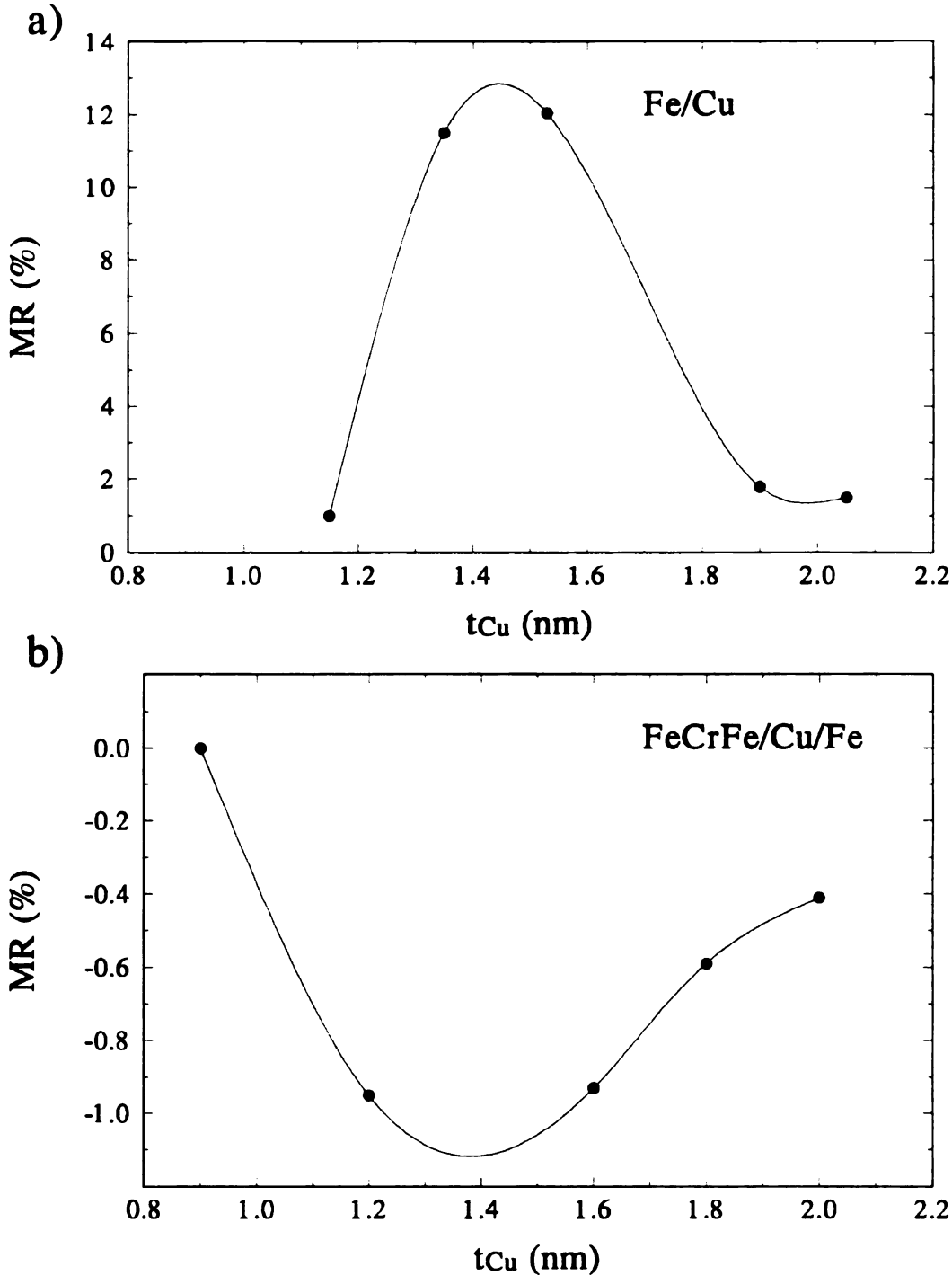

Figure 6.27: The variation of the MR with the Cu spacer thickness for a) Fe/Cu multilayers from Petroff, *et al.*[42,43] and b) $[M_1/Cu(t_{Cu})/M_2/Cu(t_{Cu})]\times 5$ samples where M_1 consists of an *Fe(1.2nm)/Cr(0.4nm)/ Fe(1.2nm)* trilayer and M_2 is a single *Fe(1.5nm)* layer.

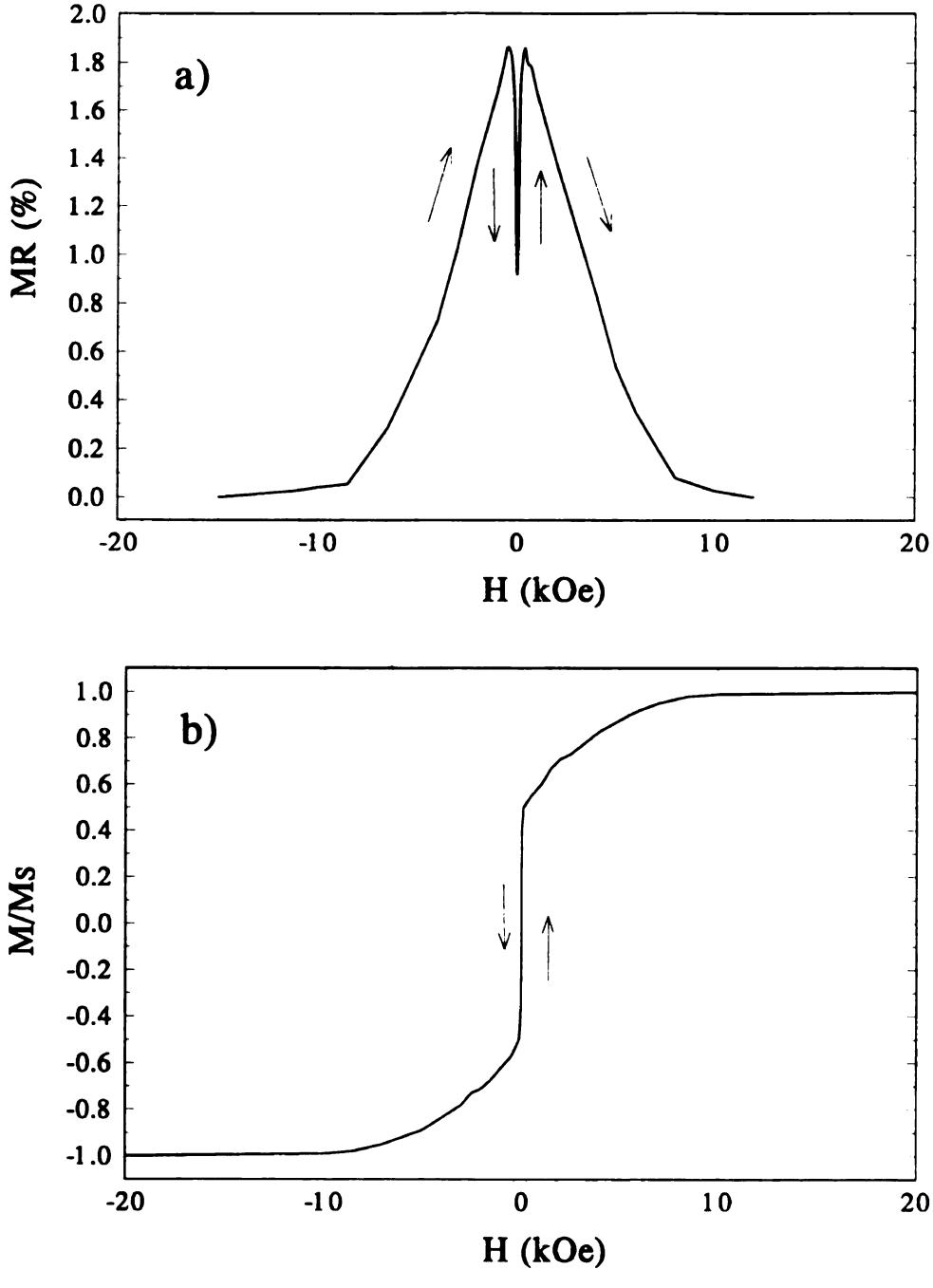

Figure 6.28: The high field behavior of a) the CIP-MR and b) the magnetization of the sample in Figure 6.28. The hysteresis is not seen on this scale.

Applying a strong magnetic field to improve the parallel alignment of the Fe moments on either side of the Cr spacer layer is consistent with the observed high field MR behavior. The inset of Figure 6.28a shows the MR of a *[Fe(1.2nm)/Cr(0.6nm)]×10* multilayer exhibiting high field behavior similar to that shown by the $M_1/Cu/M_2/Cu$ multilayers in both the magnitude of the MR and the magnitude of the saturation field.

As a further test, samples were prepared in which $M_1=M_2$ so that α_1 and α_2 would be the same for every magnetic layer. Data previously published[42,43] for the Fe/Cu system showed the normal negative MR. Similarly, multilayers with $M_1=M_2=Fe/Cr/Fe$ also exhibited the normal negative MR over the entire field range. This test confirms that the α for the Fe/Cr/Fe trilayer must be different from the α for Fe/Cu, since the inverted MR only appears when $M_1=Fe/Cr/Fe$ and $M_2=Fe$ and vice versa. As yet it is not possible to determine whether $\alpha_1 > 1$ or $\alpha_2 > 1$ from these MR measurements.

The magnitude of the inverted MR $\approx$1% is smaller than the few % predicted by the Camley-Barnas free electron model[48]. This may be due to either or both of the following[49]: Recently, non-free electron models have shown that channeling effects by the periodic potential of multilayers can considerably change the magnitude of the MR predicted by free electron models[5,50]. The nature of M_1 necessitates that both Fe/Cu and Fe/Cr interfaces exist for this magnetic layer. The small inverted MR's may be a result of the competition between the α's at the Fe/Cu and Fe/Cr interfaces in M_1 making the overall α for M_1 just slightly less than one. An α close to one would tend make the scattering in each spin channel about the same, severely reducing the MR.

Recently another type of multilayer system was shown to have an inverted MR. Renard, *et al.*[51] showed that CIP multilayers of FeV/Au/Co/Au with V concentrations of 30 at.% in Fe produced an inverted MR. This system clearly demonstrated the inverted effect without the complication of a large background normal MR seen for the system mentioned above. Electrons near the Fermi level in the *3d* band of the FeV alloy are strongly scattered in the spin up band resulting in an $\alpha<1$ for the FeV alloy. The Co/Au interface provides $\alpha>1$ necessary for the realization of the inverted MR. The inverted MR's reported by Renard[51] are also quite small $\approx$1%.

The first CPP measurements of an inverted MR were made at MSU by A. Barthélémy[52] on a similar FeV multilayer system, FeV/Cu/Co/Cu. This system combined the principles used for the hybrid system, i.e., discontinuous Co layers for increased magnetic contrast, with $\alpha<1$ for FeV. Figure 6.29 shows a typical CPP inverted MR. Currently, CPP resistance measurements of this system are being continued by S.Y. Hsu at MSU.

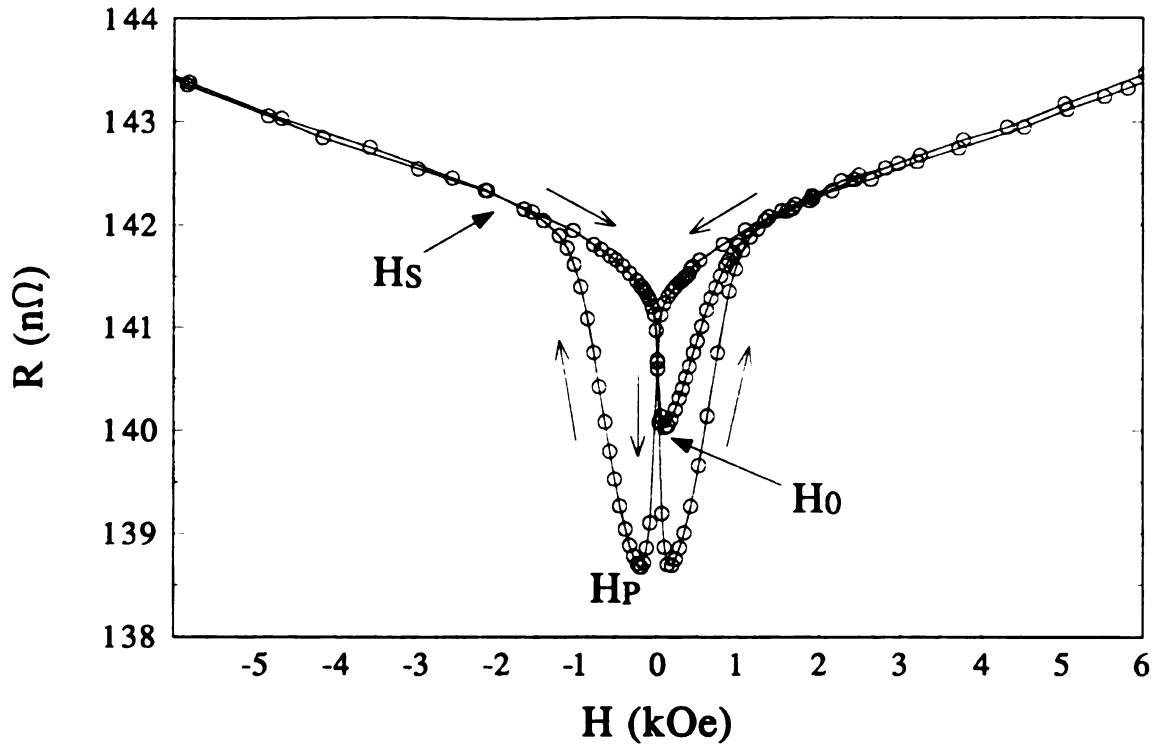

Figure 6.29: The field dependence of the CPP resistance is plotted for a multilayer of *[Co(0.4nm)/Cu(2.3nm)/FeV(6.0nm)/Cu(2.3nm)]×20*. The V concentration is 27%. Here the H_S resistance is the high resistance state. The MR of these samples are less than 3%.

[1] W.P. Pratt Jr., S.F. Lee, J.M. Slaughter, R. Loloee, P.A. Schroeder and J.Bass, Phys. Rev. Lett. **66**, 3060 (1991).

[2] R. Loloee, P.A. Schroeder, W.P. Pratt Jr., J. Bass and A. Fert, Physica **B204**, 274 (1995).

[3] S. Araki, K. Yasui and Y. Narumiya, J. Phys. Soc. Jpn. **60**, 2827 (1991).

[4] E.A.M. van Alphen, P.A.A. van der Heijden and W.J.M. de Jonge, J. Appl. Phys. **76**, 6607 (1994).

[5] R.Q. Hood and L.M. Falicov, Phys. Rev. **B46**, 8287 (1992); J. Magn. Magn. Mater., **121**, 362 (1993); Phys. Rev. **B49**, 368 (1994).

[6] Lithographic techniques have now been utilized to reduced the cross sectional area enough so that standard (non-SQUID based) measuring techniques are possible. M.A.M. Gijs, S.K.J. Lenczowski and J.B. Giesbers, Phys. Rev. Lett. **70**, 3343 (1993); M.A.M. Gijs *et al.*, Appl. Phys. Lett. **63**, 111 (1993); S.K.J. Lenczowski *et al.*, J. Appl. Phys. **75**, 5154 (1992).

[7] IBM hard drives now use GMR devices as read heads.

[8] S.S.P. Parkin, Phys. Rev. Lett. **67**, 493 (1991).

[9] T.L. Hylton, K.R. Coffey, M.A. Parker and J.K. Howard, Science **261**, 1021 (1993).

[10] B. Rodmarq, G. Palumbo and P. Gerard, J. Magn. Magn. Mater. **118**, L11 (1993).

[11] P.A. Schroeder, P. Holody, R. Loloee, J.L. Duvail, A. , L.B. Steren, R. Morel and A. Fert in *Magnetic Ultrathin Films: Multilayers and Surfaces*, edited by E.E. Marinero, B. Heinrich, W.F. Egelhoff Jr., A. Fert, H. Fujimori, G. Guntherodt and R.L. White, MRS Symposium Proceedings Vol. **384**, Material Research Society, Pittsburgh, PA., p. 415 (1995).

[12] T. Shinjo and H. Yamamoto, J. Phys. Soc. Jpn. **59**, 3061 (1990).

[13] T. Valet, J.C. Jacquet, P. Galtier, J. M. Coutellier, L.G. Pereira, R. Morel, D. Lottis and A. Fert, Appl. Phys. Lett. **61**, 3187 (1992).

[14] B. Dieny, V.S. Speriosu, S.S.P. Parkin and B.A. Gurney, Phys. Rev. **B43**, 1293 (1991).

[15] P. Holody, L.B. Steren, R. Morel, A. Fert, R. Loloee and P.A. Schroeder, Phys. Rev. **B50**, 12999 (1994).

[16] B.D. Cullity, *Introduction to Magnetic Materials*, Addison-Wesley, Reading, MA (1972) p.236.

[17] Y. Cheng and M.B. Sterns, unpublished; P. Galtier, unpublished.

[18] E. Bauer and J.H. van der Merwe, Phys. Rev. **B33**, 3657 (1986).

[19] J.R. Clem, Phys. Rev. **B43**, 7837 (1991).

[20] A. Vedyayev, C. Cowache, N. Ryzhanova and B. Dieny, J. Phys. Condens. Matter **5**, 8289 (1993).

[21] L.B. Steren, A. Barthélémy, J.L. Duvail, A. Fert, R. Morel, F. Petroff, P. Holody, R. Loloee and P.A. Schroeder, Phys. Rev. **B51**, 292 (1995).

[22] B. Dieny, V.S. Speriosu, S.S.P. Parkin, A Gurney, D.R. Wilhoit and D. Mauri, Phys. Rev. **B43**, 1297 (1991).

[23] M. Patel, T. Fujimoto, E. Gu, C. Daboo and J.A.C. Bland, J. Appl. Phys. **75**, 6528 (1994).

[24] A. Chaiken, G.A. Prinz and J.J. Krebs, J. Appl. Phys. **67**, 4892 (1990).

[25] B.D. Cullity, *Introduction to Magnetic Materials*, Addison-Wesley, Reading, MA (1972) p.585.

[26] H. Hegde, S.U. Jen, K. Chen and F.J. Cadieu, J. Appl. Phys. **73**, 5926 (1993).

[27] Y. Liu, B.W. Robertson, Z.S. Shan, S. Malhorta, M.J. Yu, S.K. Renukunta, S.H. Liou and D.J. Sellmyer, IEEE Trans. Magn. 30, 4035 (1994).

[28] Y. Okumura, H. Fujimori, O. Suzuki, N. Hosoyo, X.B. Yang and H. Morita, IEEE Trans. Magn. 30, 4038 (1994).

[29] E.M.T. Velu, D.N. Lambeth, J.T. Thornton and P.E. Russell, J. Appl. Phys. **75**, 6132, (1994).

[30] K. Chen, H. Hegde and F.J. Cadieu, Appl. Phys. Lett. **61**, 1861 (1992).

[31] K. Chen, H. Hegde, S.U. Jen and F.J. Cadieu, J. Appl. Phys. **73**, 5923 (1993).

[32] S.F. Lee, *et al.*, J. Magn. Magn. Mater. **118**, L1 (1993); Phys. Rev. **B46**, 548 (1992).

[33] P.A. Schroeder, J. Bass, P. Holody, S.F. Lee, R. Loloee, W.P. Pratt Jr. and Q. Yang, NATO ASI Series B **309**, 129 (1993).

[34] P. Holody, to be published.

[35] J.E.C. Williams, Superconductivity and its Applications, Pion Ltd., London, England (1970) p.47.

[36] S.F. Lee, Ph.D. Dissertation, Michigan State University (1994).

[37] For a proper analysis of Py/Ag multilayers, several series similar to those done by Lee in Ref. 30 must be measured and globally fit to obtain the parameters $AR_{Py/Ag}$, β and γ.

[38] Attempts thus far have not been completed by W.P. Pratt, Jr., *et al.*

[39] A.M. Gijs and M. Okada, Phys. Rev. **B46**, 2908 (1992).

[40] J. Inoue and S. Maekawa, Prog. Thoer. Phys. **106**, 187 (1991).

[41] A. Fert and I.A. Campbell, in *Ferromagnetic Materials*, edited by E.P. Wohlfarth (North-Holland, Amsterdam, 1982), Vol. **3**, p.769.

[42] F. Petroff, A. Barthélémy, D.H. Mosca, D.K. Lottis, A. Fert, P.A. Schroeder, W.P. Pratt Jr., R. Loloee and S. Lequien, Phys. Rev. **B44**, 5355 (1991).

[43] S. Pizzini, F. Baudelet, D. Chandesris, A. Fountaine, H. Magnan, J.M. George, F. Petroff, A. Barthélémy, A. Fert, R. Loloee and P.A. Schroeder, Phys. Rev. **B46**, 1253 (1992).

[44] A. Fert and I.A. Campbell, J. Phys. F 6, 849 (1976).

[45] A. Fert and I.A. Campbell, in *Ferromagnetic Materials*, edited by E.P. Wohlfarth (North-Holland, Amsterdam, 1982), Vol. **3**, p.752.

[46] S.S.P. Parkin, N. More and K.P. Roche, Phys. Rev. Lett. **64**, 2304 (1990).

[47] T.C. Slonczewski, Phys. Rev. Lett. **67**, 3172 (1991).

[48] P.E. Camley and J. Barnas, Phys. Rev. Lett. **63**, 664 (1989).

[49] J.M. George, L.G. Pereira, A. Barthélémy, F. Petroff, L.B. Steren, J.L. Duvail, A. Fert, R. Loloee, P. Holody and P.A. Schroeder, Phys. Rev. Lett. **72**, 408 (1994).

[50] S. Zhang and P. Levy, Mater. Res. Soc. Symp. Proc. **313**, 53 (1993).

[51] J.P. Renard, P. Bruno, R. Mégy, B. Bartenlian, P. Beauvillain, C. Chappert, C. Dupas, E. Kolb, M. Mulloy, P. Veillet and E. Vélu, Phys. Rev. **B51**, 12821 (1995).

[52] A. Barthélémy, *et al.*, to be published.

Chapter 7:

Summary and Conclusions

In this dissertation the transport properties of several magnetic multilayered systems were studied in detail. Transport in these systems has been successfully described by the two spin channel model. In the limit where spin flipping is negligible, the current is independently carried by parallel channels of spin up and spin down electrons. Large negative MR's arise from *spin dependent scattering* occurring in these channels. Electrons with their spins parallel to the local magnetization undergo a different amount of scattering from those with their spins antiparallel to the local magnetization. Consequently, the sample's resistance can be controlled through the relative orientation of the F layer magnetizations. Usually multilayers with adjacent F moments aligned antiparallel (parallel) have a high (low) resistance, so that changing from an antiparallel to a parallel alignment produces a decrease in the resistance. Various methods of producing GMR by changing from antiparallel to parallel alignment have been used in the following projects studied in this thesis.

(1) *Determination of Spin Dependent Scattering Parameters for Important Systems.* One of the first objectives is to decide where the spin dependent scattering occurs, in the

bulk F metal or at the F/N interfaces. This separation is clearly made through CPP measurements.

(2) *Determination of Spin Diffusion Lengths.* The analysis used in (1) above depends on the spin diffusion length being much greater than the layer thickness of each constituent. The CPP geometry provides a good method of determining spin diffusion lengths.

(3) *Spin Engineering.* Designing multilayers systems to have specific properties.

a) Systems with Two Ferromagnetic Components - CIP Hybrid Systems.

b) Systems with Two Ferromagnetic Components - CPP Hybrid Systems.

c) Systems having a Positive Magnetoresistance.

Conclusions from these projects are outlined below.

Magnetic multilayered systems were fabricated using a computer controlled Tri-mag sputtering system. An *in situ* masking system gave samples a well defined geometry which allowed the measuring current to be applied in the directions parallel (CIP geometry) and perpendicular (CPP geometry) to the layers. After fabrication, x-ray diffraction at both high and low angles was used to check a sample's crystal structure and bilayer thickness. For several multilayer systems a metal alloy was sputtered. The alloy concentration was measured using energy dispersive x-rays. Results from structural studies performed by others on our sputtered samples were given in chapter 3.

(1) Determination of Spin Dependent Scattering Parameters for Important Systems.

The results for the study of the Co/Cu system are given in section 5.1. Three distinct resistance states are observed in both the CIP and CPP samples. These are the H_0 state

with the as-deposited resistance, the H_S the state with the saturation resistance and the H_P the state with the highest resistance after the sample has been saturated.

For samples with negative MR's the highest resistance state typically occurs for the H_0 resistance and is therefore chosen as the AP state. The H_S resistance has the lowest resistance and is used for the P state.

Three separate series of Co/Cu multilayers were studied in which the total thickness was held constant and the Co thickness was constrained to $t_{Co}=1.5nm$, $t_{Co}=6.0nm$ or $t_{Cu}=t_{Co}$. To simplify the analysis all samples had $t_{Cu}>6.0nm$ which eliminated the complication of exchange coupling. The spin asymmetry parameters for both bulk Co and the Co/Cu interface were estimated by globally fitting the three Co/Cu series to the equations derived in chapter 4 based on the two channel model. It was found that the Co/Cu interfaces contribute significantly to the multilayer's total resistance, with a Co/Cu interface having a resistance the same as a Co thickness of 7.0nm. In addition, the bulk asymmetry parameter ($\alpha_{Co/Cu}=7.7$) was found to be greater than the interface asymmetry parameter ($\alpha_{Co}=2.7$). Therefore for a sample in which the total resistance of the multilayer is equally divided between $\rho_{Co}t_{Co}$ and $AR_{Co/Cu}$ (this corresponds to $t_{Co}=7.0nm$), the Co/Cu interface contribution to the spin dependent scattering will be nearly three times larger than the contribution to the spin dependent scattering from bulk Co.

A similar study was done on Py/Cu multilayers in section 5.2. The low coercive field of the Py lead to some ambiguities in the H_0 data. For thick Cu layers in the 1.5nm and 6.0nm Py data, the H_0 data were generally the state with the highest resistance. In cases where $AR(H_0)<AR(H_P)$, demagnetizing the sample resulted in $AR(H_D)>AR(H_0)$. For

these particular samples the AR(H_D) data were used as the AP state in the fitting. The data were analyzed in terms of the two channel model and global fits were made to equations derived in chapter 4. Fit A only considered the Py 1.5nm and 6.0nm sets of data while Fit B included the H_S data for the $t_{Py}=t_{Cu}$. (The H_0 data for the $t_{Py}=t_{Cu}$ series were not included in either fit because it was determined that the presence of a small field inside the sputtering system at the position of the substrate could be enough to alter the H_0 resistance of samples with very thick Py layers.) Overall the parameters from Fit B describe the Py/Cu system better. Fit B reasonably describes all three sets of Py/Cu data and is within the uncertainties of the independently determined Py resistivity. In contrast, while Fit A agrees better with independent measurements of the Py resistivity and fits the 1.5nm and 6.0nm Py data well, it does not represent the H_S data for the $t_{Py}=t_{Cu}$ samples well at all.

The α_{Py} values are somewhat smaller than one might have expected. The expectation that a Ni-Fe alloy should produce more spin dependent scattering in the bulk F metal than at the Py/Cu interfaces is not justified by our data. At best (Fit B) $\alpha_{Py/Cu}\approx\alpha_{Py}$ meaning that for a Py thickness of 2.0nm, the interface and bulk spin dependent scattering contributions are roughly equal.

The possibility of a finite spin diffusion length in Py was not considered in the analysis done on the Py/Cu system. If $\ell_{sf}^{Py} \leq t_{Py}$ then, to first order, only the Py within a spin diffusion length of the interface will contribute to the magnetoresistance. Since the

analysis done here assumes an infinite $\ell_{sf}^{Py} = \infty$, the value of α_{Py} would be underestimated if ℓ_{sf}^{Py} was indeed finite.

(2) Determination of Spin Diffusion Lengths.

Finite spin diffusion length (SDL) effects were studied in section 6.1 for Co/CuX multilayers where X=Pt, Mn, Ge and Ni. The Valet-Fert theory predicted a rapid drop in the MR as ℓ_{sf} approached the layer thickness of either the N or F metals. These predictions showed that a finite SDL had a stronger effect in the N metal than in the F metal. So impurities which flipped spins were added to Cu to reduce the SDL of Cu. The Pt, Ge and Ni impurities increased spin flips by increasing the spin orbit scattering in the Cu layers. The Mn impurities flipped spins via an exchange scattering. The best fit parameters for ℓ_{sf}^{CuX} agree well with estimates of the SDL based on ESR measurements of spin orbit cross sections.

Finite SDL effects were also examined for the t_{Co}=t_{Cu} data from section 5.1. The slight curvature of the square root data for thick Co layers could be explained by introducing a SDL in either the Cu or the Co. Plots comparing the t_{Co}=t_{Cu} data and predicted SDL in both Co and Cu are given at the end of section 6.1.

(3) Spin Engineering : a) Systems with Two Ferromagnetic Components - *CIP Measurements on a Hybrid System.*

Ordinarily coupling between magnetic layers is used to align adjacent magnetic layers antiparallel. However, an AP state may be formed if the adjacent magnetic layers have a large difference in their coercive forces. Here Py with its very low coercive field and Co with its higher coercive field are used to make an AP state. The contrast between the Py and Co is further enhanced by the thickness of the F metals. The Py is thick enough to form continuous layers but the Co is thin enough to be composed of discontinuous island-like structures.

These hybrid samples show remarkable transport properties at low temperatures. The MR changes rapidly in the vicinity of the Py coercive field, over 5%/Oe for CIP samples with a Ag spacer layer. However, superparamagnetism in the island-like Co clusters reduces the coercivity of these clusters to zero above the blocking temperature which severely reduces the MR in these samples at room temperature.

To raise the blocking temperature, the anisotropy energy, KV, of the Co clusters must be increased. This is done by increasing either the size of the particles or the strength of the anisotropy. Although the blocking temperature did increase with the thickness of the Co layer, it never reached room temperature. Adding Sm 10 at.% to the Co also failed to increase the strength of the anisotropy enough to bring the blocking above room temperature. Samples of Co/Ag and Py/Ag deposited in a magnetic field showed that an easy axis could be induced in sputtered samples. However, a blocking temperature above

room temperature was not seen. It is believed that inducing an easy axis in the Co/Ag/Py/Ag system should increase $\Delta R/\Delta H$ beyond 5%/Oe.

(3) Spin Engineering : b) Systems with Two Ferromagnetic Components - *CPP Measurements on Hybrid System.*

The Co/Ag/Py/Ag system (with a nominal Co thickness of 0.4nm) was studied as function of the Py thickness in the CPP geometry in section 6.2. Fields of 5.0kOe were required to saturate the discontinuous Co layers. The high saturation field caused flux trapping by the Nb leads. After expelling this trapped field the $\Delta R/\Delta H$ near the Py coercive field for the CPP geometry was found to be $\approx$10%/Oe, two times larger than for the CIP geometry. The MR was also 2 times larger in the CPP direction. The data for AR_T was compared to a two spin channel model which simultaneously varied the area of the Co/Ag interface and thickness of the Co layers such that the total volume of Co was held constant. The best fit was obtained for an effective Co thickness of 0.6nm. In addition the ΔAR_T data was compared with the two spin channel model in the limits of infinite and zero spin diffusion length. The ΔAR_T data seems to remain independent of the Py thickness beyond 20.0nm. The samples with very thick Py layers do not fit either limit of the model very well. The AR_T of these samples are much lower than the model predicts, suggesting this model is too simplistic to represent the thick Py samples.

(3) Spin Engineering : c) Systems Having a Positive Magnetoresistance.

A system designed to produce a positive MR was examined. The first observations of positive MR were made on CIP samples of M_1/Cu/M_2/Cu, where M_1=Fe/Cr/Fe and M_2=Fe. Measurements showed a small positive MR whose magnitude was dependent upon the Cu spacer thickness. The field dependent features of the MR and magnetization correlate well. Coupling through the Cr layer in M_1 complicated the analysis of the results. In addition, the first positive CPP-MR observations were made on the Co/Cu/FeV/Cu system. These samples also exhibit MR's of only a few percent.

All analyses in this study were done in the context of the two spin channel model, considering only the AP and P states. All of these results hinge on our choice of the H_0 resistance as the best approximation for the AP state. Experimentally the H_0 resistance seems to be unique and after saturation of the sample it can never be restored. Some experimental evidence was presented in chapter 5 which indicated that the H_0 resistance at least behaves like an AP state. Experiments using CPP hybrid samples of Co/Ag/Py/Ag and CPP spin valves with Py and Cu are currently underway in the department that will confirm (or otherwise) this assumption. However, it is unclear why the H_0 resistance should act like the AP resistance.

New Directions:

(1) Measurements of a series of F/N multilayers in which either the interface spin dependent scattering or the bulk spin dependent scattering is varied would provide useful information about how these parameters depend on the character of the F/N interface and

the bulk F metal. Some CoFe/Cu multilayers[1] have exhibited an enhanced MR (relative to Co/Cu multilayers) near 10 at.% Fe concentrations. A series of $Co_{(1-x)}Fe_x$/Cu CPP multilayers which vary the Fe concentration should reveal a maximum in the bulk F metal spin asymmetry parameter. Also it has been reported that a magnetically dead layer of Py exists at the Py/Cu interface[2]. Depositing a thin layer of Co at the interface should increase the interface spin dependent scattering. This has already been done for CIP multilayers by others.

(2) Measurements of the dependence of the MR on the angle between the F layers for a CPP spin valve should provide insight on the question of scattering from potential steps at the F/N interfaces.

(3) Extending the work started here on depositing magnetic multilayers in a magnetic field should prove interesting. Hybrid samples with induced easy axes in both the Co and Py layers should improve $\Delta R/\Delta H$. Hybrid samples using CoSm which is deposited in a field may prove to have T_B above room temperature. Interesting initial magnetic configurations of multilayers could be studied by applying a field during deposition at particular angles with each magnetic layer. For example inducing easy axes at 90° from one F layer to the next could be used to study biquadratic coupling in magnetic multilayers.

---

[1] K. Inomata, Y. Saito and S. Hashimoto, J. Magn. Magn. Mater. **121**, 350 (1993).

[2] J.P. Nozieres, V.S. Speriosu, B.A. Gurney, B. Dieny, H. Lefakis and T.C. Huang, J. Magn. Magn. Mater. **121**, 386 (1993).